RS2

2D finite element program for stress analysis and support design
around excavations in soil and rock

Stress Analysis Verification Manual

Table of Contents

1 Cylindrical Hole in an Infinite Elastic Medium

1.1 Problem Description

This problem considers the case of a cylindrical tunnel of radius 1 m in an isotropic, ideal elastic medium. The medium is assumed to apply a hydrostatic compressive stress field of 30 MPa. Figure 1.1 shows the model configuration, including boundary conditions, and Table 1.1 summarizes the material properties and other parameters. The tunnel radius is assumed to be small enough relative to its length that plane strain conditions are in effect.

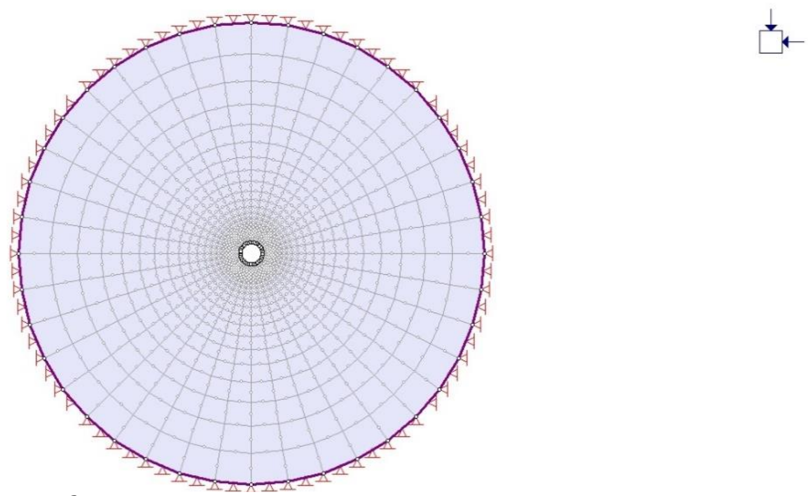

Figure 1.1: *RS2* [2] model of cylindrical hole in an infinite elastic medium

Table 1.1: Model parameters

Parameter	***Value***
Young's modulus (E)	10000 MPa
In-situ stress field (p_1, p_2)	30 MPa
Poisson's ratio (v)	0.2

The ***RS2*** model shown in Figure 1.1 uses a radial mesh containing 840 8-noded quadrilateral elements and a fixed external boundary 21 m from the hole centre. The tunnel is discretized into 40 segments.

1.2 Analytical Solution

Assuming conditions of plane strain, the radial and tangential stress and displacement fields in this problem can be predicted using the classical Kirsch equations [1]. Using polar coordinates (r,θ):

$$\sigma_r = \frac{p_1 + p_2}{2}(1 - \frac{a^2}{r^2}) + \frac{p_1 - p_2}{2}\left[1 - \frac{4a^2}{r^2} + \frac{3a^4}{r^4}\right]\cos 2\theta$$

$$\sigma_\theta = \frac{p_1 + p_2}{2}(1 + \frac{a^2}{r^2}) - \frac{p_1 - p_2}{2}(1 + \frac{3a^4}{r^4})\cos 2\theta$$

$$\tau_{r\theta} = -\frac{p_1 - p_2}{2}(1 + \frac{2a^2}{r^2} - \frac{3a^4}{r^4})\sin 2\theta$$

$$u_r = \frac{p_1 + p_2}{4G}\frac{a^2}{r} + \frac{p_1 - p_2}{4G}\frac{a^2}{r}[4(1-\nu) - \frac{a^2}{r^2}]\cos 2\theta$$

where σ_r and σ_θ represent the radial and tangential stress and μ_r the radial displacement. Figure 1.2 shows the parameters used in the above equations schematically.

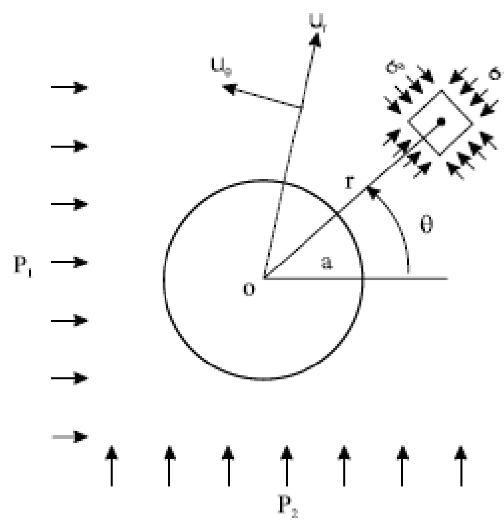

Figure 1.2: Parameters for Kirsch equations

1.3 Results

Figure 1.3, Figure 1.4, and Figure 1.5 plot radial stress, tangential stress, and total displacement with respect to radial distance for the results of each computation. As can be seen, the results from ***RS2*** are very similar to those predicted by the closed form solution. Table 1.2 quantifies the error present in the ***RS2*** analysis.

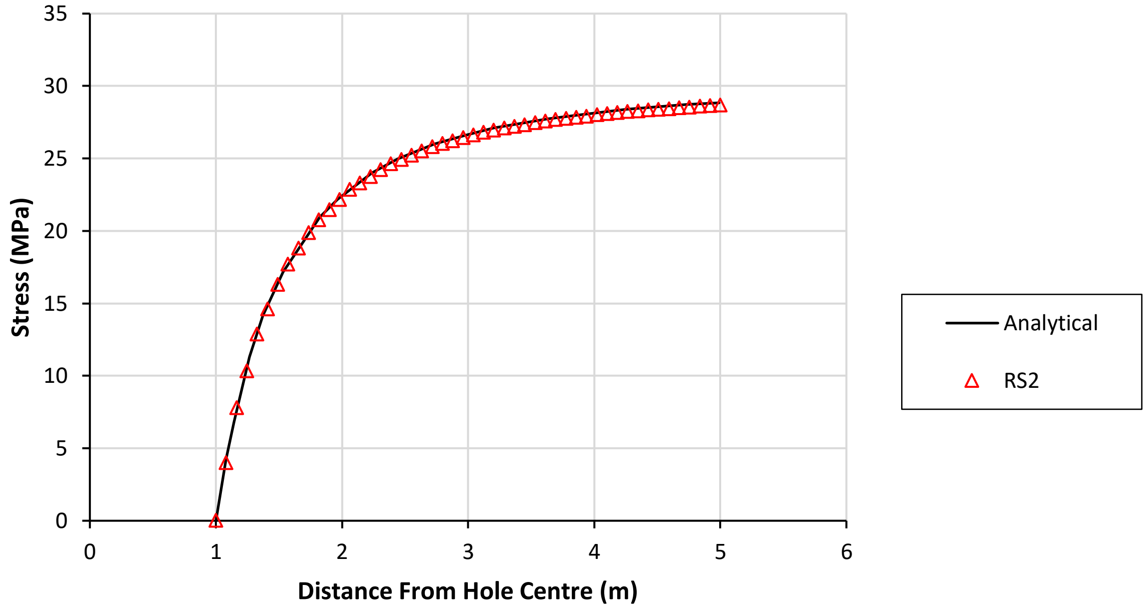

Figure 1.3: Comparison of radial stress distributions

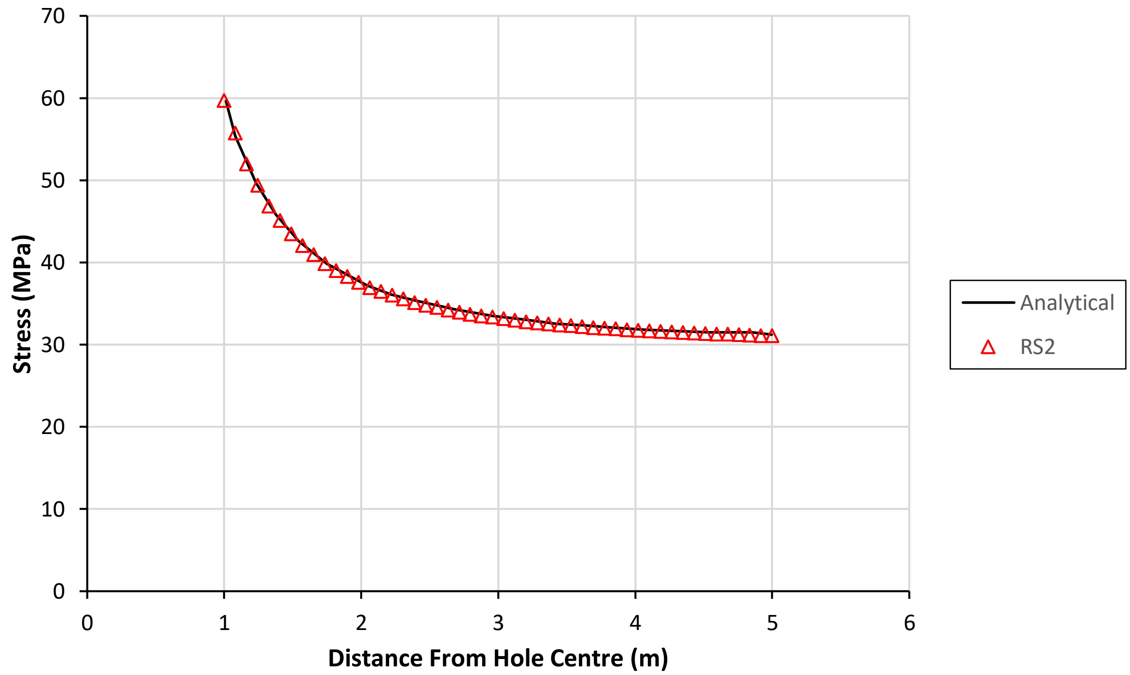

Figure 1.4: Comparison of tangential stress distributions

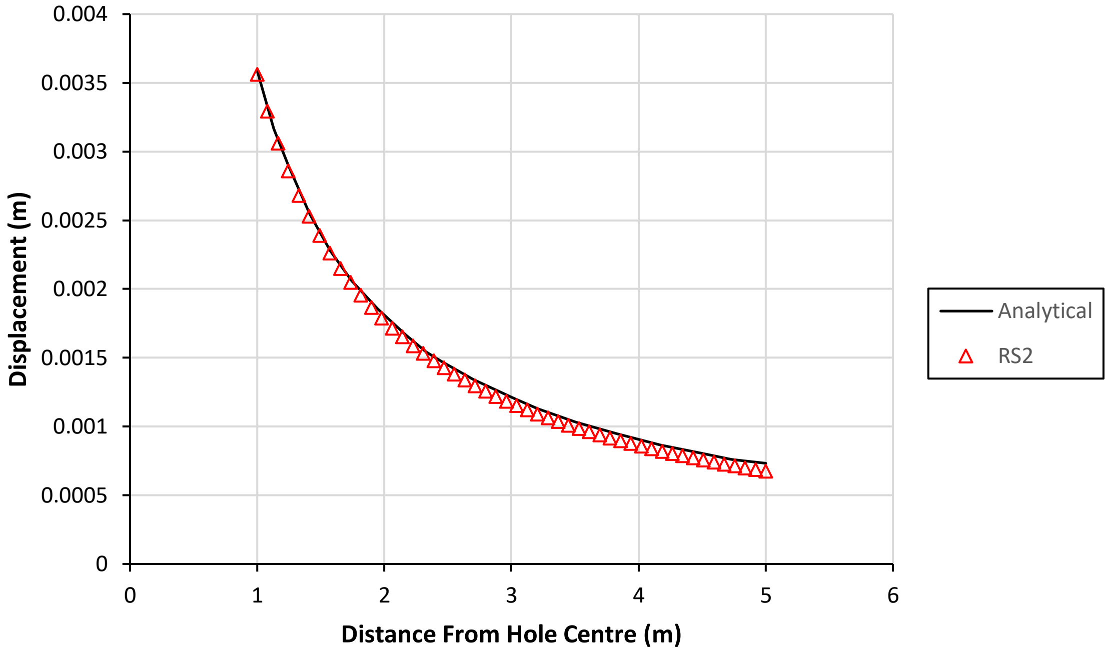

Figure 1.5: Comparison of displacement distributions

Table 1.2: Error in *RS2* analysis relative to analytical solution

	Maximum	Hole Boundary
Displacement	2.8111E-05	3.7796E-05
Radial stress	0.2386	0.0154
Tangential stress	0.2485	0.2485

Figure 1.6, Figure 1.7 and Figure 1.8 illustrate the stress and displacement contours around the hole.

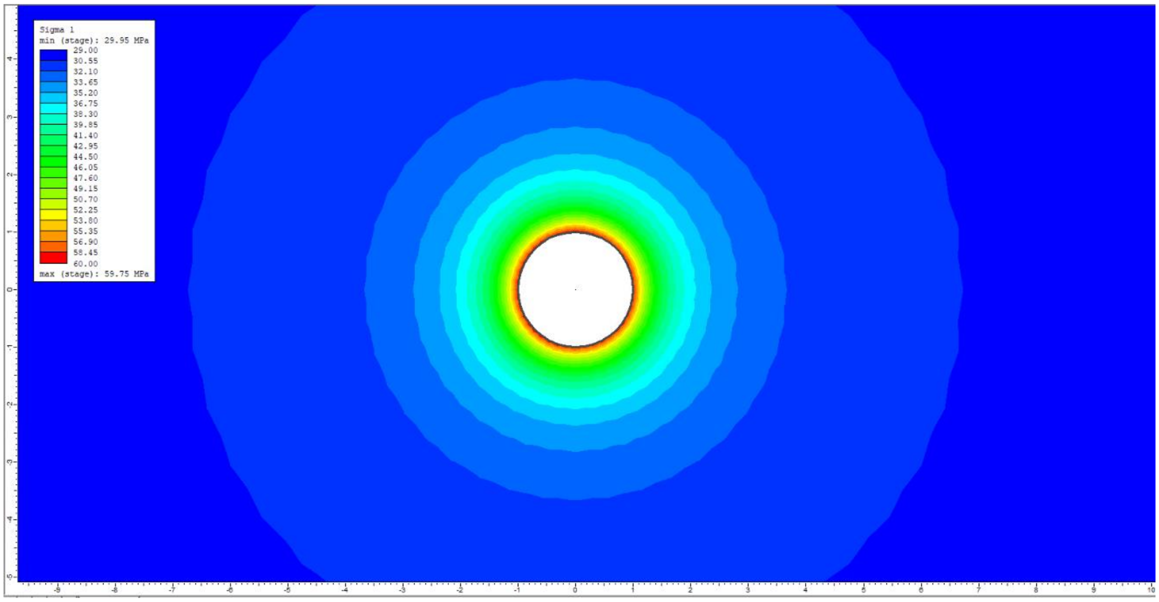

Figure 1.6: Tangential stress contours in *RS2*

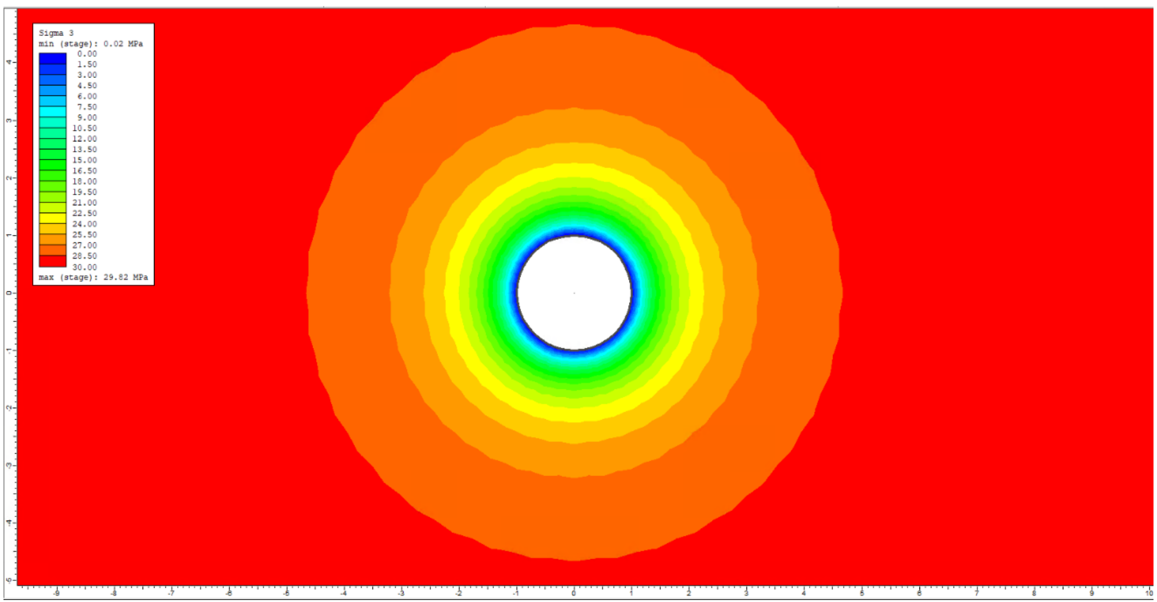

Figure 1.7: Radial stress contours in *RS2*

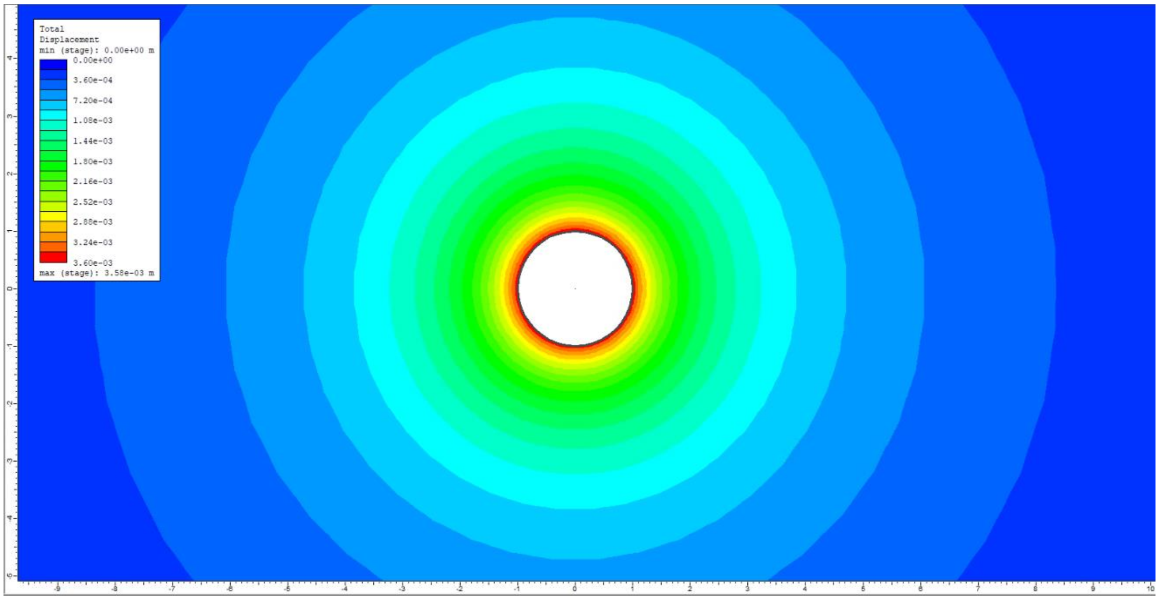

Figure 1.8: Total displacement contours in *RS2*

1.4 References

1. Jaeger, J.C. and N.G.W. Cook. (1976) "Fundamentals of Rock Mechanics", 3rd Ed. London, Chapman and Hall.

1.5 Data Files

The input file **stress#001.fez** can be downloaded from the RS2 Online Help page for Verification Manuals.

2 Cylindrical Hole in an Infinite Mohr-Coulomb Material

2.1 Problem Description

The second verification problem considers the case of a cylindrical hole in an isotropic, ideal elastoplastic material subjected to a hydrostatic compressive stress field. The surrounding medium undergoes failure according to the Mohr-Coulomb criterion. Two cases are tested using associated (dilatancy = friction angle) and non-associated (dilatancy = 0) flow. Figure 2.1 shows the problem as implemented in ***RS2***, while Table 2.1 summarizes pertinent model parameters. The radius of the tunnel is assumed to be small enough relative to its length that plane strain conditions are in effect.

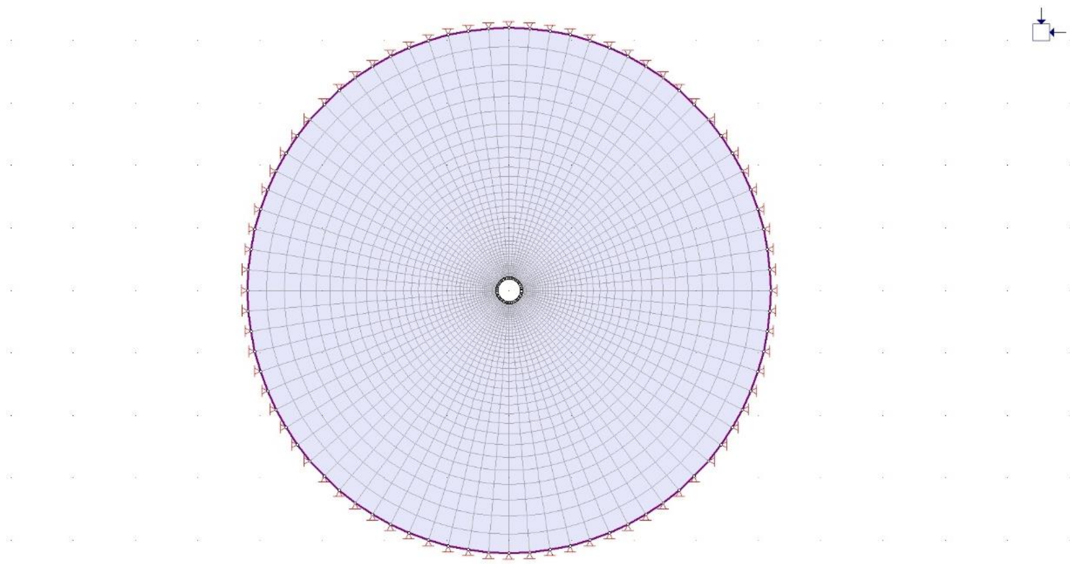

Figure 2.1: *RS2* model and boundary conditions for cylindrical tunnel in Mohr-Coulomb medium

Table 2.1: Model parameters

Parameter	Value
Young's modulus (E)	10000 MPa
In-situ stress field (P_0)	30 MPa
Poisson's ratio (v)	0.2
Cohesion (c)	3.45 MPa
Friction angle (ϕ)	30°
Hole radius (a)	1 m
Shear modulus (G)	4166.667 MPa
Dilation angle (ψ)	0°, 30°

The ***RS2*** model constructed uses a radial mesh with 3200 4-noded quadrilateral elements, a fixed external boundary 21 m from the hole centre, and a hydrostatic compressive stress field of 30 MPa.

2.2 Analytical Solution

According to Salencon (1969) [1], the yield zone radius R_0 is given by:

$$R_0 = a\left(\frac{2}{K_p+1}\frac{P_0+\frac{q}{K_p-1}}{P_i+\frac{q}{K_p-1}}\right)^{1/(K_p-1)}$$

where

$$K_p = \frac{1+\sin\phi}{1-\sin\phi}$$

$$q = 2c\tan(45+\phi/2)$$

P_i = internal pressure = 0 MPa

The radial stress at the elastic-plastic interface is:

$$\sigma_{re} = \frac{1}{K_p+1}(2P_o - q)$$

In coordinates (r, θ), stresses and radial displacement in the elastic zone are:

$$\sigma_r = P_o - (P_o - \sigma_{re})\left(\frac{R_o}{r}\right)^2$$

$$\sigma_\theta = P_o + (P_o - \sigma_{re})\left(\frac{R_o}{r}\right)^2$$

$$u_r = \frac{R_0^2}{2G}\left(P_0 - \frac{2P_0-q}{K_p+1}\right)\frac{1}{r}$$

The stresses and radial displacement in the plastic zone are:

$$\sigma_r = -\frac{q}{K_p-1} + \left(P_i + \frac{q}{K_p-1}\right)\left(\frac{r}{a}\right)^{(K_p-1)}$$

$$\sigma_\theta = -\frac{q}{K_p-1} + K_p\left(P_i + \frac{q}{K_p-1}\right)\left(\frac{r}{a}\right)^{(K_p-1)}$$

$$u_r = \frac{r}{2G}\left[(2\nu-1)\left(P_0+\frac{q}{K_p-1}\right)+\frac{(1-\nu)(K_p^2-1)}{K_p+K_{ps}}\left(P_i+\frac{q}{K_p-1}\right)\right.$$
$$\left.\left(\frac{R_0}{a}\right)^{(K_p-1)}\left(\frac{R_0}{r}\right)^{(K_{ps}+1)}+\left(\frac{(1-\nu)(K_pK_{ps}+1)}{K_p+K_{ps}}-\nu\right)\left(P_i+\frac{q}{K_p-1}\right)\left(\frac{r}{a}\right)^{(K_p-1)}\right]$$

where

$$K_{ps}=\frac{1+\sin\psi}{1-\sin\psi}$$

2.3 Results

Figure 2.2, Figure 2.3, and Figure 2.4 show stress and displacement results for the first model ($\psi = 0°$).

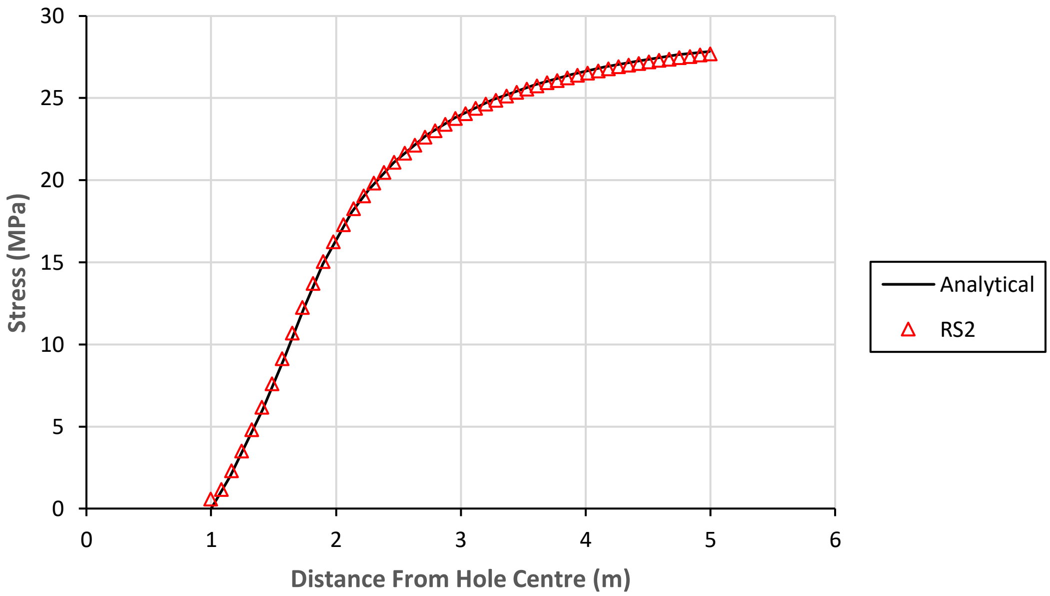

Figure 2.2: Comparison of radial stress distributions (ψ=0°)

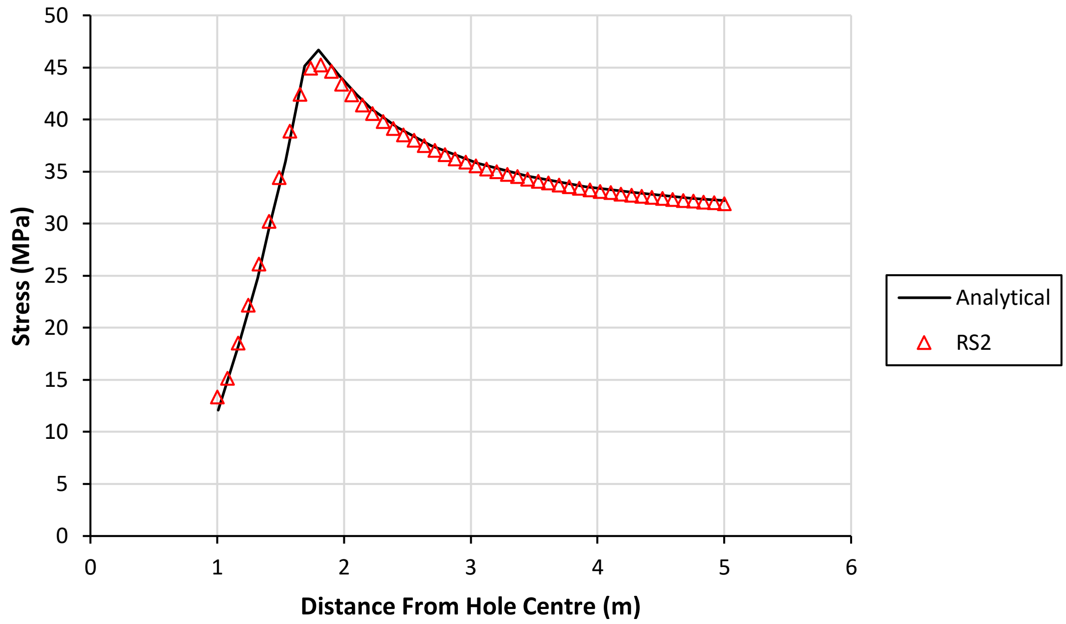

Figure 2.3: Comparison of tangential stress distributions (ψ=0°)

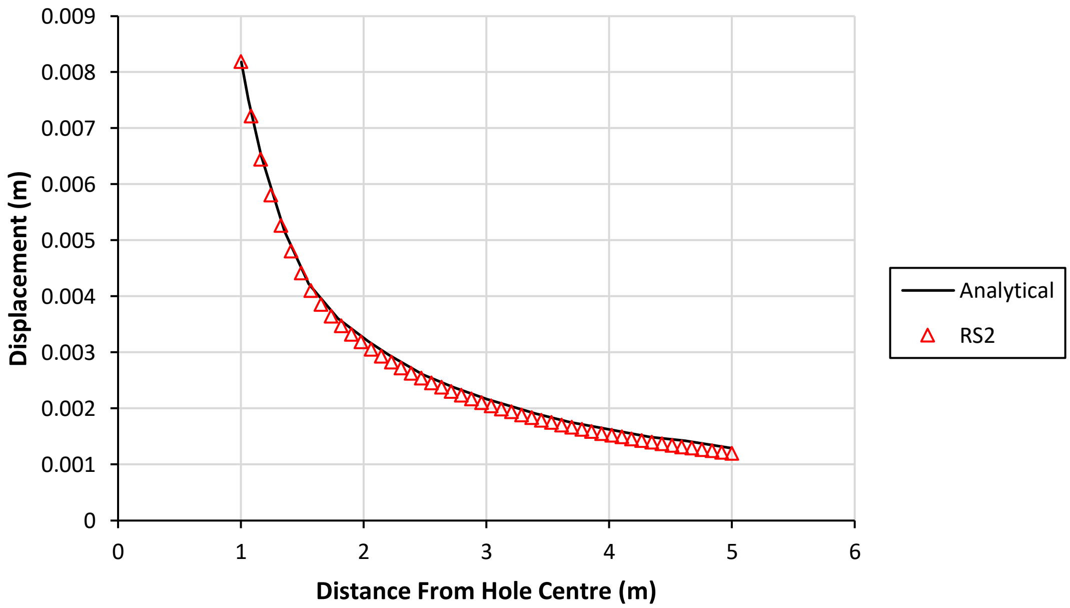

Figure 2.4: Comparison of radial displacement distributions (ψ=0°)

Figure 2.5, Figure 2.6, and Figure 2.7 show similar results for a dilation angle of 30°.

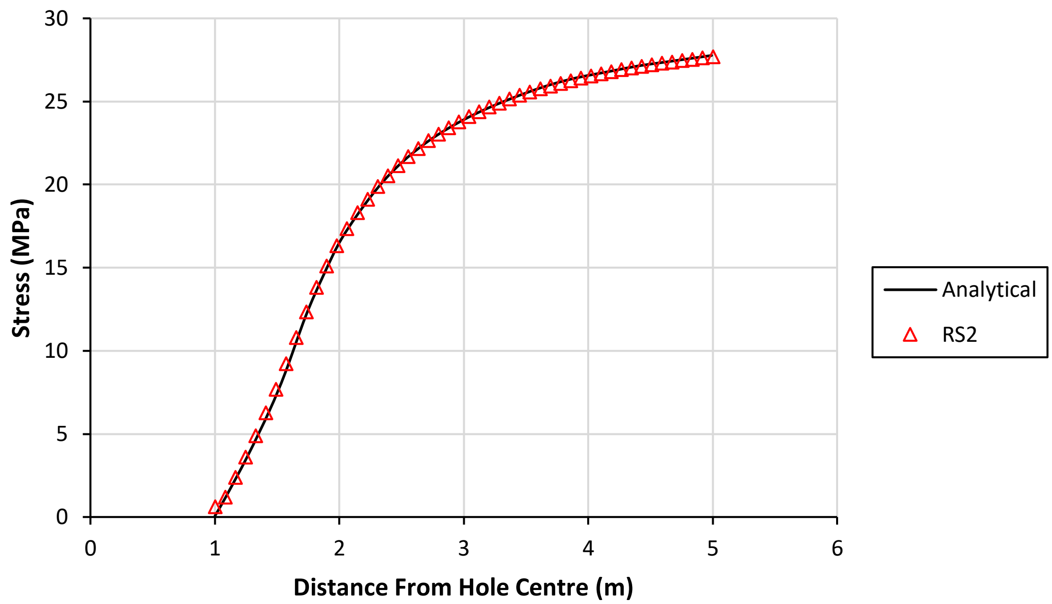

Figure 2.5: Comparison of radial stress distributions (ψ=30°)

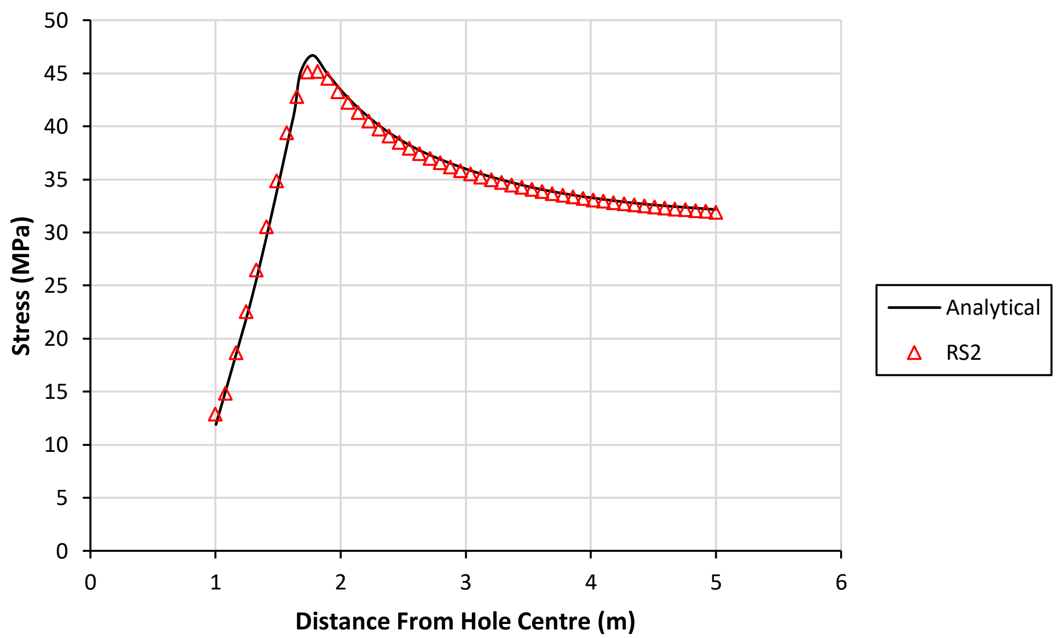

Figure 2.6: Comparison of tangential stress distributions (ψ=30°)

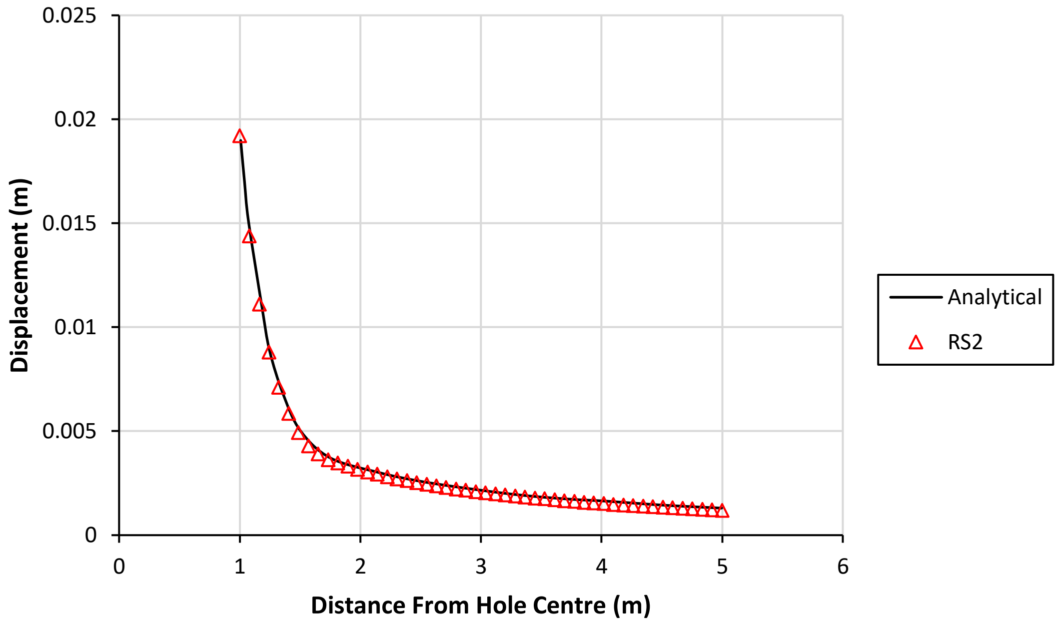

Figure 2.7: Comparison of radial displacement distributions (ψ=30̊)

Figure 2.8, Figure 2.9, Figure 2.10, and Figure 2.11 show the stress, displacement and failure contour plots produced by ***RS2*** for the first case (ψ=0̊).

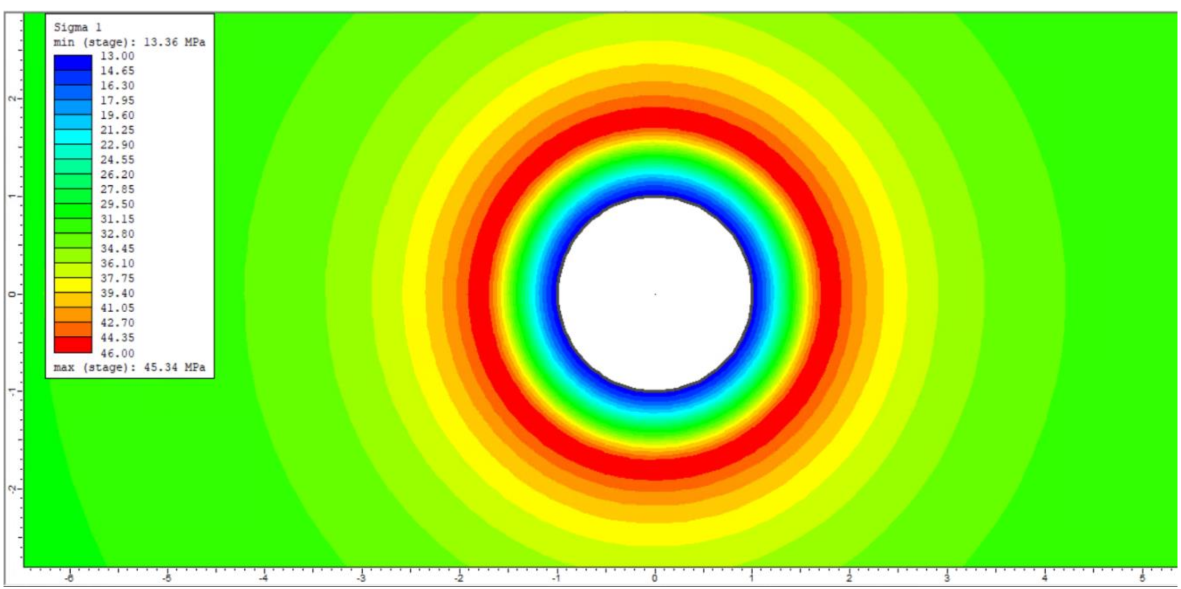

Figure 2.8: Tangential stress contours in *RS2*

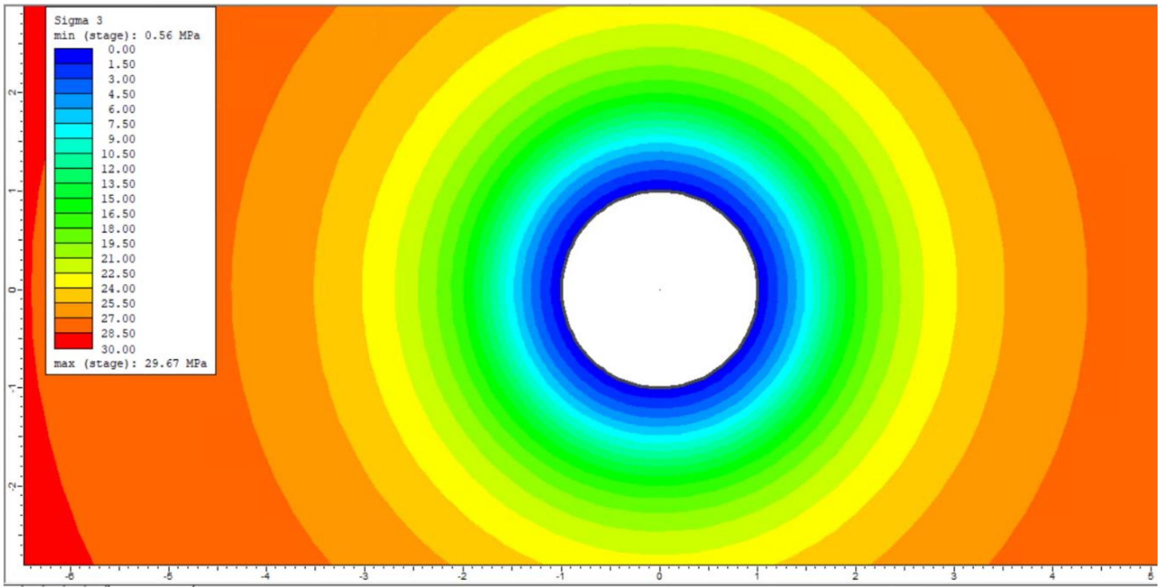

Figure 2.9: Radial stress contours in *RS2*

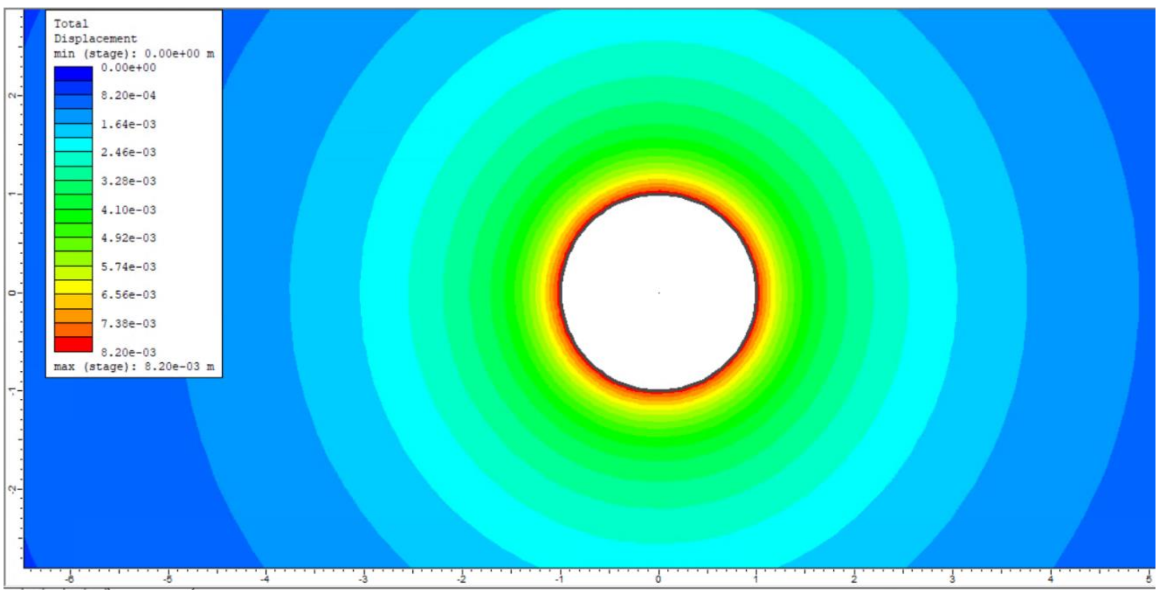

Figure 2.10 Total displacement contours in *RS2*

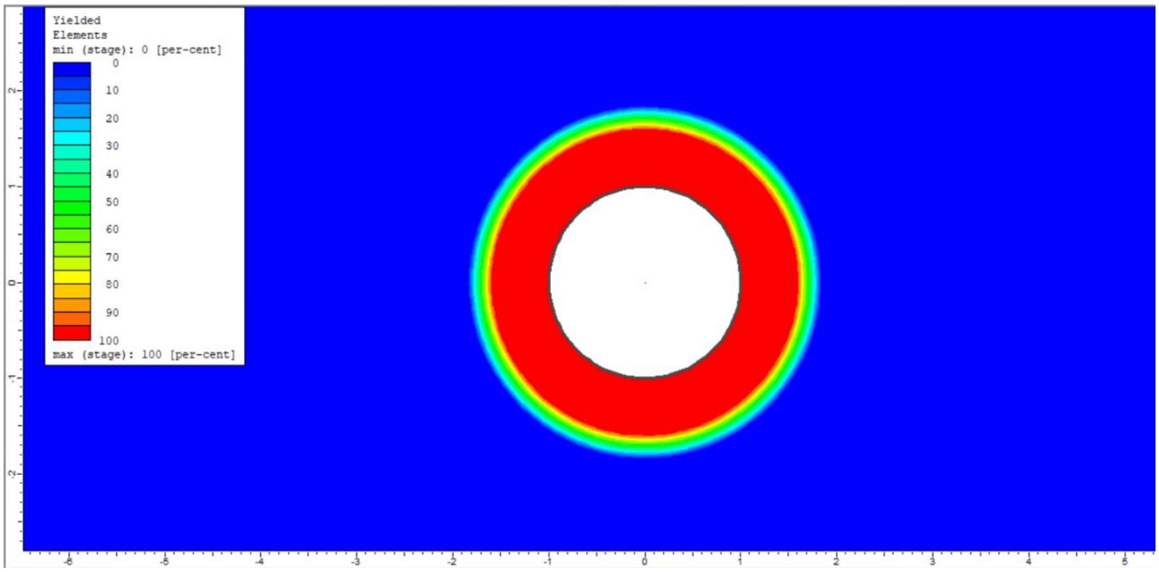

Figure 2.11: Plastic zone in *RS2*

2.4 References

1. Salencon, J. (1969), "Contraction Quasi-Statique D'une Cavite a Symetrie Spherique Ou Cylindrique Dans Un Milieu Elasto-Plastique", Annales Des Ports Et Chaussees, Vol. 4, pp. 231-236.
2. Itasca Consulting Group, INC (1993), "Cylindrical Hole in an Infinite Mohr-Coulomb Medium", *Fast Lagrangian Analysis of Continua* (Version 3.2), Verification Manual.

2.5 Data Files

The input files **stress#002_01.fez** ($\psi=0°$) and **stress#002_02.fez** ($\psi=30°$) can be downloaded from the RS2 Online Help page for Verification Manuals.

3 Cylindrical Hole in an Infinite Hoek-Brown Medium

3.1 Problem Description

This problem addresses the case of a cylindrical tunnel in an infinite Hoek-Brown medium subjected to a uniform compressive in-situ stress field. Materials with failure surfaces defined according to the Hoek-Brown criterion have non-linear and stress-dependent strength properties. Plane strain conditions are assumed.

Figure 3.1 shows the model configuration and Table 3.1 summarizes the model parameters.

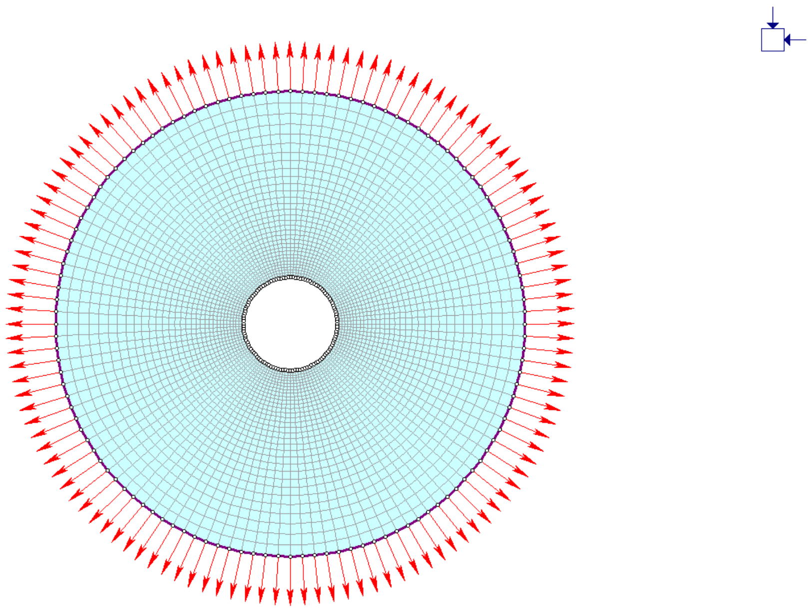

Figure 3.1: Circular tunnel in Hoek-Brown medium as constructed in *RS2*

Table 3.1: Model parameters

Model Specifications and Material Properties	***Value***
In-situ stress field (P_0)	30 MPa
Hole radius (a)	1 m
Young's modulus (E)	10000 MPa
Poisson's ratio (v)	0.25
Uniaxial compressive strength of intact rock (σ_c)	100 MPa
Dilation parameter	0°, 30°
m	2.515
s	0.003865
m_r	0.5
s_r	1e10^{-5}

The ***RS2*** model constructed uses a radial mesh with 3960 4-noded quadrilateral elements and an in-situ hydrostatic stress field of 30 MPa. The opening is discretized into 120 segments; infinite elements are used on the external boundary, which is located 5 m from the centre of hole.

3.2 Analytical Solution

According to [1] and [2], the radius of the yield zone r_e is given by:

$$r_e = ae^{\left[N - \frac{2}{m_r\sigma_c}\left(m_r\sigma_c P_i + s_r\sigma_c^2\right)^{1/2}\right]}$$

where

$$N = \frac{2}{m_r\sigma_c}\left(m_r\sigma_c P_0 + s_r\sigma_c^2 - m_r\sigma_c^2 M\right)^{1/2}$$

$$M = \frac{1}{2}\left[\left(\frac{m}{4}\right)^2 + \frac{mP_0}{\sigma_c} + s\right]^{1/2} - \frac{m}{8}$$

The radial stress at $r = r_e$ is given by:

$$\sigma_{re} = P_0 - M\sigma_c$$

In the elastic region, the radial and tangential stresses are given by:

$$\sigma_r = P_0 - (P_0 - \sigma_{re})\left(\frac{r_e}{r}\right)^2$$

$$\sigma_\theta = P_0 + (P_0 - \sigma_{re})\left(\frac{r_e}{r}\right)^2$$

In the plastic (yielded) region, the radial and tangential stresses are given by:

$$\sigma_r = \frac{m_r\sigma_c}{4}\left[\ln\left(\frac{r}{a}\right)\right]^2 + \ln\left(\frac{r}{a}\right)\left(m_r\sigma_c P_i + s_r\sigma_c^2\right)^{1/2} + P_i$$

$$\sigma_\theta = \sigma_r + \left(m_r\sigma_c\sigma_r + s_r\sigma_c^2\right)^{1/2}$$

where P_i is the internal pressure (in this example, 0 MPa).

3.3 Results

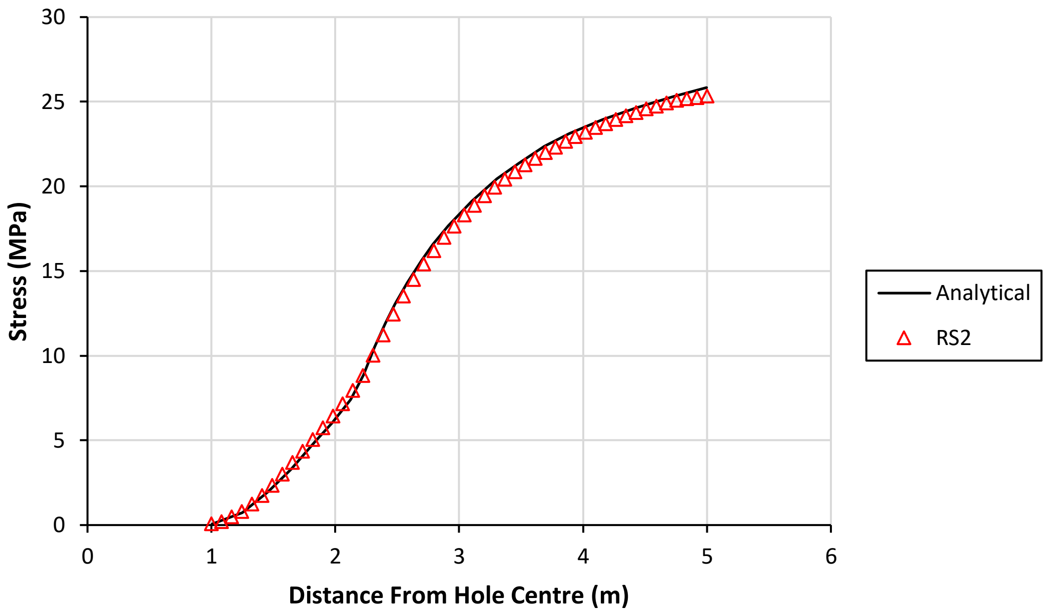

Figure 3.2 and Figure 3.3 compare the stress distributions calculated by ***RS2*** with the analytical solution.

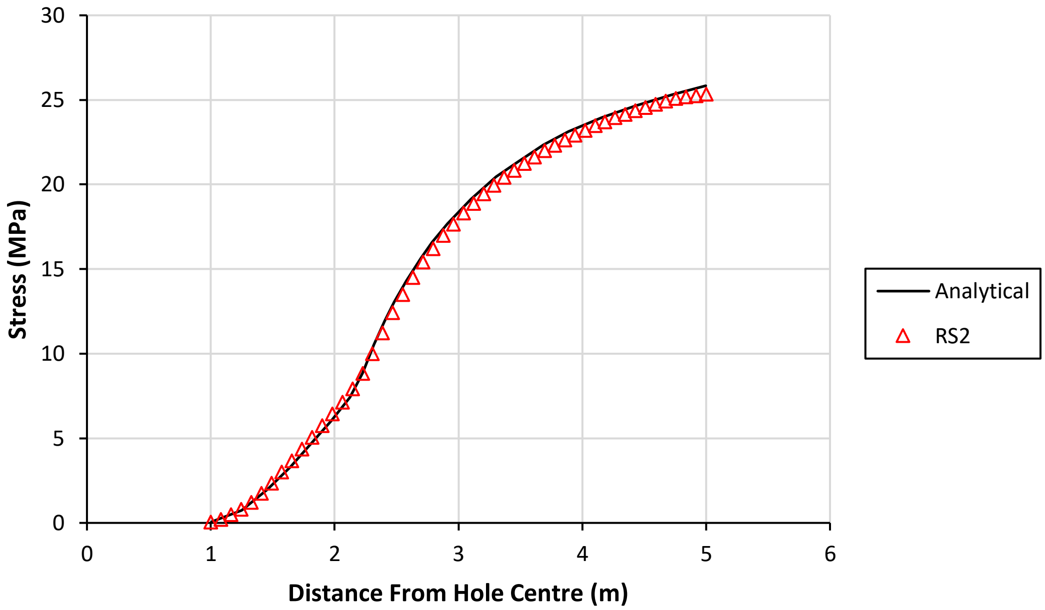

Figure 3.2: Comparison of radial stress distributions

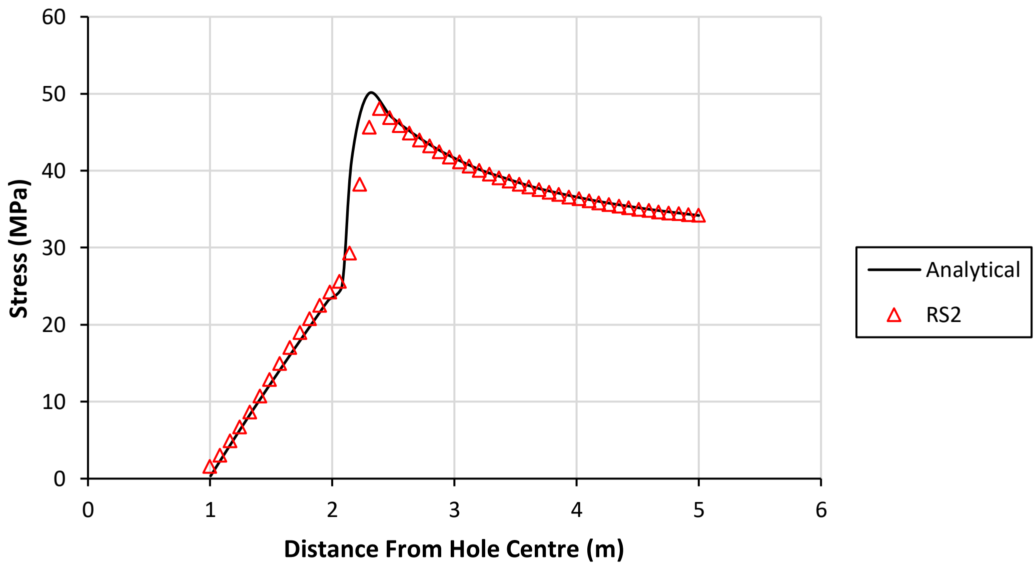

Figure 3.3: Comparison of tangential stress distributions

Figure 3.4 and Figure 3.5 illustrate the radial and tangential stress contour plots produced by ***RS2***.

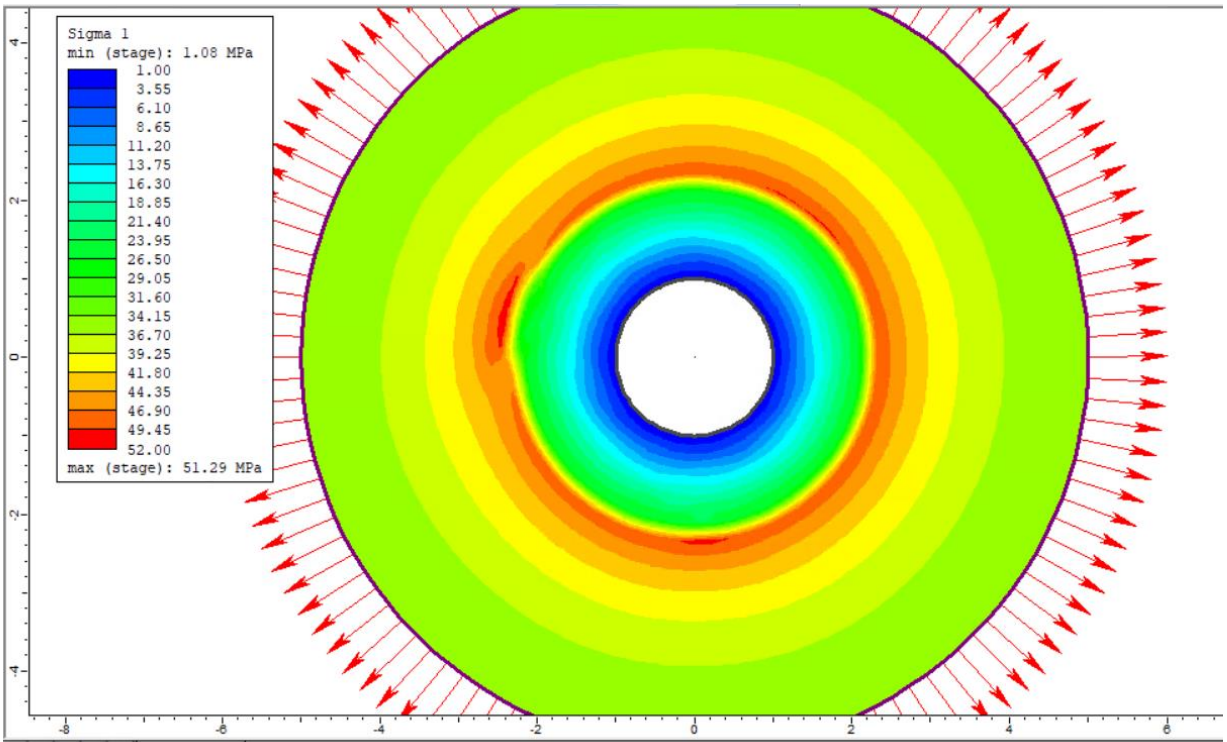

Figure 3.4: Tangential stress contour plot in *RS2*

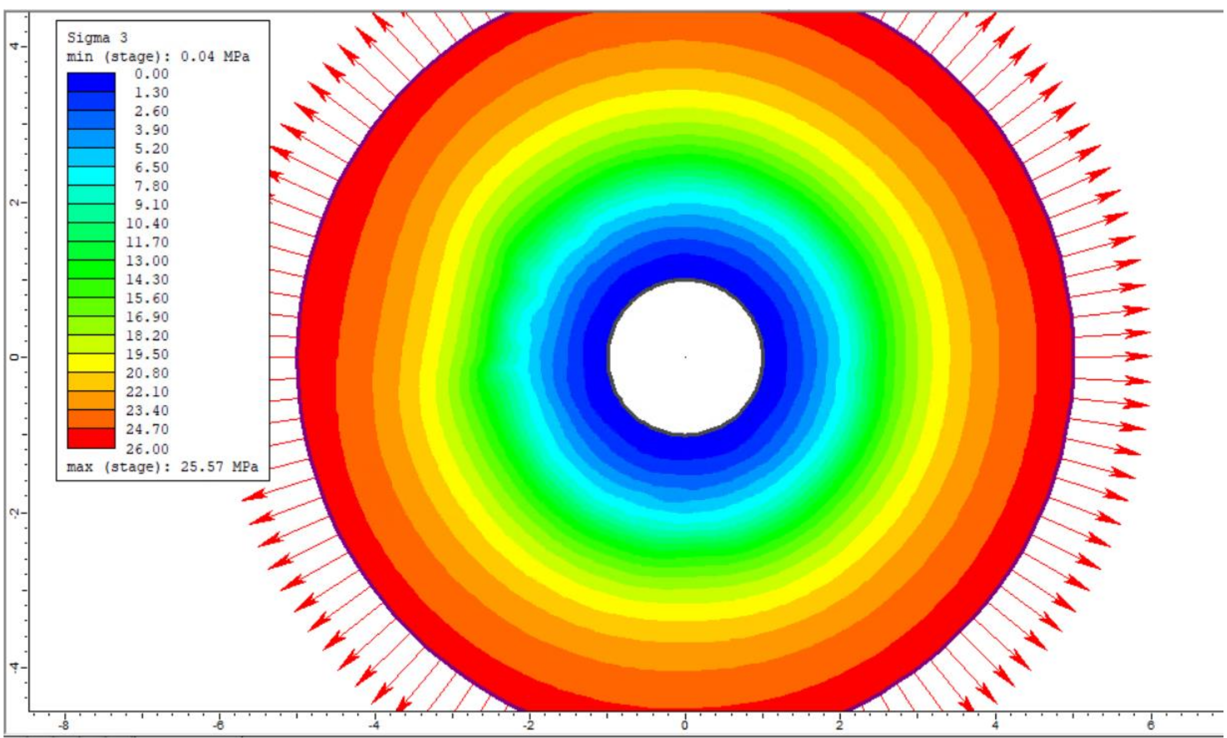

Figure 3.5: Radial stress contour plot in *RS2*

3.4 References

1. Hoek, E. and Brown, E. T., (1982) *Underground Excavations in Rock*, London: IMM, PP. 249-253.

2. Itasca Consulting Group, INC (1993), "Cylindrical Hole in an Infinite Hoek-Brown Medium", *Fast Lagrangian Analysis of Continua* (Version 3.2), Verification Manual.

3.5 Data Files

The input file **stress#003.fez** can be downloaded from the RS2 Online Help page for Verification Manuals.

4 Strip Loading on a Semi-Infinite Elastic Medium

4.1 Problem Description

This problem considers a distributed load applied uniformly over some portion of a semi-infinite isotropic elastic medium. Figure 4.1 shows the model as implemented in ***RS2***.

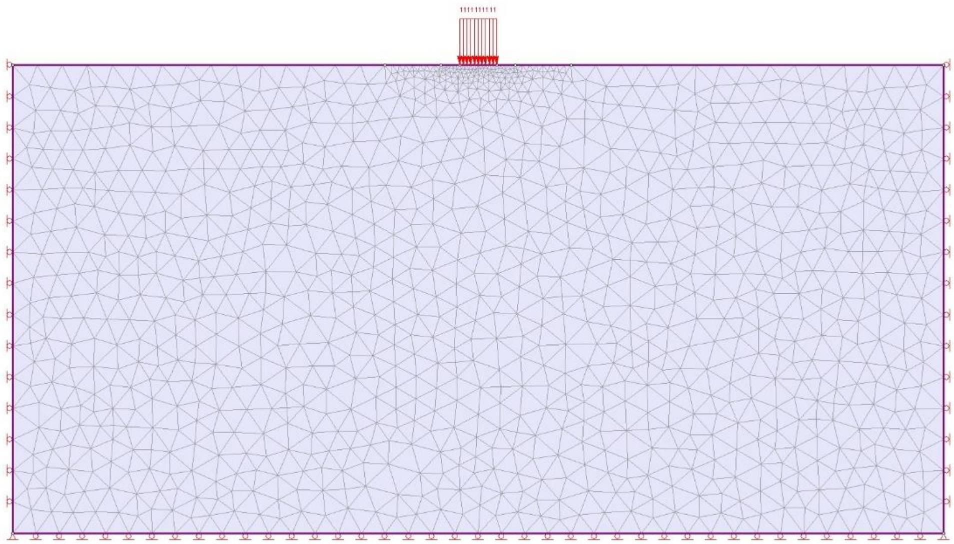

Figure 4.1: Strip loading on an infinite elastic medium as modeled in *RS2*

Table 4.1 summarizes the model parameters. Boundary conditions are as shown in Figure 4.1. No field stress is present. A graded mesh of 2176 triangular elements was used, while custom discretization was used on the external boundary. The model has a width of 50 m and a height of 25 m.

Table 4.1: Model parameters

Property	*Value*
Young’s modulus (E)	20000 MPa
Poisson’s ratio (v)	0.2
Distributed load (*P*)	1 MPa
Load half-width (*b*)	1 m

4.2 Analytical Solution

According to [1], the stress tensor at some point (α, δ) below the load has the following components:

$$\sigma_x = \frac{P}{\pi}[\alpha - \sin\,\alpha\cos(\alpha + 2\delta)]$$

$$\sigma_y = \frac{P}{\pi}[\alpha + \sin\,\alpha\cos(\alpha + 2\delta)]$$

$$\tau_{xy} = \frac{P}{\pi}\sin\,\alpha\sin(\alpha + 2\delta)$$

where δ and α are defined as shown in Figure 4.2. It can thus be shown that the principal stresses are given by:

$$\sigma_1 = \frac{P}{\pi}(\alpha + \sin\,\alpha)$$

$$\sigma_3 = \frac{P}{\pi}(\alpha - \sin\,\alpha)$$

$$\tau_{\max} = \frac{P}{\pi}\sin\,\alpha$$

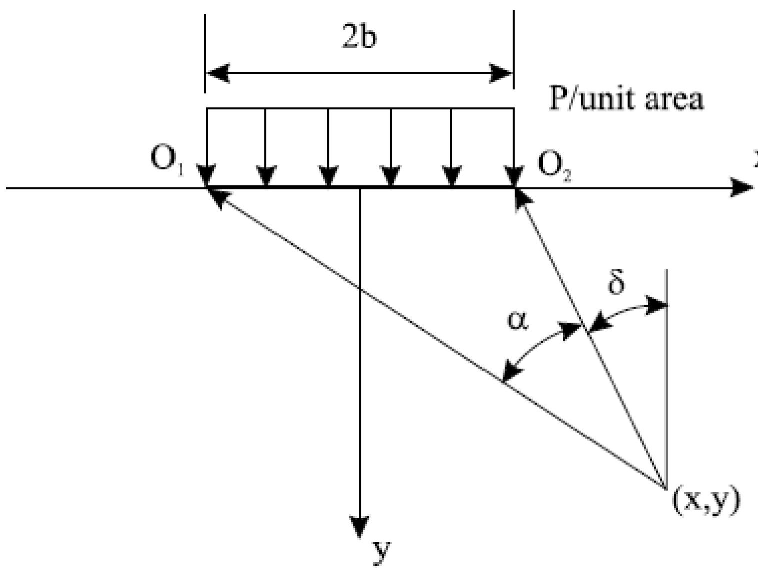

Figure 4.2: Vertical strip loading on a semi-infinite mass

4.3 Results

Figure 4.3 and Figure 4.4 plot the principal stresses as calculated along the vertical line *x=0* (directly beneath the centre of the applied load). As can be seen, all results are in good accordance with the analytical solution.

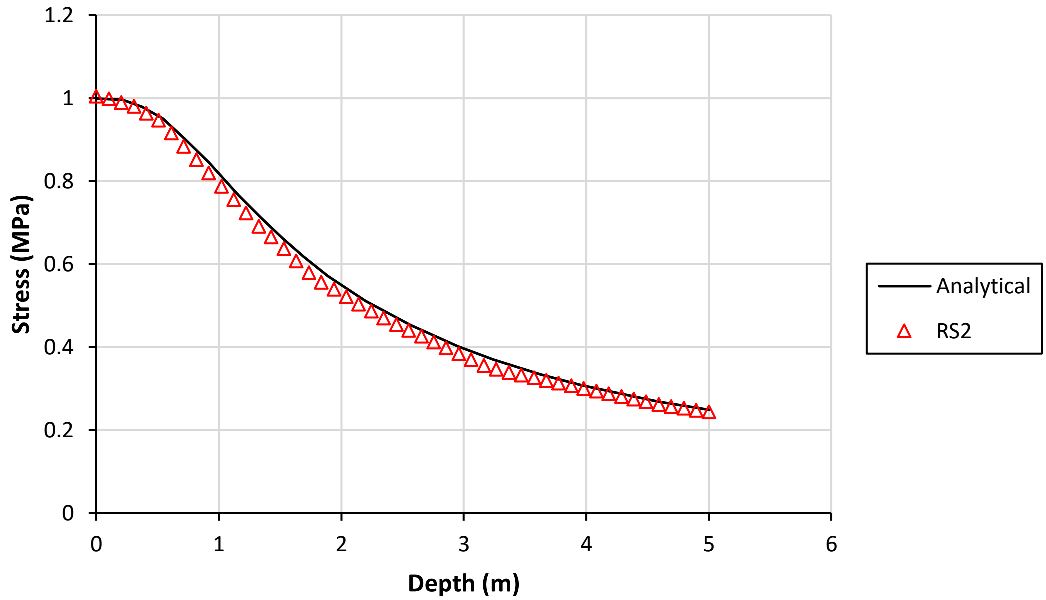

Figure 4.3: Comparison of σ_1 distributions along vertical axis

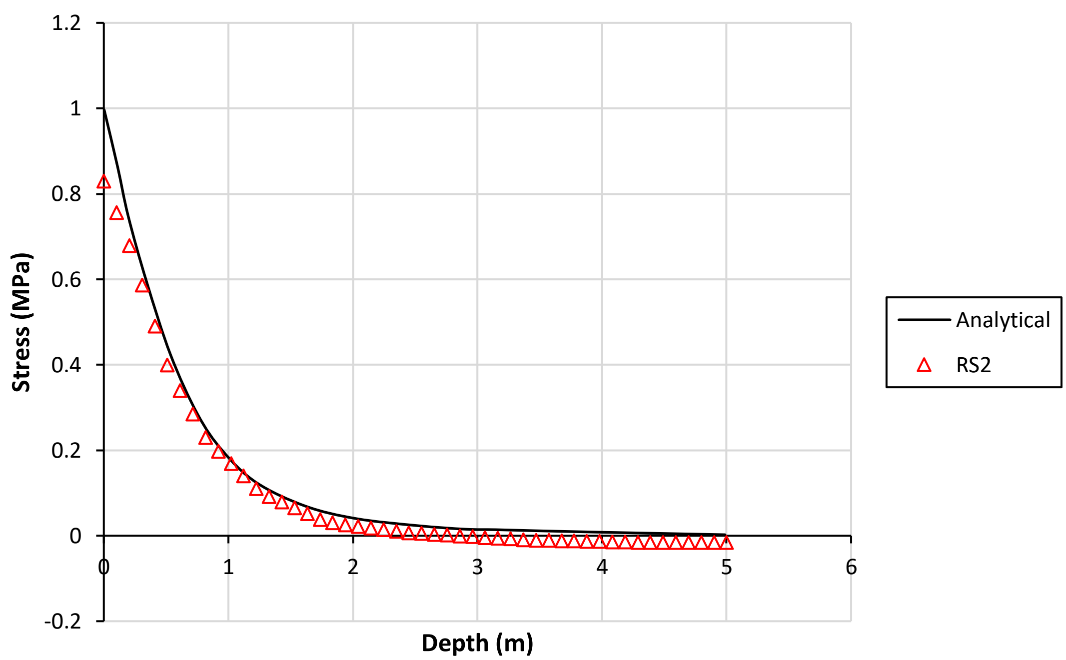

Figure 4.4: Comparison of σ_3 distributions along vertical axis

Table 4.2 quantifies the error associated with the ***RS2*** analysis. Relative errors in the σ_3 distribution are omitted due to the small absolute values of most results.

Table 4.2: Error in σ_1 values calculated by *RS2* relative to analytical solution

Maximum	0.6%

Contour plots of major and minor principal stress and total displacement are shown in Figure 4.5, Figure 4.6 and Figure 4.7.

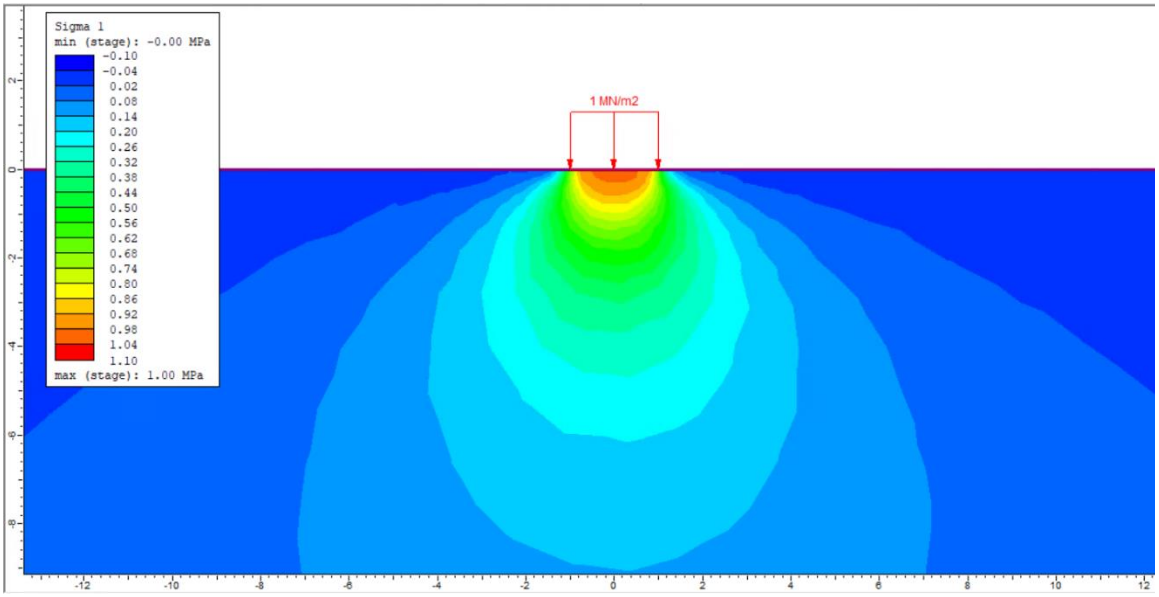

Figure 4.5: Contour plot of major principal stress beneath strip load in *RS2*

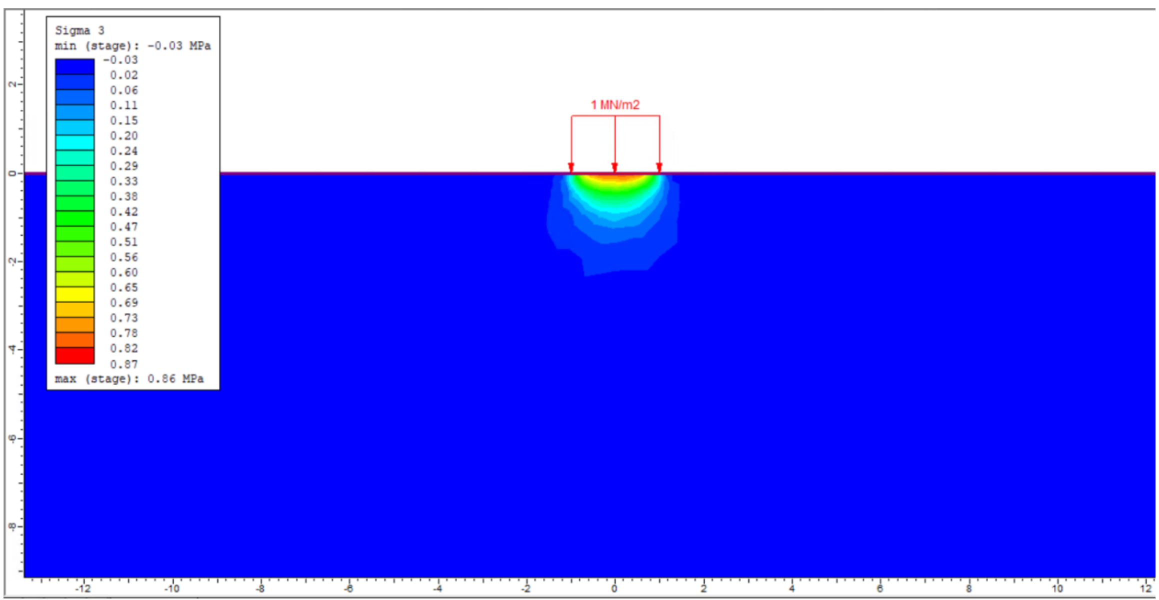

Figure 4.6: Contour plot of minor principal stress beneath strip load in *RS2*

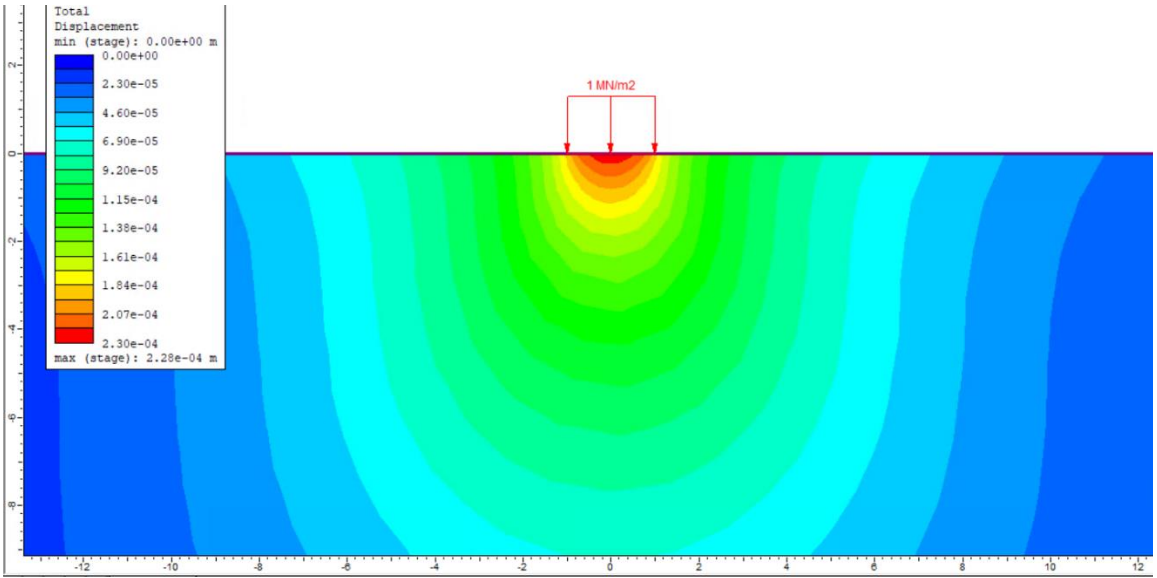

Figure 4.7: Contour plot total displacement beneath strip load in *RS2*

4.4 References

1. H.G. Poulos and E.H. Davis (1974), *Elastic Solutions for Soil and Rock Mechanics*, John Wiley & Sons, Inc., New York. London. Toronto.

4.5 Data Files

The input file **stress#004.fez** can be downloaded from the RS2 Online Help page for Verification Manuals.

5 Strip Footing on Surface of Purely Cohesive Material

5.1 Problem Description

This problem concerns the effect of an evenly distributed load strip load on a purely cohesive elastoplastic material with the Mohr-Coulomb failure criterion. Of interest is the bearing capacity of the material, in which steady plastic flow occurs. Figure 5.1 illustrates the problem as implemented (using half-symmetry) in ***RS2***, and Table 5.1 summarizes relevant material properties.

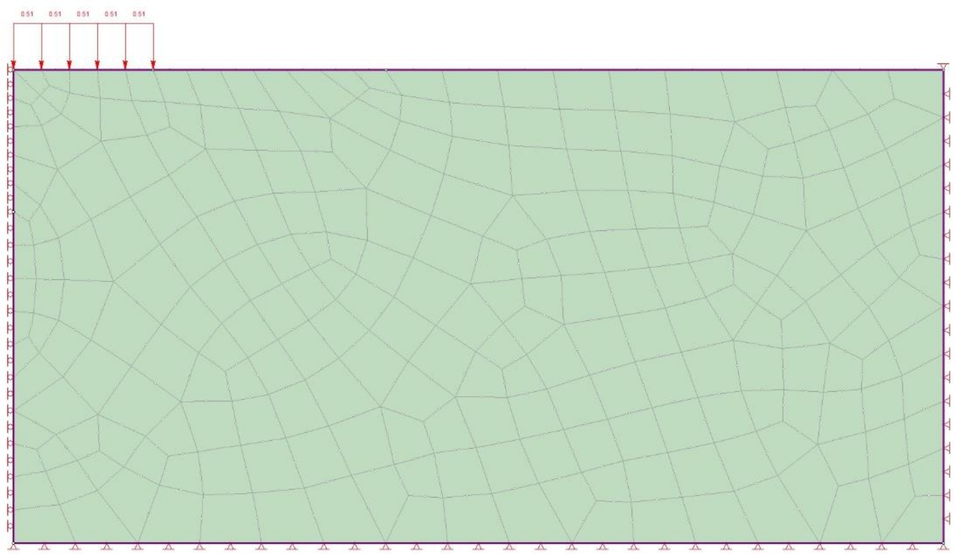

Figure 5.1: Strip footing model in *RS2*

Table 5.1: Material and model properties

Parameter	Value
Young's modulus (E)	250 MPa
Poisson's ratio (v)	0.2
Cohesion (c)	0.1 MPa
Friction angle (ϕ)	0
Strip half-width (b)	3 m

The model was tested twice using both a six-noded triangular and eight-noded quadrilateral mesh. For the quadrilateral mesh (pictured in Figure 5.1) the model was only subjected to a near-critical load, rather than all loads up to and including the critical load.

5.2 Analytical Solution

According to [1], the theoretical collapse load is given by the following equation.

$$q = (2 + \pi)c$$

where c represents the cohesion of the material. In this instance, the analytical collapse load is approximately 0.51 MPa. Figure 5.2 illustrates the plastic flow undergone by the frictionless material.

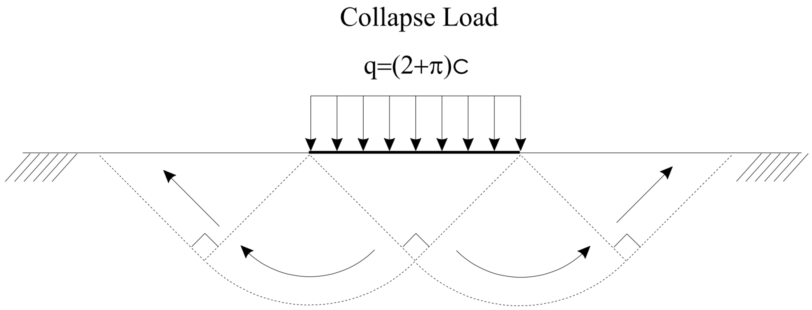

Figure 5.2: Prandtl's wedge problem of a strip loading on a frictionless soil

5.3 Results

Figure 5.3 shows the load-displacement curve generated by ***RS2***.

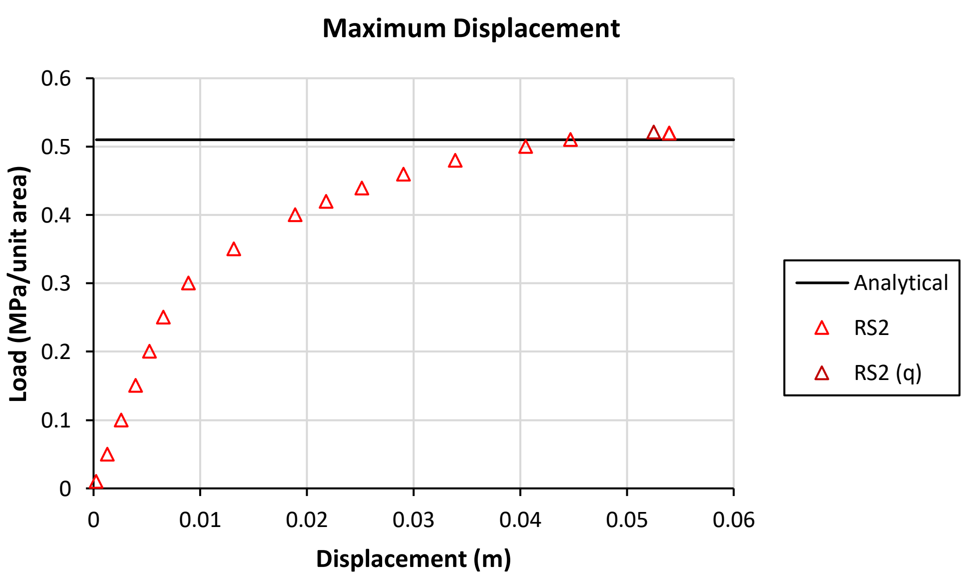

Figure 5.3: Maximum displacement for various loads and theoretical critical load.

As can be seen, all results are in close agreement with the theoretical maximum load. Calculations failed to converge at supercritical loads. The single data point generated using the quadrilateral mesh at near-critical load differs significantly from those produced by the triangular mesh.

Figure 5.4, Figure 5.5 and Figure 5.6 show contour plots of minor and major principal stresses and total displacement as produced by ***RS2***.

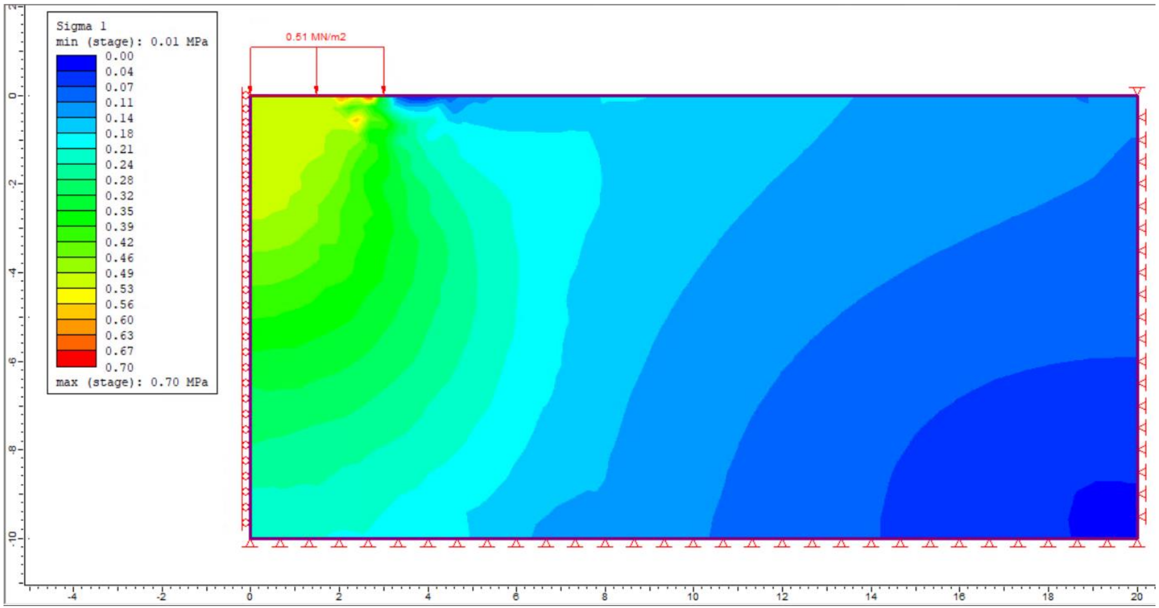

Figure 5.4: Major principal stress contours produced by *RS2*

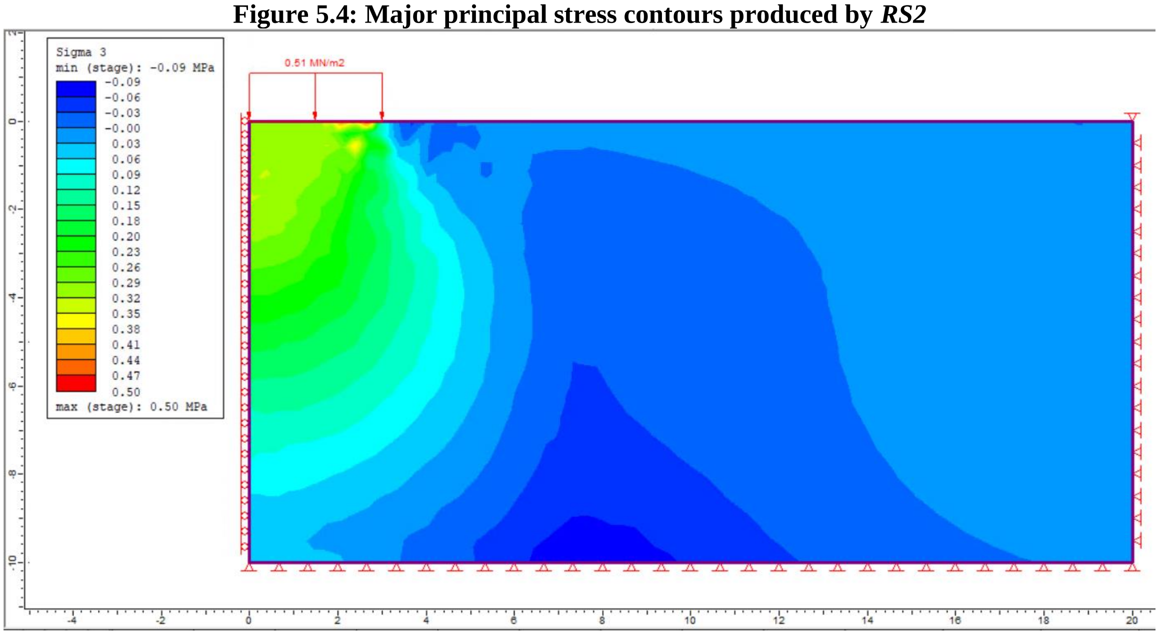

Figure 5.5 Minor principal stress contours produced by *RS2*

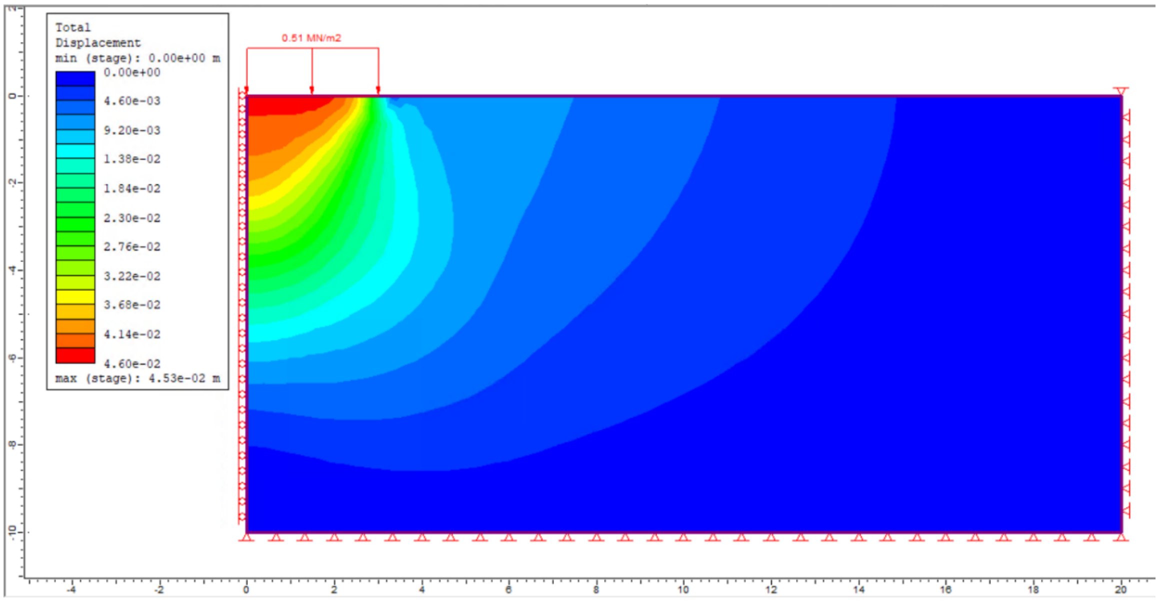

Figure 5.6: Total displacement contours produced by *RS2*

5.4 References

1. K. Terzaghi and R. B. Peck (1967), *Soil Mechanics in Engineering Practice*, 2nd Ed. New York, John Wiley & Sons.

5.5 Data Files

The input files **stress#005_01.fez** (six-noded triangular mesh) and **stress#005_02.fez** (eight-noded quadrilateral mesh) can be downloaded from the RS2 Online Help page for Verification Manuals.

6 Uniaxial Compressive Strength of Jointed Rock

6.1 Problem Description

This problem concerns a rock column subjected to a uniform compressive stress and containing a relatively weak plane. The overall strength of the column will be dependent on both the properties of the plane and the angle β at which it intersects the column. Figure 6.1 shows this problem as implemented in ***RS2*** for a joint angle $\beta = 30°$ (as measured from the vertical axis of the column).

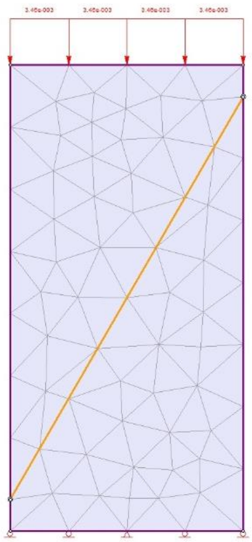

Figure 6.1: Jointed rock column as modeled in RS2

The compressive strength of the column is determined by both the rock and joint properties. Table 6.1 summarizes these parameters.

Table 6.1: Model parameters

Parameter	*Value*
Young's modulus (E)	170.27 MPa
Poisson's ratio (v)	0.216216
Cohesion (c)	0.002 MPa
Friction angle (ϕ)	40°
Dilation angle (ψ)	0°
Joint properties	
Normal stiffness	1000 MPa/m
Shear stiffness	1000 MPa/m
Cohesion (c_{joint})	0.001 MPa
Friction angle (ϕ_{joint})	30°

The model has a height of 10 m and a width of 5 m. Boundary conditions are as shown in Figure 6.1. Plane strain conditions are assumed. 3-noded triangular elements were used for mesh creation, and the value of β was varied from 27° to 90°.

6.2 Analytical Solution

The failure strength of the rock column under uniaxial loading depends on the mode of failure. According to [1], joint failure occurs when:

$$\sigma_1 - \sigma_3 \geq \frac{2(c_{joint} + \sigma_3 \tan\phi_{joint})}{(1 - \tan\phi_{joint}\tan\beta)\sin 2\beta}$$

Note that for uniaxial loading σ_3 is equal to zero. For failure of the rock mass,

$$\sigma_1 = \frac{2c\cos\phi}{1 - \sin\phi}$$

The overall failure strength of the rock column can thus be expressed as:

$$\sigma_c = \begin{cases} \min\left\{\dfrac{2c\cos\phi}{1-\sin\phi},\quad \dfrac{2c_{joint}}{(1-\tan\phi_{joint}\tan\beta)\sin 2\beta}\right\} & \mathit{if}\ (1-\tan\phi_{joint}\tan\beta) > 0 \\ \dfrac{2c\cos\phi}{1-\sin\phi} & \mathit{if}\ (1-\tan\phi_{joint}\tan\beta) < 0 \end{cases}$$

6.3 Results

At small values of β, the column fails through slip along the joint. The overall strength of the column thus increases with β to a maximum at which the mode of failure becomes shear failure of the rock elements. Table 6.2 shows the theoretical overall strength of the column for each value of β, as well as the values tested in ***RS2***.

Table 6.2: Summary of analytical and numerical results for column compressive strength

		RS2			
		Joint Slip		Rock Failure	
Joint Angle	Overall Strength (kPa)	No	Yes	No	Yes
30	3.464102	3.464	3.4642		
35	3.572655	3.5726	3.57266		
40	3.939231	3.9392	3.93924		
45	4.732051	4.73	4.7321		
50	6.510381	6.51	6.511		
55	8.578028			8.578	8.57805
60	8.578028			8.578	8.57805
65	8.578028			8.578	8.57805
70	8.578028			8.578	8.57805
75	8.578028			8.578	8.57805
80	8.578028			8.578	8.57805
85	8.578028			8.578	8.57805
90	8.578028			8.578	8.57805

Figure 6.2 plots these results. ***RS2*** results are in very good agreement with theory.

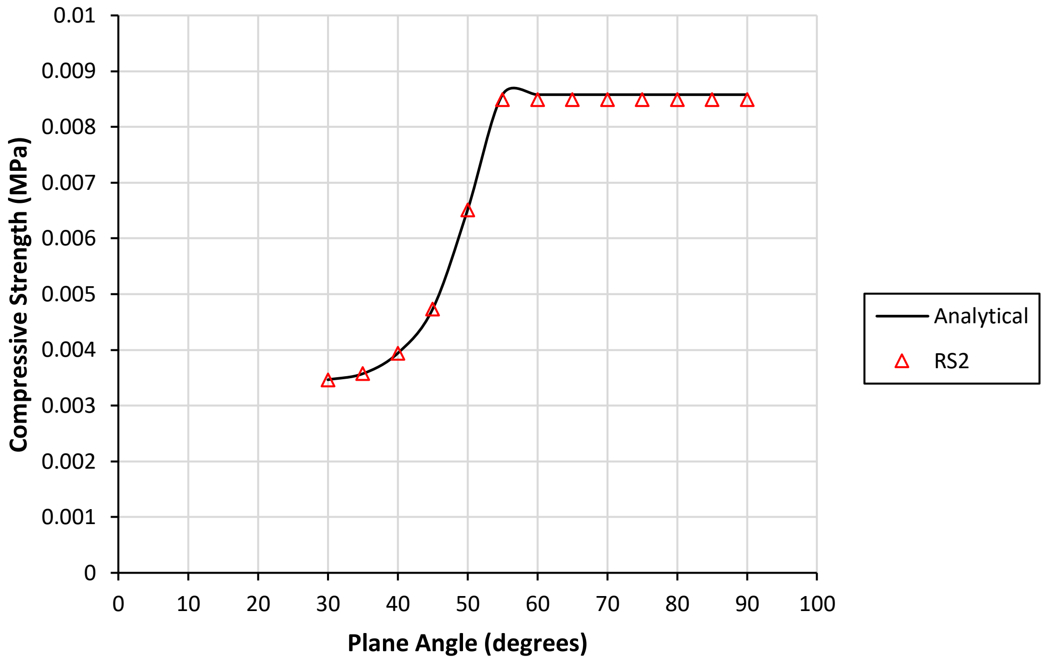

Figure 6.2: Analytical and numerical results for strength of column as a function of plane angle

Figure 6.3 shows the displacement distribution for the case when β =30°.

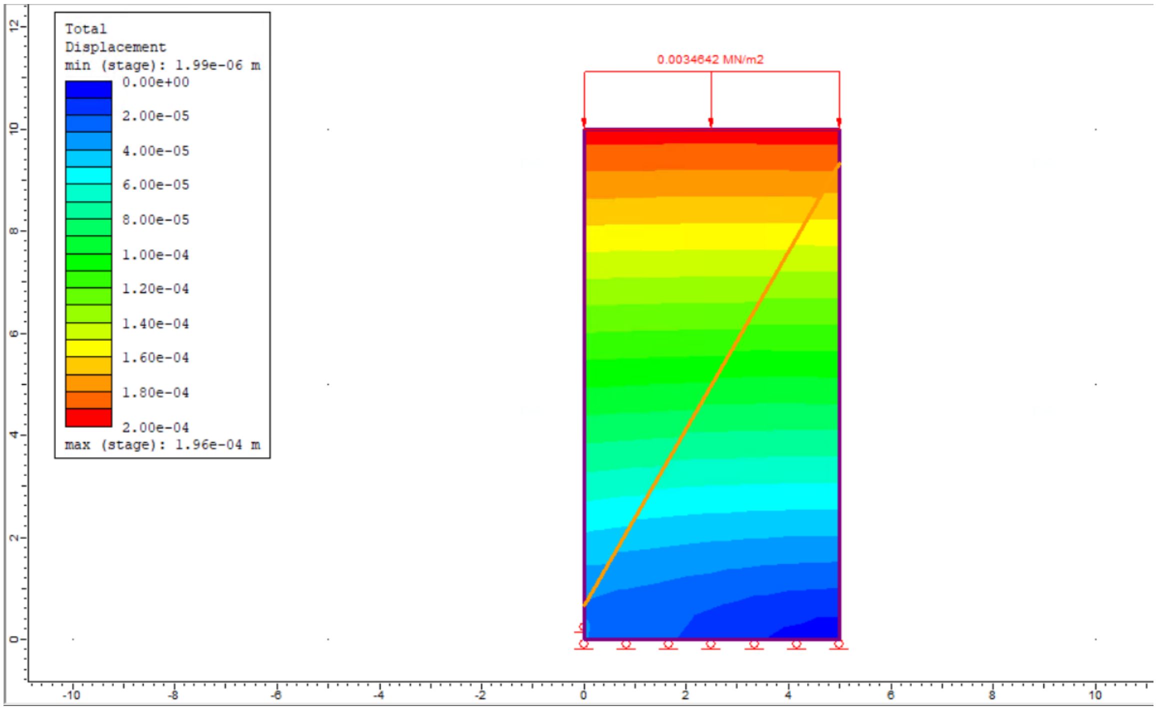

Figure 6.3: Total displacement distribution at near-critical load for β =30°

6.4 References

1. J. C. Jaeger and N. G. Cook, (1979), *Fundamentals of Rock Mechanics***,** 3rd Ed., London, Chapman and Hall.

6.5 Data Files

The input files **stress#006_30.fez** to **stress#006_90** for various values of joint angle β can be downloaded from the RS2 Online Help page for Verification Manuals.

7 Lined Circular Tunnel Support in an Elastic Medium

7.1 Problem Description

This verification problem addresses the axial forces and bending moments sustained by a liner supporting a circular tunnel in an ideal elastic medium. Figure 7.1 shows the model as implemented in ***RS2***. ***RS2*** formulates the liner as an elastic thick-walled shell subject to both flexural and circumferential deformation.

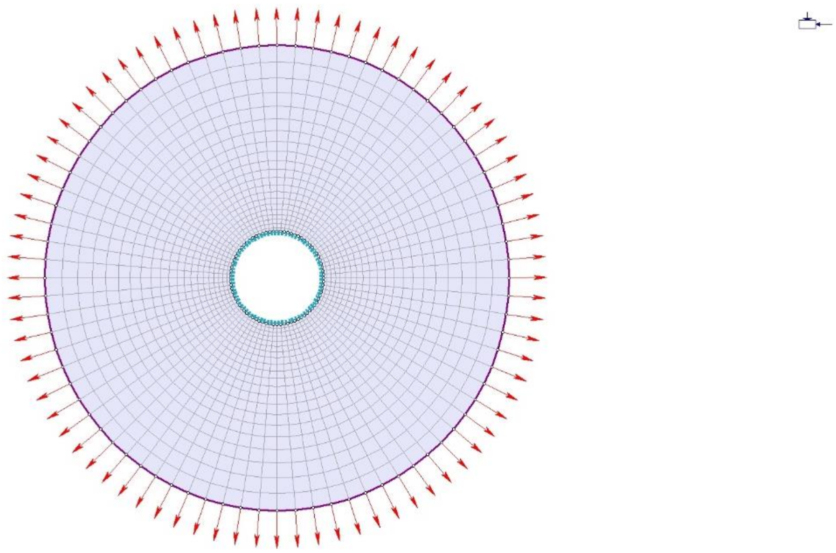

Figure 7.1: Lined tunnel as implemented in *RS2*. Liner is indicated in blue.

Relevant model parameters are summarized in Table 7.1. The model uses a radial mesh with 1680 4-noded quadrilateral elements. The tunnel and liner are discretized into 80 elements; liner elements are simplified using the Euler-Bernouilli beam equation. Infinite elements are used along the external boundary.

Table 7.1: Material and liner properties

Parameter	***Value***
Horizontal field stress (σ^0_{xx})	30 MPa
Vertical field stress (σ^0_{yy})	15 MPa
Young's modulus (E)	6000 MPa
Poisson's ratio (v)	0.2
Liner Properties	
Young's modulus (E_s)	20000 MPa
Poisson's ratio (v_s)	0.2
Thickness (h)	0.5 m
Radius (a)	2.5 m

Figure 7.2 shows the problem parameters schematically.

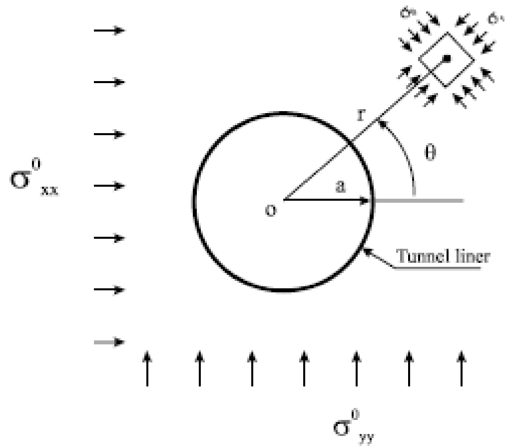

Figure 7.2: Lined circular tunnel in an elastic medium

7.2 Analytical Solution

The bending moment M and axial force N sustained by the liner are developed in [1] and can also be found in [2]. At some angle θ relative to the x axis, M and N are given by:

$$N = \frac{a\sigma_{yy}^0}{2}\left[(1+K)(1-a_0^*) + (1-K)(1+2a_2^*)\cos 2\theta\right]$$

$$M = \frac{a^2\sigma_{yy}^0}{4}(1-K)(1-2a_2^* + 2b_2^*)\cos 2\theta$$

where

$$a_0^* = \frac{C^* F^* (1-\nu)}{C^* + F^* + C^* F^* (1-\nu)}$$

$$a_2^* = \beta b_2^*$$

$$b_2^* = \frac{C^*(1-\nu)}{2[C^*(1-\nu) + 4\nu - 6\beta - 3\beta C^*(1-\nu)]}$$

$$\beta = \frac{C^*(6+F^*)(1-\nu) + 2F^*\nu}{3C^* + 3F^* + 2C^*F^*(1-\nu)}$$

$$C^* = \frac{Ea(1-\nu_s^2)}{E_s A(1-\nu^2)}$$

$$F^* = \frac{Ea^3(1-\nu_s^2)}{E_s I(1-\nu^2)}$$

and

I = Liner moment of inertia

A = Cross-sectional area of the liner

K = Ratio of horizontal to vertical stress ($\sigma_{xx}^{0} / \sigma_{yy}^{0}$)

7.3 Results

The results from ***RS2*** are shown in Figure 7.3 and Figure 7.4, together with the values predicted by the analytical approach. Bending moment and axial force vary periodically along the liner; only a single quadrant is plotted.

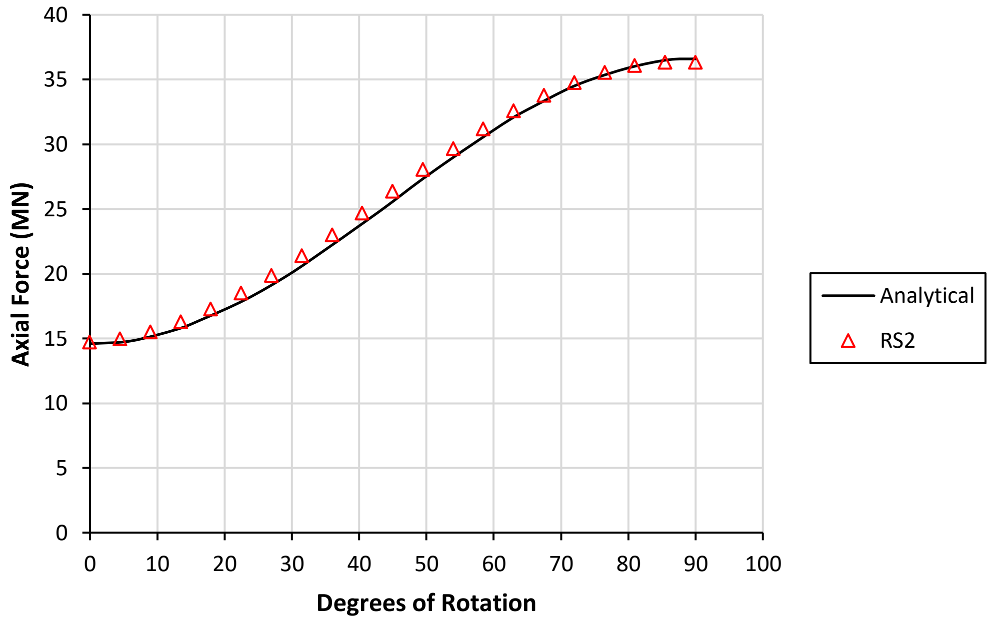

Figure 7.3: Comparison of axial force distributions around circumference of liner

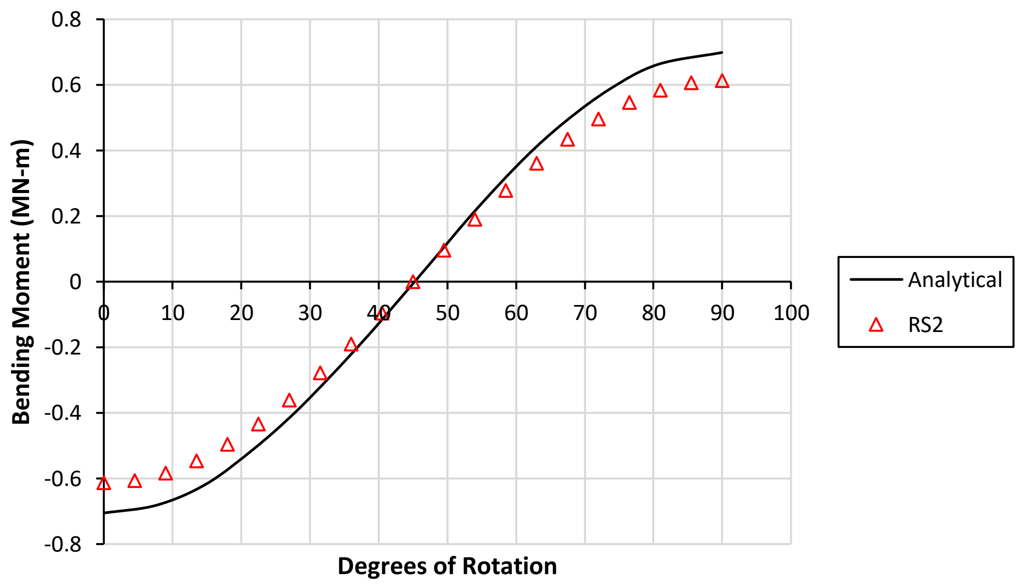

Figure 7.4: Comparison of bending moment distributions around circumference of liner

Table 7.1 quantifies the error associated with the ***RS2*** analysis.

Table 7.2: Error analysis for lined circular tunnel

	Maximum
Axial Force *N*	0.71%
Bending moment *M*	12.18%

Figure 7.5, Figure 7.6 and Figure 7.7 show contour plots for principal stress and total displacement around the tunnel.

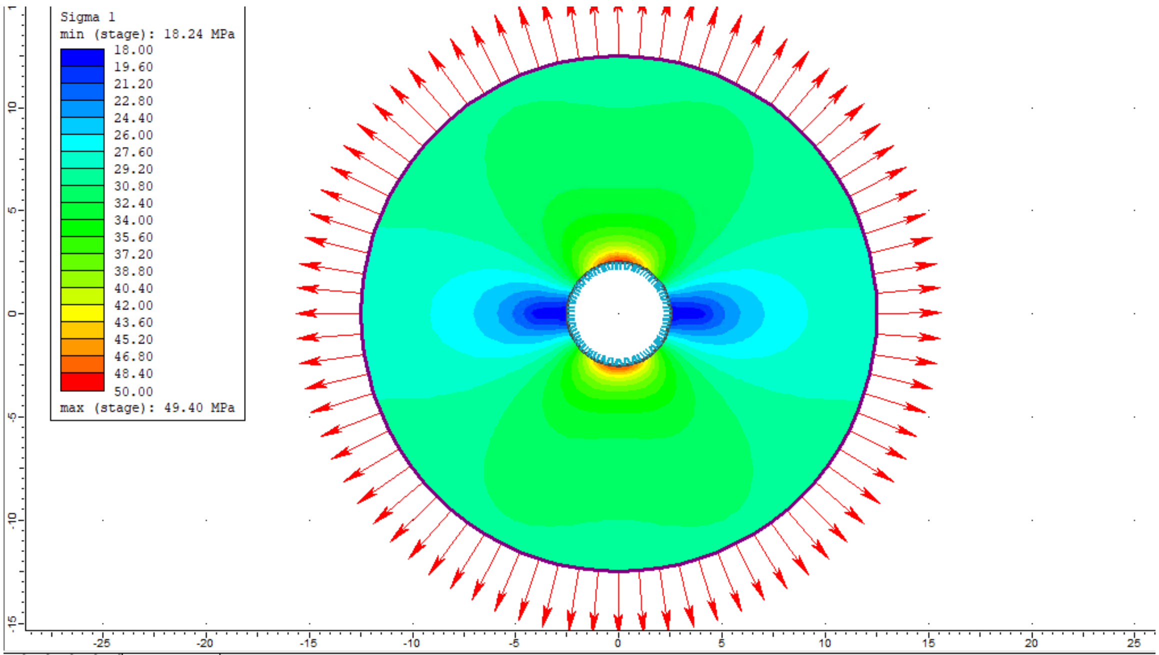

Figure 7.5: Major principal stress distribution around tunnel in *RS2*

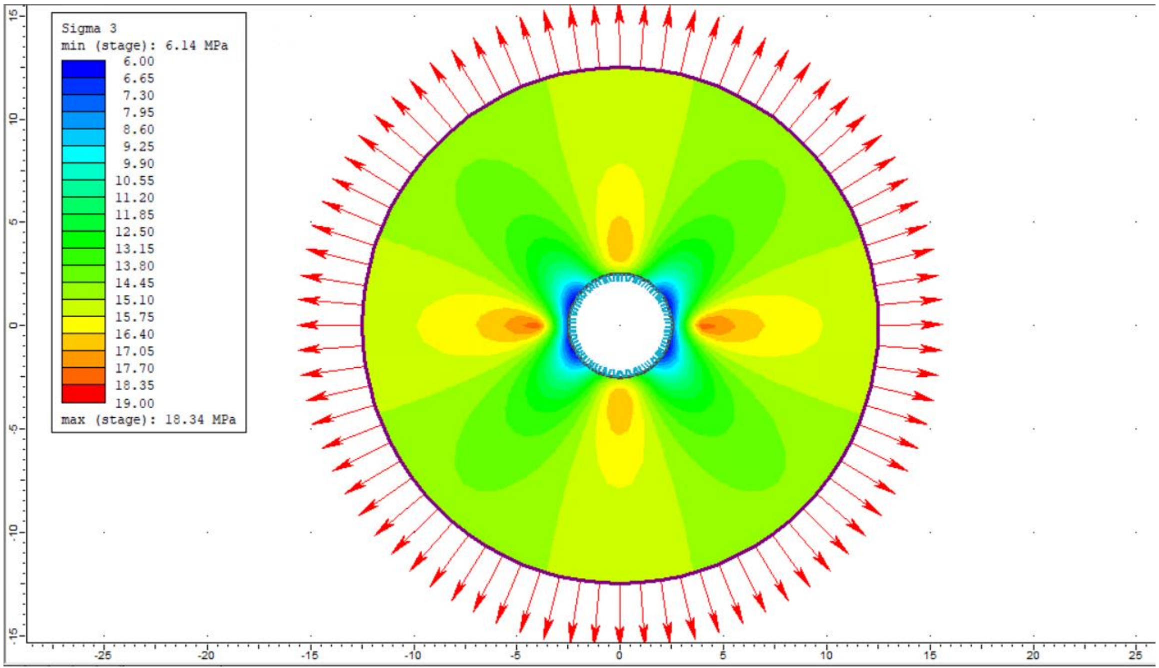

Figure 7.6: Minor principal stress distribution around tunnel in *RS2*

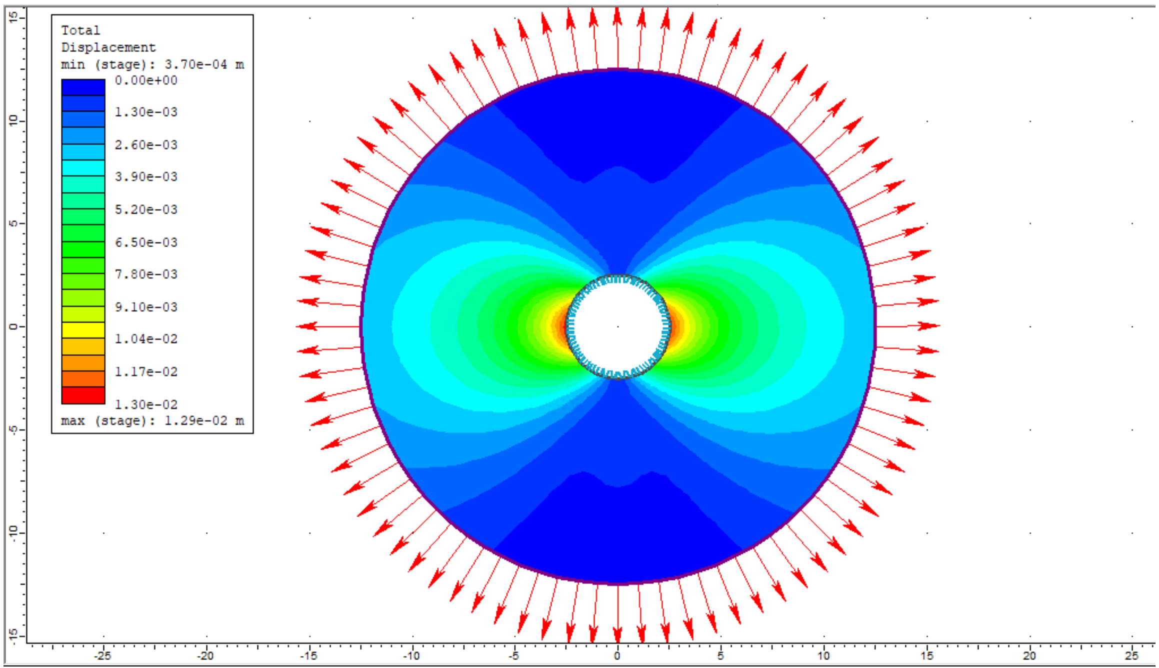

Figure 7.7: Total displacement distribution around tunnel in *RS2*

7.4 References

1. H. H. Einstein and C. W. Schwartz (1979), "Simplified Analysis for Tunnel Supports", *J. Geotech. Engineering Division*, 105, GT4, 499-518.

2. Itasca Consulting Group, INC (1993), “Lined Circular Tunnel in an Elastic Medium Subjected to Non-Hydrostatic Stresses”, *Fast Lagrangian Analysis of Continua* (Version 3.2), Verification Manual.

7.5 Data Files

The input file **stress#007.fez** can be downloaded from the RS2 Online Help page for Verification Manuals.

8 Cylindrical Hole in an Infinite Transversely Isotropic Medium

8.1 Problem Description

This problem considers a cylindrical tunnel in an infinite, elastic, transversely isotropic medium. Transversely isotropic materials contain planes of isotropy perpendicular to some axis, and it can be shown that given this condition Hooke's law reduces to:

$$\begin{bmatrix} \sigma_1 \\ \sigma_2 \\ \sigma_3 \\ \sigma_4 \\ \sigma_5 \\ \sigma_6 \end{bmatrix} = \begin{bmatrix} C_{11} & C_{12} & C_{12} & 0 & 0 & 0 \\ & C_{22} & C_{23} & 0 & 0 & 0 \\ & & C_{22} & 0 & 0 & 0 \\ & & & \frac{1}{2}\left(C_{22} - C_{23}\right) & 0 & 0 \\ & & & & C_{66} & 0 \\ & & & & & C_{66} \end{bmatrix} \begin{bmatrix} \varepsilon_1 \\ \varepsilon_2 \\ \varepsilon_3 \\ \varepsilon_4 \\ \varepsilon_5 \\ \varepsilon_6 \end{bmatrix} \quad [1]$$

Transversely isotropic materials can thus be defined by five independent elastic constants. In this case, the axis of isotropy is assumed to lie perpendicular to the axis of the cylindrical tunnel; the isotropic strata are thus parallel to the tunnel axis. The problem can therefore be simplified to two dimensions under the plane-strain assumption. Figure 8.1 illustrates the situation as modeled in *RS2* and Table 8.1 summarizes input parameters.

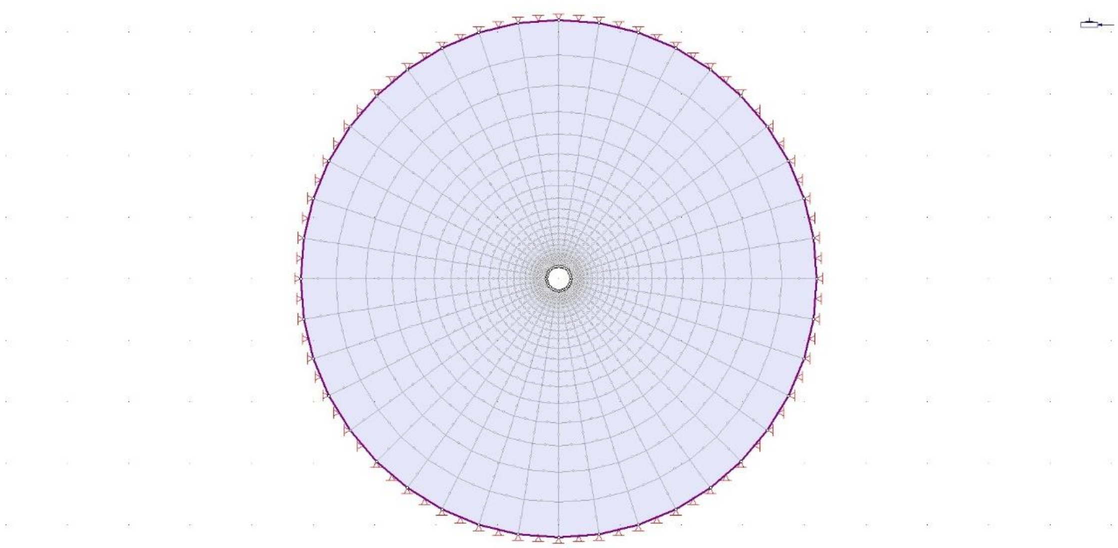

Figure 8.1: Circular hole in tranversely isotropic medium as implemented in *RS2*

Table 8.1: Model parameters

Parameter	*Value*
Young's modulus parallel to strata (E_x)	40000 MPa
Young's modulus perpendicular to strata (E_y)	20000 MPa
Poisson's ratio within *x*-*y* plane (v_{xy})	0.2
Poisson's ratio in plane of strata (v_{xz})	0.25
Shear modulus within *x*-*y* plane (G_{xy})	4000 MPa
Angle of the strata (counter-clockwise from *x*-axis) (θ)	0
Tunnel radius	1 m
Field stress (σ_{x0}, σ_{y0})	10 MPa
Field shear stress (τ_{xy0})	0 MPa

The ***RS2*** model uses a radial mesh containing 840 8-noded quadrilateral elements. The fixed external boundary is 21 m from the hole centre and the interior opening is discretized into 40 segments.

8.2 Analytical Solution

Amadei (1983) [2] develops the closed form solution to this problem and defines the displacement and stress fields as follows:

$$\sigma_x = \sigma_{x0} + 2\,\mathrm{Re}(\mu_1^2 \phi_1' + \mu_2^2 \phi_2')$$

$$\sigma_y = \sigma_{y0} + 2\,\mathrm{Re}(\phi_1' + \phi_2')$$

$$\tau_{xy} = \tau_{xy0} - 2\,\mathrm{Re}(\mu_1 \phi_1' + \mu_2 \phi_2')$$

$$u_x = -2\,\mathrm{Re}(p_1 \phi_1 + p_2 \phi_2)$$

$$u_y = -2\,\mathrm{Re}(q_1 \phi_1 + q_2 \phi_2)$$

The complex values μ_k (k = 1,2) are given by:

$$\mu_1 = i\sqrt{\frac{(2a_{12} + a_{66}) - \sqrt{(2a_{12} + a_{66})^2 - 4a_{11}a_{22}}}{2a_{11}}}$$

$$\mu_2 = i\sqrt{\frac{(2a_{12} + a_{66}) + \sqrt{(2a_{12} + a_{66})^2 - 4a_{11}a_{22}}}{2a_{11}}}$$

where $$a_{11} = \frac{1}{E_x}, \quad a_{12} = a_{21} = -\frac{\nu_{yx}}{E_y} = -\frac{\nu_{xy}}{E_x}, \quad a_{22} = \frac{1}{E_y}, \quad a_{66} = \frac{1}{G_{xy}}$$

the complex functions ϕ_k and ϕ_k' are

$$\phi_1(z_1) = (\mu_2 \bar{a}_1 - \bar{b}_1\ ) / \Delta\varepsilon_1$$

$$\phi_2(z_2) = -(\mu_1 \bar{a}_1 - \bar{b}_1\ ) / \Delta\varepsilon_2$$

$$\phi_1'(z_1) = -\frac{(\mu_2 \bar{a}_1 - \bar{b}_1\ )}{a\Delta\varepsilon_1\sqrt{\left(\frac{z_1}{a}\right)^2 - 1 - \mu_1^2}}$$

$$\phi_2'(z_2) = \frac{(\mu_1 \bar{a}_1 - \bar{b}_1\ )}{a\Delta\varepsilon_2\sqrt{\left(\frac{z_2}{a}\right)^2 - 1 - \mu_2^2}}$$

and

$$\Delta = \mu_2 - \mu_1$$

$$\varepsilon_k = \frac{1}{1 - i\mu_k}\left(\frac{z_k}{a} + \sqrt{\left(\frac{z_k}{a}\right)^2 - 1 - \mu_k^2}\right)$$

$$z_k = x + \mu_k y$$

$$\bar{a}_1 = -\frac{a}{2}(\sigma_{y0} - i\tau_{xy0})$$

$$\bar{b}_1 = \frac{a}{2}(\tau_{xy0} - i\sigma_{x0})$$

$$p_k = a_{11}\mu_k^2 + a_{12}$$

$$q_k = a_{12}\mu_k + \frac{a_{22}}{\mu_k}$$

8.3 Results

Figure 8.2, Figure 8.3 and Figure 8.4 show the tangential stress and Cartesian displacement fields surrounding the circular hole. As can be seen, results from ***RS2*** are in good agreement with the analytical solution.

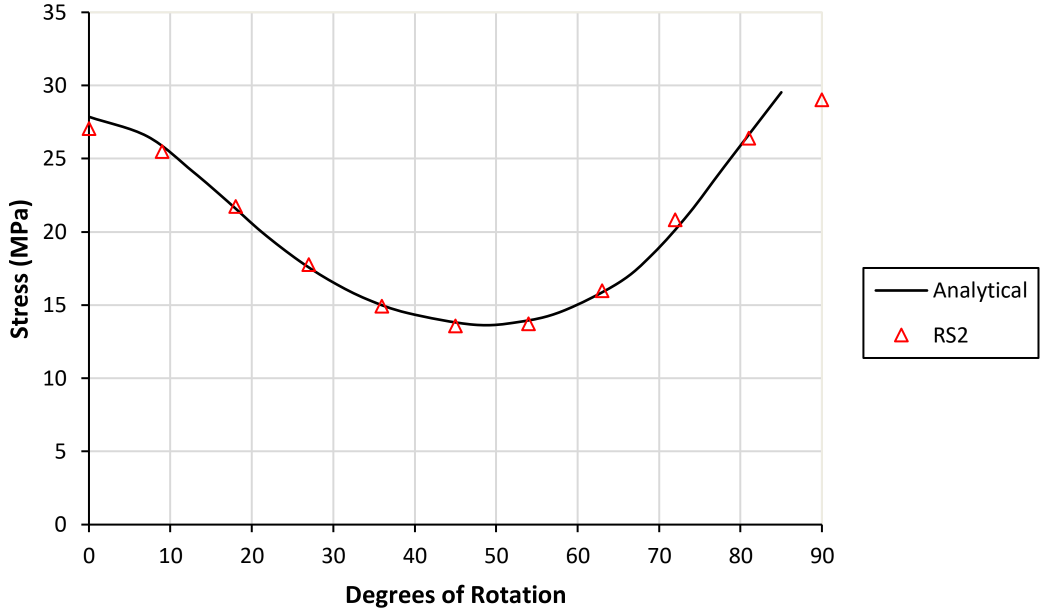

Figure 8.2: Comparison of tangential stress fields around the hole

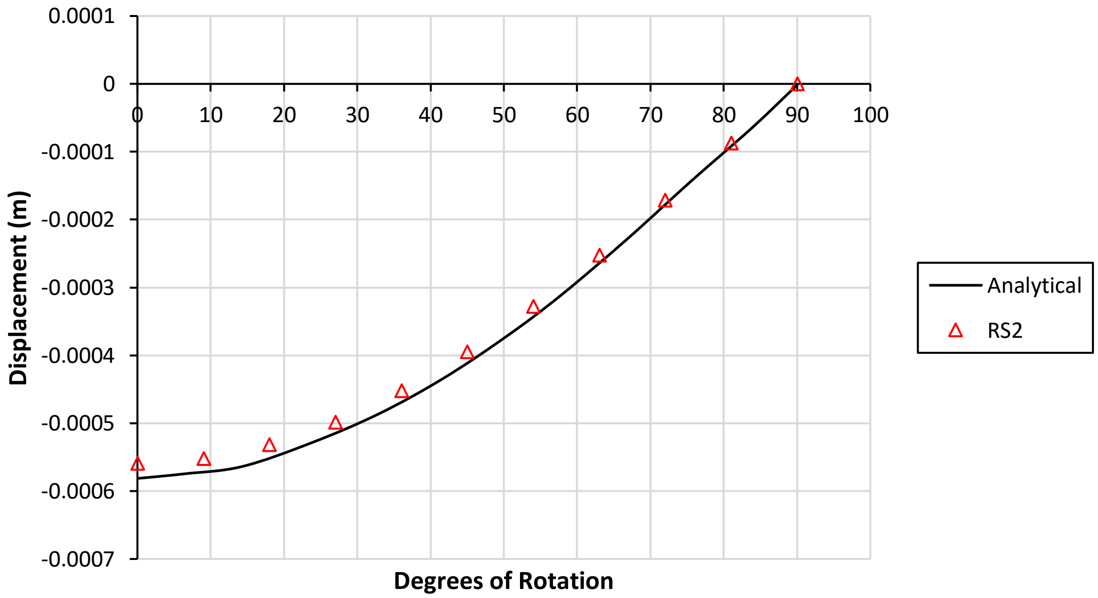

Figure 8.3: Comparison of *x*-displacement fields around the hole

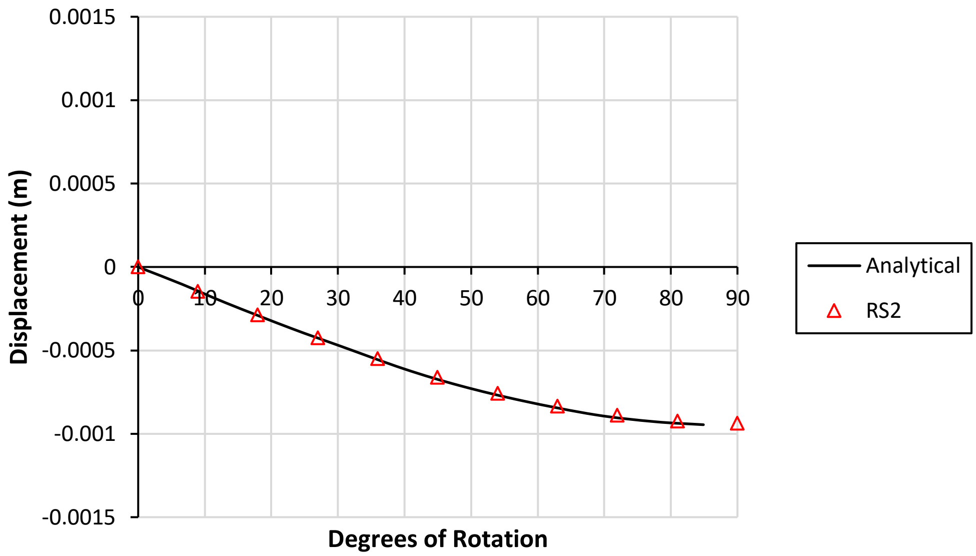

Figure 8.4: Comparison of *y*-displacement fields around the hole

Figure 8.5, Figure 8.6 and Figure 8.7 show contour plots in ***RS2*** surrounding the tunnel.

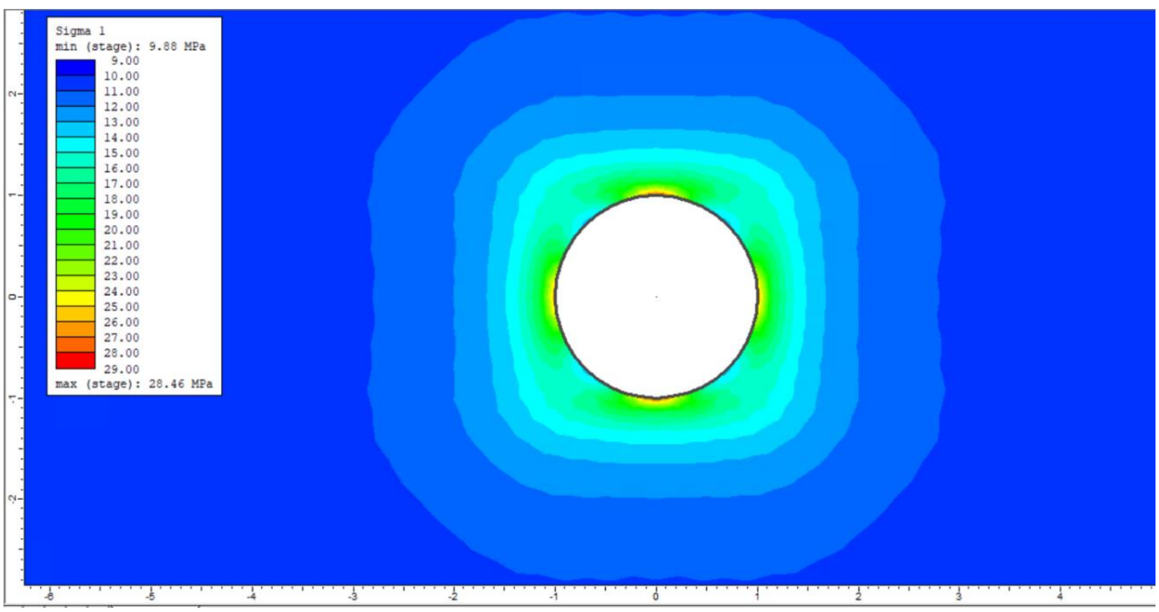

Figure 8.5: Major principal (tangential) stress distribution surrounding tunnel in *RS2*

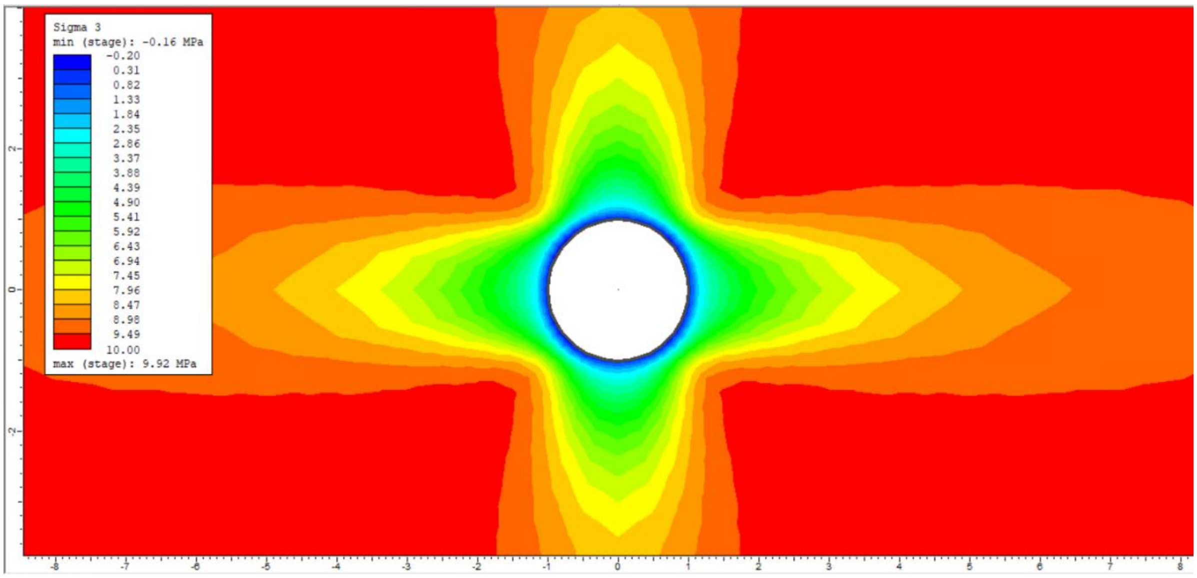

Figure 8.6: Minor principal (radial) stress distribution surrounding tunnel in *RS2*

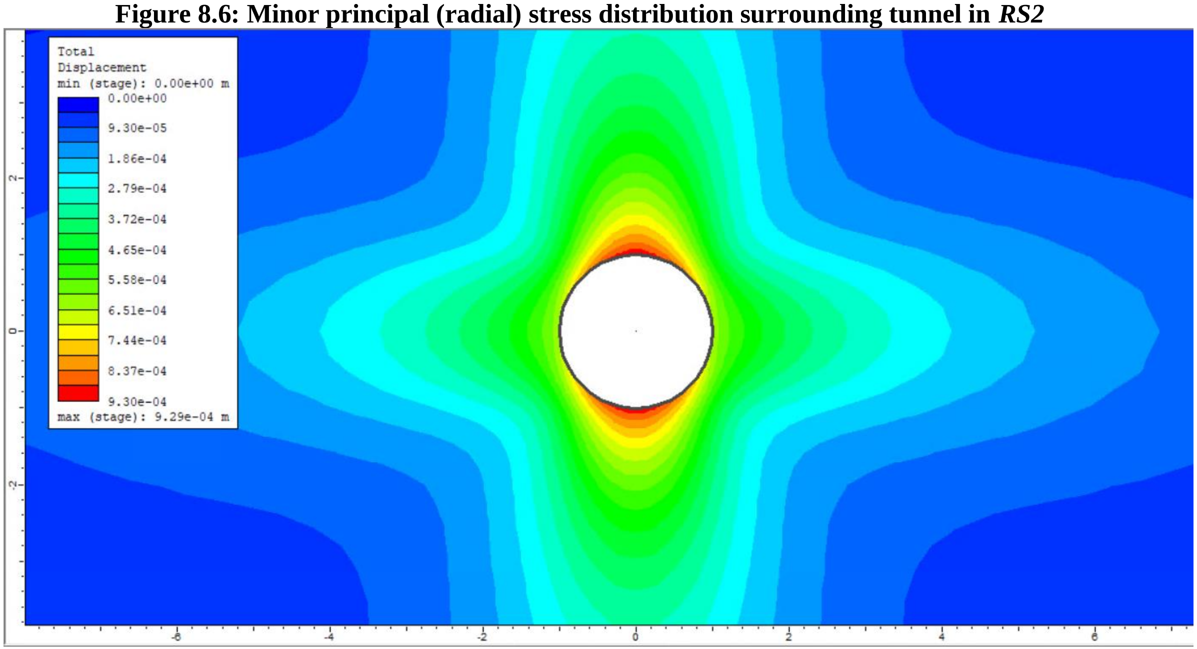

Figure 8.7: Total displacement distribution surrounding tunnel in *RS2*

8.4 References

1. Christensen, R.M. (1979). *Mechanics of Composite Materials*. John Wiley & Sons, New York Chichester Brisbane Toronto.

2. Amadei, B. (1983), *Rock Anisotropy and the Theory of Stress Measurements***,** Eds. C.A. Brebbia and S.A. Orszag, Springer-Verlag, Berlin Heidelberg New York Tokyo.

8.5 Data Files

The input file **stress#008.fez** can be downloaded from the RS2 Online Help page for Verification Manuals.

9 Spherical Cavity in an Infinite Elastic Medium

9.1 Problem Description

This problem considers a spherical cavity surrounded by an infinite, elastic, isotropic medium.   A hydrostatic field stress of 10 MPa is applied, and the resultant stresses and displacement around the cavity are observed. This three-dimensional situation can be modeled in ***RS2*** using the axisymmetric modeling option. Figure 9.1 shows the problem as implemented in ***RS2***.

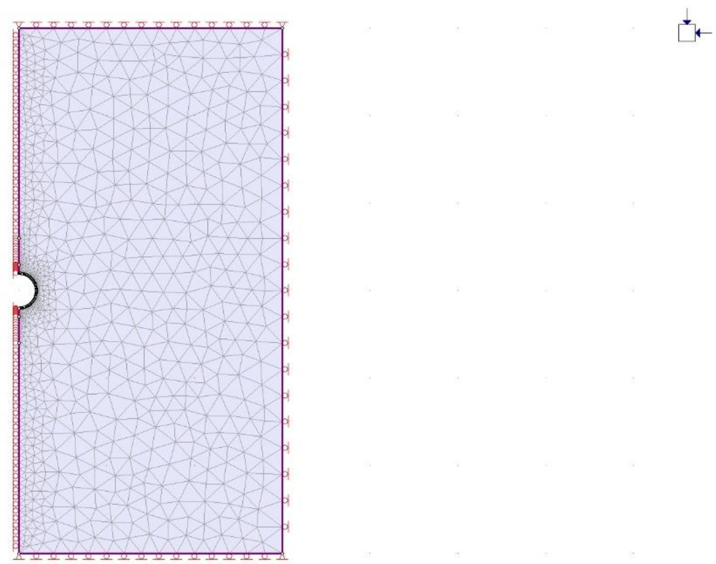

Figure 9.1: Axisymmetric view of spherical cavity, as modeled in *RS2*

The surrounding material is assumed to have a Young's modulus of 20000 MPa and a Poisson's ratio of 0.2. The cavity has a radius of 1 m. The ***RS2*** model uses a graded mesh containing 2028 3-noded triangular elements. The half-circle has been discretized into 80 elements, while the external boundary uses a custom discretization.

9.2 Analytical Solution

This is spherically symmetric problem in which only radial displacements are observed. According to [1] and [2], the following equations can be used to predict the radial displacement, radial stress, and tangential stress. Spherical coordinates of the form (r, θ, ϕ) are used.

$$\mu_r = \frac{P_0 a^3}{4Gr^2}$$

$$\sigma_{rr} = P_0\left(1 - \frac{a^3}{r^3}\right)$$

$$\sigma_{\theta\theta} = \sigma_{\phi\phi} = P_0\left(1 + \frac{a^3}{2r^3}\right)$$

where

a = cavity radius
P_0 = field stress
G = shear modulus

9.3 Results

Figure 9.2 and Figure 9.3 show the displacement and stress distributions produced by ***RS2***. All results are in excellent agreement with theory.

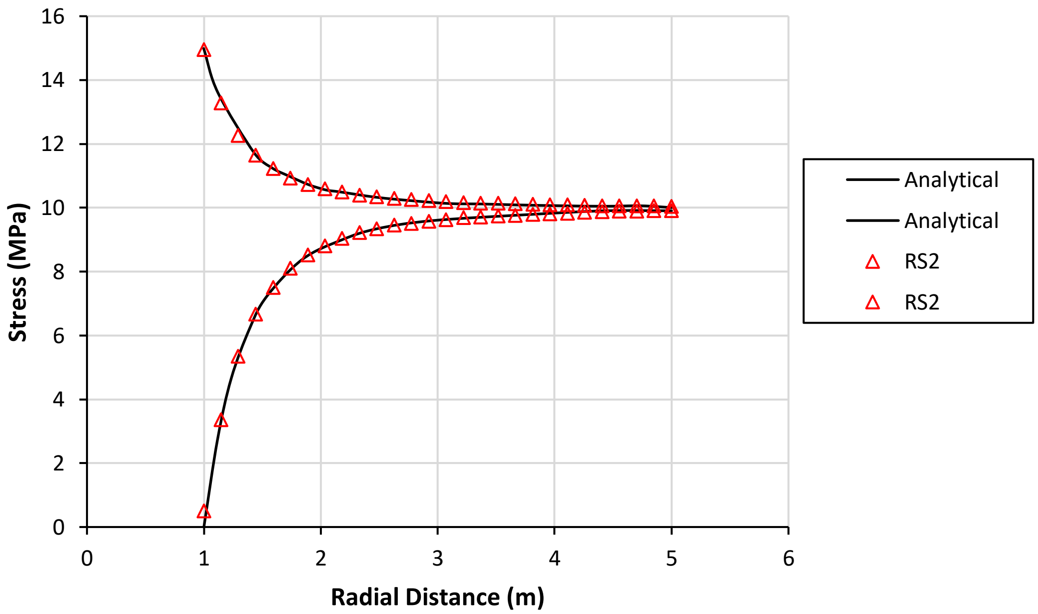

Figure 9.2: Analytical and computational distributions for radial (lower) and tangential (upper) stress

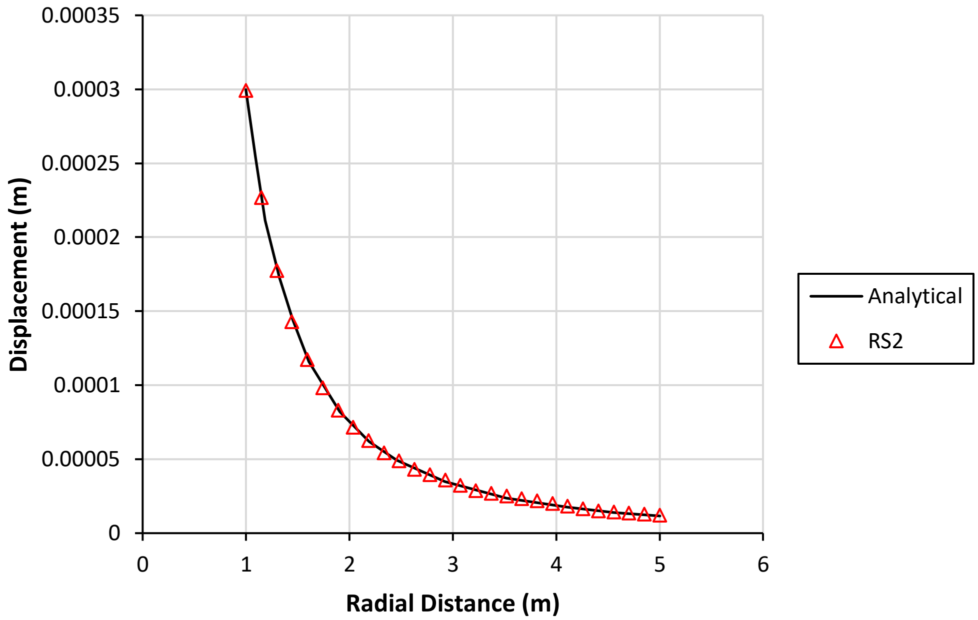

Figure 9.3: Analytical and computational distributions for radial displacement

Figure 9.4, Figure 9.5 and Figure 9.6 show principal stress and displacement contour plots as generated by ***RS2***.

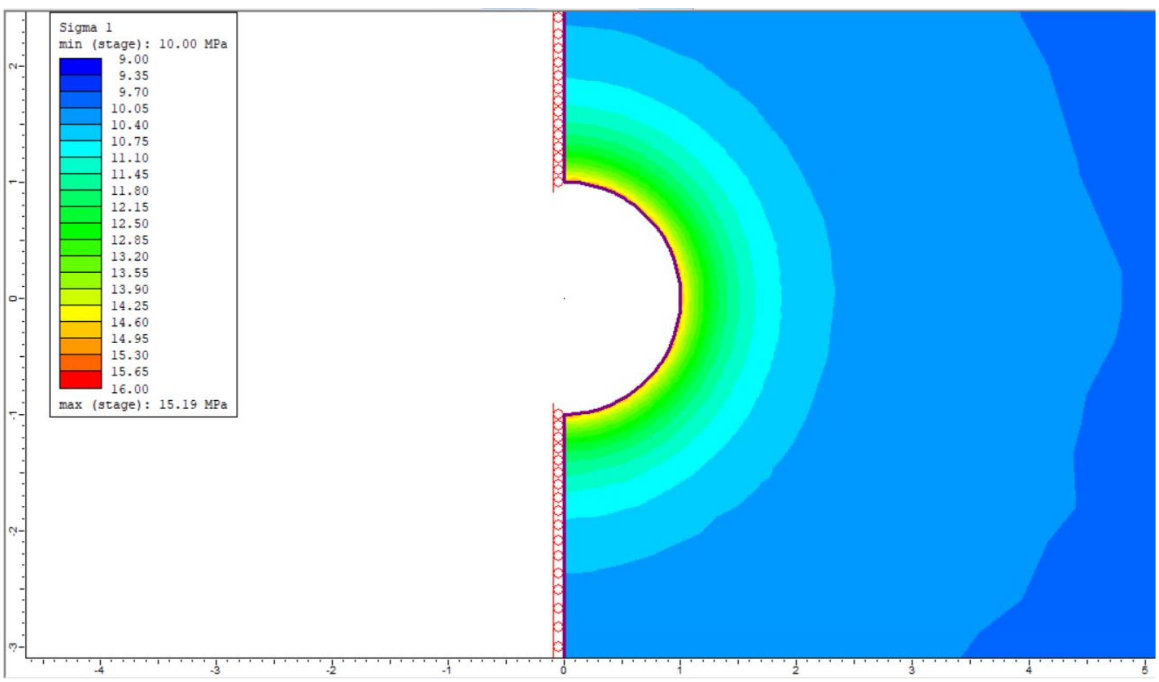

Figure 9.4: Major principal stress contours surrounding spherical cavity, as produced by *RS2*

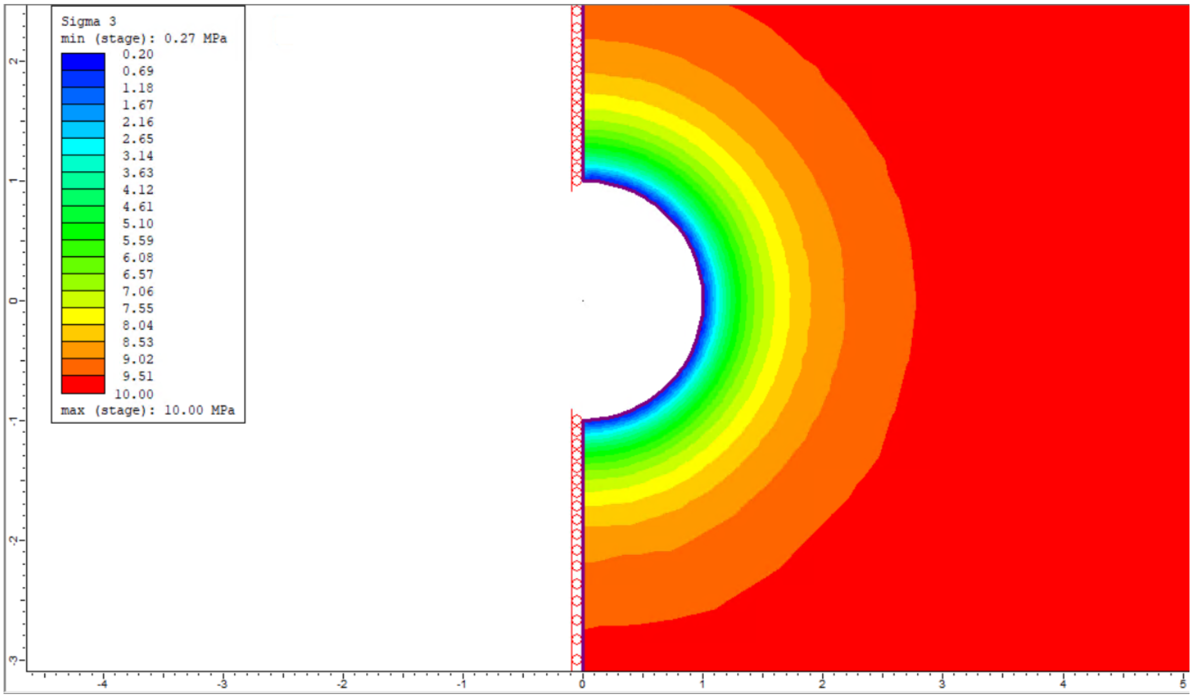

Figure 9.5: Minor principal stress contours surrounding spherical cavity, as produced by *RS2*

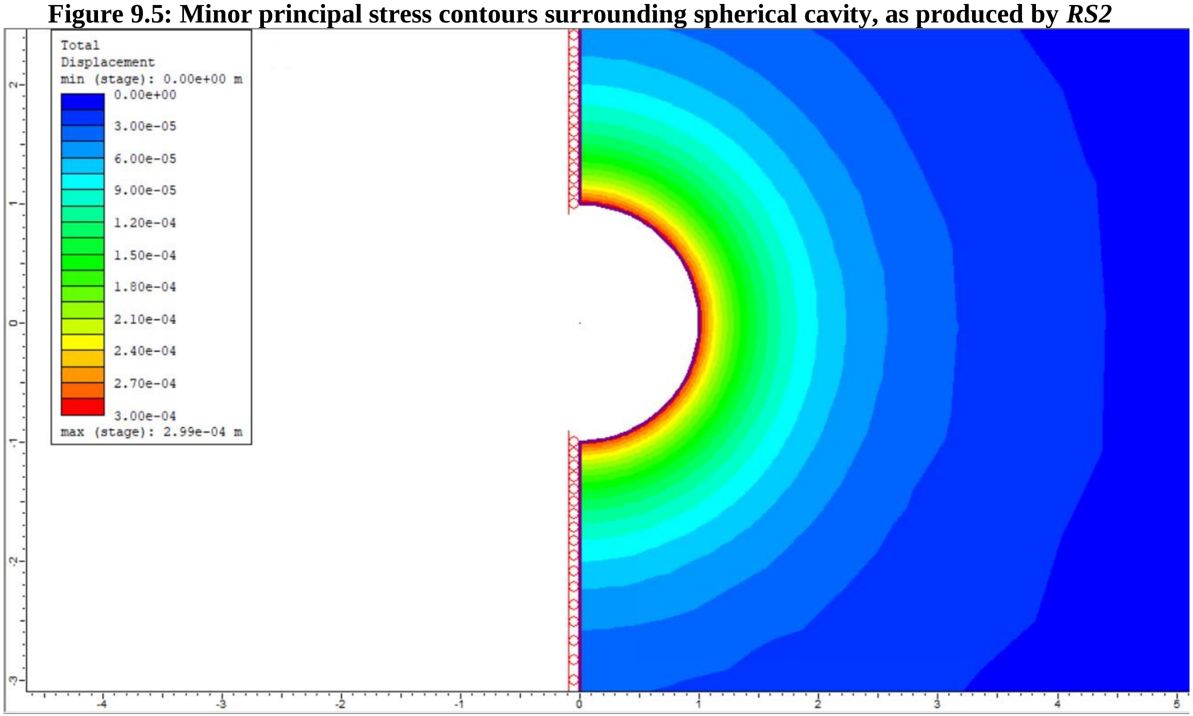

Figure 9.6: Total displacement contours surrounding spherical cavity, as produced by *RS2*

9.4 References

1. S. P., Timoshenko, and J. N. Goodier (1970), *Theory of Elasticity*, New York, McGraw Hill.

2. R. E., Goodman (1980), *Introduction to Rock Mechanics*, New York, John Wiley and Sons.

9.5 Data Files

The input file **stress#009.fez** can be downloaded from the RS2 Online Help page for Verification Manuals.

10 Axisymmetric Bending of a Spherical Dome

10.1 Problem Description

This problem concerns a thick-walled spherical shell spanning some arc α and subjected to a uniform normal pressure field of magnitude P. The edges of the dome are assumed to be fixed. The problem is axisymmetric and can be analyzed using the axisymmetric option in ***RS2***. Figure 10.1 and Figure 10.2 illustrate the problem diagrammatically and as implemented in ***RS2***.

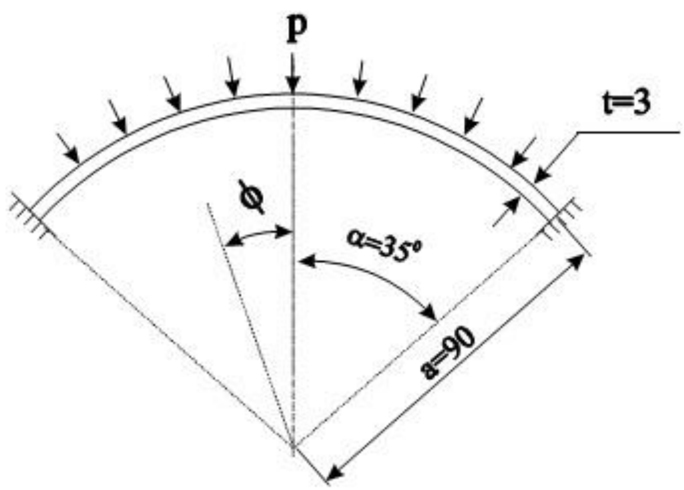

Figure 10.1: Thick-walled spherical dome with fixed edges under uniform pressure

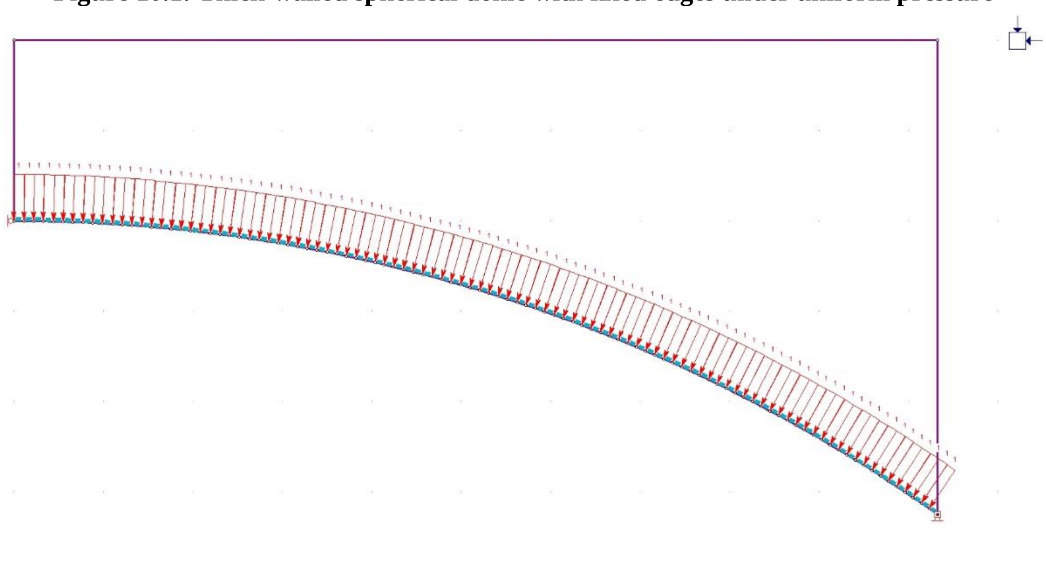

Figure 10.2: Spherical dome as implemented in *RS2*

RS2 models the shell as an elastic liner with an additional rotation restraint applied at its edges. The liner is constructed using the Timoshenko beam formulation and discretized into 60 elements. The model exploits half-symmetry. Table 10.1 summarizes the liner properties.

Table 10.1: Shell properties

Property	*Value*
Shell radius (a)	90 m
Shell thickness (t)	3 m
External pressure (p)	1 MPa
Poisson's ratio (v)	1/6
Young's modulus (E)	30000 MPa
Shell arc (α)	35°

10.2 Approximate Solution

In [1] Alphose Zingoni presents the Hetenyi approximation, a simplification of the hypergeometric series method for the analysis of spherical shells. Figure 10.3 indicates the meridional and hoop components of axial force and bending moment, being the metrics of interest.

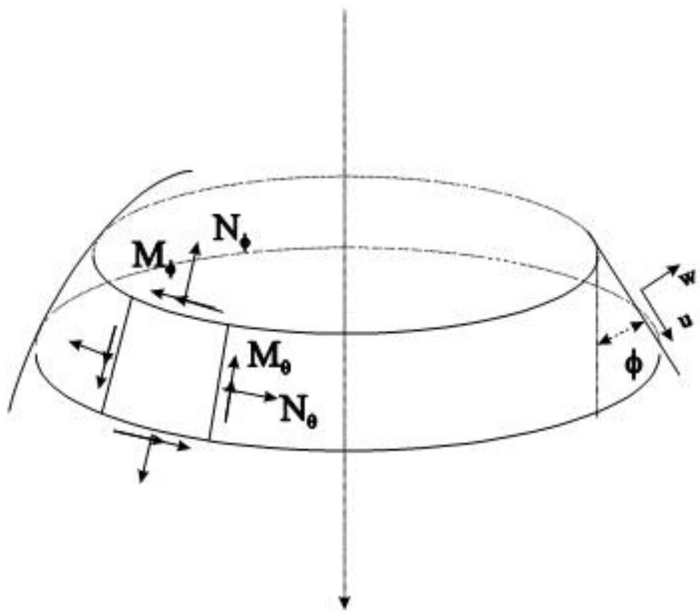

Figure 10.3: Meridional and hoop force/moment components in a spherical shell

The force and moment distributions at meridional angle ϕ can be defined respectively as:

$$N_\phi = -\cot(\alpha - \phi) A \left[\frac{2\lambda}{aK_1} \sqrt{\sin\alpha}\, \sin(\lambda\phi) M_o - \frac{\sqrt{(1+K_1^2)}}{K_1} (\sin\alpha)^{3/2} \sin(\lambda\phi - \tan^{-1} K_1) H \right] + \frac{ap}{2}$$

$$N_\theta = \frac{A\lambda\sqrt{\sin\alpha}}{K_1}\left\{\begin{array}{l} \frac{\lambda}{a}\left[2\cos(\lambda\phi)-(k_1+k_2)\sin(\lambda\phi)\right]M_o \\ -\frac{\sqrt{(1+K_1^2)}}{2}(\sin\alpha)\left[2\cos(\lambda\phi-\tan^{-1}K_1)-(k_1+k_2)\sin(\lambda\phi-\tan^{-1}K_1)\right]H \end{array}\right\}+\frac{ap}{2}$$

$$M_\phi = \frac{A\sqrt{\sin\alpha}}{K_1}\left\{\begin{array}{l} \left[k_1\cos(\lambda\phi)+\sin(\lambda\phi)\right]M_o \\ -\frac{a\sqrt{(1+K_1^2}}{2\lambda}(\sin\alpha)\left[k_1\cos(\lambda\phi-\tan^{-1}K_1)+\sin(\lambda\phi-\tan^{-1}K_1)\right]H \end{array}\right\}$$

$$M_\theta = \frac{aA}{4\nu\lambda}\left\{\begin{array}{l} \frac{2\lambda}{aK_1}\sqrt{\sin\alpha}\left[((1+\nu^2)(k_1+k_2)-2k_2)\cos(\lambda\phi)+2\nu^2\sin(\lambda\phi)\right]M_o \\ -\frac{\sqrt{(1+K_1^2}}{K_1}(\sin\alpha)^{3/2}\left[\begin{array}{l}((1+\nu^2)(k_1+k_2)-2k_2)\cos(\lambda\phi-\tan^{-1}K_1) \\ +2\nu^2\sin(\lambda\phi-\tan^{-1}K_1)\end{array}\right]H \end{array}\right\}$$

where

$$A = \frac{e^{-\lambda\phi}}{\sqrt{\sin(\alpha-\phi)}}$$

$$k_1 = 1-\frac{1-2\nu}{2\lambda}\cot(\alpha-\phi)\,; \qquad k_2 = 1-\frac{1+2\nu}{2\lambda}\cot(\alpha-\phi)$$

$$K_1 = 1-\frac{1-2\nu}{2\lambda}\cot(\alpha)\,; \qquad K_2 = 1-\frac{1+2\nu}{2\lambda}\cot(\alpha)$$

$$M_o = \frac{pa^2(1-\nu)}{4\lambda^2K_2}\,; \qquad H = \frac{pa(1-\nu)}{2\lambda\sin(\alpha)K_2}$$

and λ is the dimensionless *shell slenderness parameter*, as calculated by:

$$\lambda^4 = 3\left(1-\nu^2\right)\left(\frac{a}{t}\right)^2$$

10.3 Results

Figure 10.4 and Figure 10.5 plot the meridional bending moment M_ϕ and the hoop force N_θ as calculated by ***RS2***. There is good agreement with the approximate solution, and ***RS2*** seems to yield more accurate results at values of ϕ, i.e. near the centre of the shell.

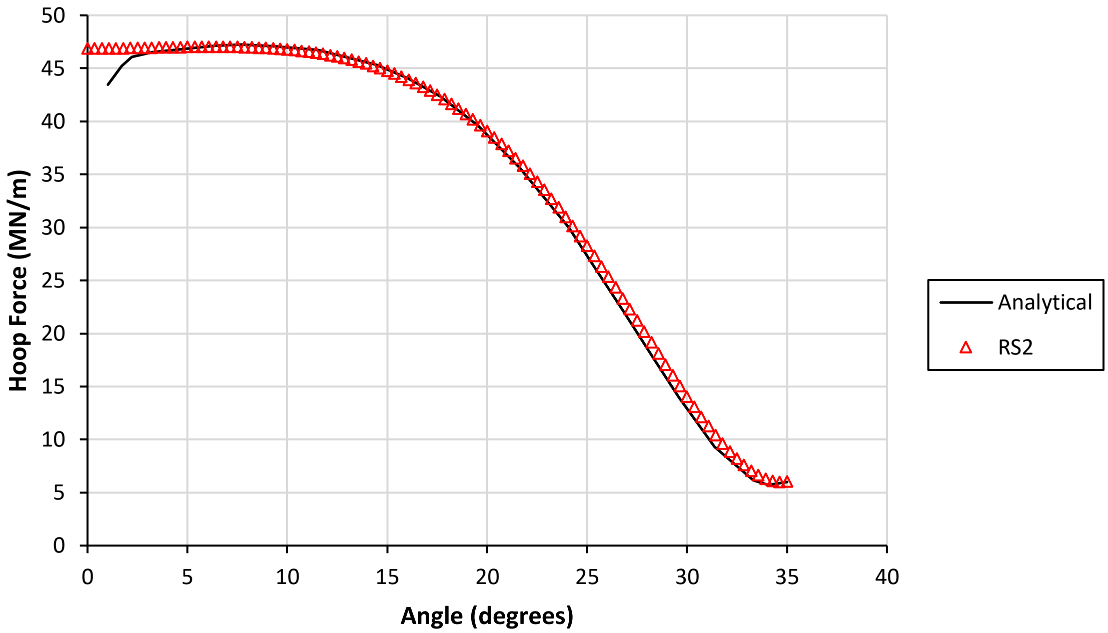

Figure 10.4: Hoop force distribution as determined by *RS2* and the Hetenyi approximation

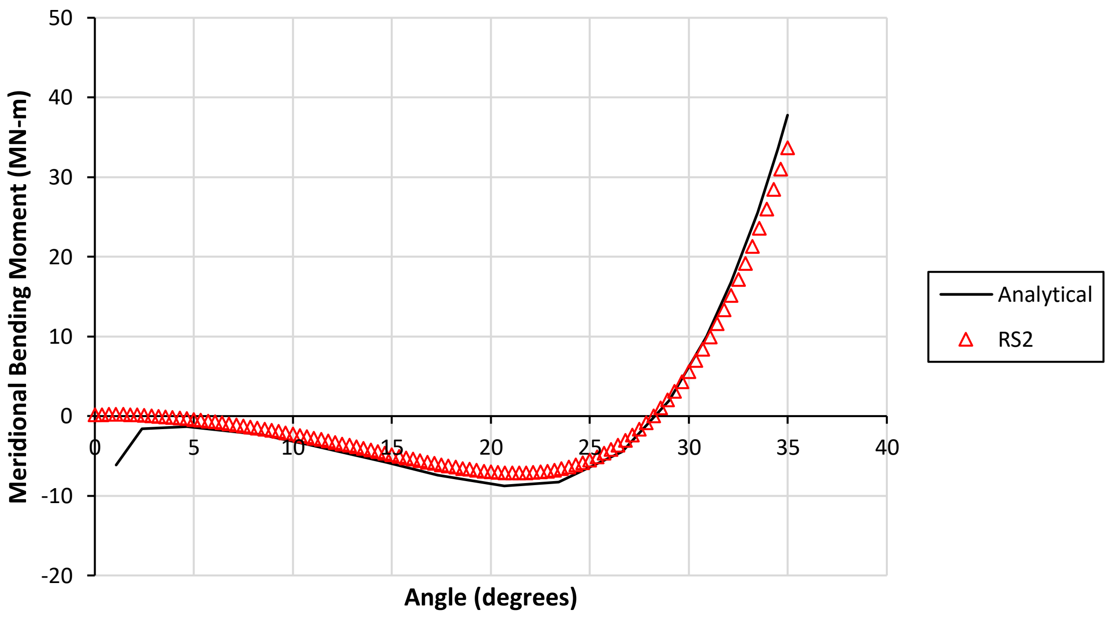

Figure 10.5: Bending moment distribution as determined by *RS2* and the Hetenyi approximation

10.4 References

1. Alphose Zingoni (1997), Shell Structures in Civil and Mechanical Engineering, University of Zimbabwe, Harare, Thomas Telford.

10.5 Data Files

The input file **stress#010.fez** can be downloaded from the RS2 Online Help page for Verification Manuals.

11 Lined Circular Tunnel in a Plastic Medium

11.1 Problem Description

This problem considers the case of a lined elastic circular tunnel in a plastic medium, as well as that of a plastic liner supporting a tunnel in an elastic medium. The liner consists of beam elements constructed according to the Bernoulli formulation. The tunnel is exposed to anisotropic biaxial field stresses. For both cases, the plastic failure surface is defined according to the Drucker-Prager criterion, which can be expressed as:

$$f_s = \sqrt{J_2} + q_\phi \frac{I_1}{3} - k_\phi$$

The plastic potential flow surface is:

$$g_s = \sqrt{J_2} + q_\psi \frac{I_1}{3} - k_\phi$$

in which

$$I_1 = \sigma_1 + \sigma_2 + \sigma_3$$

$$J_2 = \frac{1}{6}\left[(\sigma_x - \sigma_y)^2 + (\sigma_y - \sigma_z)^2 + (\sigma_x - \sigma_z)^2\right] + \tau_{xy}^2 + \tau_{yz}^2 + \tau_{zx}^2$$

The associated (q_ϕ=q_ψ) flow rule is used. Table 11.1 summarizes material, liner and model properties.

Table 11.1: Model parameters

Parameter	***Value***
Horizontal field stress (σ_{xx}^0)	30 MPa
Vertical field stress (σ_{yy}^0)	60 MPa
Out-of-plane field stress (σ_{zz}^0)	30 MPa
Young’s modulus (E_m)	6000 MPa
Poisson’s ratio (v_m)	0.2
k_ϕ	3 MPa
q_ϕ, q_ψ	0.5
Liner Properties	
Young’s modulus (E_b)	(variable)
Poisson’s ratio (v_s)	0.01
Radius (a)	1 m
Yield stress	60 MPa

Figure 11.1 shows the lined tunnel as constructed in ***RS2***. The model uses a radial mesh with 2080 8-noded quadrilateral elements and an infinite element boundary 7 m from the hole centre. The tunnel profile is discretized into 80 elements, as is the liner.

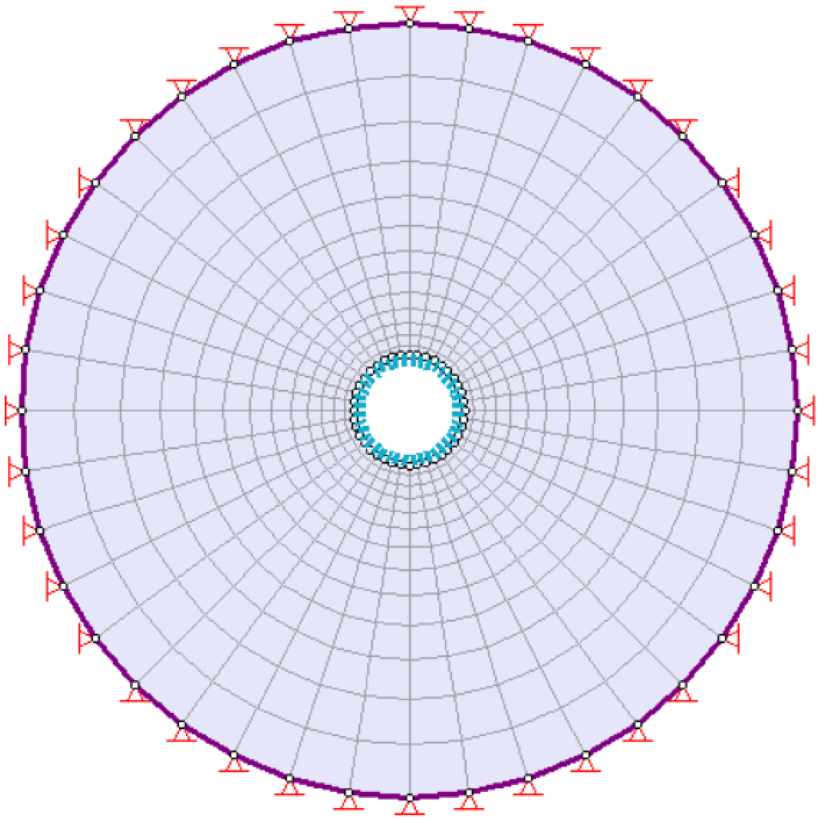

Figure 11.1: Lined circular tunnel as implemented in *RS2*

Table 11.2 summarizes the 10 separate cases considered, using various values of liner thickness and elastic modulus.

Table 11.2: Liner properties for ten cases

	#	File	Thickness (m)	E_b / E_m
Elastic liner in plastic medium	1	**stress#011_01.fez**	0.1	1.5
	2	**stress#011_02.fez**	0.1	2.0
	3	**stress#011_03.fez**	0.1	2.5
	4	**stress#011_04.fez**	0.2	1.5
	5	**stress#011_05.fez**	0.2	2.0
	6	**stress#011_06.fez**	0.2	2.5
Plastic liner in elastic medium	7	**stress#011_11.fez**	0.05	1.0
	8	**stress#011_12.fez**	0.05	2.0
	9	**stress#011_13.fez**	0.2	1.0
	10	**stress#011_14.fez**	0.2	2.0

11.2 Analytical Solution

RS2 results are compared against those from ABAQUS, a commercial finite-element package. ABAQUS also uses the Drucker-Prager model for plastic flow and the Euler-Bernoulli model for beam elements. The results from ***RS2*** do not perfectly match with ABAQUS due to the different liner formulations of each program.

11.3 Results

Figure 11.2Figure 11.2: Axial force distributions for 0.1 m elastic liner with various moduli and Figure 11.3 show the axial force distributions in the elastic liner for the two liner thicknesses studied.

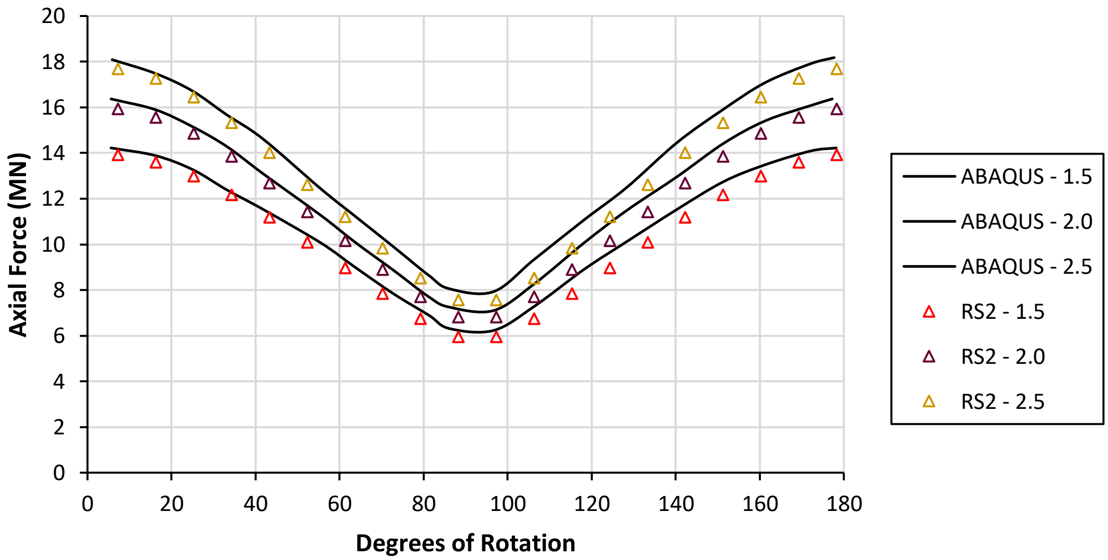

Figure 11.2: Axial force distributions for 0.1 m elastic liner with various moduli

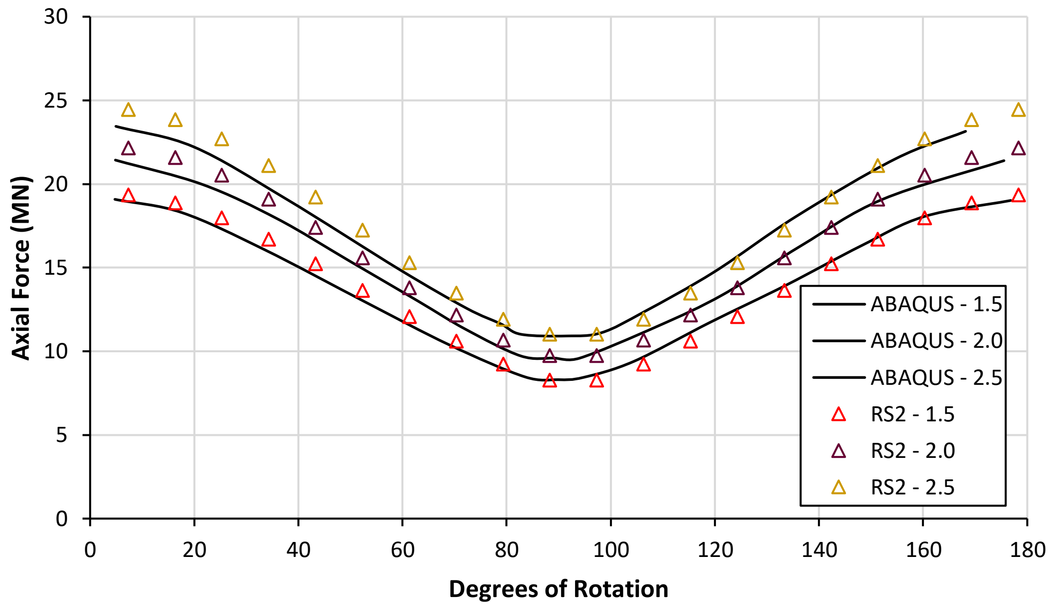

Figure 11.3: Axial force distributions for 0.2 m elastic liner with various moduli

Figure 11.4 and Figure 11.5 show bending moment distributions for cases 1-6.

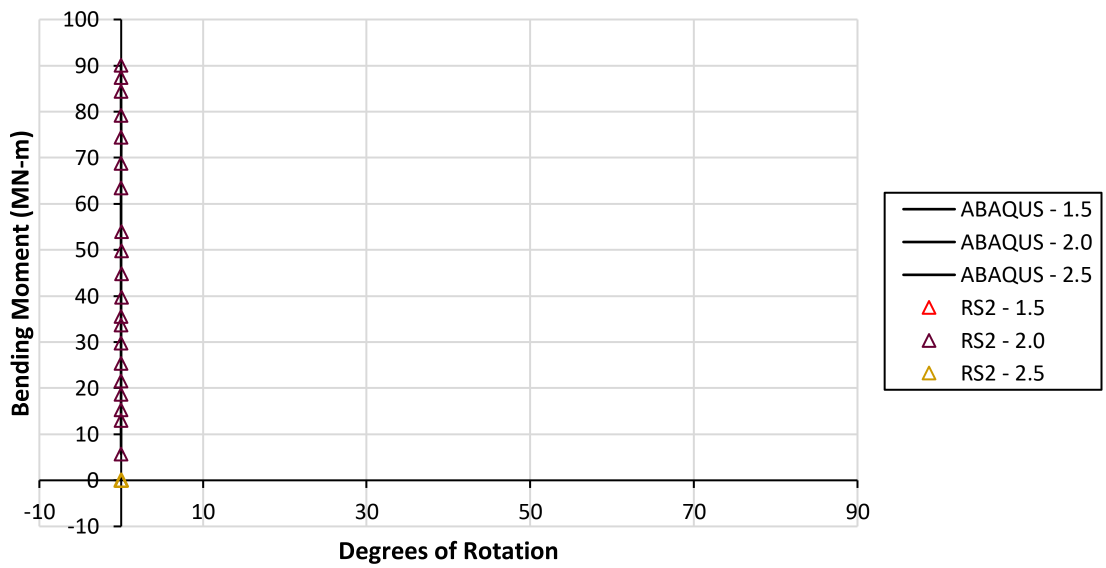

Figure 11.4: Bending moment distributions for 0.1 m elastic liner with various moduli

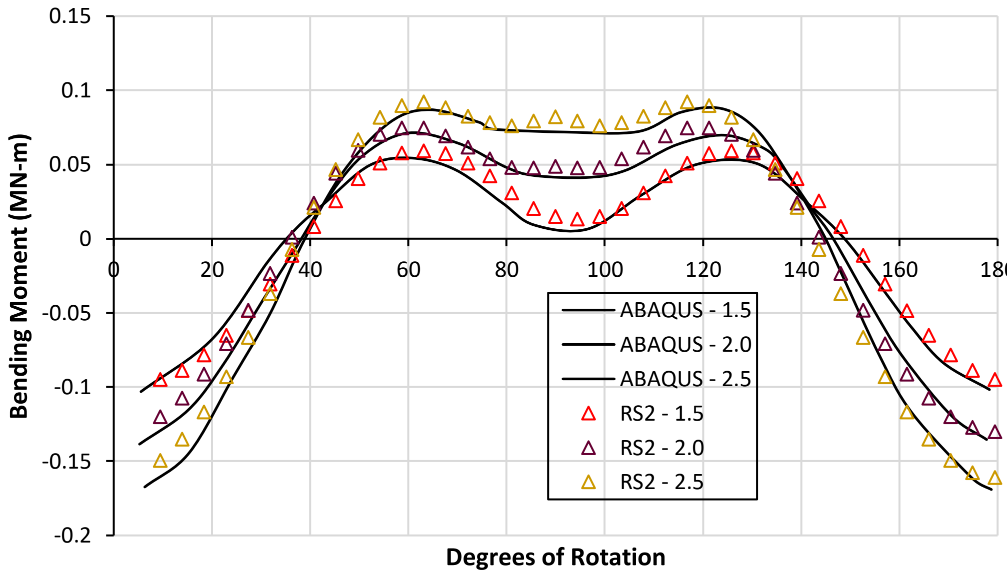

Figure 11.5: Bending moment distributions for 0.2 m elastic liner with various moduli

Figure 11.6 and Figure 11.7 show the axial force distributions for cases 7-10.

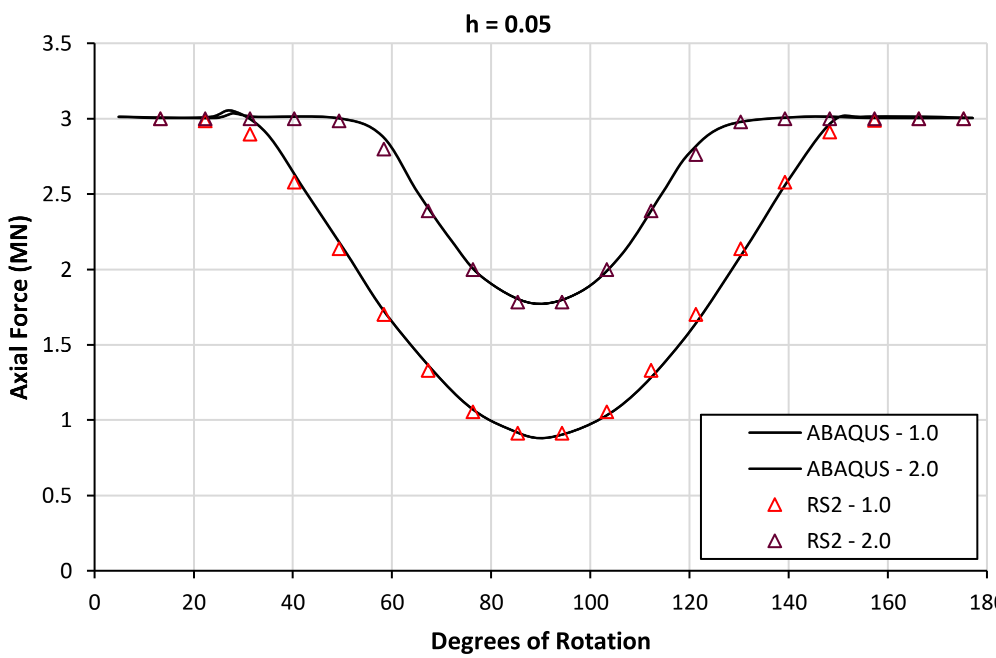

Figure 11.6: Axial force distributions for 0.05 m plastic liner with various moduli

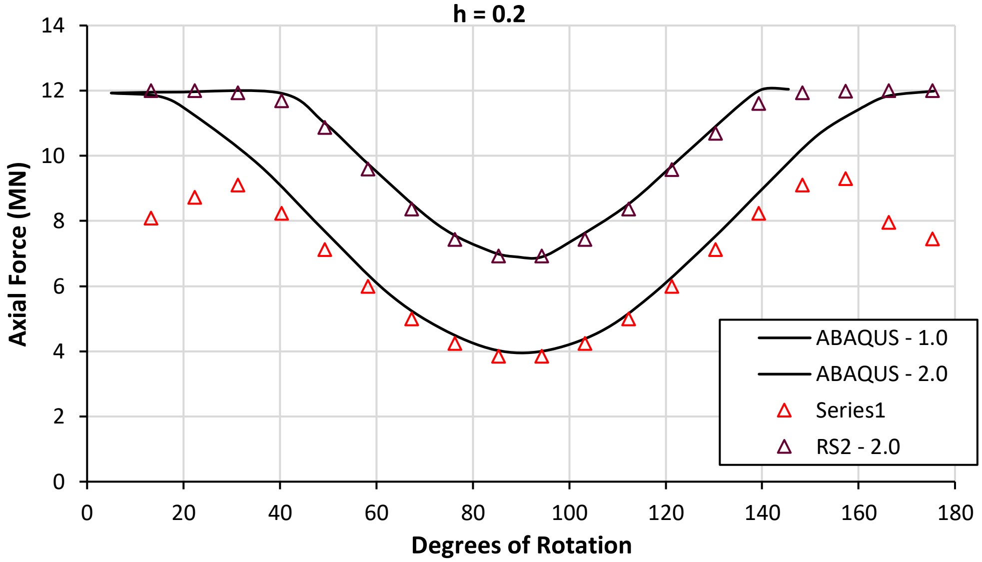

Figure 11.7: Axial force distributions for 0.2 m plastic liner with various moduli

Figure 11.8 and Figure 11.9 show bending moment distributions for cases 7-10.

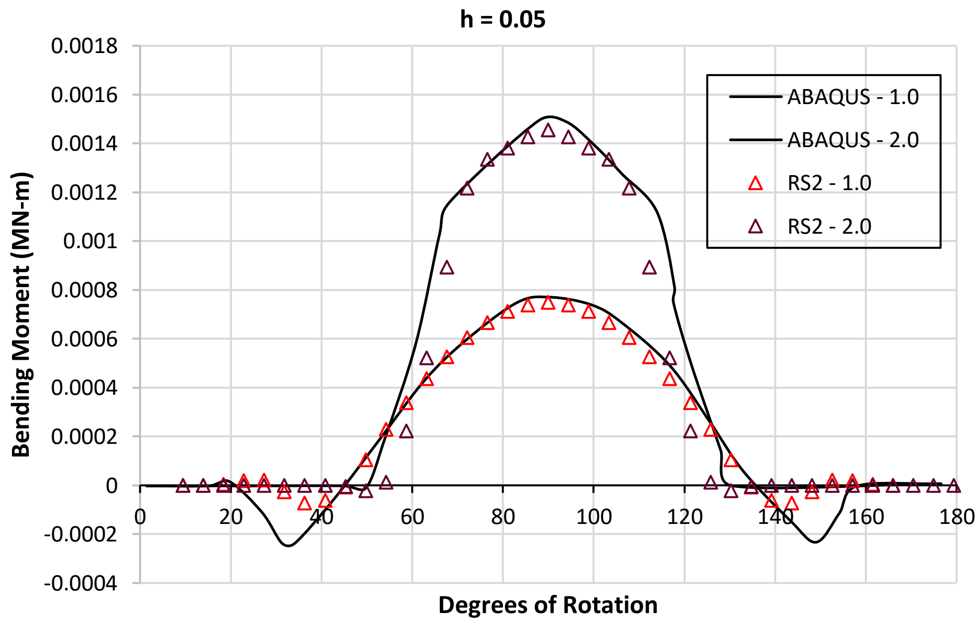

Figure 11.8: Bending moment distributions for 0.05 m liner with various moduli

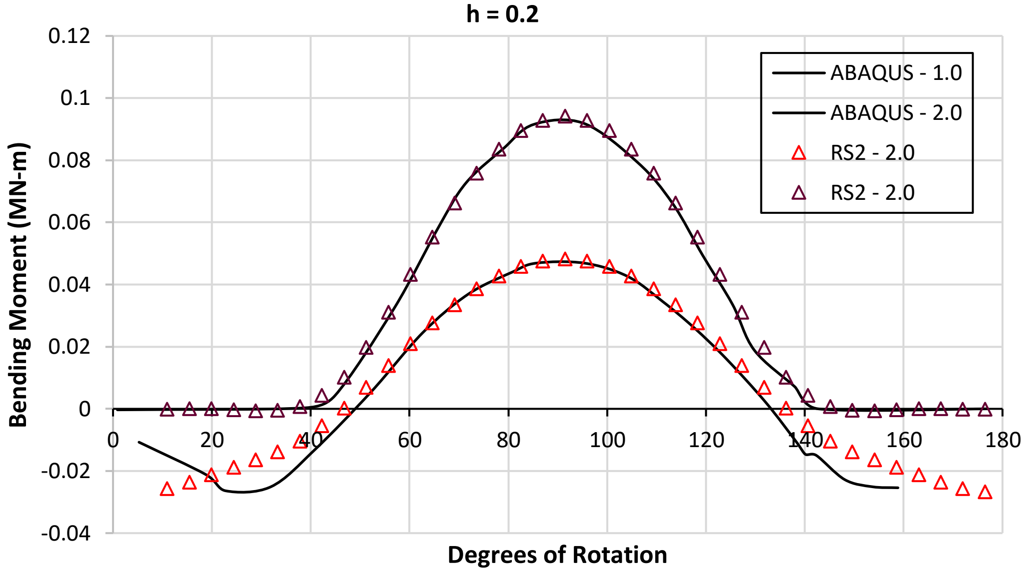

Figure 11.9: Bending moment distributions for 0.2 m liner with various moduli

11.4 Data Files

The input data files for this problem can be downloaded from the RS2 Online Help page for Verification Manuals. Refer to Table 11.2 for the properties associated with each data file.

12 Pull-Out Tests for Shear Bolts (Swellex/Split Set)

12.1 Problem Description

This problem concerns the properties of ungrouted shear bolts in an elastic rock mass. Swellex rockbolts can be considered to be a special case of grouted rockbolt in which the grouting material has no cohesion [5]. The conventional criterion for the performance of a Swellex/split set bolt is the pull-out test, which measures the force per unit length of bolt required for failure of the bolt-rock interface. The pull-out strength of a bolt is a function both of the frictional resistance generated by the expansion of the bolt and the mechanical interlock between the bolt and asperities (extrusions) in the borehole. The latter is usually the dominant factor in hard, stiff rocks [1]. The pull-out force required can thus be expressed as:

$$F_{pull} = \min\left(R_f, S\right)$$

where R_f is the total frictional resistance and S is the shear strength of all asperities in direct contact with the bolt. ***RS2*** does not make this distinction; the bolt-rock interface is assumed to have a single stiffness and pull-out strength.

Figure 12.1 shows a bolt in a rock mass as modeled in RS2. The bolt and rock properties are summarized in

Table 12.1. The bolt is defined as plastic to allow for failure, but is assumed to have no residual tensile capacity.

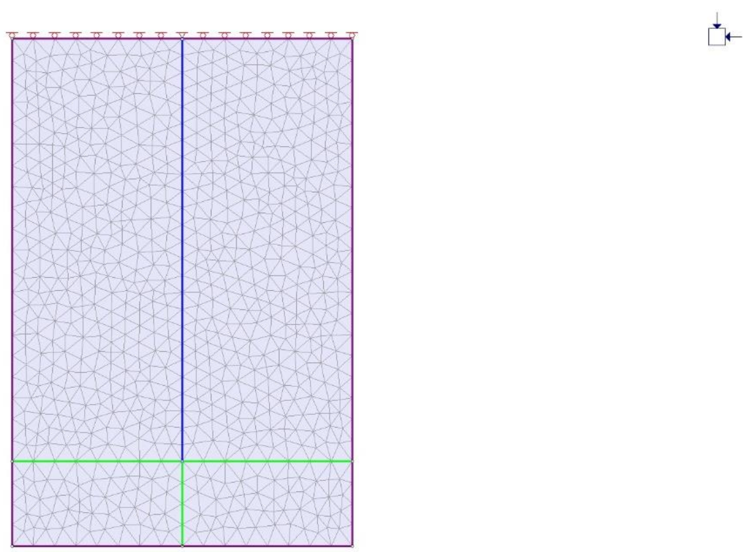

Figure 12.1: Swellex/split set rockbolt as modeled in *RS2*

Table 12.1: Model parameters

Parameter	***Value***
Young's modulus (E)	7500 MPa
Poisson's ratio (v)	0.25
Bolt properties	
Tensile capacity	1.3 MN
Tributary area	181 mm^2
Bolt modulus (E_b)	98600 MPa
Bond strength	0.175 MN/m
Out-of-plane spacing	1 m
Bond shear stiffness	11.2 MN/m^2
Residual tensile capacity	0 MN

The model shown in Figure 12.1 is made up of an elastic host material containing a 50 cm bolt, to which three different pull-out forces (53, 84 and 87 kN) were applied.

12.2 Analytical Solution

The equilibrium equation of a fully grouted rock bolt, as shown in Figure 12.2, may be written as [2,3]:

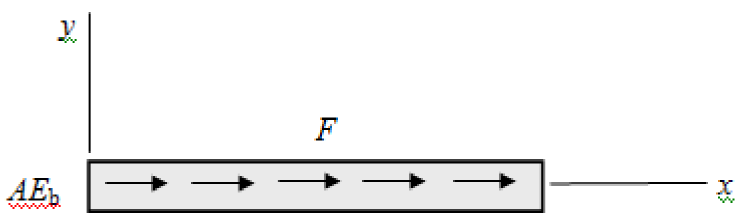

Figure 12.2: Shear bolt model

$$AE_b \frac{d^2 u_x}{dx^2} + F_s = 0 \qquad (12.1)$$

where F_s is the shear force per unit length, A is the cross-sectional area of the bolt and E_b is the modulus of elasticity for the bolt. The shear force is assumed to be a linear function of the relative movement between the rock, μ_r and the bolt, μ_x and is presented as:

$$F_s = k(u_r - u_x) \qquad (12.2)$$

Usually, k is the shear stiffness of the bolt-grout interface measured directly in laboratory pull-out tests. Substituting equation (12.1) in (12.2), then the weak form can be expressed as:

$$\delta\Pi = \int (AE_b \frac{d^2 u_x}{dx^2} - ku_x + ku_r)\, \delta u\, dx \tag{12.3}$$

$$\begin{aligned} &= \int \left\{ AE_b \left[\frac{d}{dx}(\frac{du_x}{dx}\delta u) - \frac{du_x}{dx}\frac{d\delta u}{dx} \right] - (ku_x - ku_r)\delta u \right\} dx \\ &= AE_b \delta u \frac{du_x}{dx}\Big|_0^L \quad - \int \left(AE_b \frac{du_x}{dx}\frac{d\delta u}{dx} + ku_x \delta u \right) dx \quad + \int \left(ku_r \delta u \right) dx \end{aligned} \tag{12.4}$$

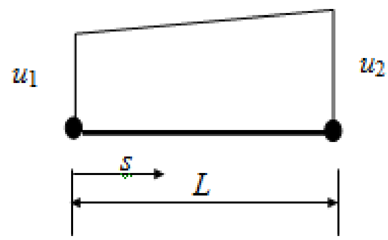

Figure 12.3: Linear displacement variation

The displacement field *u*, is assumed to be linear in the axial coordinate, *s* [4] (see Figure 12.3). This displacement field linearly varies from u_1 at one end to u_2 at the other end. The displacement at any point along the element can be given as:

$$u = \frac{L-s}{L} u_1 + \frac{s}{L} u_2 \qquad \text{or} \quad u = \lfloor N \rfloor \{d\} \tag{12.5}$$

where $\lfloor N \rfloor = \left\lfloor \frac{L-s}{L} \quad \frac{s}{L} \right\rfloor$ and $\{d\} = \begin{Bmatrix} u_1 \\ u_2 \end{Bmatrix}$

for the two displacement fields, equation (12.5) can be written as

$$u = \begin{Bmatrix} u_x \\ u_r \end{Bmatrix} = \begin{bmatrix} N_1 & N_2 & 0 & 0 \\ 0 & 0 & N_1 & N_2 \end{bmatrix} \begin{Bmatrix} u_{x1} \\ u_{x2} \\ u_{r1} \\ u_{r2} \end{Bmatrix} \tag{12.6}$$

Equation (12.2) can be written as

$$-\int \left(AE_b \frac{du_x}{dx}\frac{d\delta u}{dx} + ku_x \delta u \right) dx + \int \left(ku_r \delta u \right) dx = - \quad \lfloor u_{x1} \quad u_{x2} \quad u_{r1} \quad u_{r2} \rfloor \begin{bmatrix} K_b & 0 \\ 0 & -K_r \end{bmatrix} \delta \begin{Bmatrix} u_{x1} \\ u_{x2} \\ u_{r1} \\ u_{r2} \end{Bmatrix} \tag{12.7}$$

By introducing the notation $\lfloor B \rfloor = \lfloor N_{,x} \rfloor$ the strain can be expressed as

$$u_{,x} = \frac{du}{dx} = \lfloor B \rfloor \{d\} = \left\lfloor -\frac{1}{L} \quad \frac{1}{L} \right\rfloor \begin{Bmatrix} u_1 \\ u_2 \end{Bmatrix} \tag{12.8}$$

Hence,

$$[K_b] = \int_0^L \left\{ AE_b \begin{bmatrix} N_{1,x}N_{1,x} & N_{1,x}N_{2,x} \\ N_{2,x}N_{1,x} & N_{2,x}N_{2,x} \end{bmatrix} + k \begin{bmatrix} N_1N_1 & N_1N_2 \\ N_2N_1 & N_2N_2 \end{bmatrix} \right\} dx \tag{12.9}$$

$$[K_b] = \frac{AE_b}{L} \begin{bmatrix} 1 & -1 \\ -1 & 1 \end{bmatrix} + k \int_0^L \begin{bmatrix} \left(1 - \frac{x}{L}\right)^2 & \left(1 - \frac{x}{L}\right)\frac{x}{L} \\ \left(1 - \frac{x}{L}\right)\frac{x}{L} & \left(\frac{x}{L}\right)^2 \end{bmatrix} dx \tag{12.10}$$

$$[K_b] = \frac{AE_b}{L} \begin{bmatrix} 1 & -1 \\ -1 & 1 \end{bmatrix} + \frac{kL}{3} \begin{bmatrix} 1 & 0.5 \\ 0.5 & 1 \end{bmatrix} \tag{12.11}$$

and

$$[K_r] = k \begin{bmatrix} N_1N_1 & N_1N_2 \\ N_2N_1 & N_2N_2 \end{bmatrix} = \frac{kL}{3} \begin{bmatrix} 1 & 0.5 \\ 0.5 & 1 \end{bmatrix} \tag{12.12}$$

RS2 uses equations (12.11) and (12.12) to assemble the stiffness for the shear bolts.

12.3 Results

Figure 12.4 and Figure 12.5 show principal stress contours as calculated by ***RS2*** for a pull-out force of 53 kN.

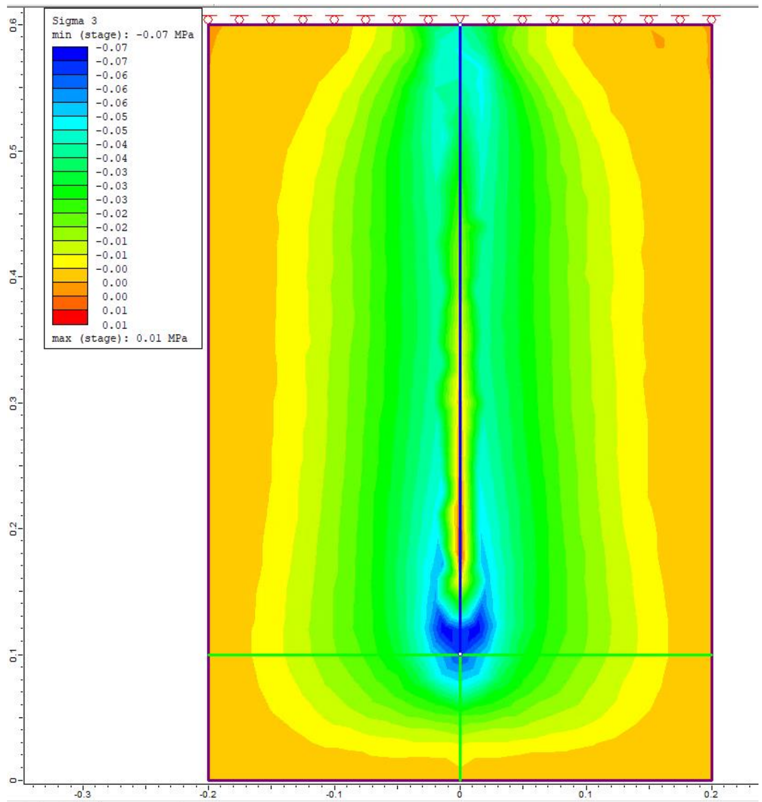

Figure 12.4: σ_3 contours surrounding bolt

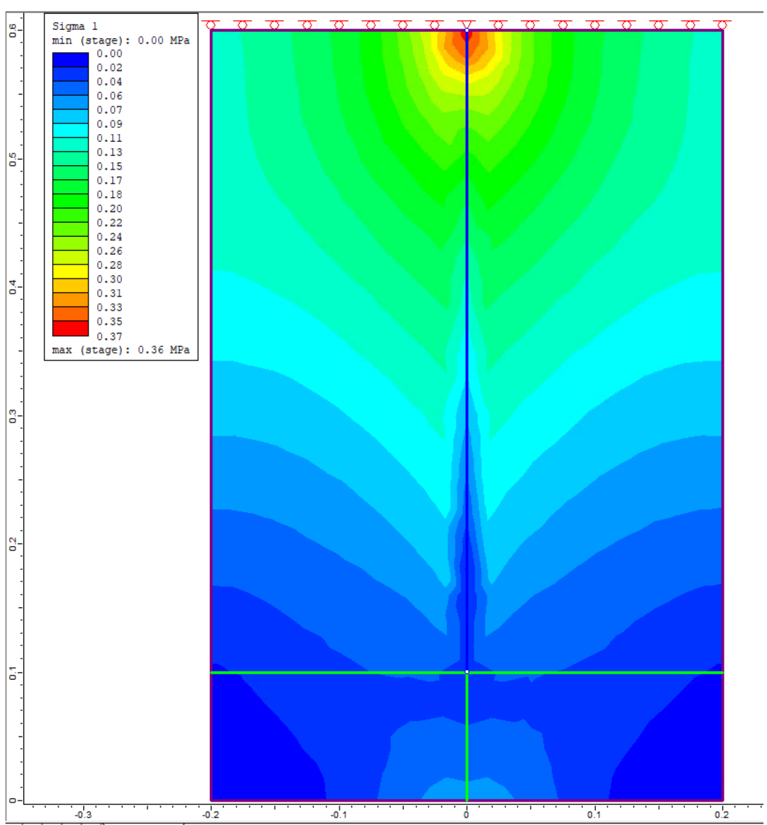

Figure 12.5: σ_1 contours surrounding bolt

Figure 12.6 shows the axial force distribution along the bolt for a pull-out force of 84 kN. The lighter blue elements at the upper extremity of the bolt indicate failure. No failure occurs for the 53 kN load and almost complete failure occurs at 87 kN.

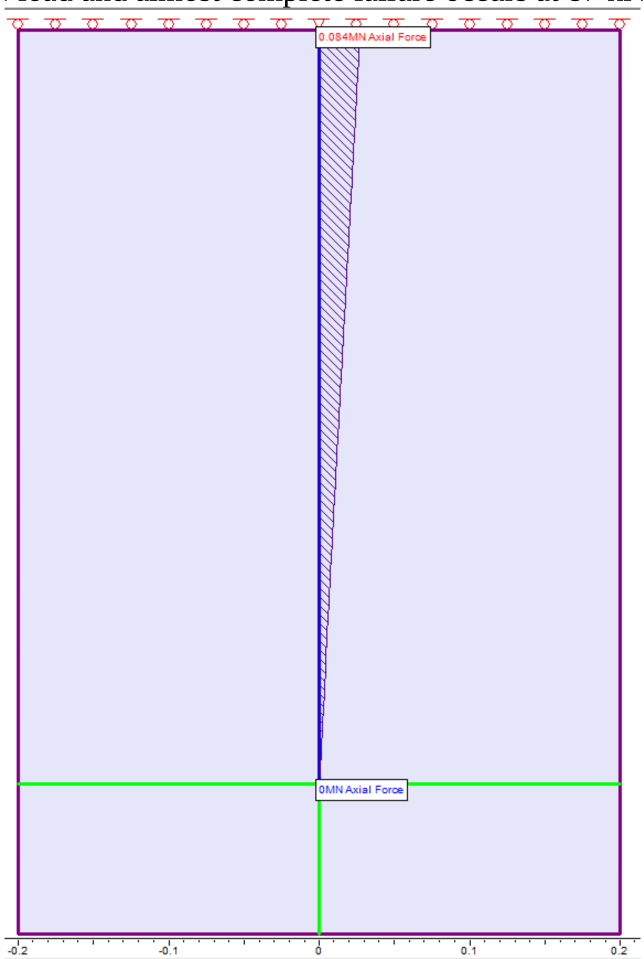

Figure 12.6: Axial force distribution along partially failed bolt in *RS2*

In all three cases, agreement between ***RS2*** and theoretical results was very good. Figure 12.7 plots the force-displacement curve for the bolt, illustrating its perfectly elastic behaviour.

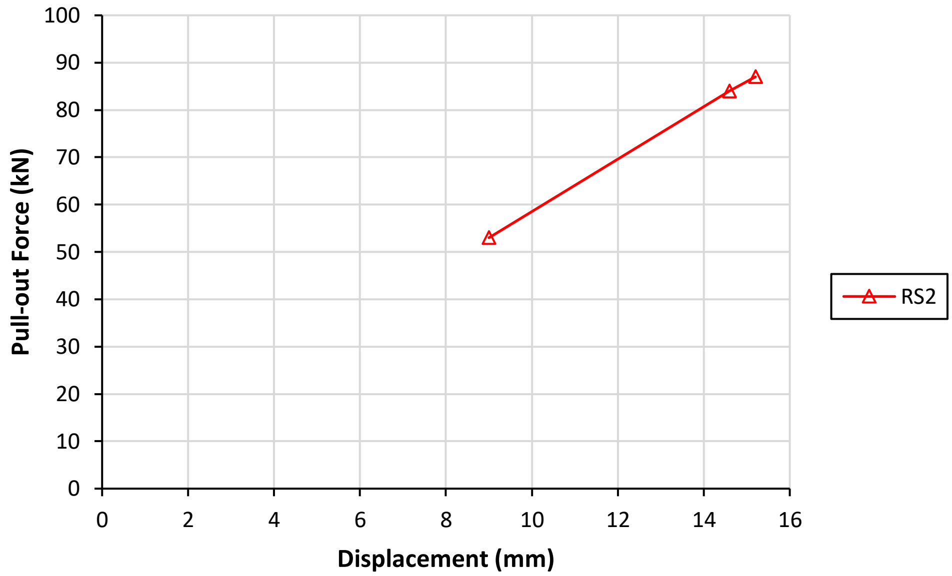

Figure 12.7: Elastic force-displacement behaviour of single rock bolt, as calculated by *RS2*

12.4 References

1. Li, C. & Hakansson, U. (1999), "Performance of the Swellex bolt in hard and soft rocks". *Rock Support and Reinforcement Practice in Mining*, Villaescusa, Windsor & Thompson. Balkema, Rotterdam. ISBN 90 5809 045 0

2. Farmer, I.W. (1975), "Stress distribution along a resin grouted rock anchor", *Int. J. of Rock Mech. And Mining Sci & Geomech. Abst*., 12, 347-351.

3. Hyett, A.J., Moosavi, M. and Bawden, W.F. (1996), "Load distribution along fully grouted bolts, with emphasis on cable bolt reinforcement", *Int. J. Numer and Analytical meth. In Geomech.*, 20, 517-544

4. Cook, R.D., Malkus, D.S., Plesha, M.E (1981), *Concepts and applications of finite element analysis*, 3rd Edition, Wiley

5. Carranza-Torres, C. (2008), "Analytical and Numerical Study of the Mechanics of Rockbolt Reinforcement around Tunnels in Rock Masses", *Rock Mech. Rock Engng.* 42: 175-228.

12.5 Data Files

The input data file **stress#012.fez** can be downloaded from the RS2 Online Help page for Verification Manuals.

13 Drained Triaxial Compressive Test of Modified Cam Clay Material

13.1 Problem Description

The Modified Cam Clay (MCC) constitutive relationship is one of the earliest critical state models for realistically describing the behaviour of soft soils. As a result it is one of the most widely applied stress-strain relationship in the non-linear finite element modeling of practical geotechnical problems. The state at a point in an MCC soil is characterized by three parameters: effective mean stress (p’), deviatoric (shear stress) (q), and specific volume v.

Due to the complexity of the MCC model, very few MCC problems have closed-form solutions, which can be used to verify the accuracy, stability and convergence of MCC finite element algorithms. One of the problems with an analytical solution is the consolidated-drained triaxial test on a Modified Cam Clay sample. In this test, the sample is first consolidated under a hydrostatic pressure, and then sheared by applying additional axial load (see Figure 13.1). The drainage condition is such that there is no build up of excess pore water pressures (i.e. excess pore pressures are allowed to fully dissipate).

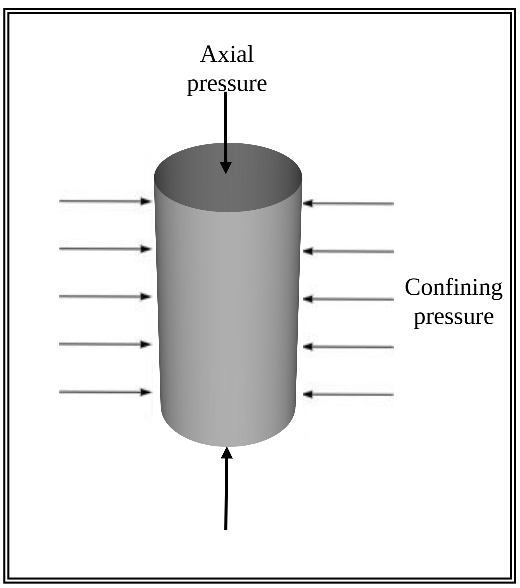

Figure 13.1: Triaxial compressive test of cylindrical soil sample

In ***RS2***, the MCC constitutive model is integrated implicitly over a finite strain increment using the approach presented by Borja [1]. Major advantages of the approach are its accuracy, robustness and efficiency. The performance of this algorithm in ***RS2*** will be tested on three examples of drained triaxial tests. The first test on a normally consolidated clay sample involves only post-yield (elasto-plastic) loading; a behavior that is associated with hardening of the material. The second test is on a lightly over consolidated clay sample where the initial behavior is elastic and it is followed by a transition to elastoplastic response. The last example demonstrates the behavior of a highly over consolidated clay sample that includes an initial elastic behavior followed by failure and a softening branch in its stress path. The stress paths, initial and final yield surfaces of these tests are shown in Figure 13.2 to Figure 13.4.

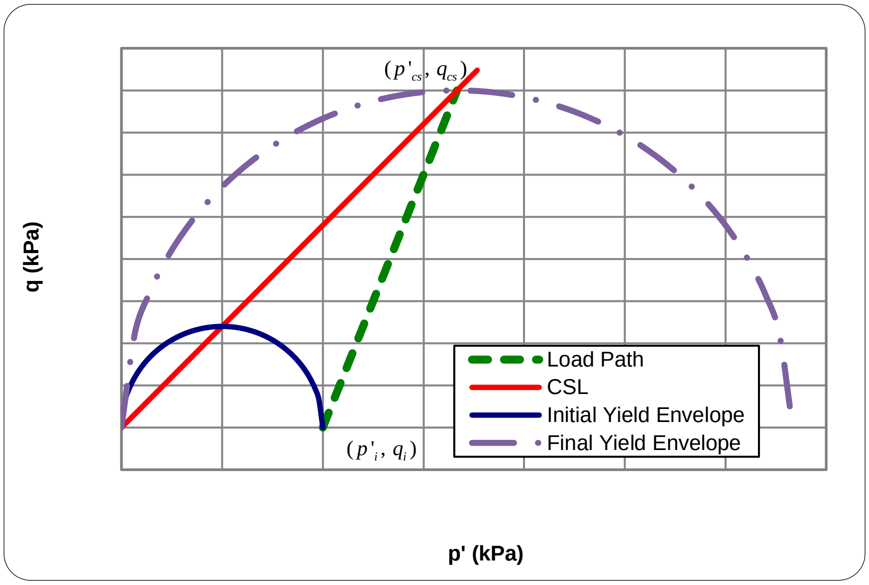

Figure 13.2: Example 1, drained triaxial compressive test on a normally consolidated clay sample, stress path, initial and final yield surfaces in *p'*-*q* space

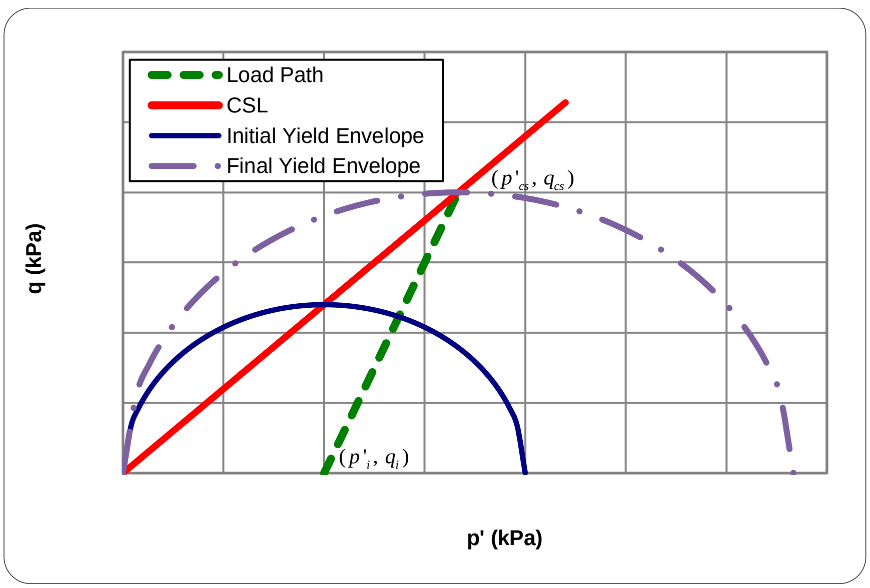

Figure 13.3: Example 2, drained triaxial compressive test on a lightly over consolidated clay sample (OCR=2), stress path, initial and final yield surfaces in *p'*-*q'* space

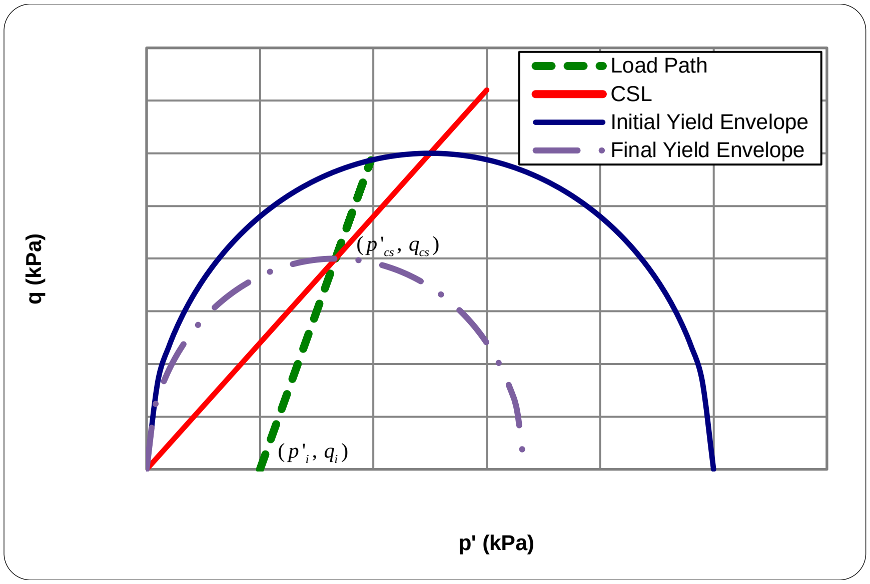

Figure 13.4: Example 3, drained triaxial compressive test on a highly over consolidated clay sample (OCR=5), stress path, initial and final yield surfaces in *p'-q'* space

For each triaxial test, two plots will be generated to compare the performance of the MCC implementation in ***RS2*** in relation to the drained triaxial test benchmark solution. The first plot examines the relationship between deviatoric (shear stress), q , and axial strain, ε_a , of the test sample, while the second compares volumetric strains, ε_v , to axial strains.

Five material parameters are required to specify the behaviour of the MCC sample. These are:

1. λ – the slope of the normal compression (virgin consolidation) line and critical state line (CSL) in $v - \ln p'$ space
2. κ – the slope of a swelling (loading-unloading) line in $v - \ln p'$ space
3. M – the slope of the CSL in $q - p'$ space
4. N – the specific volume of the normal compression line at unit pressure
   or
   Γ – the specific volume of the CSL at unit pressure
5. μ – Poisson's ratio
   or
   G – shear modulus.

As can be seen from the description of input parameters, the MCC formulation requires specification of either a constant shear modulus G or a constant Poisson's ratio μ , but not both. The verification example will examine the performance of ***RS2*** using both of these options.

The initial state of consolidation of the MCC soil is specified in terms of a pre-consolidation pressure, p_o. (***RS2*** also allows users to specify the initial state of consolidation through the over-consolidation ratio.)

For the test, the following material properties and conditions are assumed:

Table 13.1: Model parameters

Parameter	***Value***
N	1.788
M	1.2
λ	0.077
κ	0.0066
G (for the case of constant elasticity)	20000 kPa
μ (for the case of variable elasticity)	0.3
Initial State of the Normally Consolidated Clay	
Preconsolidation pressure, p_o	200 kPa
Initial mean volumetric stress, p'	200 kPa
Initial shear stress, q	0 kPa
Initial State of the Lightly Over Consolidated Clay	
Preconsolidation pressure, p_o	200 kPa
Initial mean volumetric stress, p'	100 kPa
Initial shear stress, q	0 kPa
Initial State of Highly Over Consolidated Clay	
Preconsolidation pressure, p_o	500 kPa
Initial mean volumetric stress, p'	100 kPa
Initial shear stress, q	0 kPa

13.2 Analytical Solution

The analytical solution presented here is adopted form an article by Peric [2]. The solution distinguishes between the volumetric, (p', ε_v), and the deviatoric, (q, ε_q), behavior of the material.

13.2.1 The volumetric behavior

Decomposing to its elastic and plastic parts, the rate of the volumetric strain can be obtained from its nonlinear elastic behavior and the hardening rule.

$$\dot{\varepsilon}_v^e = K\dot{p}' = \left(\frac{\kappa}{\nu_n}\right)\frac{\dot{p}'}{p'} \qquad \dot{\varepsilon}_v^p = \left(\frac{\lambda-\kappa}{\nu_n}\right)\frac{\dot{p}_0}{(p_0)_n}$$

Considering a general rate of stress, using the definition of the yield surface the rate of plastic volumetric strain can be rewritten as

$$\dot{\varepsilon}_v^p = \left(\frac{\lambda-\kappa}{\nu_n}\right)\left(\frac{\dot{p}'}{p'}+\frac{2\eta\dot{\eta}}{M^2+\eta^2}\right) \quad , \quad \eta = \frac{q}{p'} \quad , \quad \dot{\eta} = \frac{\dot{q}}{\dot{p}'}$$

Integrating the above equation over a finite time increment (step n to step $n+1$), assuming that the change in specific volume is insignificant, results in the following incremental equation

$$\Delta\varepsilon_v^e = \frac{1}{\nu_n}\ln\left(\frac{p'_{n+1}}{p'_n}\right)^{\kappa} \qquad \Delta\varepsilon_v^p = \frac{1}{\nu_n}\ln\left(\left(\frac{p'_{n+1}}{p'_n}\right)\left(\frac{M^2+\eta_{n+1}^2}{M^2+\eta_n^2}\right)\right)^{\lambda-\kappa}$$

Thus the total increment of volumetric strain is

$$\Delta\varepsilon_v = \frac{1}{\nu_n}\ln\left(\left(\frac{p'_{n+1}}{p'_n}\right)^{\lambda}\left(\frac{M^2+\eta_{n+1}^2}{M^2+\eta_n^2}\right)^{\lambda-\kappa}\right)$$

Considering a straight stress path in $(p'-q)$ space, with a slope of $(\Delta q/\Delta p') = k$, the above equation can be rewritten as

$$\Delta\varepsilon_v = \frac{1}{\nu_n}\ln\left(\left(\frac{k-\eta_n}{k-\eta_{n+1}}\right)^{\lambda}\left(\frac{M^2+\eta_{n+1}^2}{M^2+\eta_n^2}\right)^{\lambda-\kappa}\right)$$

Note that in the case of a drained triaxial test $k=3$.

The change in the specific volume can also be calculated from the increment of volumetric strain as follows.

$$\Delta\nu = \frac{\Delta\varepsilon_v}{\nu_n}$$

13.2.2 The deviatoric behavior

According to the flow rule the rate of plastic strains are calculated as

$$\dot{\varepsilon}_v^p = \dot{\lambda}\frac{\partial F}{\partial p'} \qquad \dot{\varepsilon}_q^p = \dot{\lambda}\frac{\partial F}{\partial q}$$

So the relation between the rate of volumetric strain and the deviatoric one is

$$\dot{\varepsilon}_q^p \frac{\partial F}{\partial p'} = \dot{\varepsilon}_v^p \frac{\partial F}{\partial q}$$

Thus the rate of deviatoric plastic strain is

$$\dot{\varepsilon}_q^p = \frac{2\eta}{M^2-\eta^2}\dot{\varepsilon}_v^p = \left(\frac{\lambda-\kappa}{\nu_n}\right)\left(\frac{2\eta}{M^2-\eta^2}\right)\left(\frac{\dot{p}'}{p'}+\frac{2\eta\dot{\eta}}{M^2+\eta^2}\right)$$

Once again by considering a straight stress path, with a slope of $(\Delta q/\Delta p') = k$, the plastic deviatoric strain can be calculated as

$$\dot{\varepsilon}_q^p = \left(\frac{\lambda-\kappa}{\nu_n}\right)\left(\frac{2\eta}{\left(M^2-\eta^2\right)\left(k-\eta\right)}+\frac{4\eta^2}{M^4+\eta^4}\right)\dot{\eta}$$

The elastic portion of the deviatoric strain can be calculated from Hooke's law:

$$\dot{\varepsilon}_q^e = \frac{\dot{q}}{3G}$$

In case the model uses a constant poisson's ratio the shear modulus should be calculated as

$$G = \alpha K = \frac{\alpha \nu_n p'}{\kappa} \quad , \quad \alpha = \frac{3(1-2\mu)}{2(1+\mu)}$$

Integrating the rate of deviatoric strain over a finite time increment (step n to step $n+1$), results in the following incremental equation for the plastic and elastic portion of deviatoric strain

$$\Delta\varepsilon_q^p = \frac{1}{\nu_n}\left\{ \ln\left[\left(\frac{M-\eta_{n+1}}{M-\eta_n}\right)^{(\lambda-\kappa)k/(M(M-k))} \left(\frac{M+\eta_{n+1}}{M+\eta_n}\right)^{(\lambda-\kappa)k/(M(M+k))} \left(\frac{M+\eta_{n+1}}{M+\eta_n}\right)^{2(\lambda-\kappa)k/(k^2-M^2)} \right] \right\}$$

$$-\frac{2(\lambda-\kappa)}{M\nu_n}\left[\arctan\left(\frac{\eta_{n+1}}{M}\right) - \arctan\left(\frac{\eta_n}{M}\right)\right]$$

In the case of constant shear modulus the elastic part of the increment of deviatoric strain is

$$\Delta\varepsilon_q^e = \frac{q_{n+1}-q_n}{3G}$$

Otherwise,

$$\Delta\varepsilon_q^e = \frac{1}{\nu_n}\ln\left(\frac{k-\eta_{n+1}}{k-\eta_n}\right)^{-(\kappa k)/(3\alpha)}$$

The volumetric and shear strains calculated in a triaxial test can be related to the axial and radial strains, ε_a and ε_r, respectively, of the test sample. The relationships are as follows:

$$\varepsilon_a = \frac{1}{3}\varepsilon_v + \varepsilon_q$$

$$\varepsilon_r = \frac{1}{3}\varepsilon_v - \frac{1}{2}\varepsilon_q \, .$$

The formulations presented above have been implemented in Excel spreadsheets included with this document.

13.3 *RS2* Model

The drained compressive triaxial tests of the MCC sample were modeled in ***RS2*** using a single 8-noded quadrilateral element. The simulation is axisymmetric. The deviatoric stress is generated in the sample in two different ways using load-control and displacement-control processes. In the load–control method the axial load is increased in a number of stages that match the load steps used in the analytical solution. In the displacement-control simulations axial displacement is imposed on the sample, once again in a number of stages that match the displacement history of analytical solutions. The mesh, boundary conditions, and an example of the applied axial and radial loads used are shown on Figure 13.7 for both cases of load-control and displacement-control simulations.

As mentioned before, for each example the stage factors for the axial loads or axial deformation were calculated (from the attached spreadsheet) such that the resulting effective mean and deviatoric stresses conformed to the selected triaxial loading path. In the first test, which starts with stresses on the initial yield envelope, the load path (shown on Figure 13.2) was applied in 32 stages. In Examples 2 and 3 (Figure 13.3 and Figure 13.4), the load path was applied in 35 stages.

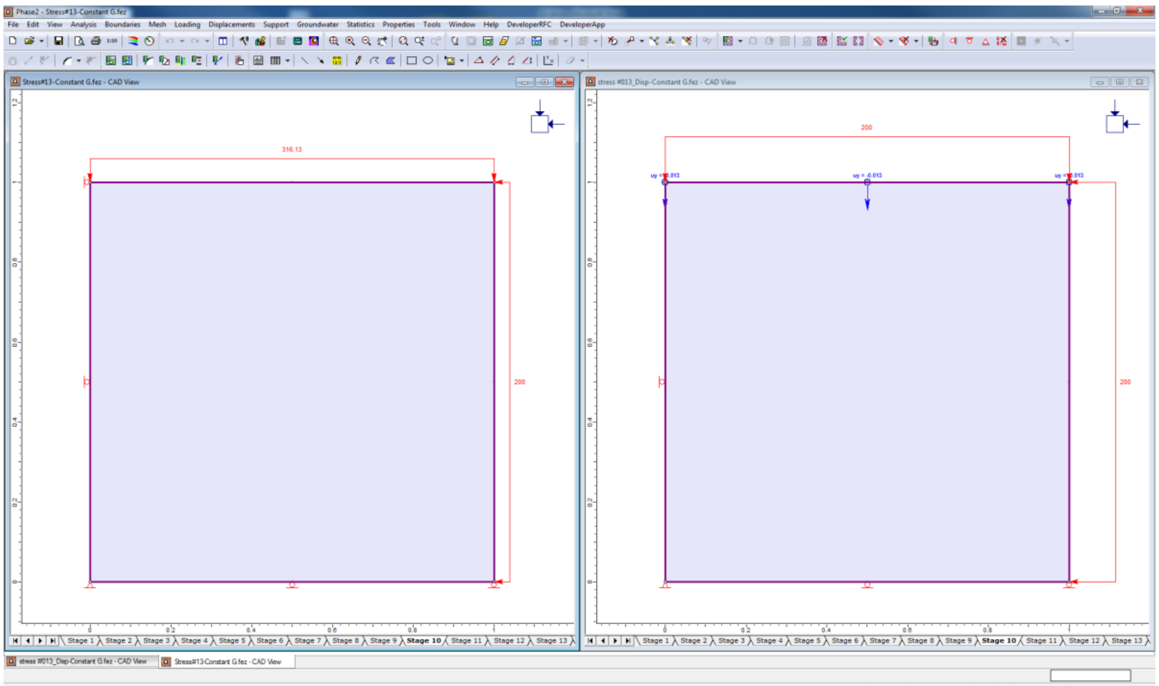

Figure 13.5: Mesh, boundary conditions and loads for axisymmetric *RS2* analysis; load-control and displacement-control simulations

13.4 **Results**

Table 13.2 and Table 13.3 present the variation of the deviatoric stress, axial and volumetric strains calculated from the analytical solution and from *RS2* for the first triaxial test example (Example 1). Table 13.2 represents the case of constant shear modulus, while in Table 13.3 the Poisson’s ratio is constant.

Figure 13.6Figure 13.8 and Figure 13.7 show the plots of $\varepsilon_a - q$ and $\varepsilon_a - \varepsilon_v$ obtained from the analytical and numerical solutions for the case of constant shear modulus. Figure 13.8 and Figure 13.9 show the same results but for the case of constant Poisson’s ratio.

Accordingly, the results for the second and third examples are summarized in Table 13.4 to Table 13.6 and Figure 13.10 to Figure 13.15.

For all the cases analyzed here, there is a good agreement between the analytical results and the numerical results obtained from ***RS2***.

Table 13.2: Example 1, Triaxial test on a normally consolidated clay sample; results for case of constant shear modulus

	RS2 **Load-Control**			***RS2*** **Displacement-Control**			**Analytical Solution**		
No.	***q (kPa)***	**Axial strain, ε_a**	**Volumetric strain, ε_v**	***q (kPa)***	**Axial strain, ε_a**	**Volumetric strain, ε_v**	***q (kPa)***	**Axial strain, ε_a**	**Volumetric strain, ε_v**
1	0	3.59E-20	1.21E-18	0	1.72E-19	1.19E-18	0.00	0	0
2	12.59	0.00044324	0.000567552	15.55	0.00062246	0.00084442	12.90	0.000622462	0.001088486
3	25.16	0.0012687	0.00183158	26.51	0.0014151	0.0020714	25.81	0.00141506	0.0023609
4	37.77	0.0022852	0.00325994	39.33	0.0023933	0.00338998	38.71	0.002393307	0.003790463
5	50.4	0.0035023	0.00482618	51.22	0.0035673	0.00488228	51.61	0.003567347	0.005351034
6	63.08	0.0049249	0.00650388	63.24	0.0049437	0.00649088	64.52	0.004943718	0.007018538
7	75.77	0.0065547	0.00826862	75.41	0.0065266	0.00819132	77.42	0.006526576	0.008771246
8	88.5	0.0083925	0.0100995	87.72	0.0083187	0.00996338	90.32	0.008318725	0.010589882
9	101.24	0.010439	0.0119786	100.12	0.010323	0.0117902	103.23	0.010322481	0.012457593
10	113.99	0.012695	0.0138909	112.58	0.01254	0.0136547	116.13	0.012540392	0.014359832
11	126.94	0.015215	0.0158661	125.1	0.014976	0.0155467	129.03	0.014975865	0.016284187
12	139.73	0.017905	0.0178122	137.66	0.017634	0.0174536	141.94	0.017633727	0.018220172
13	152.47	0.020806	0.0197528	150.25	0.020521	0.0193666	154.84	0.020520757	0.020159017
14	165.22	0.023931	0.0216854	163.41	0.023646	0.0212382	167.74	0.023646238	0.022093453
15	178.13	0.027345	0.0236356	175.81	0.027023	0.0231318	180.65	0.027022563	0.024017511
16	190.86	0.03096	0.0255388	188.26	0.030666	0.025015	193.55	0.030665968	0.025926344
17	203.73	0.034887	0.0274432	200.75	0.034597	0.0268862	206.45	0.034597444	0.027816052
18	216.42	0.039048	0.0292956	213.62	0.038844	0.0287036	219.35	0.03884394	0.029683544
19	229.21	0.043569	0.03114	225.88	0.04344	0.030545	232.26	0.043439997	0.03152641
20	242.13	0.048502	0.0329748	238.78	0.04843	0.0323916	245.16	0.048430026	0.033342806
21	254.87	0.053775	0.0347552	251.23	0.053872	0.0342848	258.06	0.053871587	0.035131362
22	267.8	0.059603	0.036531	264.49	0.05984	0.036142	270.97	0.059840239	0.036891106
23	280.67	0.065967	0.038269	277.99	0.066437	0.037961	283.87	0.066436968	0.038621387
24	293.55	0.073009	0.039977	291.5	0.0738	0.039742	296.77	0.07380002	0.040321827
25	306.41	0.08087	0.04165	304.98	0.082125	0.041489	309.68	0.082124707	0.041992264
26	319.21	0.089735	0.043287	318.54	0.091699	0.043253	322.58	0.091698587	0.043632716
27	332.13	0.10006	0.04491	332.29	0.10297	0.044938	335.48	0.102969054	0.045243348
28	345.03	0.11229	0.046496	345.91	0.11669	0.046624	348.39	0.116687321	0.046824438
29	357.86	0.12726	0.048048	359.68	0.13426	0.048276	361.29	0.134263575	0.04837636
30	370.78	0.14693	0.04957	373.37	0.15887	0.04989	374.19	0.15886608	0.049899558
31	383.66	0.17562	0.051064	387.09	0.20061	0.051474	387.10	0.200607645	0.051394535

Table 13.3: Example 1, Triaxial test on a normally consolidated clay sample; results for case of constant Poisson's ratio

	RS2 Load-Control			*RS2* Displacement-Control			Analytical Solution		
No.	*q* *(kPa)*	Axial strain, ε_a	Volumetric strain, ε_v	*q* *(kPa)*	Axial strain, ε_a	Volumetric strain, ε_v	*q* *(kPa)*	Axial strain, ε_a	Volumetric strain, ε_v
1	0	5.27E-20	1.23E-18	0	2.12E-19	1.20E-18	0.00	0	0
2	12.62	0.00047801	0.000568042	15.64	0.00065421	0.000822004	12.90	0.00065421	0.001088486
3	25.25	0.0013383	0.00183488	26.67	0.0014737	0.00204806	25.81	0.001473681	0.0023609
4	37.88	0.0023863	0.00326686	38.41	0.0024742	0.00341716	38.71	0.002474176	0.003790463
5	50.53	0.0036312	0.00483668	51.39	0.0036661	0.00487104	51.61	0.003666066	0.005351034
6	63.2	0.005077	0.0065169	63.37	0.0050561	0.00647596	64.52	0.005056096	0.007018538
7	75.9	0.0067247	0.00828266	75.47	0.0066486	0.00817452	77.42	0.006648613	0.008771246
8	88.6	0.0085742	0.0101126	87.71	0.0084466	0.00994532	90.32	0.008446594	0.010589882
9	101.31	0.010626	0.0119893	100.07	0.010453	0.0117702	103.23	0.010452514	0.012457593
10	114.02	0.012879	0.0138962	112.5	0.012669	0.0136355	116.13	0.012669068	0.014359832
11	126.92	0.015388	0.0158644	125	0.0151	0.0155272	129.03	0.015099799	0.016284187
12	139.66	0.01806	0.0178033	137.54	0.01775	0.0174345	141.94	0.017749657	0.018220172
13	152.35	0.020934	0.0197351	150.77	0.020626	0.019305	154.84	0.02062554	0.020159017
14	165.2	0.024076	0.0216906	163.12	0.023737	0.0212064	167.74	0.023736837	0.022093453
15	177.87	0.027399	0.0236026	175.52	0.027096	0.0231034	180.65	0.027096045	0.024017511
16	190.68	0.031005	0.0255192	188.08	0.03072	0.025042	193.55	0.030719492	0.025926344
17	203.48	0.034872	0.0274132	201.36	0.034628	0.0269224	206.45	0.034628261	0.027816052
18	216.23	0.039013	0.029278	213.84	0.038849	0.0288186	219.35	0.038849385	0.029683544
19	228.93	0.043451	0.03111	226.55	0.043417	0.030696	232.26	0.043417483	0.03152641
20	241.74	0.048276	0.0329292	238.86	0.048377	0.0326228	245.16	0.048377042	0.033342806
21	254.64	0.053539	0.0347314	252.2	0.053786	0.0345034	258.06	0.053785695	0.035131362
22	267.47	0.05924	0.036494	265.74	0.059719	0.036339	270.97	0.059719067	0.036891106
23	280.31	0.065494	0.038228	279.34	0.066278	0.03814	283.87	0.066278209	0.038621387
24	293.14	0.072402	0.039932	292.78	0.073601	0.039903	296.77	0.073601431	0.040321827
25	305.94	0.080092	0.0416	306.11	0.081884	0.041674	309.68	0.081884102	0.041992264
26	318.82	0.088845	0.043245	319.76	0.091414	0.043402	322.58	0.091413837	0.043632716
27	331.7	0.09894	0.04486	333.4	0.10264	0.045108	335.48	0.102638085	0.045243348
28	344.52	0.11083	0.04644	347.02	0.11631	0.046762	348.39	0.116308109	0.046824438
29	357.39	0.12547	0.047992	360.62	0.13383	0.048396	361.29	0.133834148	0.04837636
30	370.25	0.14449	0.049516	374.23	0.15839	0.050004	374.19	0.158384512	0.049899558
31	383.12	0.17201	0.05101	387.7	0.20007	0.051548	387.10	0.200072057	0.051394535

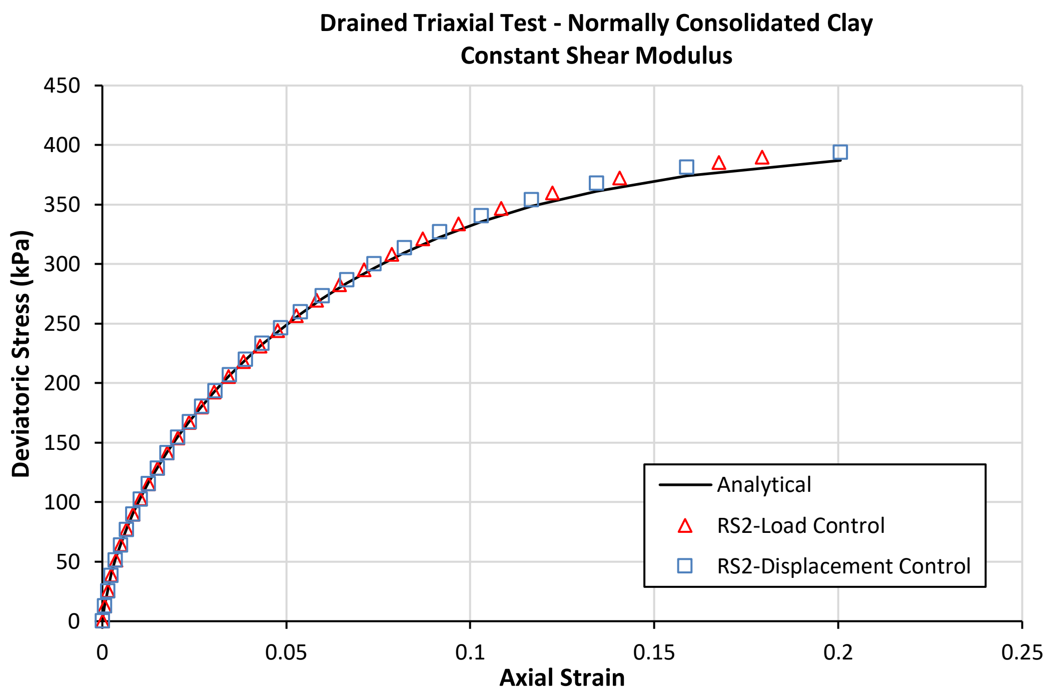

Figure 13.6: Variation of deviatoric stress with axial strain for Example 1 case of constant shear modulus

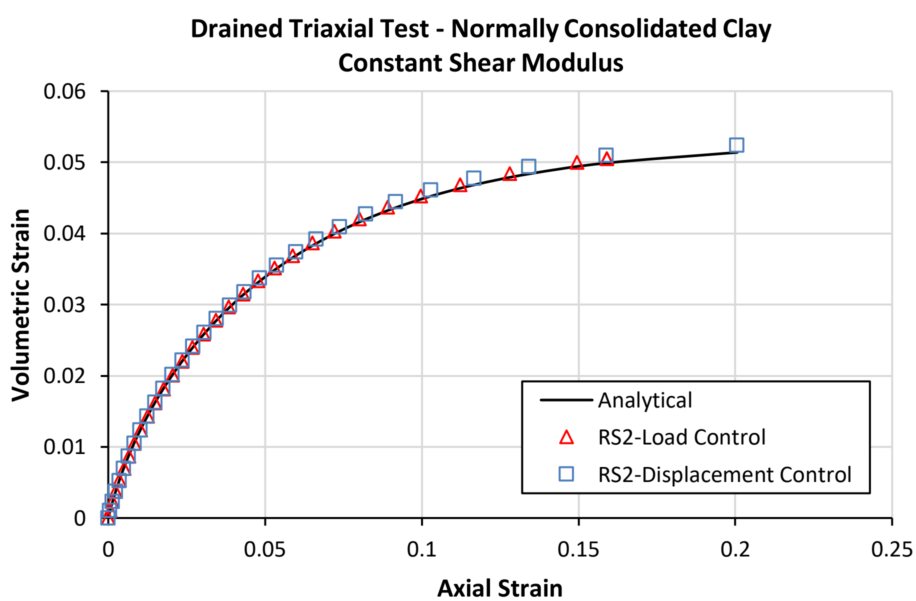

Figure 13.7: Variation of volumetric strain with axial strain for Example 1 case of constant shear modulus

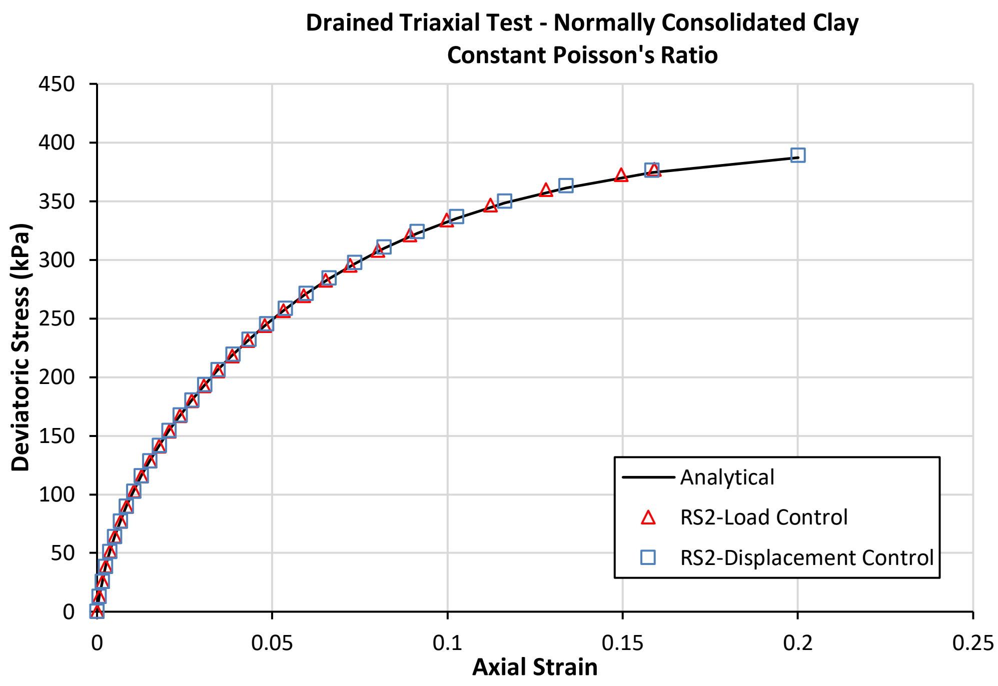

Figure 13.8: Variation of deviatoric stress with axial strain for Example 1 case of constant Poisson's ratio

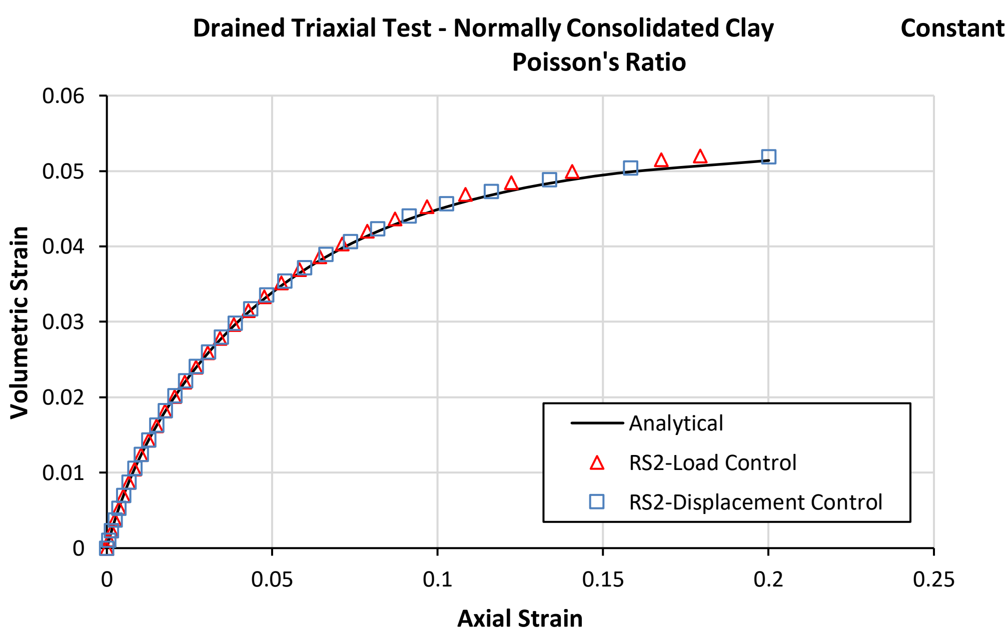

Figure 13.9: Variation of volumetric strain with axial strain for Example 1 case of constant Poisson's ratio

Table 13.4: Example 2, Triaxial test on a lightly over consolidated clay sample; results for case of constant shear modulus

	RS2 Load-Control			*RS2* Displacement-Control			Analytical Solution		
No.	*q* *(kPa)*	Axial strain, ε_a	Volumetric strain, ε_v	*q* *(kPa)*	Axial strain, ε_a	Volumetric strain, ε_v	*q* *(kPa)*	Axial strain, ε_a	Volumetric strain, ε_v
1	0	3.10E-20	1.13E-18	0	3.44E-20	1.12E-18	0.00	0	0
2	27.852	0.00062141	0.000471508	27.54	0.00062209	0.000489538	27.85	0.000622093	0.000473563
3	55.71	0.0012309	0.0009072	55.45	0.0012314	0.00092154	55.71	0.001231409	0.000908796
4	83.56	0.0018295	0.00131032	83.34	0.0018299	0.00132278	83.56	0.00182991	0.001311586
5	111.28	0.0024217	0.00168678	111.22	0.0024191	0.00169636	111.42	0.002419124	0.001686512
6	111.36	0.002482	0.00172484	113.85	0.0043447	0.00251568	114.27	0.004344737	0.00247815
7	113.94	0.0042137	0.00244834	116.68	0.0063424	0.0033134	117.13	0.006342392	0.00326492
8	116.77	0.0061615	0.0032297	119.53	0.0084162	0.0041092	119.99	0.008416193	0.004046572
9	119.61	0.0081927	0.0040107	122.38	0.010571	0.0049036	122.85	0.010570787	0.004822987
10	122.46	0.010302	0.0047874	125.54	0.012811	0.0056424	125.70	0.012811401	0.005594063
11	125.32	0.012489	0.005558	128.37	0.015144	0.0064092	128.56	0.015143927	0.00635971
12	128.16	0.014755	0.0063206	131.3	0.017575	0.0071732	131.42	0.017575032	0.007119855
13	130.99	0.017105	0.0070764	134.16	0.020112	0.0079414	134.28	0.020112284	0.007874433
14	133.81	0.019542	0.007823	137.06	0.022764	0.0087012	137.13	0.022764315	0.008623393
15	136.7	0.022135	0.0085794	139.94	0.025541	0.0094616	139.99	0.025541008	0.009366695
16	139.53	0.0248	0.0093186	142.83	0.028454	0.0102206	142.85	0.028453745	0.010104307
17	142.34	0.027557	0.010044	145.77	0.031516	0.010968	145.71	0.031515713	0.010836206
18	145.19	0.030486	0.0107748	148.68	0.034742	0.01172	148.56	0.034742285	0.011562376
19	148.05	0.033569	0.011501	151.61	0.038151	0.012473	151.42	0.038151524	0.01228281
20	150.9	0.036808	0.01222	154.69	0.041765	0.013175	154.28	0.041764829	0.012997508
21	153.73	0.040207	0.012929	157.57	0.045608	0.013896	157.14	0.045607798	0.013706473
22	156.6	0.043842	0.01364	160.46	0.049711	0.014619	159.99	0.049711382	0.014409717
23	159.48	0.0477	0.014344	163.4	0.054114	0.01535	162.85	0.054113475	0.015107254
24	162.32	0.051788	0.01504	166.38	0.058861	0.016085	165.71	0.058861134	0.015799106
25	165.14	0.056126	0.015722	169.44	0.064014	0.016768	168.57	0.064013772	0.016485294
26	168.01	0.060861	0.016409	172.37	0.069648	0.01748	171.42	0.069647881	0.017165849
27	170.87	0.065977	0.017089	175.37	0.075864	0.018206	174.28	0.075864243	0.0178408
28	173.73	0.071554	0.017764	178.43	0.082799	0.018889	177.14	0.082799414	0.018510181
29	176.58	0.077674	0.01843	181.44	0.090645	0.019613	180.00	0.090644911	0.019174029
30	179.41	0.08443	0.019088	184.55	0.099681	0.020313	182.85	0.099681298	0.019832384
31	182.27	0.092118	0.019746	187.65	0.11034	0.021012	185.71	0.110343622	0.020485287
32	185.13	0.10088	0.020398	190.7	0.12336	0.021684	188.57	0.123360803	0.02113278
33	187.98	0.11111	0.02104	193.76	0.1401	0.022378	191.43	0.140099422	0.021774909
34	190.83	0.12349	0.02168	196.87	0.16363	0.023066	194.28	0.163627615	0.022411721
35	193.68	0.13908	0.022318	200.21	0.20374	0.023806	197.14	0.203735574	0.023043261

Table 13.5: Example 2, Triaxial test on a lightly over consolidated clay sample; results for case of constant Poisson's ratio

	RS2 Load-Control			*RS2* Displacement-Control			Analytical Solution		
No.	***q* *(kPa)***	**Axial strain, ε_a**	**Volumetric strain, ε_v**	***q* *(kPa)***	**Axial strain, ε_a**	**Volumetric strain, ε_v**	***q* *(kPa)***	**Axial strain, ε_a**	**Volumetric strain, ε_v**
1	0	0.00E+00	0.00E+00	0	2.11E-19	1.20E-18	0.00	0	0
2	27.73	0.0011788	0.00047154	27.85	0.0011839	0.00047356	27.85	0.001183908	0.000473563
3	55.6	0.0022679	0.00090714	55.71	0.002272	0.0009088	55.71	0.00227199	0.000908796
4	83.47	0.0032757	0.00131026	83.56	0.003279	0.00131162	83.56	0.003278965	0.001311586
5	111.472	0.00425	0.0017	111.42	0.0042163	0.0016865	111.42	0.00421628	0.001686512
6	111.982	0.0045895	0.0018391	114.18	0.0061746	0.0024697	114.27	0.006174552	0.00247815
7	114.73	0.0065027	0.0026075	116.94	0.0082044	0.0032508	117.13	0.008204383	0.00326492
8	117.58	0.0085409	0.0033939	119.69	0.01031	0.004035	119.99	0.010309882	0.004046572
9	120.44	0.010673	0.0041824	122.46	0.012496	0.0048196	122.85	0.012495704	0.004822987
10	123.21	0.01281	0.0049404	125.25	0.014767	0.0056048	125.70	0.014767079	0.005594063
11	126.04	0.01507	0.0057084	128.05	0.01713	0.006392	128.56	0.017129907	0.00635971
12	128.9	0.01743	0.0064742	131.14	0.019591	0.0071254	131.42	0.01959086	0.007119855
13	131.74	0.019884	0.0072348	133.97	0.022158	0.007884	134.28	0.022157513	0.007874433
14	134.59	0.022433	0.0079882	136.8	0.024838	0.0086428	137.13	0.0248385	0.008623393
15	137.42	0.02508	0.0087328	139.65	0.027644	0.009402	139.99	0.027643713	0.009366695
16	140.25	0.027833	0.00947	142.51	0.030585	0.01016	142.85	0.030584539	0.010104307
17	143.14	0.030774	0.010216	145.55	0.033674	0.010868	145.71	0.033674167	0.010836206
18	145.97	0.033797	0.010941	148.39	0.036928	0.0116	148.56	0.036927977	0.011562376
19	148.77	0.036935	0.011655	151.24	0.040364	0.012332	151.42	0.040364038	0.01228281
20	151.62	0.040286	0.012372	154.19	0.044004	0.013068	154.28	0.044003752	0.012997508
21	154.47	0.043829	0.013085	157.14	0.047873	0.013795	157.14	0.047872723	0.013706473
22	157.3	0.047566	0.013788	160.07	0.052002	0.014528	159.99	0.052001907	0.014409717
23	160.12	0.05151	0.014482	163.03	0.056429	0.015269	162.85	0.056429201	0.015107254
24	162.97	0.055756	0.015178	166.09	0.061202	0.015958	165.71	0.061201666	0.015799106
25	165.81	0.060293	0.015865	169.01	0.066379	0.016671	168.57	0.066378722	0.016485294
26	168.66	0.065212	0.01655	171.98	0.072037	0.017397	171.42	0.072036864	0.017165849
27	171.5	0.070514	0.017226	175.01	0.078277	0.018079	174.28	0.078276878	0.0178408
28	174.34	0.076304	0.017894	177.98	0.085235	0.018785	177.14	0.085235324	0.018510181
29	177.19	0.082682	0.018558	180.98	0.093104	0.019466	180.00	0.093103724	0.019174029
30	180.04	0.089829	0.019221	184.01	0.10216	0.020182	182.85	0.102162646	0.019832384
31	182.87	0.097846	0.019872	187.15	0.11285	0.0209	185.71	0.11284714	0.020485287
32	185.71	0.10712	0.02052	190.36	0.12589	0.021634	188.57	0.125886131	0.02113278
33	188.57	0.1181	0.02117	193.66	0.14265	0.02237	191.43	0.142646202	0.021774909
34	191.41	0.13143	0.021798	196.86	0.1662	0.023056	194.28	0.166195495	0.022411721
35	194.26	0.14863	0.022434	200.08	0.20632	0.023762	197.14	0.206324204	0.023043261

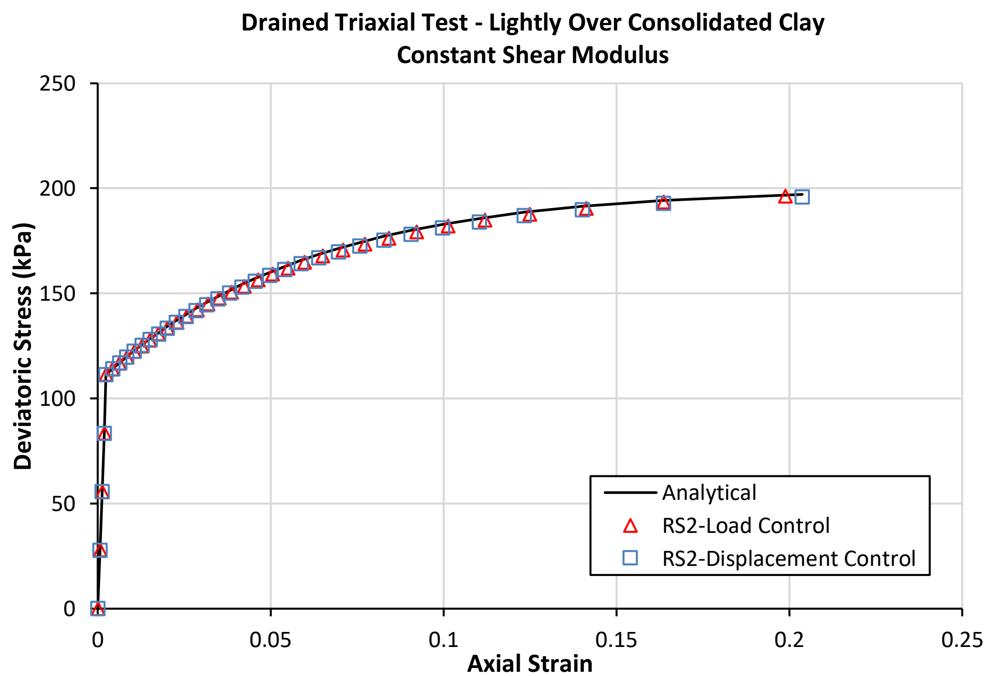

Figure 13.10: Variation of deviatoric stress with axial strain for Example 2 case of constant shear modulus

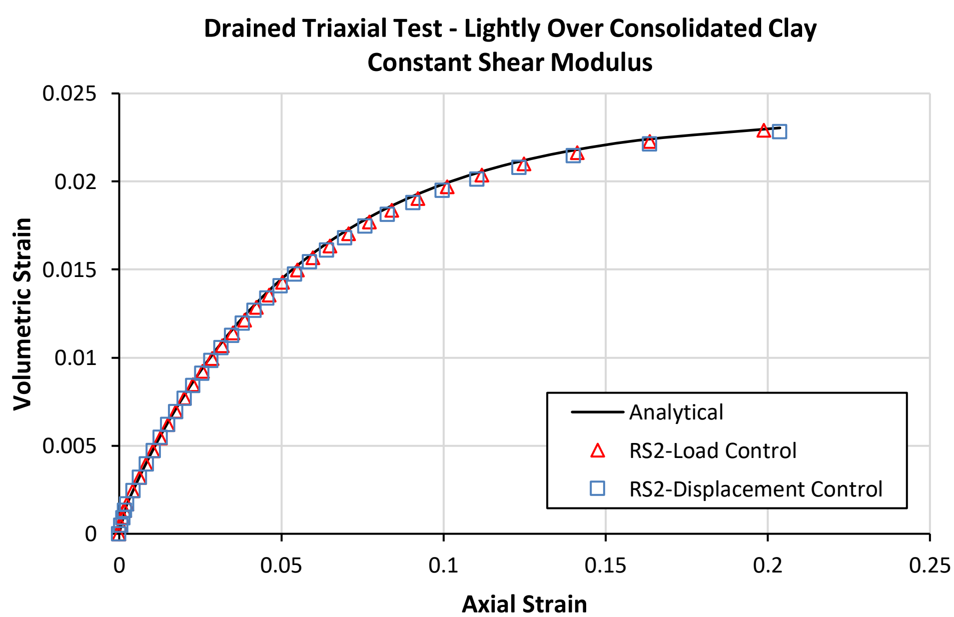

Figure 13.11: Variation of volumetric strain with axial strain for Example 2 case of constant shear modulus

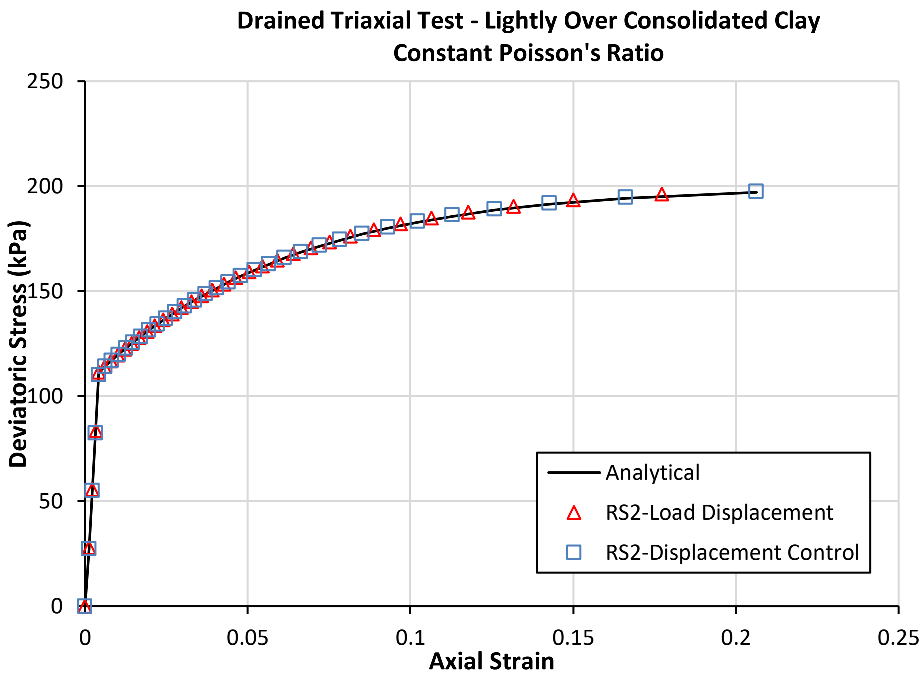

Figure 13.12: Variation of deviatoric stress with axial strain for Example 2 case of constant Poisson's ratio

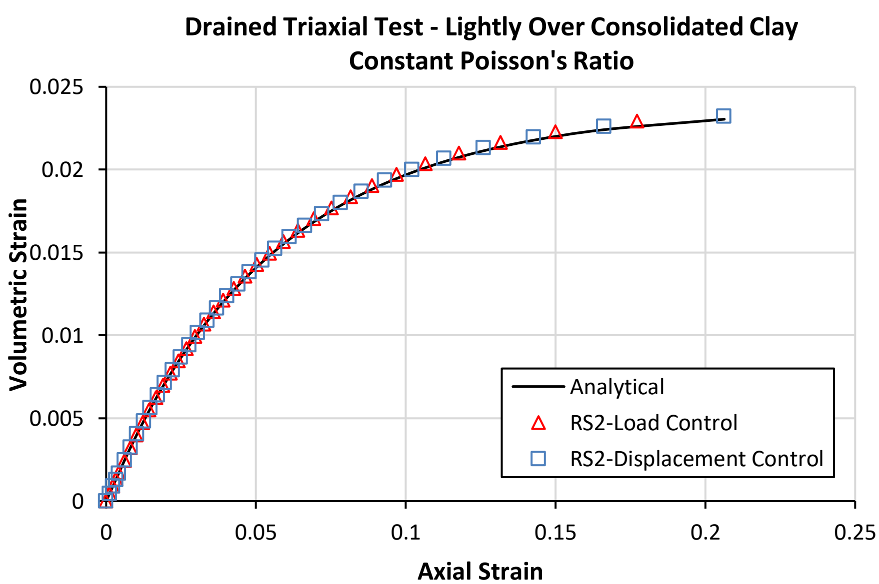

Figure 13.13: Variation of volumetric strain with axial strain for Example 2 case of constant Poisson's ratio

Table 13.6: Example 2, Triaxial test on a highly over consolidated clay sample; results for case of constant Poisson's ratio

	RS2 Displacement-Control			Analytical Solution		
No.	*q (kPa)*	Axial strain, ε_a	Volumetric strain, ε_v	*q (kPa)*	Axial strain, ε_a	Volumetric strain, ε_v
1	0	2.19E-19	1.24E-18	0.00	0	0
2	73.35	0.0030286	0.00121144	73.35	0.003028603	0.001211441
3	146.69	0.0055182	0.0022072	146.69	0.005518199	0.00220728
4	220.04	0.0076341	0.0030536	220.04	0.007634054	0.003053621
5	293.39	0.0094743	0.0037896	293.39	0.009474246	0.003789698
6	290.79	0.011149	0.0033342	290.37	0.011149174	0.003279757
7	287.91	0.012888	0.0028432	287.36	0.012887755	0.00276466
8	285.01	0.014695	0.002347	284.35	0.014694901	0.002245512
9	282.13	0.016576	0.001848	281.34	0.016575634	0.00172226
10	279.24	0.018536	0.0013446	278.32	0.018535538	0.001194852
11	276.35	0.020581	0.0008396	275.31	0.020580857	0.000663232
12	273.48	0.022719	0.000331	272.30	0.022718594	0.000127346
13	270.61	0.024957	-0.000179	269.29	0.024956647	-0.00041286
14	267.75	0.027304	-0.000694	266.27	0.027303962	-0.000957444
15	264.89	0.029771	-0.001209	263.26	0.029770733	-0.001506461
16	262.06	0.032369	-0.001727	260.25	0.032368642	-0.002059968
17	259.22	0.035111	-0.002247	257.24	0.035111167	-0.002618024
18	256.4	0.038014	-0.002766	254.22	0.038013967	-0.003180687
19	253.33	0.041095	-0.003339	251.21	0.041095383	-0.003748016
20	250.43	0.044377	-0.003885	248.20	0.044377091	-0.00432007
21	247.47	0.047885	-0.004445	245.19	0.047884959	-0.00489691
22	244.51	0.05165	-0.005012	242.17	0.051650204	-0.005478596
23	241.56	0.055711	-0.005581	239.16	0.055710988	-0.006065189
24	238.64	0.060115	-0.006145	236.15	0.060114636	-0.00665675
25	235.72	0.064921	-0.006715	233.14	0.064920833	-0.007253342
26	232.88	0.070206	-0.007272	230.12	0.070206351	-0.007855026
27	229.88	0.076072	-0.007876	227.11	0.076072266	-0.008461864
28	226.95	0.082656	-0.008458	224.10	0.08265545	-0.009073919
29	224.14	0.090148	-0.009018	221.09	0.090147775	-0.009691254
30	221.27	0.09883	-0.009608	218.07	0.098830224	-0.010313931
31	218.38	0.10914	-0.010198	215.06	0.109138375	-0.010942012
32	215.6	0.1218	-0.010772	212.05	0.121801907	-0.011575561
33	212.9	0.13819	-0.01133	209.04	0.138188656	-0.012214638
34	210.16	0.16137	-0.011904	206.02	0.161369404	-0.012859307
35	207.88	0.20114	-0.01238	203.01	0.201142831	-0.013509627

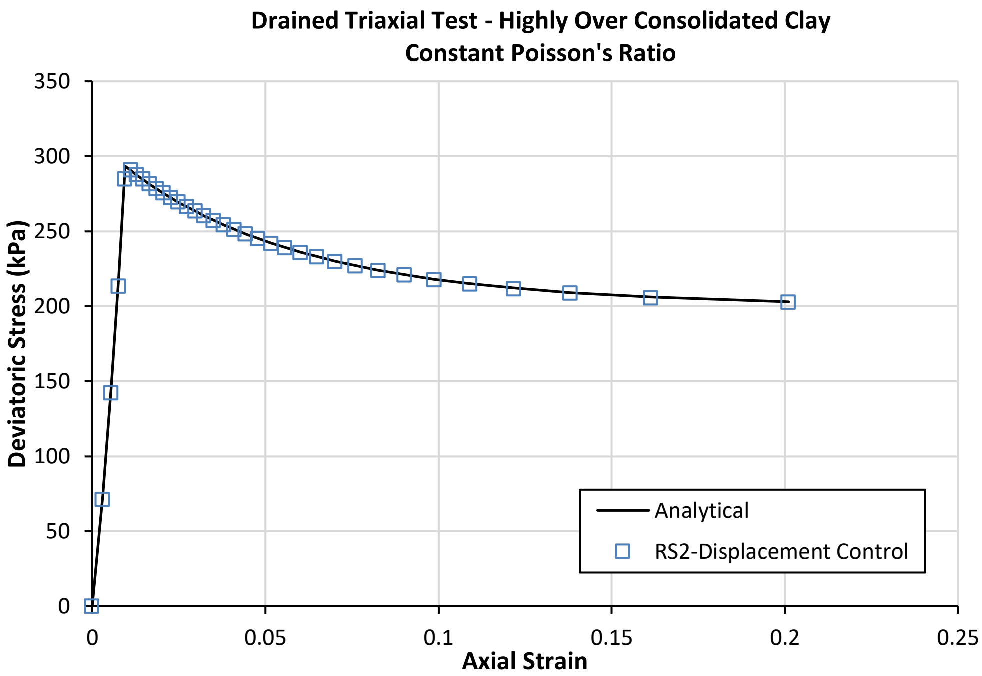

Figure 13.14: Variation of deviatoric stress with axial strain for Example 3 case of constant Poisson's ratio

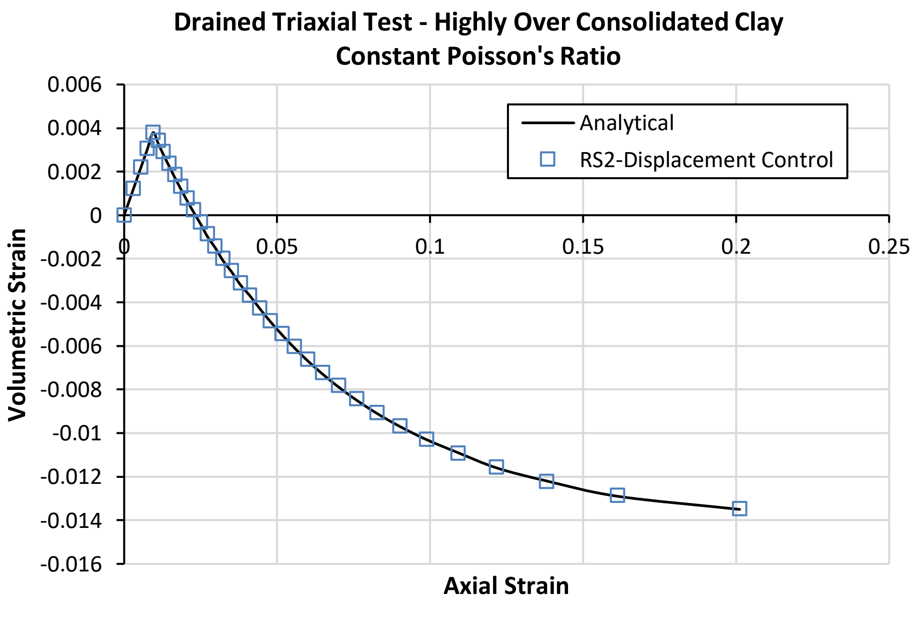

Figure 13.15: Variation of volumetric strain with axial strain for Example 3 case of constant Poisson's ratio

13.5 References

1. R.I. Borja (1991), Cam-Clay plasticity, Part II: Implicit integration of constitutive equation based on a nonlinear elastic stress predictor, Computer Methods in Applied Mechanics and Engineering, 88, 225-240.
2. D. Peric´ (2006), Analytical solutions for a three-invariant Cam clay model subjected to drained loading histories, Int. J. Numer. Anal. Meth. Geomech., 30, 363–387.

13.6 Data Files

The input data files for the drained triaxial compressive testing of Modified Cam Clay samples are:

File name	Example No.	Assumption	Simulation type
stress #013_01.fez	1	$G = const.$	Load Control
stress #013_02.fez	1	$\mu = const.$	Load Control
stress #013_01_Disp.fez	1	$G = const.$	Disp Control
stress #013_02_Disp.fez	1	$\mu = const.$	Disp Control
stress #013_03.fez	2	$G = const.$	Load Control
stress #013_04.fez	2	$\mu = const.$	Load Control
stress #013_03_Disp.fez	2	$G = const.$	Disp Control
stress #013_04_Disp.fez	2	$\mu = const.$	Disp Control
stress #013_05_Disp.fez	3	$\mu = const.$	Disp Control

These can be downloaded from the RS2 Online Help page for Verification Manuals. Also included in the installation folder are Microsoft Excel spreadsheet files:

stress #013 - drained triaxial test (constant G) – NC Clay.xls

stress #013 - drained triaxial test (constant v) – NC Clay.xls

stress #013 - drained triaxial test (constant G) – OC Clay.xls

stress #013 - drained triaxial test (constant v) – OC Clay.xls

stress #013 - drained triaxial test (constant v) – Highly OC Clay-Softening.xls

that implement the closed-form solutions for drained triaxial compressive testing for Modified Cam Clay soils.

14 Non-Linear Analysis of Strip Footing in Sand

14.1 Problem Description

This problem considers a strip footing in sand subjected to an incrementally increasing load. The sand is assumed to exhibit non-linear elastic behaviour according to the Duncan-Chang hyperbolic model. All parameters are drawn from Tomlinson's *Foundation Design and Construction* [1], which presents experimentally determined settlement results as well as the results of finite element analysis. Figure 14.1 illustrates the problem as implemented in ***RS2***. Dimensions are as indicated. Due to symmetry, only half of the footing is modeled.

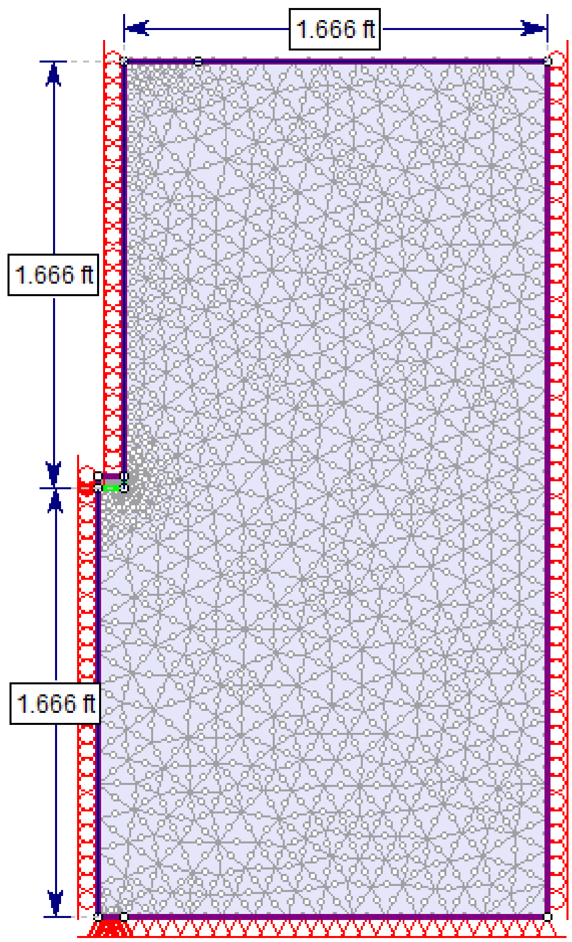

Figure 14.1: Strip footing in sand as constructed in *RS2*

The model shown in Figure 14.1 uses a graded mesh composed of six-noded triangular elements. Boundary conditions are as illustrated. A small region of stiff material is used to simulate a rigid footing.

Table 14.1 summarizes the model parameters used.

Table 14.1: Model parameters

Parameter	*Value*
Modulus number (K_E)	300
Modulus exponent (n)	0.55
Failure ratio (R_f)	0.83
Cohesion (c)	0 kPa
Friction angle (ϕ)	35.5°
Unit weight (γ)	91 lb/ft^3
Poisson's ratio (v)	0.35
Footing half-width ($b/2$)	1.22 in

14.2 Analytical Solution

The Duncan-Chang Hyperbolic constitutive model is widely used for the modeling of soils with more generalized stress-strain behavior, and is capable of modeling the stress-dependent strength and stiffness of soils. The Duncan-Chang Hyperbolic elasticity model can only be used in conjunction with the Mohr-Coulomb failure criterion in ***RS2***. The following equations are derived, based on a hyperbolic stress-strain curve and stress-dependent material properties for the Duncan-Chang Hyperbolic model.

The tangential modulus, (E_t), is given by

$$E_t = \mathrm{K_E}\, p_{atm}\left(\frac{\sigma_3}{p_{atm}}\right)^n \left[1 - \frac{R_f(1-\sin\phi)(\sigma_1-\sigma_3)}{2c\cos\phi + 2\sigma_3\sin\phi}\right]^2$$

where

p_{atm} = atmospheric pressure

σ_3 = minor principal stress

σ_1 = major principal stress

and other parameters are as identified in Table 14.1.

Tomlinson presents experimental load-settlement results in [1] as well as the results of finite element analysis. These are compared with ***RS2*** results in the next section.

14.3 Results

Figure 14.2 shows settlement as a function of increasing average footing pressure, as predicted by [1] and ***RS2***. It can be seen that ***RS2*** is in good agreement with experimental results.

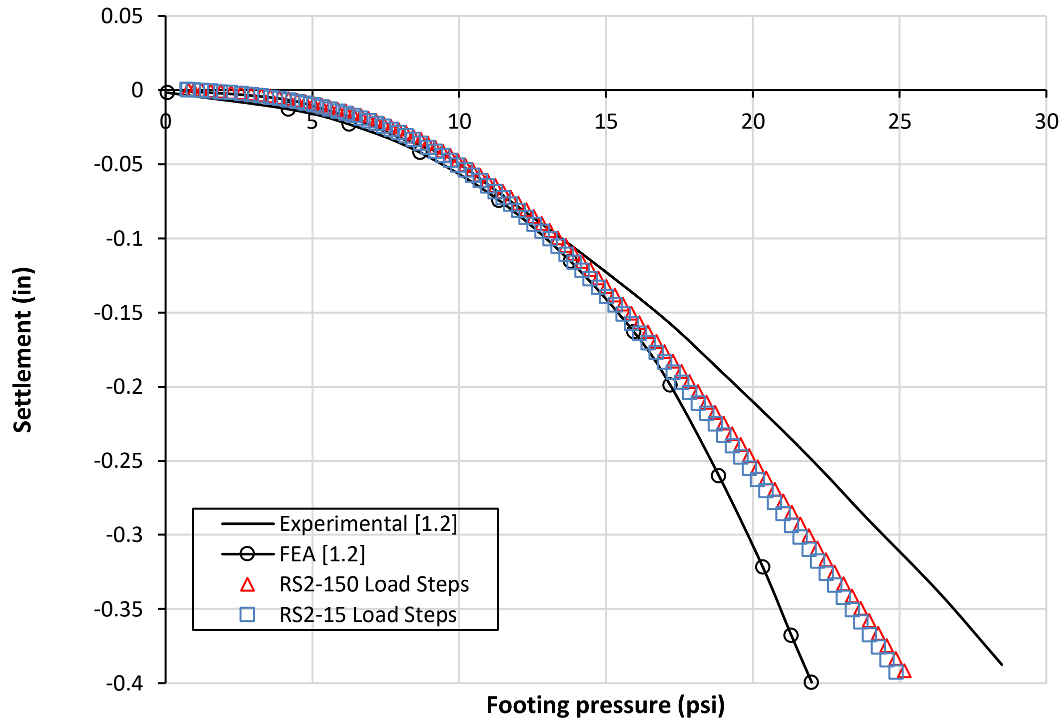

Figure 14.2: Settlement with increasing load as predicted by *RS2* and [1]

14.4 References

1. M. J. Tomlinson (2001), Foundation Design and Construction, 7th Ed., Upper Saddle River, NJ: Prentice Hall.
2. J. M. Duncan and C. Y. Chang (1970), "Nonlinear analysis of stress and strain in soils", J. of Soil Mech. and Foundation Division, ASCE, 96 (SM5), pp. 1629-1653.

14.5 Data Files

The input data file **stress#014.fez** can be downloaded from the RS2 Online Help page for Verification Manuals.

15 Non-Linear Analysis of Circular Footing on Saturated, Undrained Clay

15.1 Problem Description

This problem considers the response of a circular footing on saturated, undrained clay when subjected to uniform distributed loads. The material is assumed to exhibit non-linear elastoplasticity that can be modeled using the Duncan & Chang hyperbolic stress-strain relationship. Table 15.1 summarizes the material properties and parameters required for the Duncan & Chang model, while Figure 15.1 shows the model as implemented axisymmetrically in ***RS2.*** Note that the material is purely cohesive.

Table 15.1: Model parameters

Parameter	*Value*
Modulus number (K_E)	47
Modulus exponent (n)	0
Failure ratio (R_f)	0.9
Cohesion (c)	0.5 t/ft^2
Friction angle (ϕ)	0
Unit weight (γ)	110 lb/ft^3
Poisson's ratio (v)	0.48
Footing radius (a)	4 ft

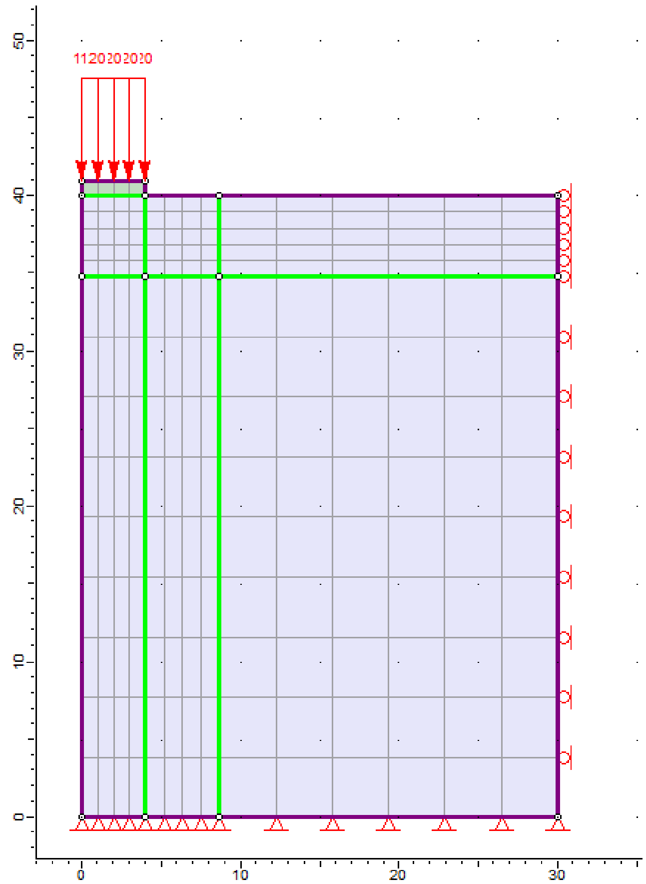

Figure 15.1: Axisymmetric model of circular footing as implemented in *RS2*

The model shown in Figure 15.1 uses a graded mesh of 200 4-noded quadrilateral finite elements and custom discretization. Boundary conditions are as shown.

15.2 Analytical Solution

The Duncan-Chang hyperbolic model is widely used to predict the behaviour of soils that display a non-linear, stress-dependent, stress-strain relation. The two-parameter Mohr-Coulomb criterion is used to predict failure. Both a tangential modulus E_t and a tangential Poisson's ratio v_t are calculated.

The tangential modulus, (E_t), is given by

$$E_t = \mathrm{K_E}\, p_{atm} \left(\frac{\sigma_3}{p_{atm}} \right)^n \left[1 - \frac{R_f (1 - \sin\phi)(\sigma_1 - \sigma_3)}{2c\cos\phi + 2\sigma_3 \sin\phi} \right]^2$$

where

p_{atm} = atmospheric pressure

σ_3 = minor principal stress

σ_1 = major principal stress

Tomlinson presents a load-settlement relation based on his own finite element analysis in [2]. These results are compared with those of ***RS2*** in the following section.

15.3 Results

Figure 15.2 shows vertical settlement as a function of average footing pressure. Results from ***RS2*** are in good agreement with the finite element analysis conducted in [1].

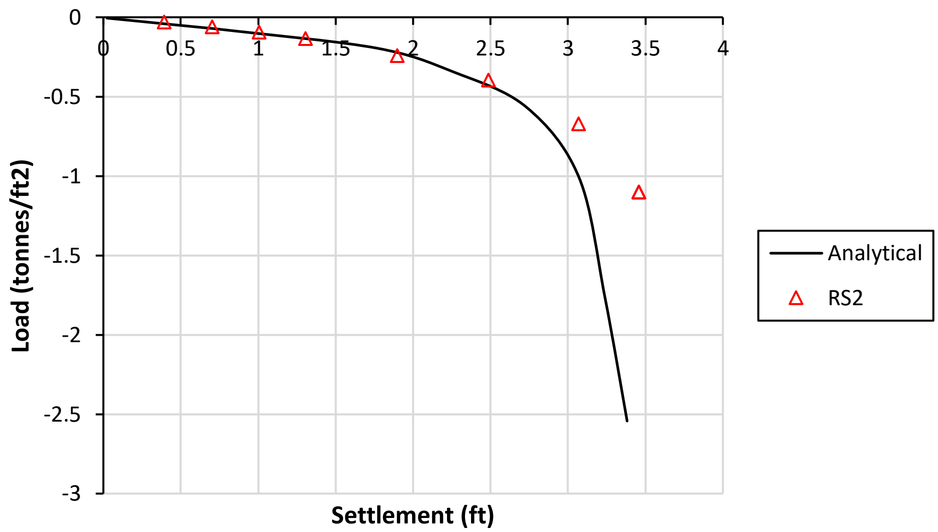

Figure 15.2: Settlement with increasing load as predicted by *RS2* and [1]

15.4 References

1. J. M. Duncan and C. Y. Chang (1970), "Nonlinear analysis of stress and strain in soils", J. of Soil Mech. and Foundation Division, ASCE, 96 (SM5), pp. 1629-1653.
2. M. J. Tomlinson (2001), *Foundation Design and Construction*, 7th Ed., Upper Saddle River, NJ: Prentice Hall.

15.5 Data Files

The input data files **stress#015.fez** can be downloaded from the RS2 Online Help page for Verification Manuals.

16 Classical Beam Verification

16.1 Problem Description

This verification example addresses five classical beam problems under various end conditions. In ***RS2***, beams are constructed as liner elements using the Timoshenko beam formulation. Figure 16.1 to Figure 16.5 show the five cases schematically. All beams are subjected to a uniform vertical distributed load of 10 kPa/m.

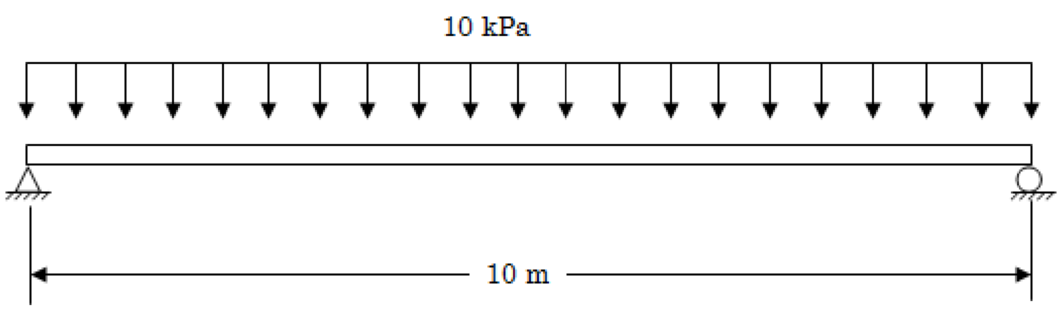

Figure 16.1: Simply supported beam

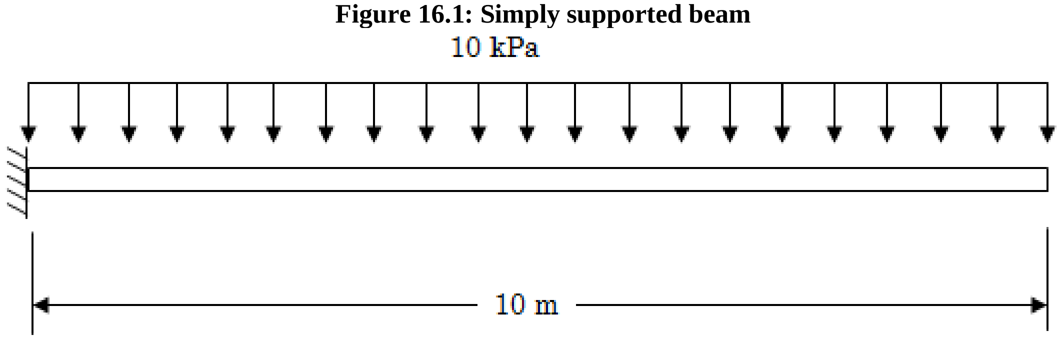

Figure 16.2: Simple cantilever

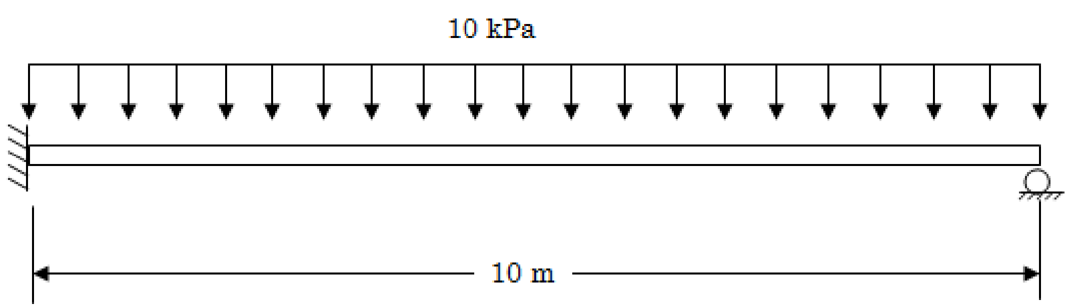

Figure 16.3: Simply propped cantilever

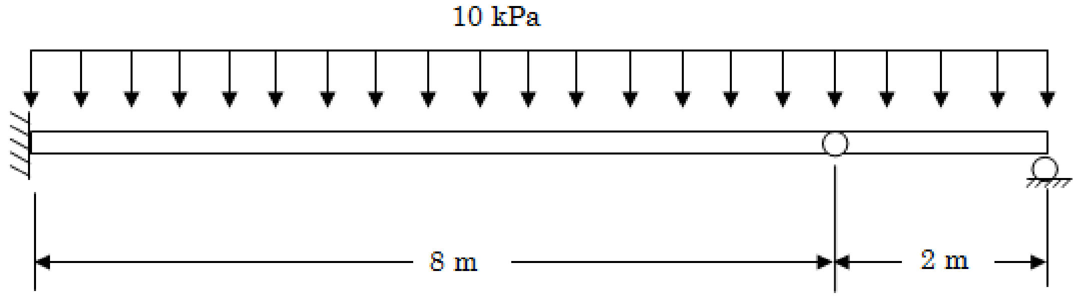

Figure 16.4: Simply propped cantilever with hinge

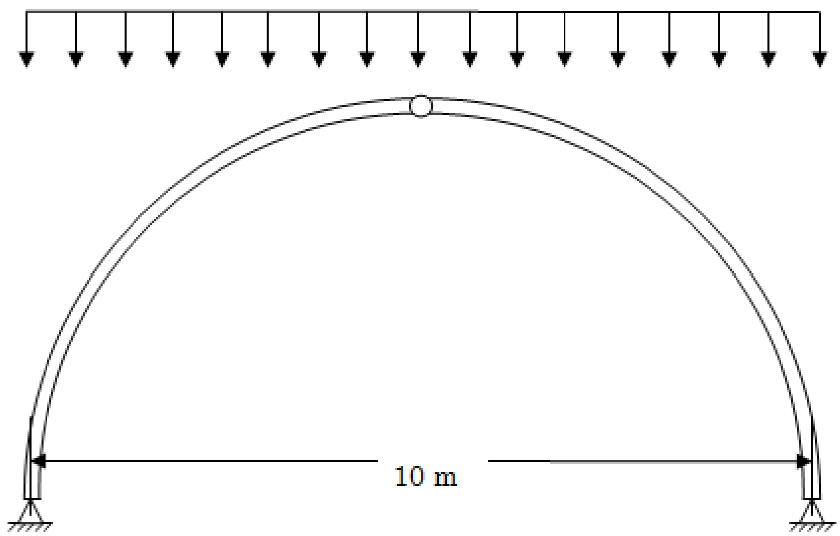

Figure 16.5: Circular beam with hinge

Table 16.1 summarizes the material and model parameters used. Figure 16.6 shows the fourth case as constructed in ***RS2***. Note the use of a liner hinge to enforce a zero-moment condition.

Table 16.1: Model parameters

Parameter	*Value*
Distributed load (*w*)	10 kPa
Beam length (*L*)	10 m
Young's modulus (*E*)	200 000 kPa
Poisson's ratio (*v*)	10^{-5}

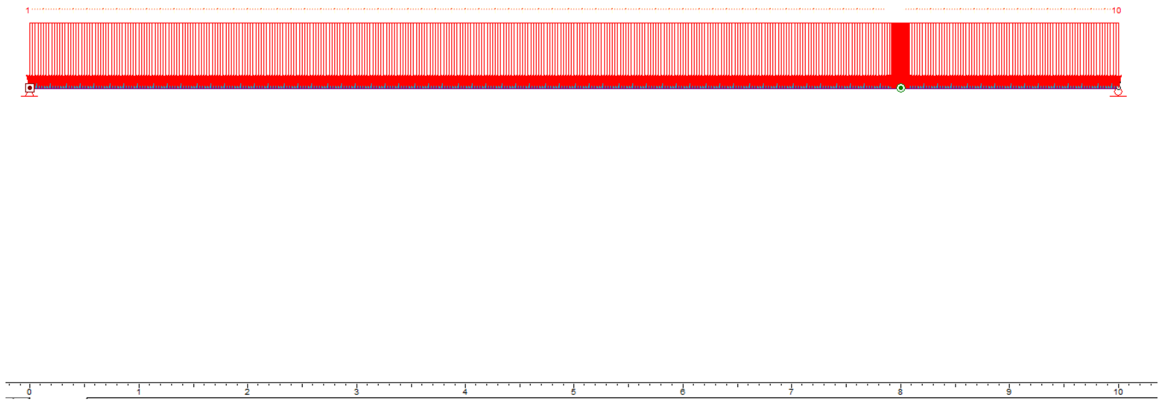

Figure 16.6: Liner beam with hinge as constructed in *RS2*

16.2 Analytical Solution

The bending moment and shear force distributions for these beams can be calculated using equilibrium equations and the specified end conditions. Table 16.2 summarizes the analytical solutions for each problem.

Table 16.2: Theoretical shear force and bending moment distributions

Beam	Shear Force *V(x)*	Bending Moment *M(x)*
1	$\frac{wL}{2} - wx$	$\frac{wL}{2}x - \frac{w}{2}x^2$
2	$wL - wx$	$Lwx - \frac{w}{2}x^2 - \frac{wL^2}{2}$
3	$\frac{5wL}{8} - wx$	$\frac{5wLx}{8} - \frac{wx^2}{2} - \frac{wL^2}{8}$
4	$\frac{w(L+h)}{2} - wx$	$\frac{wLh}{2} - \frac{wx^2}{2} + \frac{w(L+h)x}{2}$
	Shear Force *V(θ)*	**Bending Moment *M(θ)***
5	$wr\left(\frac{\pi}{2} - \theta\right)\sin\theta$ $+\frac{\pi}{2}wr\left(1 - \frac{2}{\pi}\right)\cos\theta$	$-\frac{\pi}{2}wr^2(1-\cos\theta) + wr^2\theta\left(\frac{\sin\theta}{\theta} - \cos\theta\right)$ $+\frac{\pi}{2}wr^2\left(1 - \frac{2}{\pi}\right)\sin\theta$
Note: Where applicable, h denotes the position of the hinge.		

16.3 Results

In all cases, ***RS2*** results were in perfect agreement with the analytical solutions. Figure 16.7 to Figure 16.16 plot the shear force and bending moment distributions for each case. Note that the ***RS2*** results do not follow the typical sign convention for bending moments.

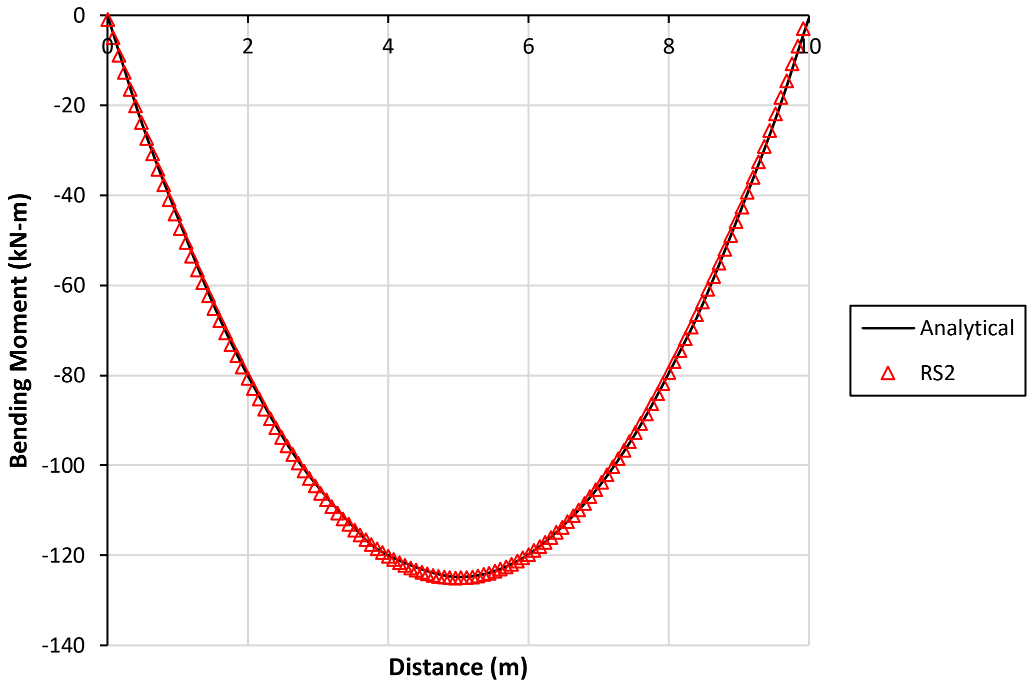

Figure 16.7: Bending moment distribution for simply supported beam

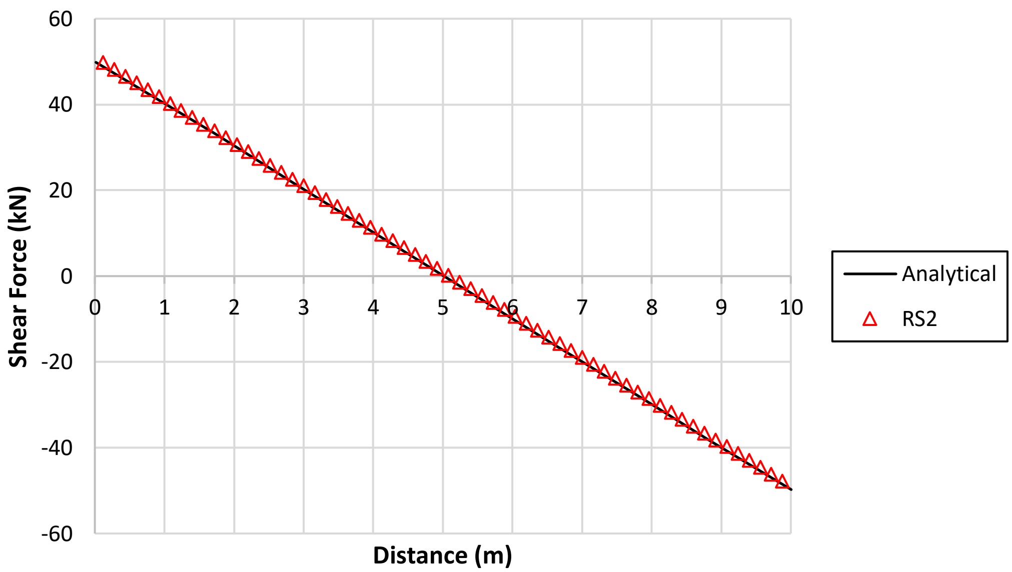

Figure 16.8: Shear force distribution for simply supported beam

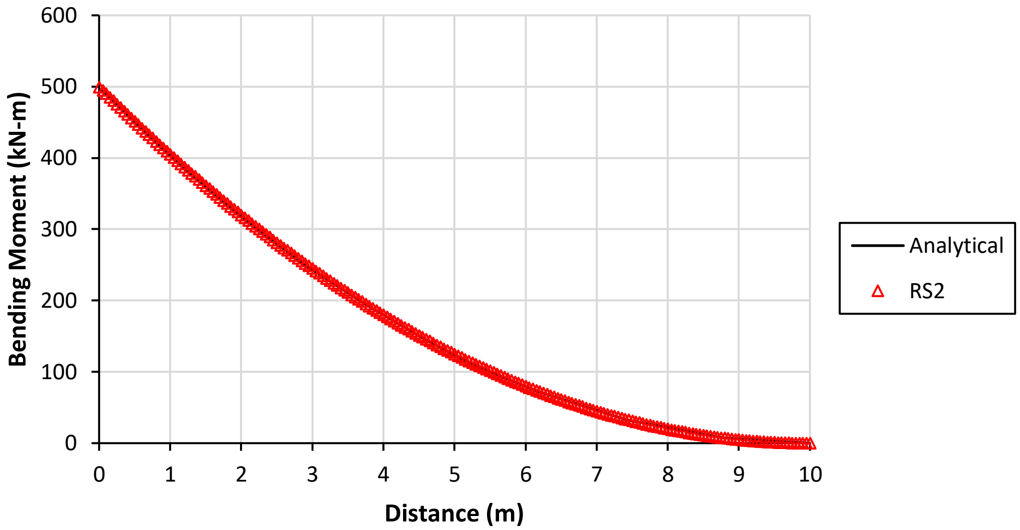

Figure 16.9: Bending moment distribution for simple cantilever

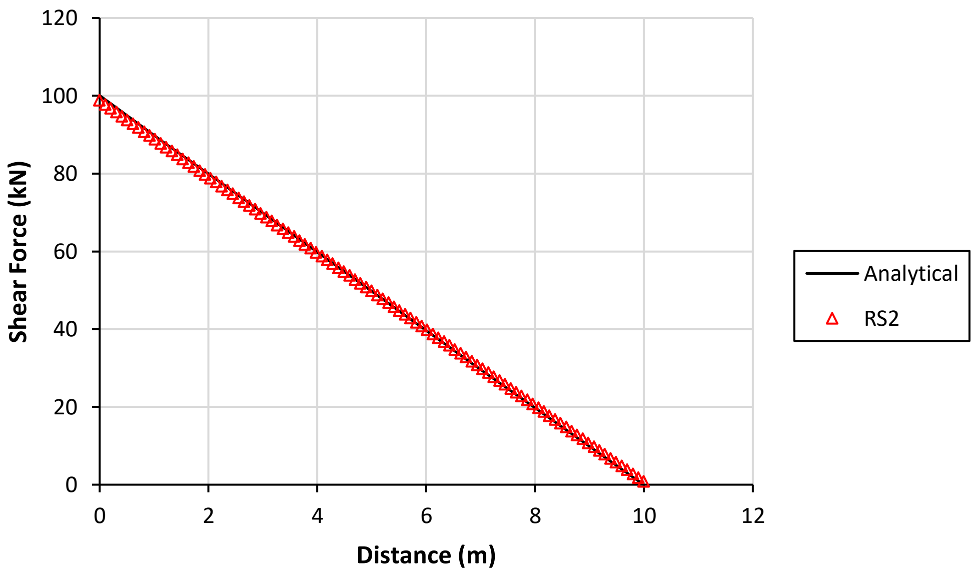

Figure 16.10: Shear force distribution for simple cantilever

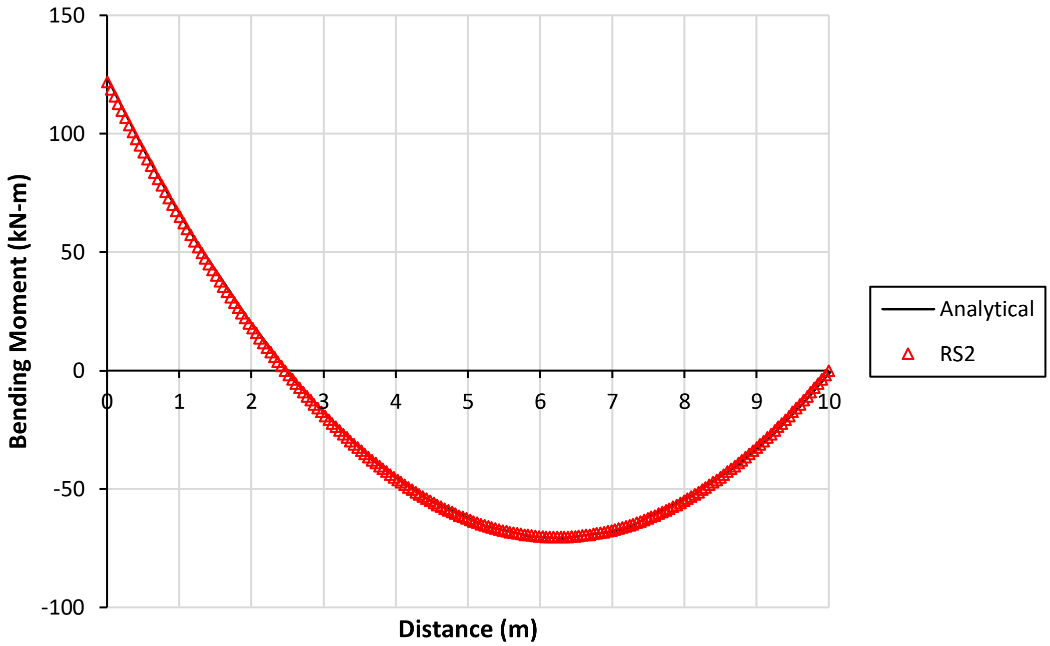

Figure 16.11: Bending moment distribution for propped cantilever

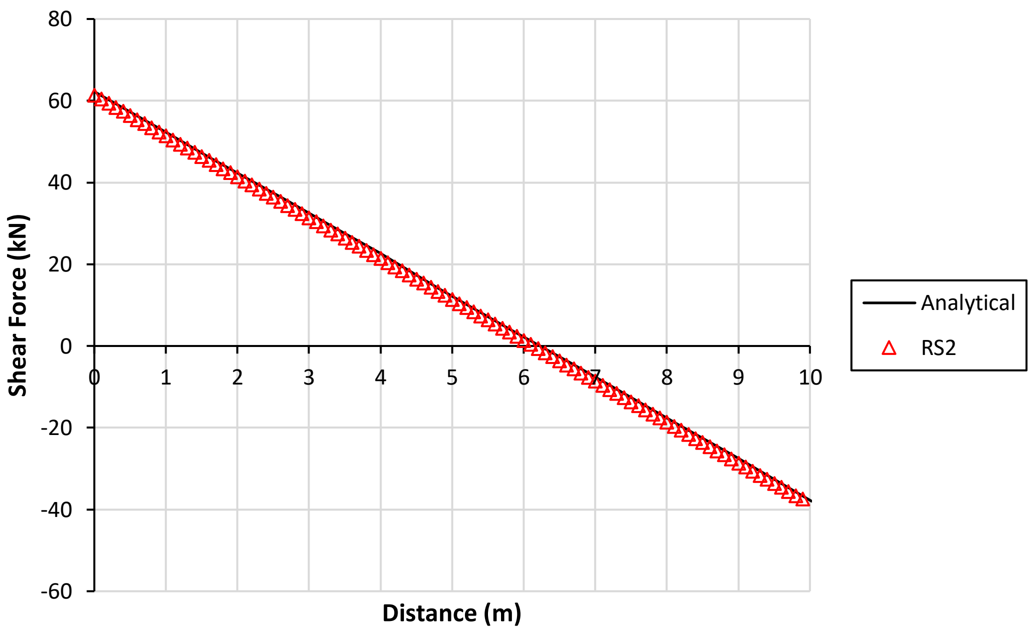

Figure 16.12: Shear force distribution for propped cantilever

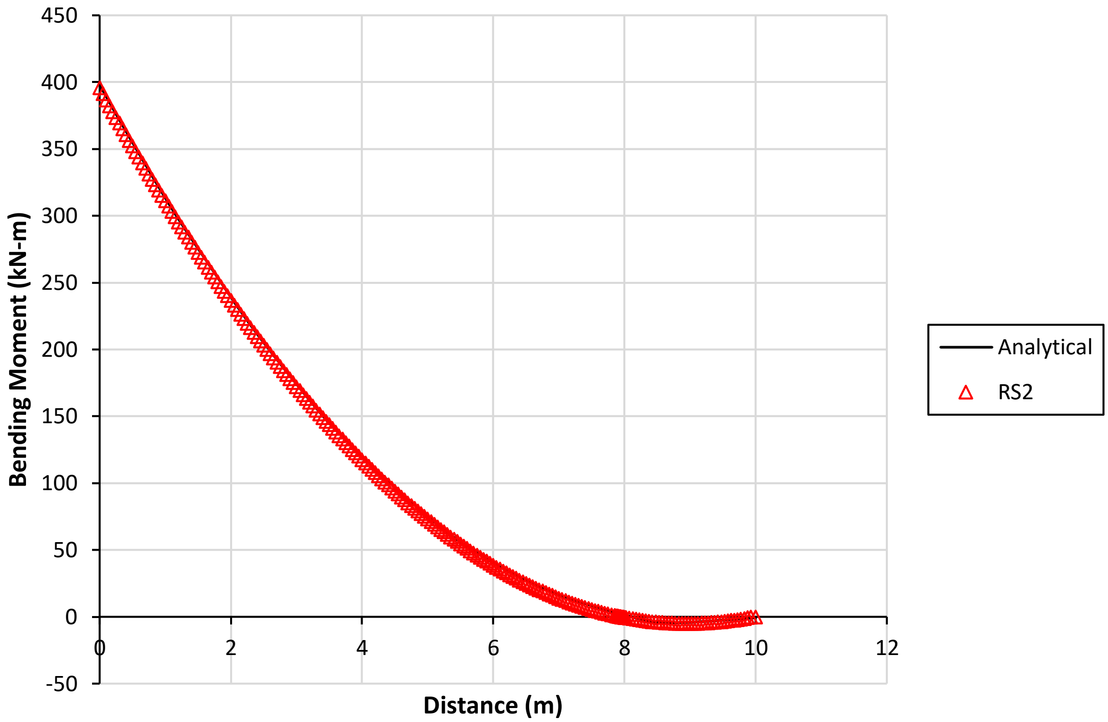

Figure 16.13: Bending moment distribution for propped cantilever with hinge

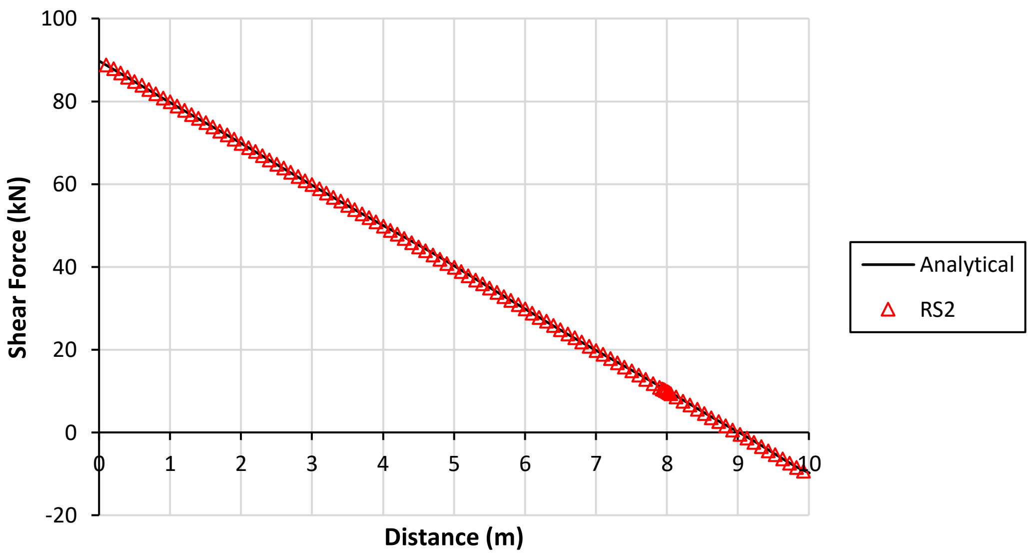

Figure 16.14: Shear force distribution for propped cantilever with hinge

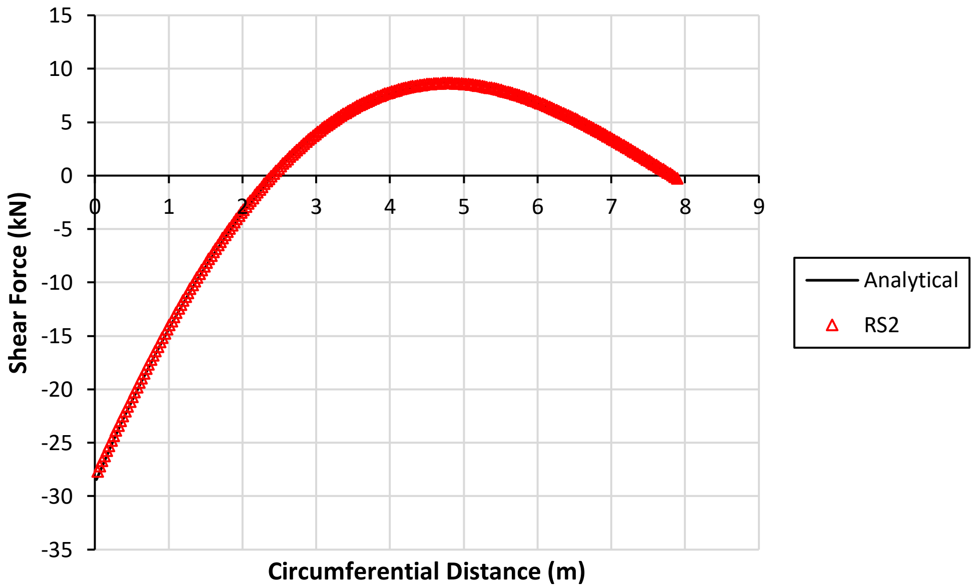

Figure 16.15: Shear force distribution for circular beam with hinge

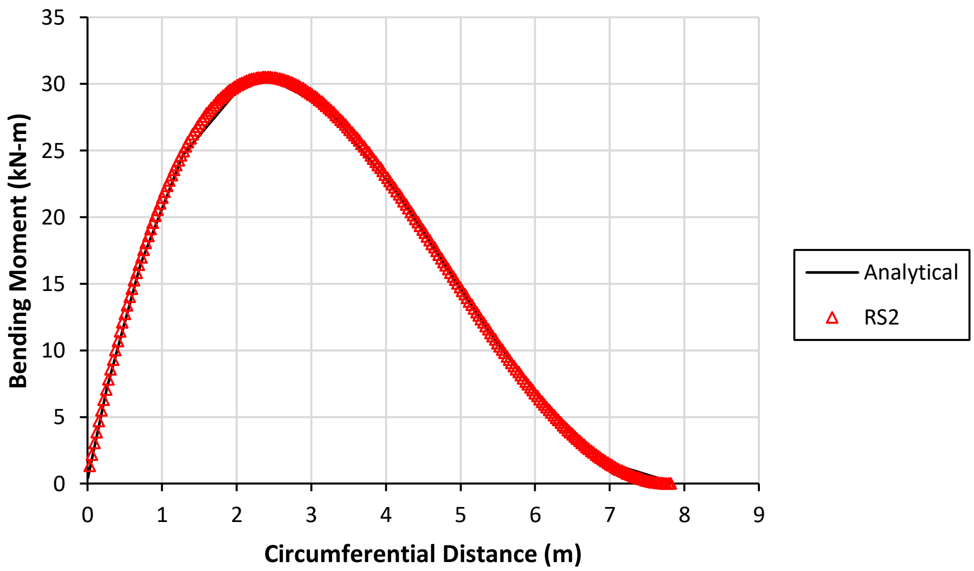

Figure 16.16: Bending moment distribution for circular beam with hinge

16.4 Data Files

The input data files **stress#016_01.fez** to **stress#016_05.fez** can be downloaded from the RS2 Online Help page for Verification Manuals. Refer to Table 16.3 for the contents of each data file.

Table 16.3: Input data files for classic beam problems

File	***Beam***
stress#016_01.fez	Simply supported
stress#016_02.fez	Simple cantilever
stress#016_03.fez	Propped cantilever
stress#016_04.fez	Propped cantilever with hinge
stress#016_05.fez	Circular beam with hinge

17 Tunnel Stability in Purely Cohesive Soil

17.1 Problem Description

This problem considers the case of a circular excavation in a purely cohesive soil. The effect on tunnel stability of various ratios of tunnel diameter to depth of cover will be examined. Both a surface pressure σ_n and an internal pressure σ_t are assumed to be present. Figure 17.1 shows the problem schematically, while Figure 17.2 shows it as implemented in ***RS2***.

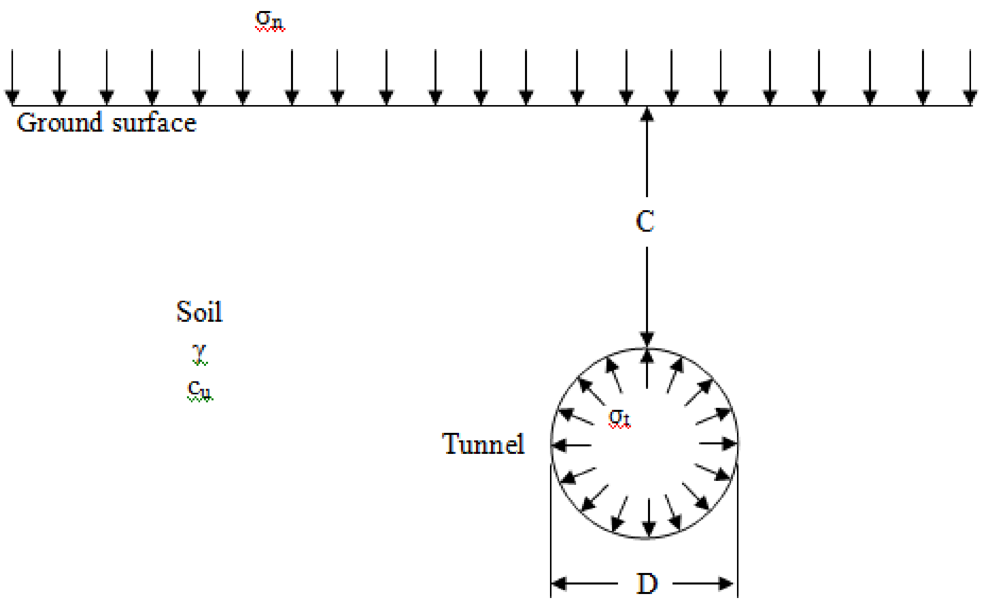

Figure 17.1: Circular excavation with internal pressure and surface loading in a purely cohesive soil

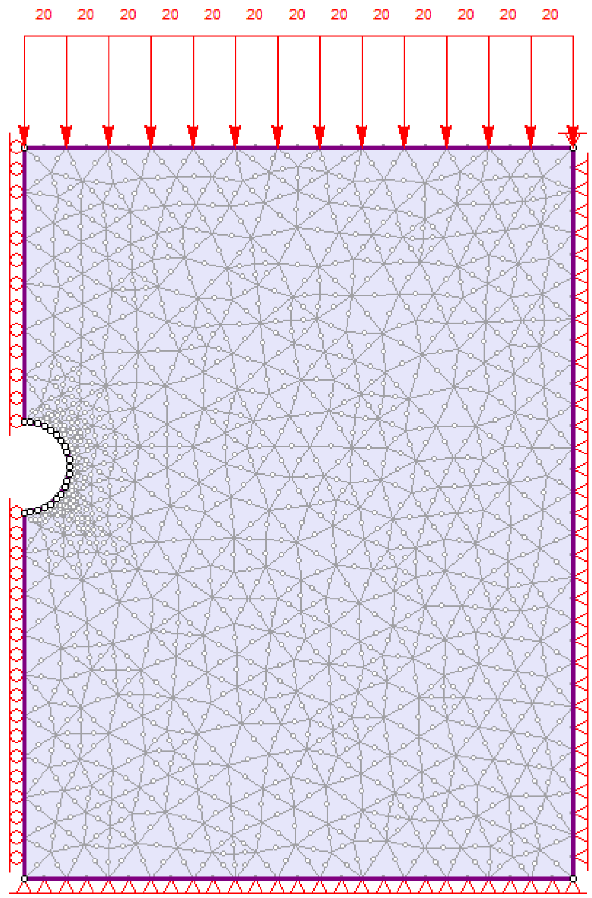

Figure 17.2: Circular tunnel in cohesive soil as constructed in *RS2*

Broms & Bennermark (1967) [1] and Peck (1969) [2] define an overload factor N as a measure of tunnel stability, calculated as follows:

$$N = \frac{\sigma_s + \gamma \times H - \sigma_t}{c_u}$$

where σ_s is the stress applied at the ground surface, σ_t is the internal pressure on the excavation, c_u is the material cohesion, H is the tunnel depth, and γ is the material self-weight. In the ***RS2*** model, no initial element stresses are applied, and thus the effect of overburden can be ignored. Tunnel internal pressure is also assumed to be zero. This reduces the above equation to:

$$N = \frac{\sigma_s}{c_u}$$

The model shown in Figure 17.2 exploits the half-symmetry of the problem. It uses 944 six-noded triangular elements. Tunnel stability is determined using the shear strength reduction (SSR) method, which reduces the shear strength (in this case, the cohesion only) of the material by a strength reduction factor (SRF) until a critical SRF is reached.

At this point, the excavation is rendered unstable and calculations do not converge. When calculating *N*, the material cohesion is then reduced by this critical SRF.

17.2 Analytical Solution

Davis and Gunn [3] provide theoretical upper and lower bounds for the critical overload factor *N* as a function of cover-to-depth ratio.

17.3 Results

Figure 17.3 compares the results obtained from ***RS2*** and ***RS3*** to those presented in [3]. Both programs are in good agreement with theory.

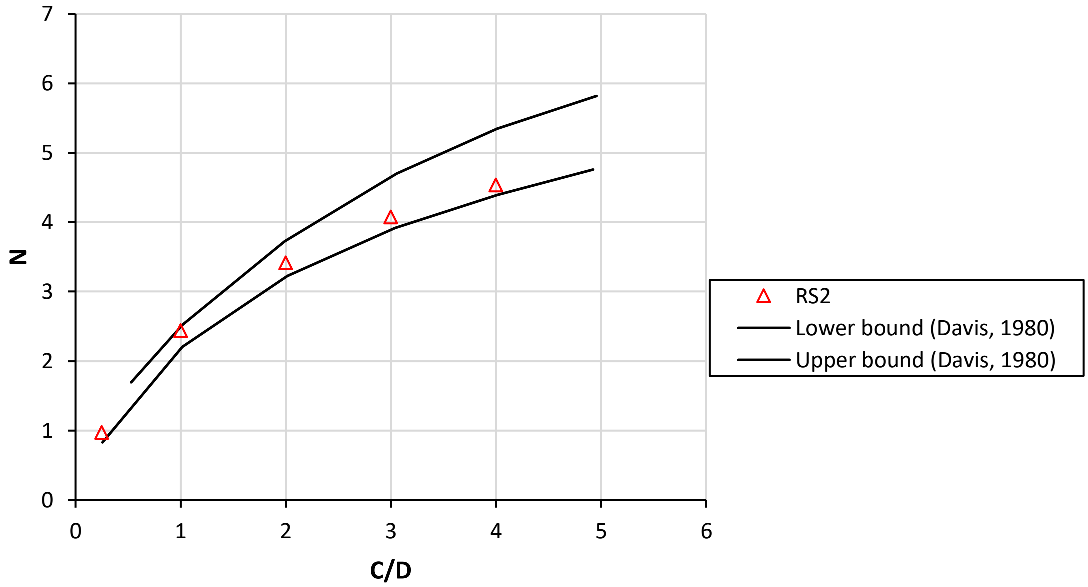

Figure 17.3: Tunnel overload factor as function of depth-to-cover ratio – analytical/numerical results

Figure 17.4 to Figure 17.8 show maximum shear strain and deformation vectors at near-critical loads for each tunnel depth.

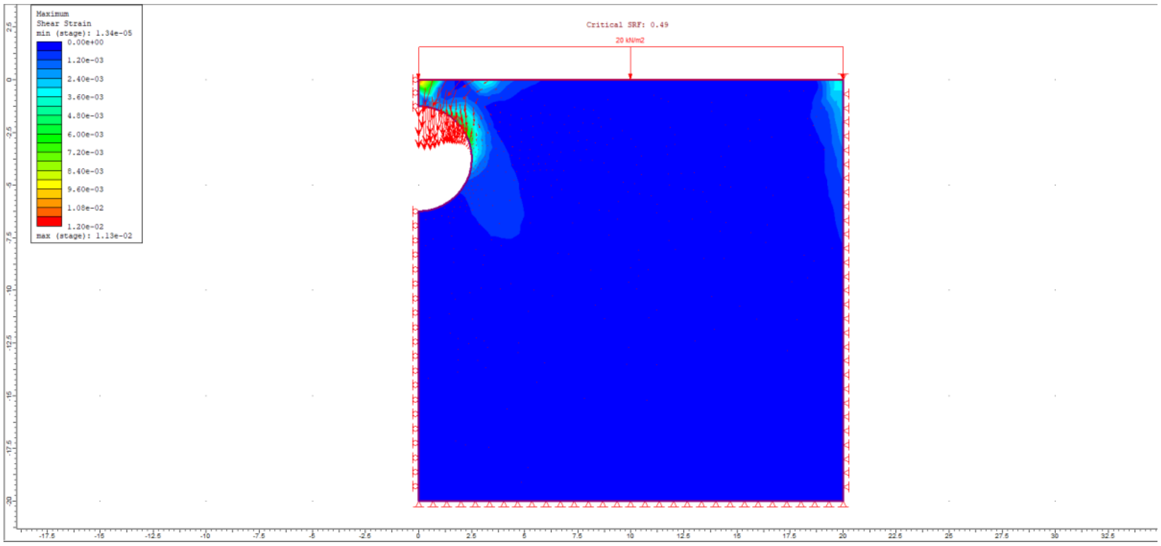

Figure 17.4: Maximum shear strain contours and deformation vectors for C/D = 0.25

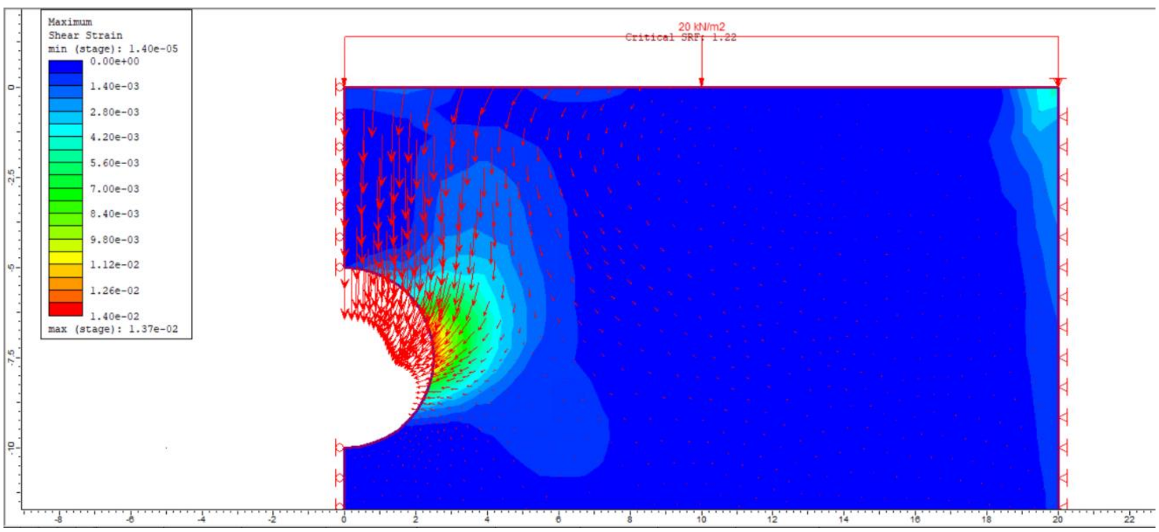

Figure 17.5: Maximum shear strain contours and deformation vectors for C/D = 1

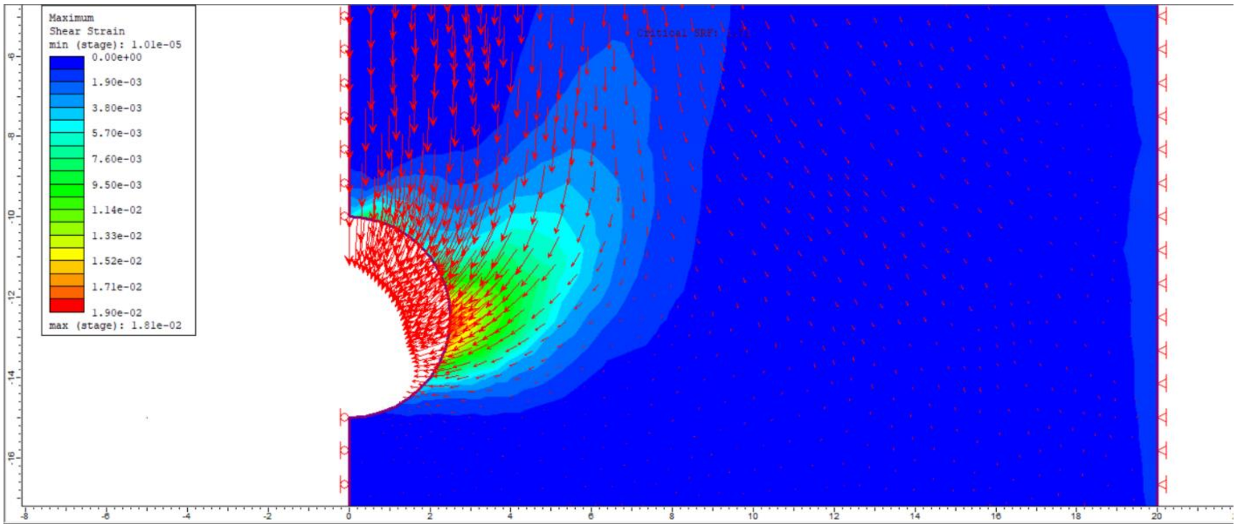

Figure 17.6: Maximum shear strain contours and deformation vectors for C/D = 2

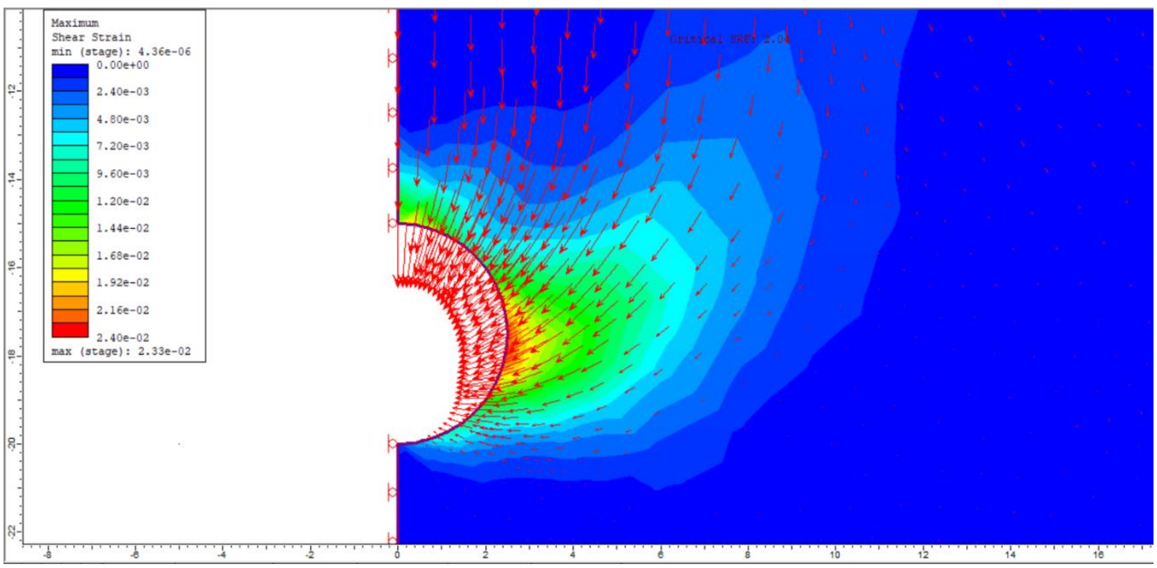

Figure 17.7: Maximum shear strain contours and deformation vectors for C/D = 3

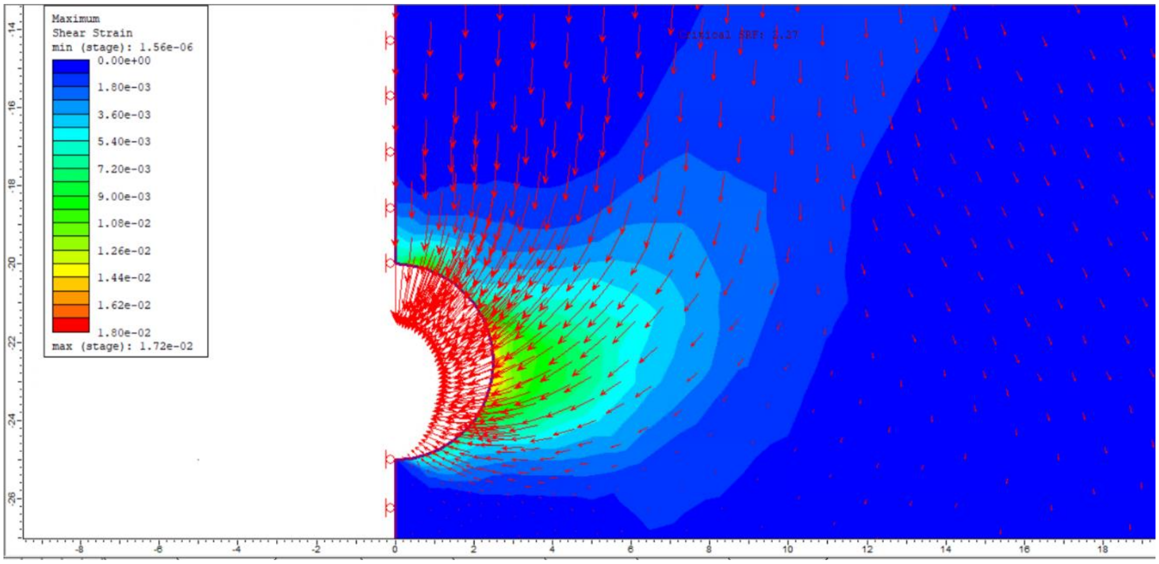

Figure 17.8: Maximum shear strain contours and deformation vectors for C/D = 4

17.4 References

1. Broms, B.B., and Bennermark, H., (1967), “Stability of clay at vertical openings.” Proc. ASCE 93(SM1), pp. 71-94.

2. Peck, R.B., (1969), Deep Excavations and Tunneling in Soft Ground”, Proc., 7th Int. Conf. Soil Mech. Found. Engrg., 225-281.

3. Davis, E.H., Gunn, M.J., Mair, R.J. & Seneviratne, H. (1980), “The stability of shallow tunnels and underground openings in cohesive material. Geotechnique, 30: 397-416.

17.5 Data Files

The input data files **stress#017_01.fez** to **stress#017_05.fez** can be downloaded from the RS2 Online Help page for Verification Manuals. Table 17.1 identifies the tunnel diameter to cover depth ratio (*C/D*) for each data file.

Table 17.1: Input data files for tunnel stability in purely cohesive soil

File	*C/D*
stress#017_01.fez	0.25
stress#017_02.fez	1
stress#017_03.fez	2
stress#017_04.fez	3
stress#017_05.fez	4

18 Circular Load on Surface of a Single-Layered Half-Space

18.1 Problem Description

This problem considers the case of a uniform circular distributed load on a single-layered half space consisting of undrained clay. The material is assumed to be elasto-plastic with failure defined by the Mohr-Coulomb criterion. The problem is described in "Limit loads for multilayered half-space using the linear matching method" (Boulbibane & Ponter, 2008) [1]. Results from ***RS2*** were compared to those presented in [1] and to Prandtl's analytical solution for collapse loads on purely cohesive soil. Figure 18.1 illustrates the problem schematically.

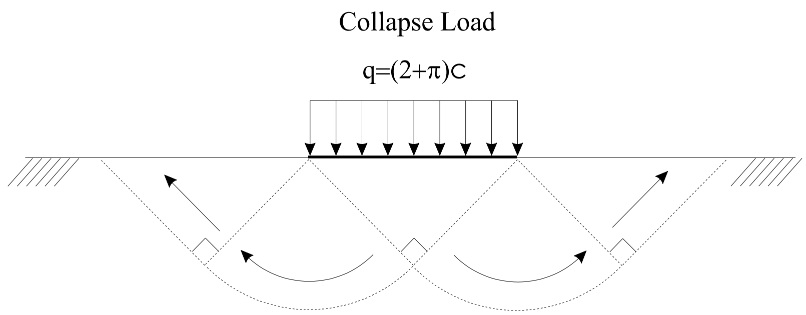

Figure 18.1: Prandtl's wedge problem of a strip load on a frictionless soil

Seven cases were considered using friction angles varying from 0 to 30°. Table 18.1 summarizes other material and model parameters.

Table 18.1: Model parameters

Parameter	Value
Unit weight (γ)	23 kN/m^2
Poisson's ratio (v)	0.3
Cohesion (c)	1 kPa
Young's modulus (E)	20 000 kPa
Friction angle (ϕ)	0°, 5°, 10°, 15°, 20°, 25°, 30°

Figure 18.2 illustrates the problem as implemented axisymmetrically in ***RS2***. The model has depth 2.5m and radius 3.5m, and uses an 8-noded quadrilateral mapped mesh. Boundary conditions are as shown and there is no initial element loading.

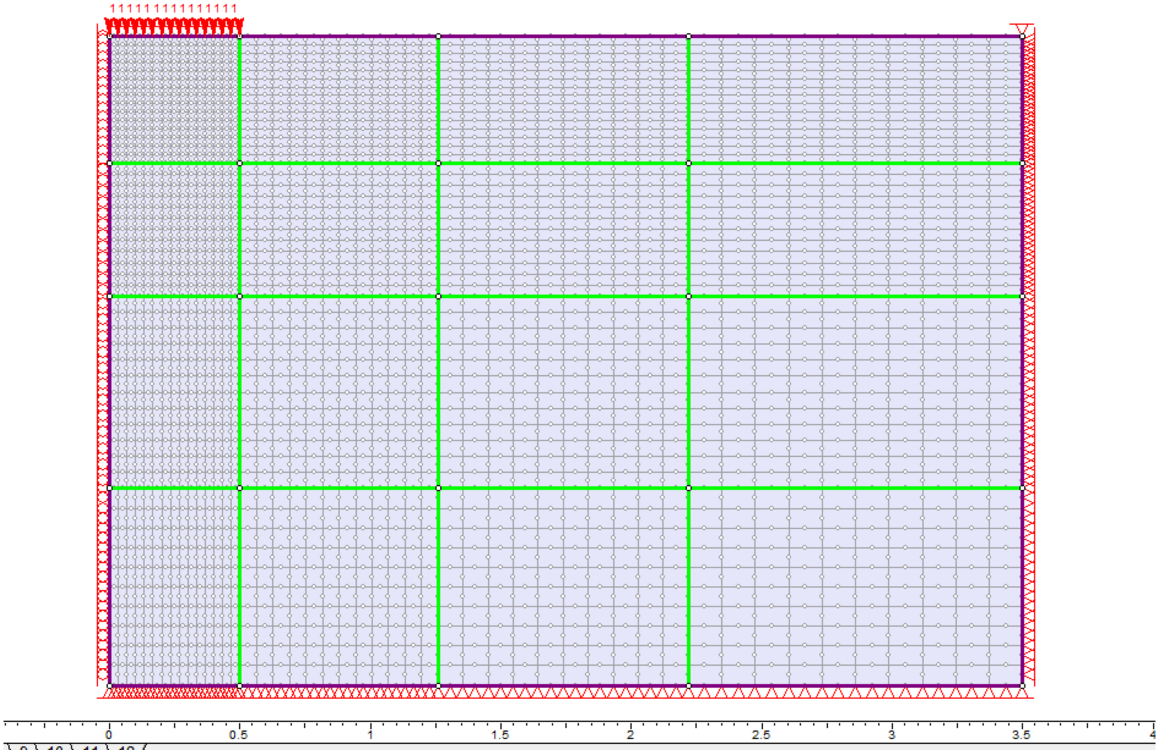

Figure 18.2: Circular loading on Mohr-Coulomb half-space

18.2 Analytical Solution

Prandtl's Wedge solution can be found in Terzaghi and Peck (1967) [2]. It predicts that the collapse load q for a purely cohesive material with cohesion c is given by:

$$\begin{aligned} q &= (2+\pi)c \\ &\cong 5.14c \end{aligned}$$

If $\phi > 0$, the collapse load can be determined using a semi-empirical method described in [2]. For the relevant values of ϕ, Table 18.2 shows analytical values of the collapse load.

Table 18.2: Prandtl's theoretical collapse loads for Mohr-Coulomb soils

Internal friction angle ϕ, ($^\circ$)	0	5	10	15	20	25	30
Prandtl's Solution Load (kPa)	5.14	6.49	8.34	10.97	14.83	20.72	30.14

18.3 Results

Figure 18.3 to Figure 18.9 show the load-displacement curves produced by ***RS2***. Prandtl's analytical collapse load is also plotted for reference.

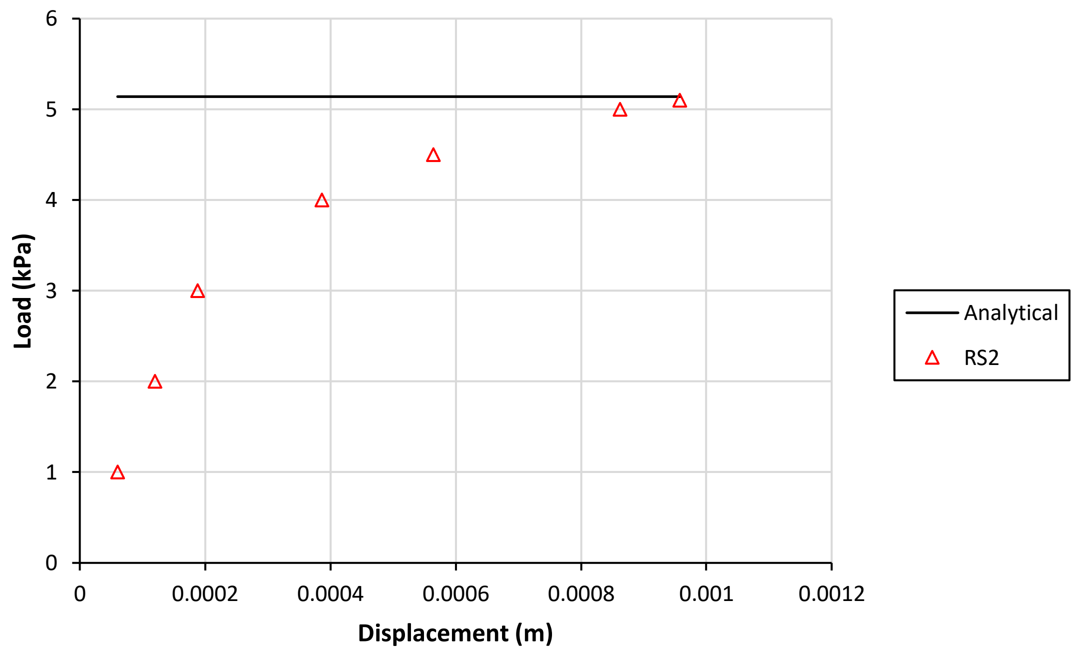

Figure 18.3: Load-displacement curves for $\phi = 0^{\circ}$

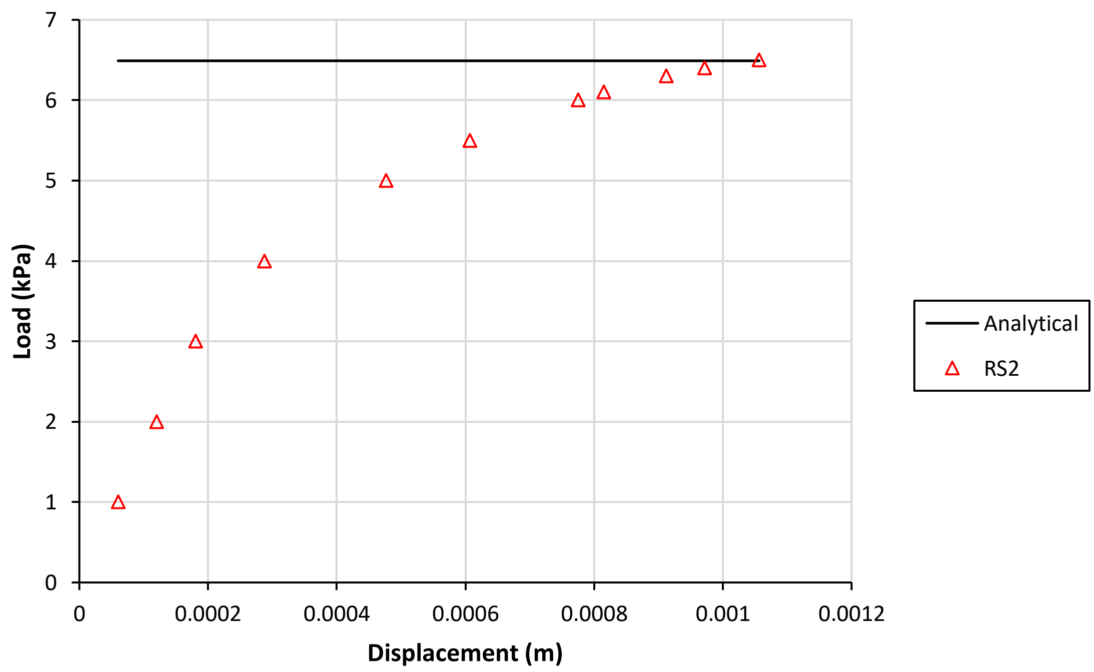

Figure 18.4: Load-displacement curves for $\phi = 5^{\circ}$

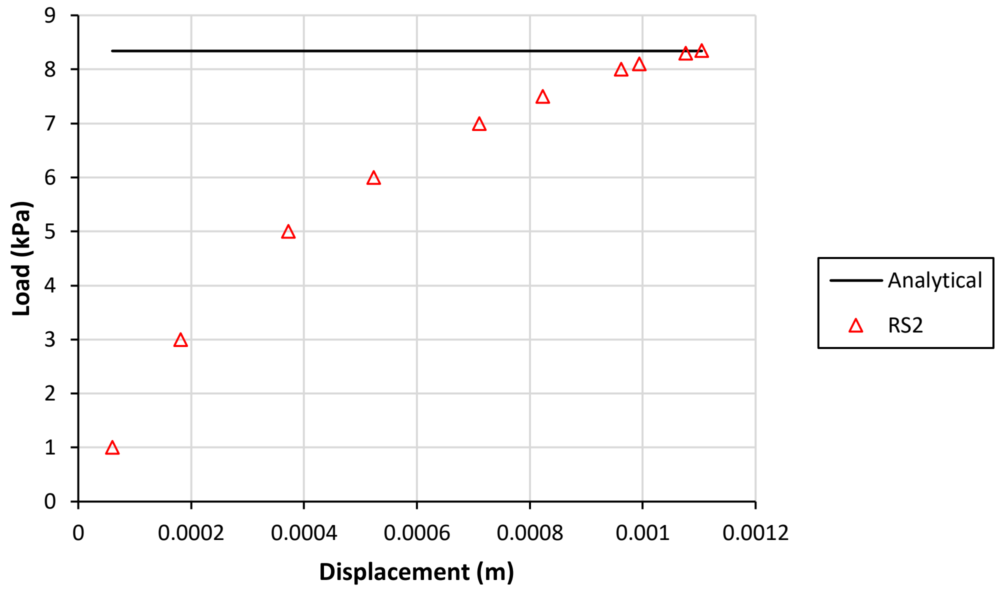

Figure 18.5: Load-displacement curves for $\phi = 10^{\circ}$

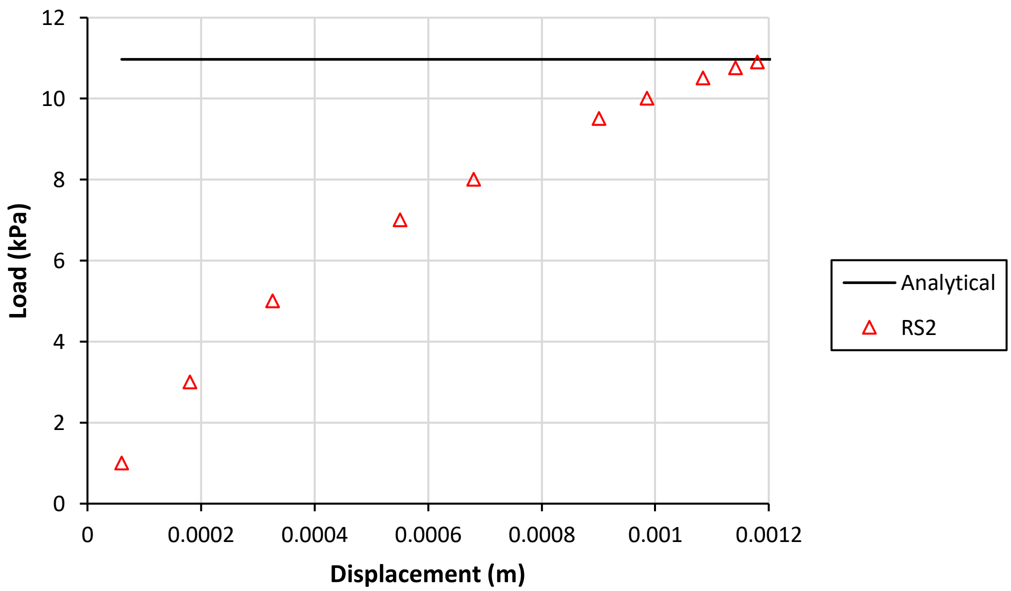

Figure 18.6: Load-displacement curves for $\phi = 15^{\circ}$

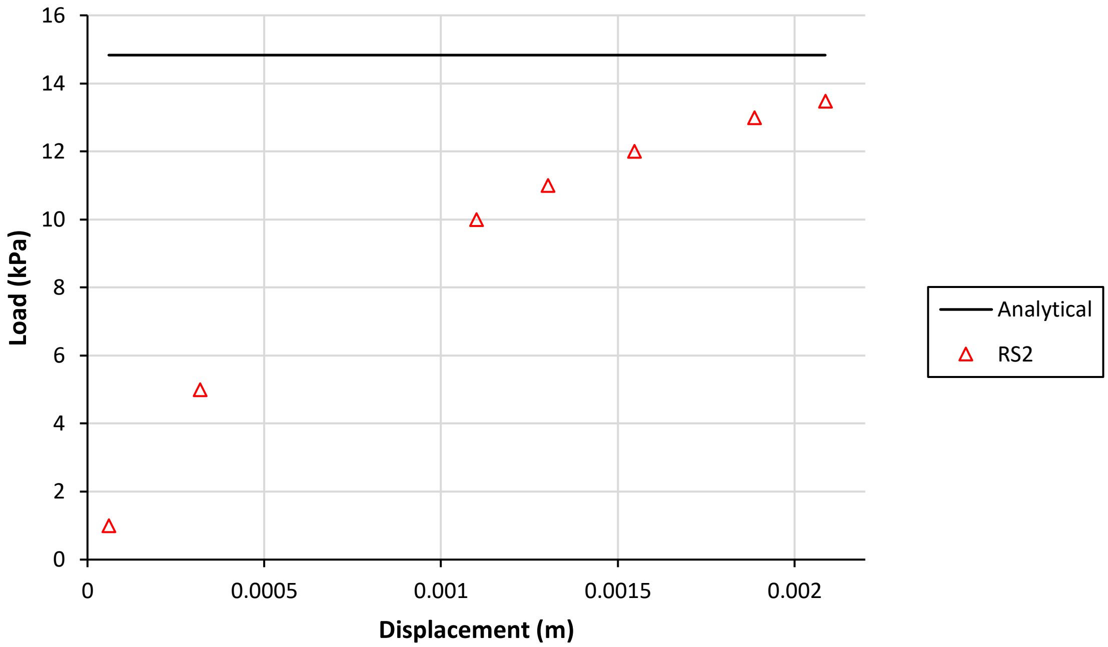

Figure 18.7: Load-displacement curves for $\phi = 20^{\circ}$

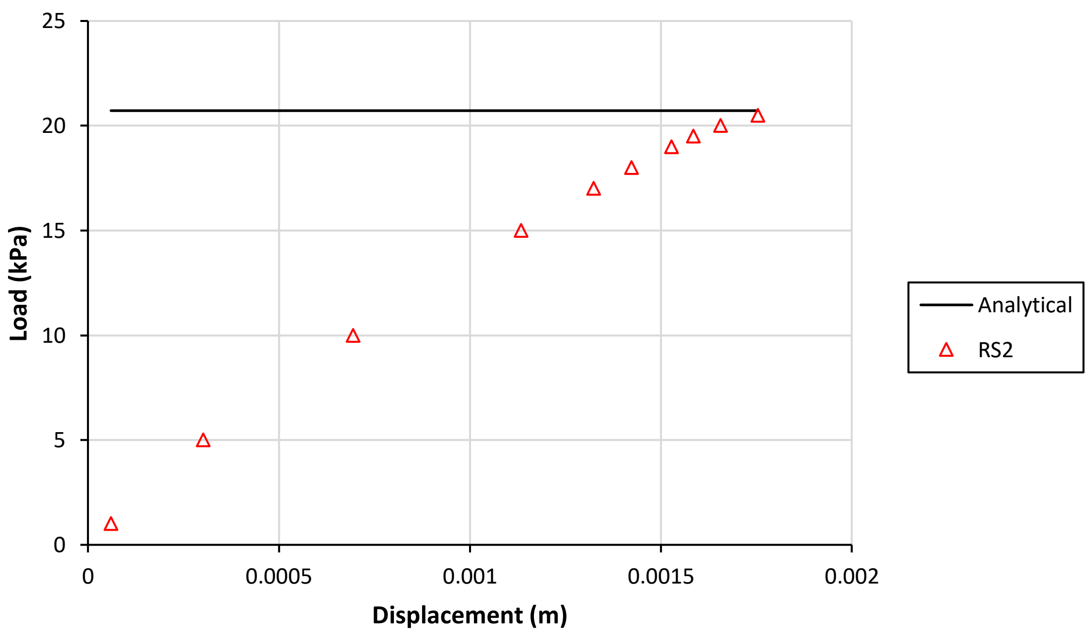

Figure 18.8: Load-displacement curves for $\phi = 25^{\circ}$

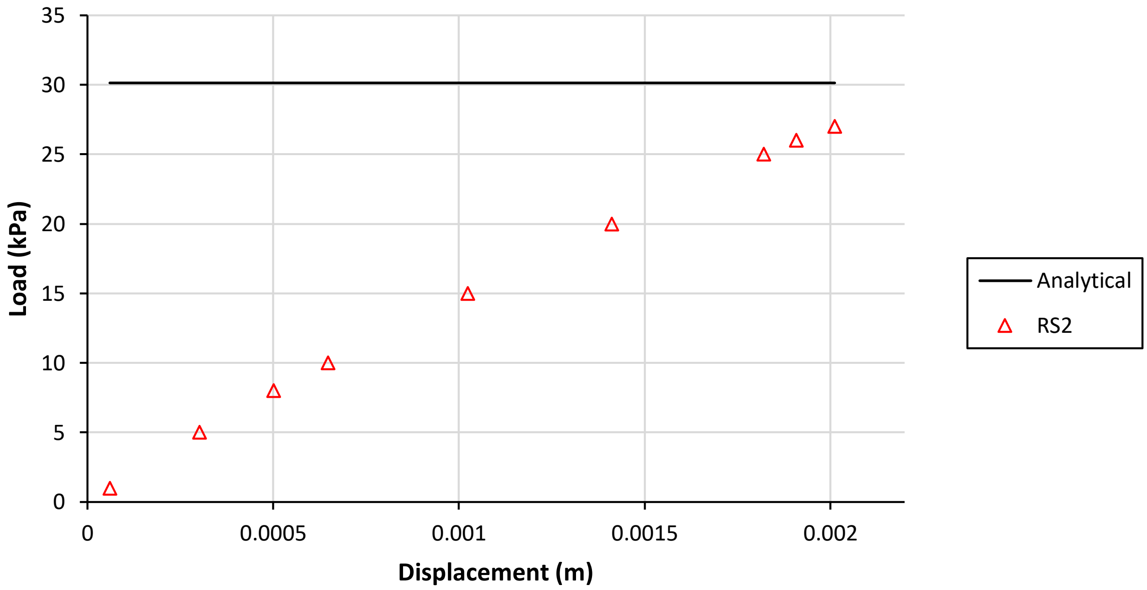

Figure 18.9: Load-displacement curves for ϕ =30˚

Figure 18.10 to Figure 18.12 show principal stress and total displacement contour plots for ϕ = 5˚.

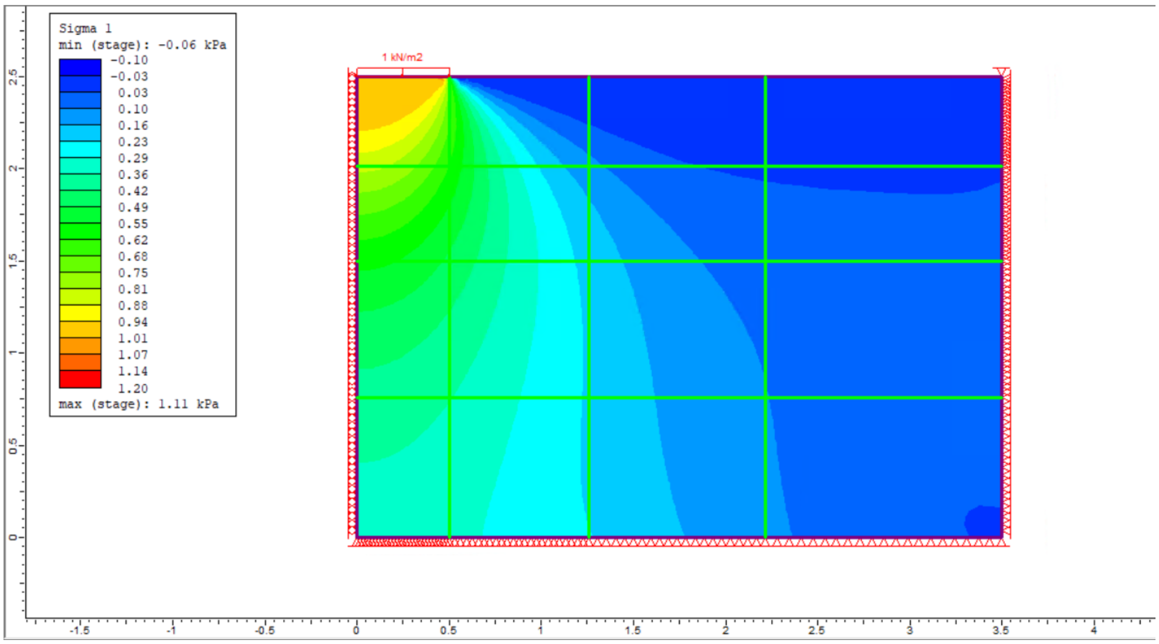

Figure 18.10: Major principal stress contours under strip load in *RS2*

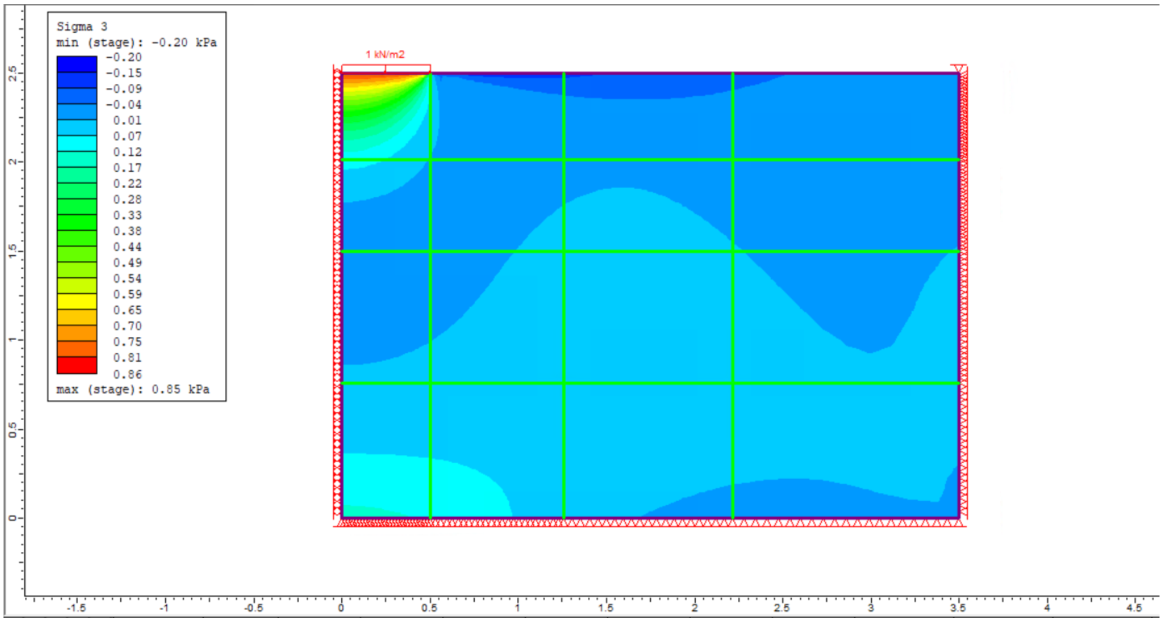

Figure 18.11: Minor principal stress contours under strip load in *RS2*

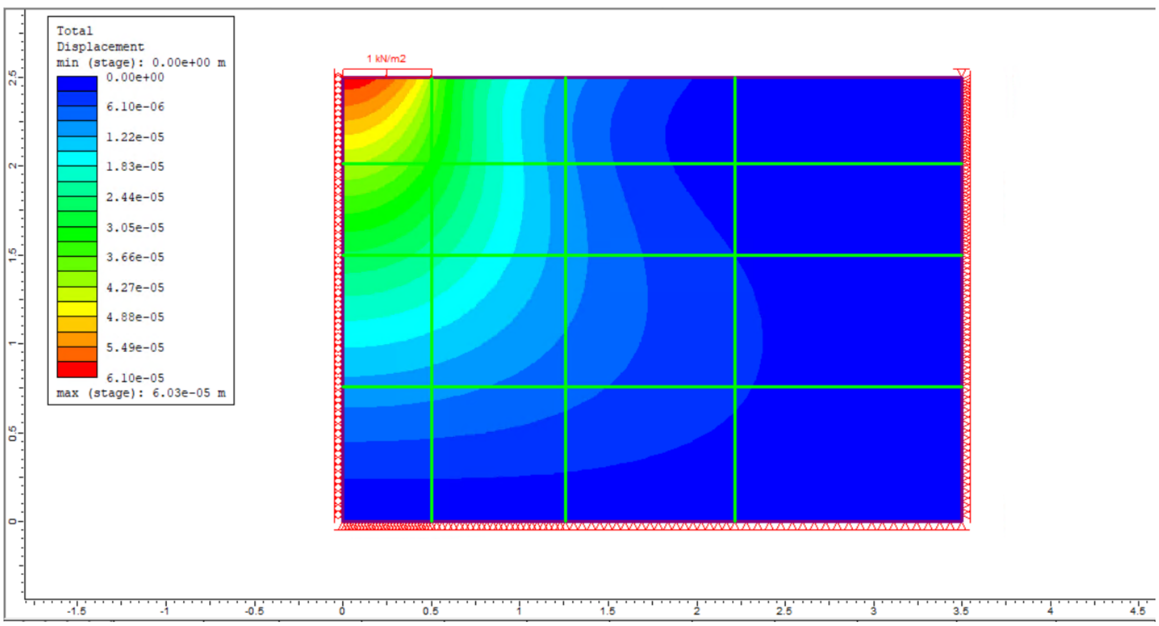

Figure 18.12: Total displacement contours under strip load in *RS2*

18.4 References

1. M. Boulbibane, A.R.S. Ponter (2005), “Limit loads for multilayered half-space using the linear matching method”, Computers and Geotechnics, 32, pp. 535-544.
2. K. Terzaghi and R. B. Peck (1967), *Soil Mechanics in Engineering Practice*, 2nd Ed. New York, John Wiley and Sons.

18.5 Data Files

The input data files **stress#018_01.fez** to **stress#018_07.fez** can be downloaded from the RS2 Online Help page for Verification Manuals. Table 18.3 identifies the corresponding soil friction angle for each data file.

Table 18.3: Input data files for circular load on single-layered Mohr-Coulomb material

File	*Friction Angle (ϕ)*
stress#018_01.fez	0°
stress#018_02.fez	5°
stress#018_03.fez	10°
stress#018_04.fez	15°
stress#018_05.fez	20°
stress#018_06.fez	25°
stress#018_07.fez	30°

19 Circular Load on Surface of a Two-Layered Mohr-Coulomb Material

19.1 Problem Description

This problem is drawn from Boulbibane et al. (2005) [1] and considers a circular load applied at the surface of a half-space consisting of two distinct layers of elastoplastic undrained clay. Figure 19.1 illustrates the problem schematically (note that $D = 0$ in this case). The bearing capacity of the materials is determined by increasing the surface load until failure according to the Mohr-Coulomb criterion.

Several cases were studied using various strength ratios (c_t/c_b) for the two materials. Table 19.1 summarizes these and other relevant parameters

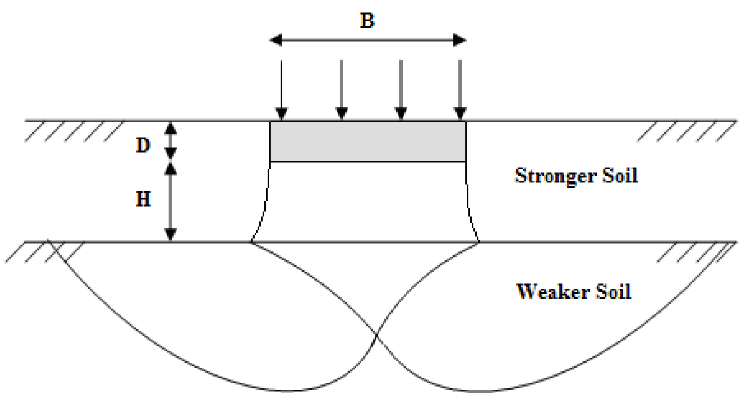

Figure 19.1: Circular load applied to two-layered half-space

Table 19.1: Model parameters

	Strength Ratio c_t/c_b	Unit weight γ (kN/m^2)	Poisson's ratio ν	Friction Angle ϕ	Young's Modulus E (kPa)	Depth/Width ratio H/B
Case 1	0.2	23	0.3	0	20 000	0.5
Case 2	0.4					
Case 3	0.6					
Case 4	0.8					
Case 5	1.0					
Case 6	1.5					
Case 7	2.0					
Case 8	2.5					
Case 9	3.0					
Case 10	3.5					
Case 11	4.0					

Figure 19.2 shows the problem as constructed in ***RS2***. The model shown uses an 8-noded quadrilateral mapped mesh. Note that axisymmetry is used.

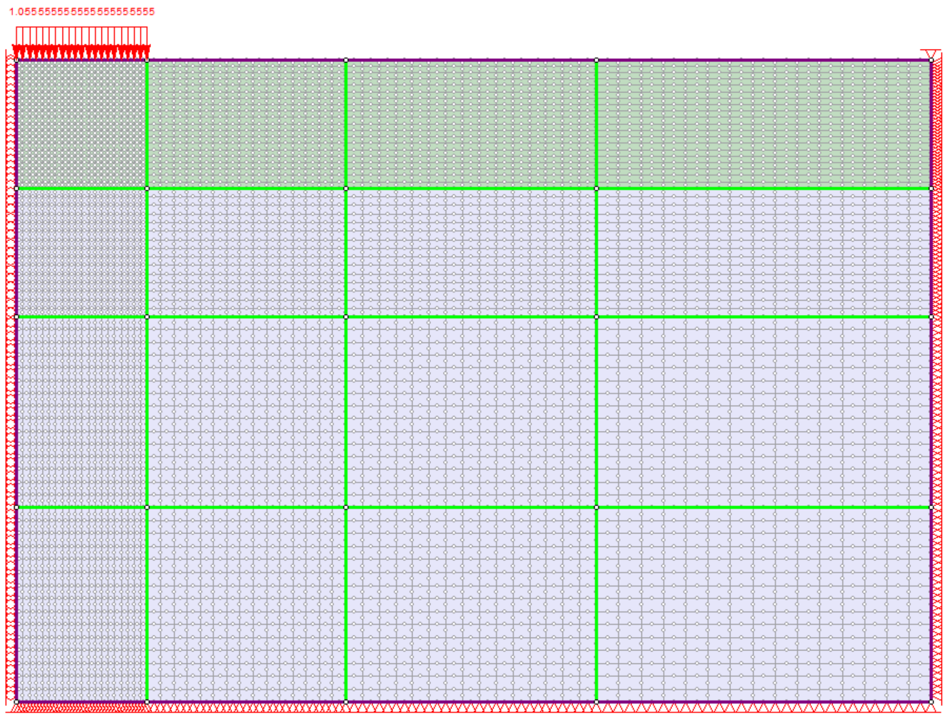

Figure 19.2: Axisymmetric model of circular load in *RS2*

19.2 Analytical Solution

Table 19.2 shows Prandtl's solution for the bearing capacity of a two-layered cohesive soil for each case studied.

Table 19.2: Analytical bearing capacities for various strength ratios

Strength Ratio, c_t/c_b (kPa)	0.2	0.4	0.6	0.8	1.0	1.5	2.0	2.5	3.0	3.5	4.0
Prandtl's Solution Load (kN)	1.06	2.12	3.18	4.24	5.26	6.68	7.64	8.55	9.27	9.84	10.3

19.3 Results

Figure 19.3 to Figure 19.13 show the load-displacement curves generated by ***RS2*** for each case. For all strength ratios, agreement with the theoretical limit load was good.

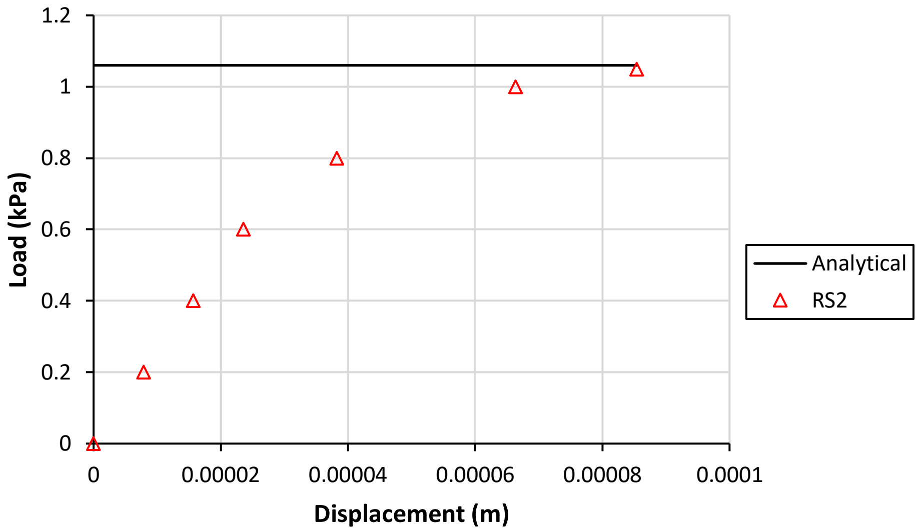

Figure 19.3: Load-displacement curve for c_t/c_b = *0.2*

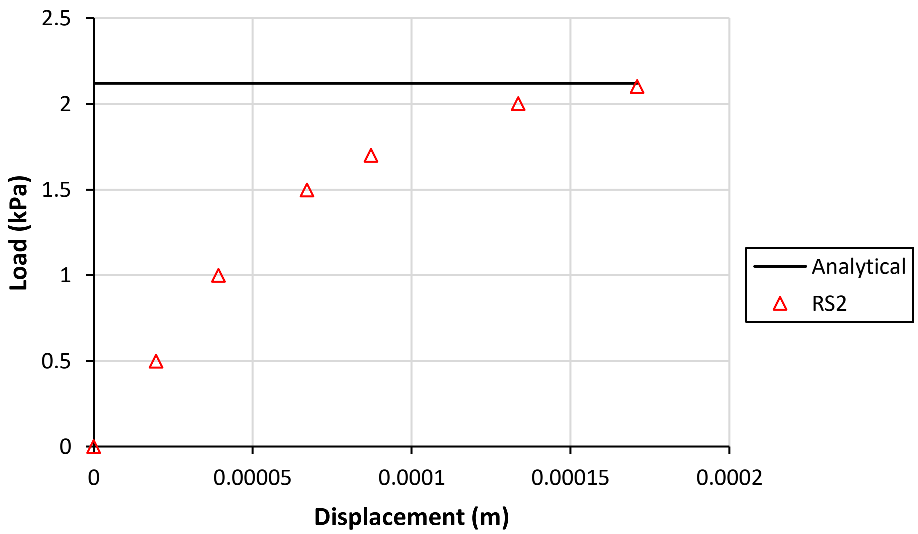

Figure 19.4: Load-displacement curve for c_t/c_b = *0.4*

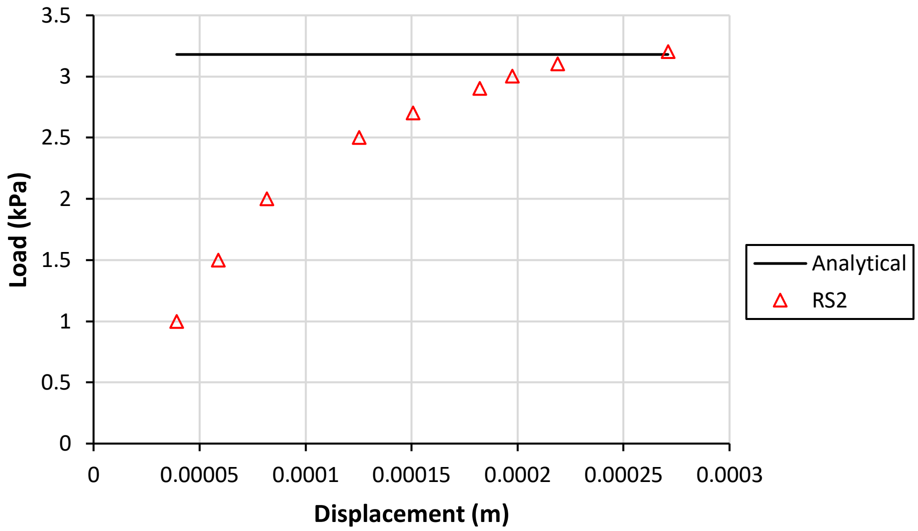

Figure 19.5: Load-displacement curve for c_t/c_b = *0.6*

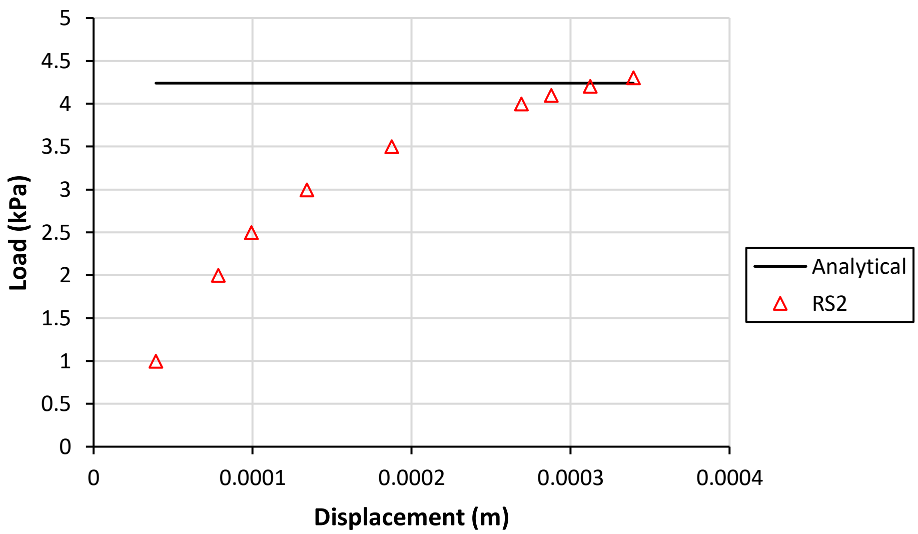

Figure 19.6: Load-displacement curve for c_t/c_b = *0.8*

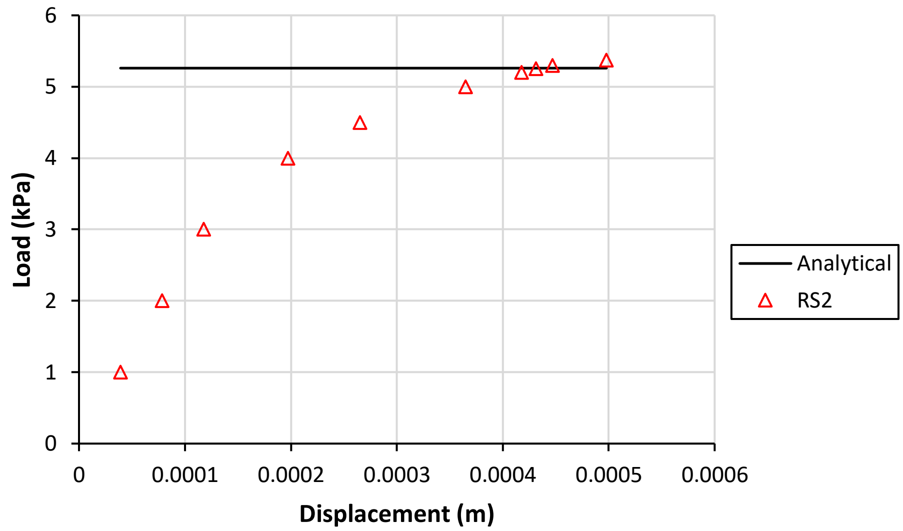

Figure 19.7: Load-displacement curve for c_t/c_b = *1.0*

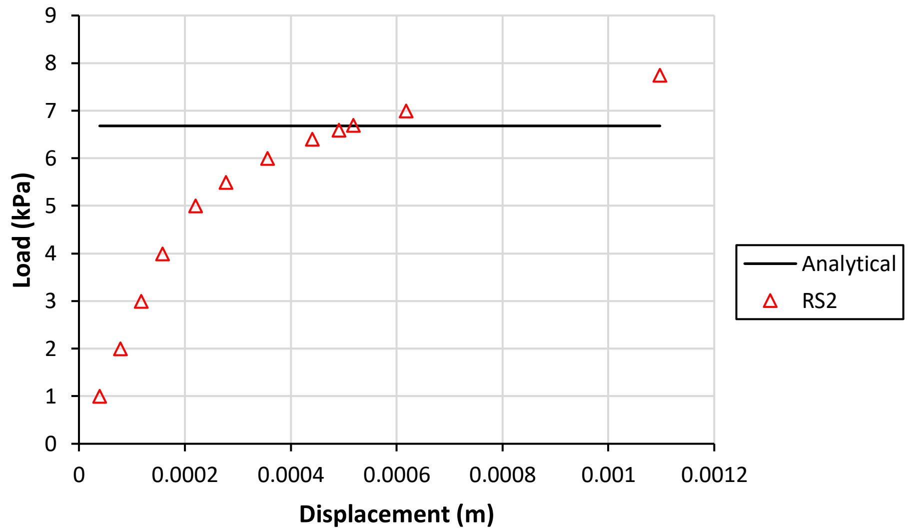

Figure 19.8: Load-displacement curve for c_t/c_b = *1.5*

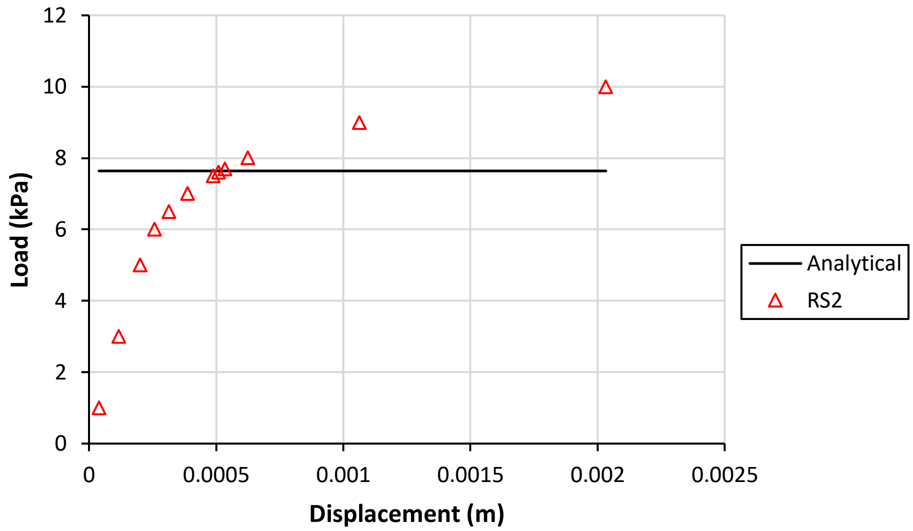

Figure 19.9: Load-displacement curve for c_t/c_b = *2.0*

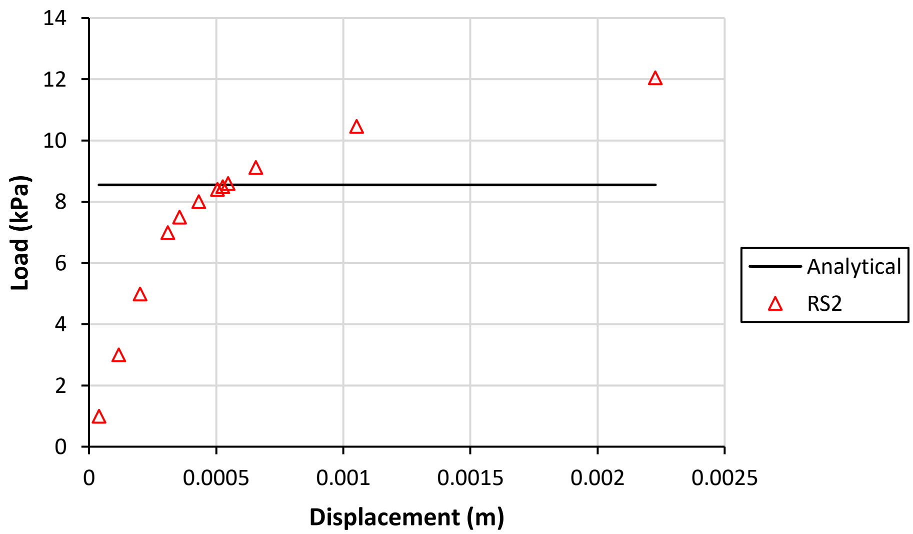

Figure 19.10: Load-displacement curve for c_t/c_b = *2.5*

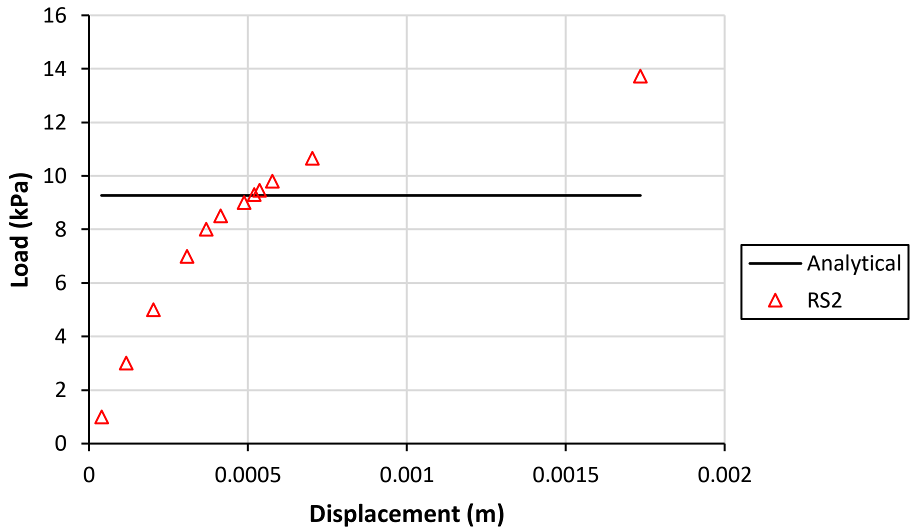

Figure 19.11: Load-displacement curve for c_t/c_b **= *3.0***

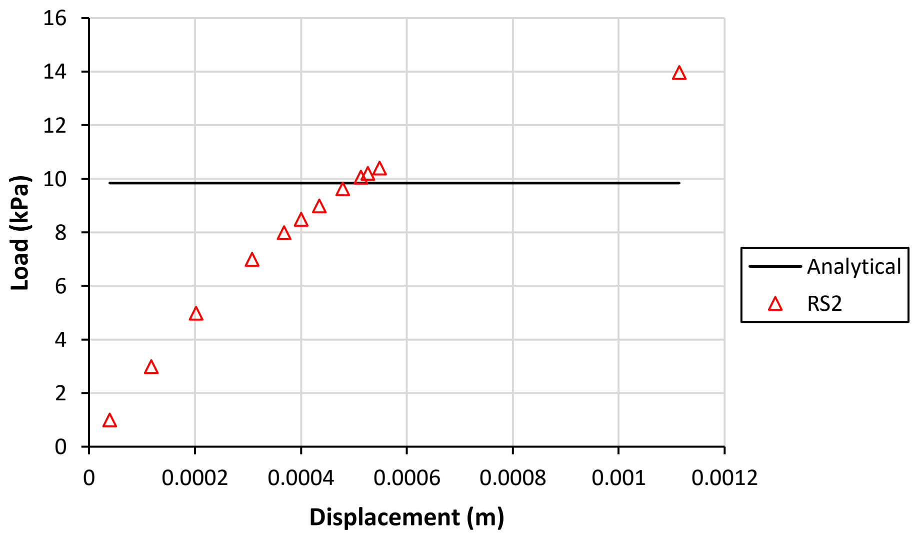

Figure 19.12: Load-displacement curve for c_t/c_b **= *3.5***

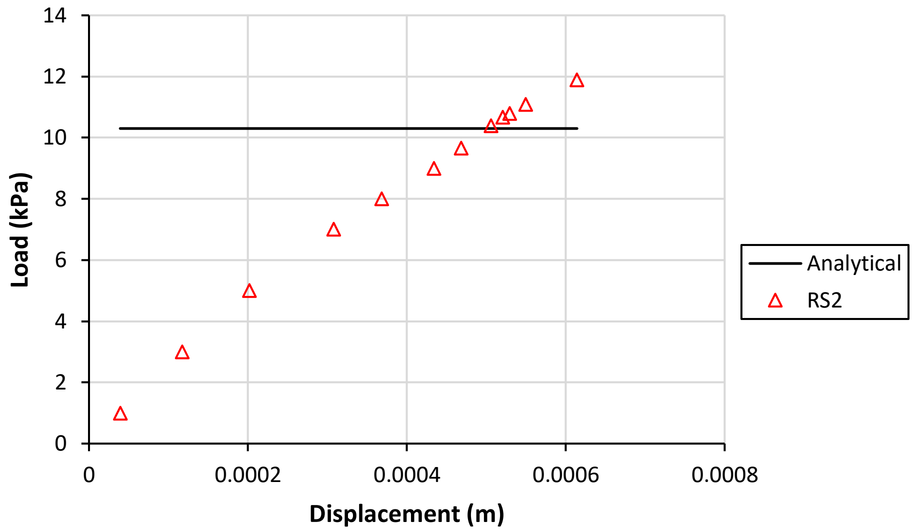

Figure 19.13: Load-displacement curve for c_t/c_b = 4.0

19.4 References

1. M. Boulbibane, A.R.S. Ponter (2005), "Limit loads for multilayered half-space using the linear matching method", Computers and Geotechnics, 32, pp. 535-544.

2. Braja M. Das (2007), ***Principles of Foundation Engineering***, 6th Edition. Thomson Canada Limited.

19.5 Data Files

The input data files **stress#019_01.fez** to **stress#019_11.fez** can be downloaded from the RS2 Online Help page for Verification Manuals. Table 19.3 identifies the strength ratio assigned to each file.

Table 19.3: Data input files for circular load on two-layered Mohr-Coulomb soil

File	*Strength Ratio (c_t/c_b)*
stress#019_01.fez	0.2
stress#019_02.fez	0.4
stress#019_03.fez	0.6
stress#019_04.fez	0.8
stress#019_05.fez	1.0
stress#019_06.fez	1.5
stress#019_07.fez	2.0
stress#019_08.fez	2.5
stress#019_09.fez	3.0
stress#019_10.fez	3.5
stress#019_11.fez	4.0

20 Stress Distribution Along a Grouted Rock Bolt

20.1 Problem Description

This problem examines the shear stress distribution along a thin annulus of grout around a grouted rock bolt subjected to an axial pull-out force. Figure 20.1 illustrates the situation and relevant parameters, while Figure 20.2 shows the problem as constructed in ***RS2***.

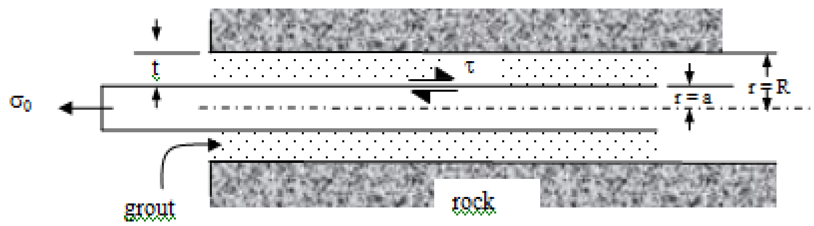

Figure 20.1: Fully grouted rockbolt in elastic rock mass

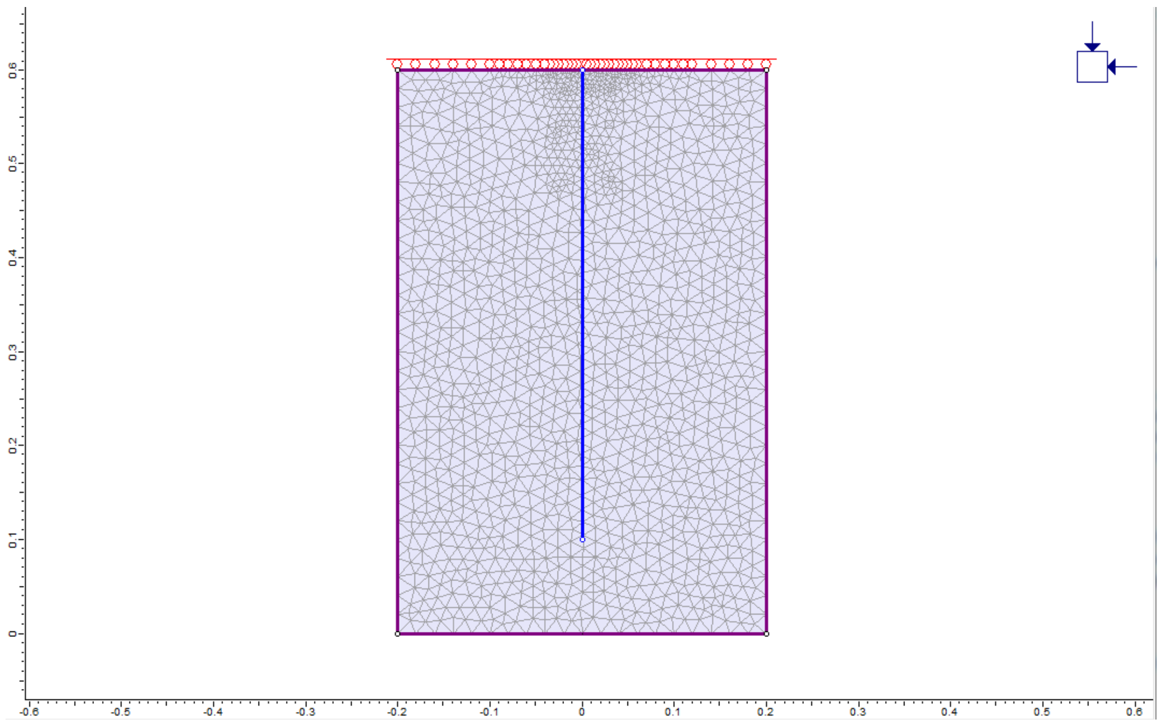

Figure 20.2: Fully grouted rockbolt as modelled in *RS2*

Table 20.1 summarizes the material and rockbolt properties used.

Table 20.1: Model parameters

Parameter	*Value*
Young's modulus (E)	75000 MPa
Poisson's ratio (v)	0.25
Hole radius (R)	10.825 mm
Bolt properties	
Tributary area	232.5 mm^2
Young's modulus (E_a)	98600 MPa
Bond shear stiffness	13882 MPa
Grout shear modulus (G_g)	493 MPa
Bolt radius (a)	8.6 mm
Pull-out force	0.1 MN

20.2 Analytical Solution

According to Farmer (1975) [1], the shear stress distribution along a fully grouted rock bolt is given by

$$\frac{\tau}{\sigma_0} = 0.1 \exp \frac{-0.2x}{a}$$

where τ_x is the shear force in the grout, σ_0 is the applied pull-out stress, x is the distance from the head of the bolt and a is the bolt radius. This equation is developed using the following assumptions:

1. The grout shear modulus $G_g = 0.005E_a$
2. The hole radius $R = 1.25a$, where a is the bolt radius

In order for the above assumptions to hold true, the grout shear modulus was set to 493 MPa. The grout shear stiffness was then calculated using the following equation [2]:

$$K_g = \frac{2\pi G_g}{\ln(1 + t/a)}$$

The bolt tributary area was set to 232.5 mm^2, equivalent to a bolt having a radius a = 8.6 mm. By assumption 2 above, the radius of the hole R = 10.825 mm.

20.3 Results

Figure 20.3 shows the σ_3 contours in the rock mass and the shear force distribution along the bolt, as calculated by ***RS2***. The shear stress acting on the bolt can be calculated for two scenarios:

1. The shear stress acts at the boundary between the bolt and the grout. In this case, the shear stress is given by:

$$\tau = \frac{F_s}{2\pi a}$$

where F_s is the shear force.

2. The shear stress acts at the boundary between the grout and the rock. In this case, the shear stress is given by:

$$\tau = \frac{F_s}{2\pi R}$$

Both of these cases are plotted in Figure 20.4, which shows the shear stress distribution along the bolt length. As can be seen, the two bracket the analytical solution.

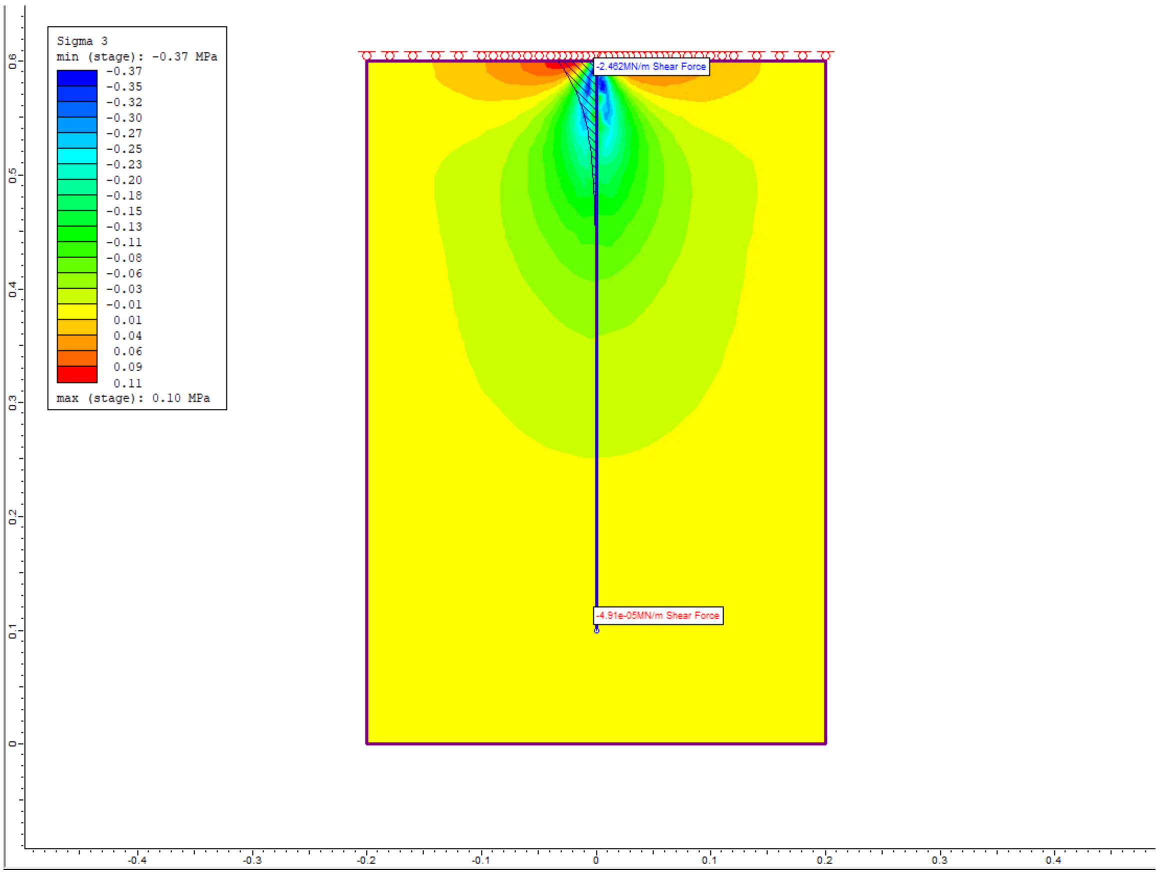

Figure 20.3: Secondary principal stress contours and shear force per unit length along bolt

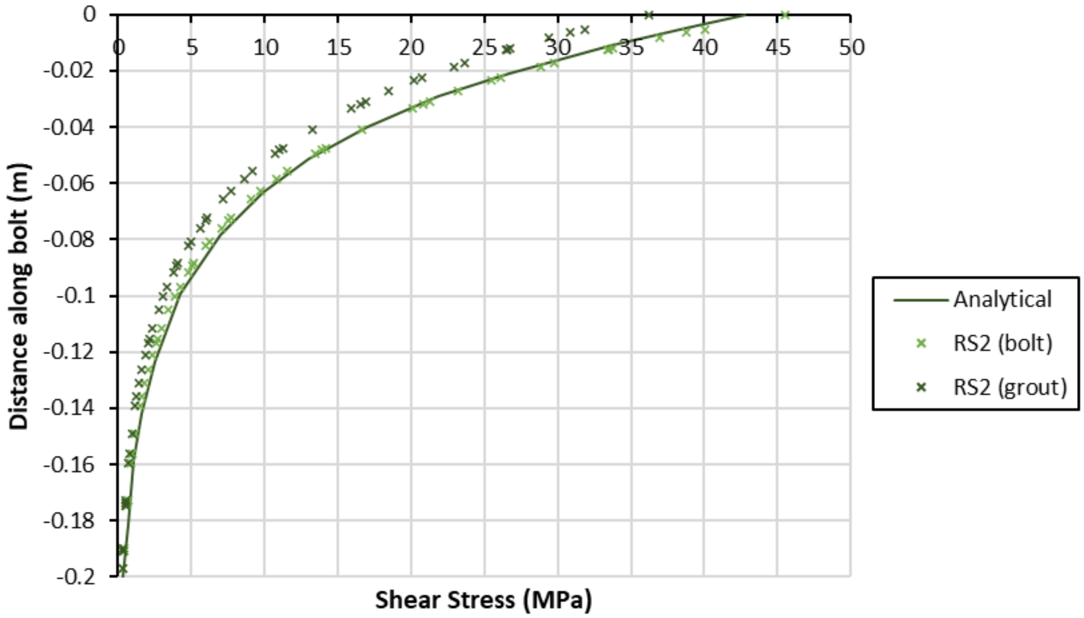

Figure 20.4: Shear stress distributions along bolt

20.4 References

1. Farmer, I.W., (1975), "Stress distribution along a resin grouted rock anchor", *Int. J. Rock Mech. Min. Sci. Geomech. Abstr*., **11**, 347-351.

2. Itasca Consulting Group Inc., 2004. *FLAC v 5.0 User's Guide – Structural Elements*, Minneapolis, Minnesota, USA.

20.5 Data Files

The input data file **stress#020.fez** can be downloaded from the RS2 Online Help page for Verification Manuals.

21 Circular Tunnel Reinforced by Rock Bolts

21.1 Problem Description

This problem considers a circular tunnel in an elastic, isotropic rock mass reinforced with a circular array of rockbolts. Both end-anchored and grouted elastic rockbolts are considered; the former is assumed to interact with the rockmass only at the bolt ends and the latter is fully bonded to the rock along its entire length. The tunnel is exposed to an in-situ hydrostatic compressions field of 10 MPa.

Figure 21.1 shows the problem as constructed in ***RS2***. The model uses a radial mesh of 4-noded quadrilateral elements. Infinite elastic elements are used on the outer boundary, which is located 6 m from the hole centre.

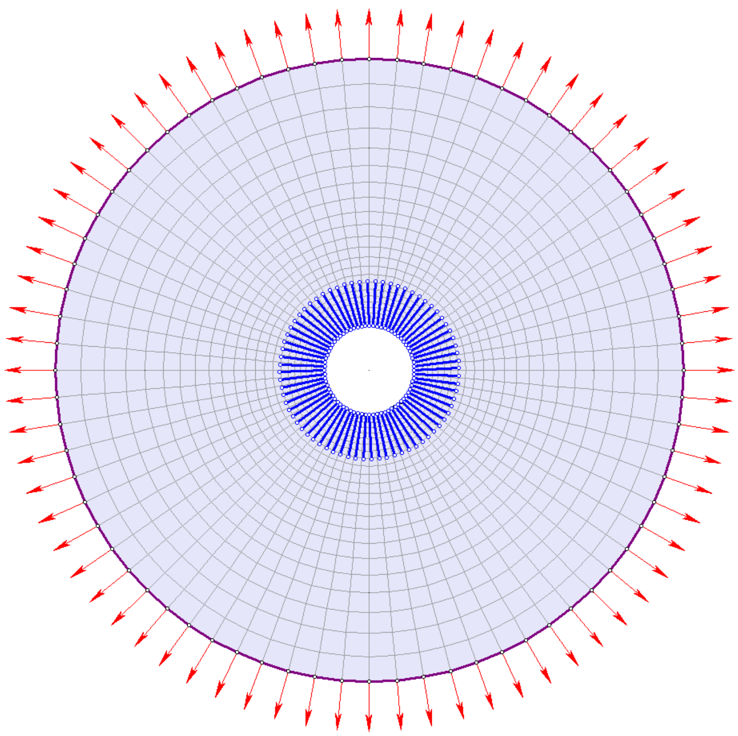

Figure 21.1: Tunnel in elastic medium supported by rockbolts as constructed in *RS2*

Table 21.1 summarizes material and bolt properties.

Table 21.1: Model parameters

Parameter	*Value*
Tunnel radius (*a*)	1 m
In-situ stresses (σ_1, σ_3, σ_z, σ_0)	10 MPa
Young's modulus (*E*)	250 MPa
Poisson's ratio (*v*)	0.3
Bolt properties	
Diameter (d_b)	25 mm
Young's modulus (E_b)	116667 MPa
Length (L_b)	1 m
Number of bolts (N_b)	72
Bolt spacing along tunnel axis (*D*)	1 m

21.2 Analytical Solution

Carranza-Torres [1] presents analytical stress and displacement distributions for both end-anchored and fully grouted rockbolts in an elastic medium. This solution assumes that the effect of the support can be "smeared" circumferentially and along the tunnel axis to produce a single axisymmetric stress/displacement distribution. Figure 21.2 illustrates the tunnel schematically

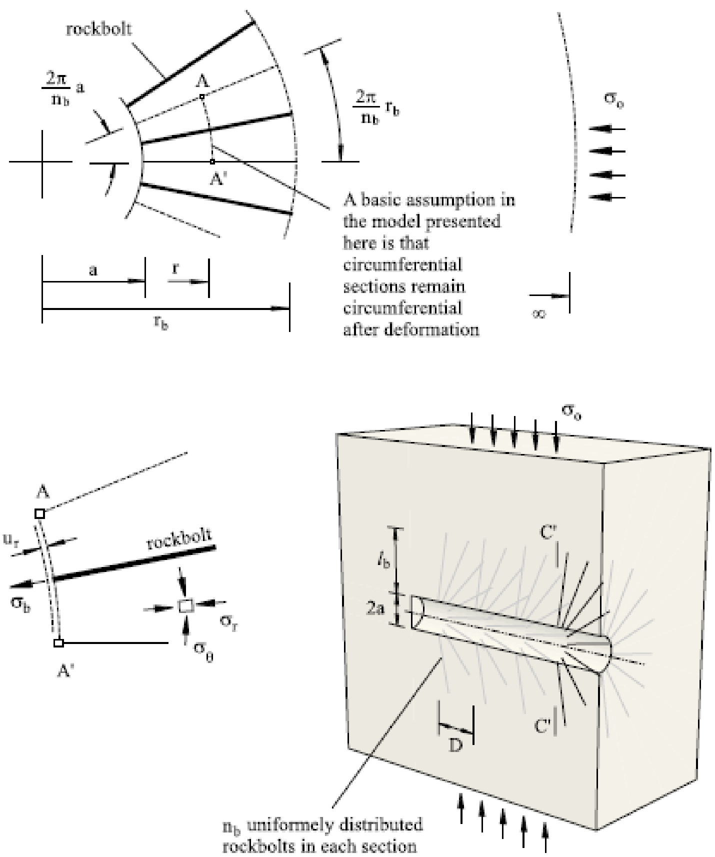

Figure 21.2: Reinforced circular tunnel [1]

Dimensionless parameters *β, α,* μ, and *ρ* are defined as follows:

$$\alpha = \frac{N_b A_b}{2\pi a D}$$

$$\beta = \frac{\alpha E_b}{2G}$$

$$\rho = \frac{a}{r}$$

$$\mu = \frac{v}{1-2v}$$

where *r* is the radial distance from the centre of the tunnel and *G* is the shear modulus of the rockmass. At the ends of the rockbolts, i.e. $r = r_b$, the non-dimensional parameter *ρ* has the value:

$$\rho_b = \frac{r_b}{a}$$

For the end-anchored case, the radial stress σ_r^b at $r = r_b$ is:

$$\frac{\sigma_r^{\ b}}{\sigma_0} = \frac{2\left(1-\rho_b^{\ 2}\right)+2\mu\left(1-\rho_b\right)\left(1+\rho_b+\beta\right)+\beta\rho_b\left(1-\rho_b\right)\left(3+\rho_b\right)}{2+\beta\rho_b\left(3-\rho_b\right)+2\mu\left(1+\beta\rho_b-\beta\rho^2\right)}$$

For the fully grouted case, the radial stress σ_r^b at $r = r_b$ is:

$$\frac{\sigma_r^{\ b}}{\sigma_0} = \frac{\beta N+\left(1+\mu\right)\left(N_4-N_3\right)-2\beta\rho_b\left(N_2-N_1\right)+2\left(1+\mu\right)\left(N_2-N_1\right)\ln\left(\dfrac{1+\mu+\beta\rho_b}{1+\mu}\right)}{\beta N-N_3\left(1+\mu\right)+2\beta\rho_b N_1-2\left(1+\mu\right)N_1\ln\left(\dfrac{1+\mu+\beta\rho_b}{1+\mu}\right)}$$

where, in the fully grouted case:

$$N = -2\beta(1-\rho_b)(1+2\mu)^2 + 2(1+\mu)(1+\beta+2\mu)(1+2\mu+\beta\rho_b)\ln\left(\frac{1+\mu+\beta}{1+\mu+\beta\rho_b}\right)$$

$$N_1 = \beta(1+2\mu+\beta)$$

$$N_2 = \beta(1+2\mu+\beta\rho_b)$$

$$N_3 = 2\beta^2\frac{1+2\mu}{1+\mu} - 2\beta(1+2\mu+\beta)\ln\left(\frac{1+\mu+\beta}{1+\mu}\right)$$

$$N_4 = 2\beta^2\rho_b\frac{1+2\mu}{1+\mu} - 2\beta(1+2\mu+\beta\rho_b)\ln\left(\frac{1+\mu+\beta\rho_b}{1+\mu}\right)$$

$$C_1 = -\frac{N_1\left(1-\frac{\sigma_r{}^b}{\sigma_0}\right) - N_2}{N}$$

$$C_2 = -\frac{N_3\left(1-\frac{\sigma_r{}^b}{\sigma_0}\right) - N_4}{N}$$

In the end-anchored case:

$$C_1 = \frac{(1-\rho_b)(1+\rho_b+\beta\rho_b) - (1+\beta\rho_b)\frac{\sigma_r{}^b}{\sigma_0}}{2\beta\rho_b(1+\mu)(1-\rho_b) + (1+2\mu)(1-\rho_b{}^2)}$$

$$C_2 = -\frac{\beta(1-\rho_b) - (1+2\mu+\beta)\frac{\sigma_r{}^b}{\sigma_0}}{2\beta\rho_b(1+\mu)(1-\rho_b) + (1+2\mu)(1-\rho_b{}^2)}$$

For both cases, the stress and displacements in the unreinforced region $r \geq r_b$ are given by:

$$\frac{2G\mu_r}{\sigma_0 a} = \left(1-\frac{\sigma_r{}^b}{\sigma_0}\right)\frac{\rho}{\rho_b{}^2}$$

$$\frac{\sigma_r}{\sigma_0} = 1-\left(1-\frac{\sigma_r{}^b}{\sigma_0}\right)\frac{\rho^2}{\rho_b{}^2}$$

$$\frac{\sigma_\theta}{\sigma_0} = 1+\left(1-\frac{\sigma_r{}^b}{\sigma_0}\right)\frac{\rho^2}{\rho_b{}^2}$$

In the reinforced region $r < r_b$, the solution for the end-anchored case is:

$$\mu_r = \frac{a\sigma_0}{2G}\left(\frac{C_1}{\rho} + C_2\rho\right)$$

$$\sigma_r = \sigma_0 + 2G\mu\rho\frac{\mu_r}{a} - 2G(1+\mu)\frac{\rho^2}{a}\frac{d\mu_r}{d\rho}$$

$$\sigma_\theta = \sigma_0 + 2G(1+\mu)\rho\frac{u_r}{a} - 2G\mu\frac{\rho^2}{a}\frac{d\mu_r}{d\rho}$$

$$\frac{d\mu_r}{d\rho} = -\frac{a\sigma_0}{2G}\left(\frac{C_1}{\rho^2} - C_2\right)$$

The solution for the fully grouted case is:

$$\frac{2G}{\sigma_0}\frac{\mu_r}{a} = -C_2\frac{1}{\rho}\frac{1+\mu}{\beta} + 2C_1\left(1 - \frac{1}{\rho}\frac{1+\mu}{\beta}\ln\left(\frac{1+\mu+\beta\rho}{1+\mu}\right)\right)$$

$$\sigma_r = \sigma_0 + 2G\mu\rho\frac{u_r}{a} - 2G(1+\mu)\frac{\rho^2}{a}\frac{du_r}{d\rho}$$

$$\sigma_\theta = \sigma_0 + 2G(1+\mu)\rho\frac{u_r}{a} - 2G\mu\frac{\rho^2}{a}\frac{du_r}{d\rho}$$

$$\frac{du_r}{d\rho} = C_2\frac{1}{\rho^2}\frac{1+\mu}{\beta} - 2C_1\left(\frac{1+\mu}{\rho(1+\mu+\beta\rho)} - \frac{1}{\rho^2}\frac{1+\mu}{\beta}\ln\left(\frac{1+\mu+\beta\rho}{1+\mu}\right)\right)$$

21.3 Results

Figure 21.3 to Figure 21.6 shows the analytical stress and displacement distributions as determined analytically and using ***RS2***. Both sets of results are very similar.

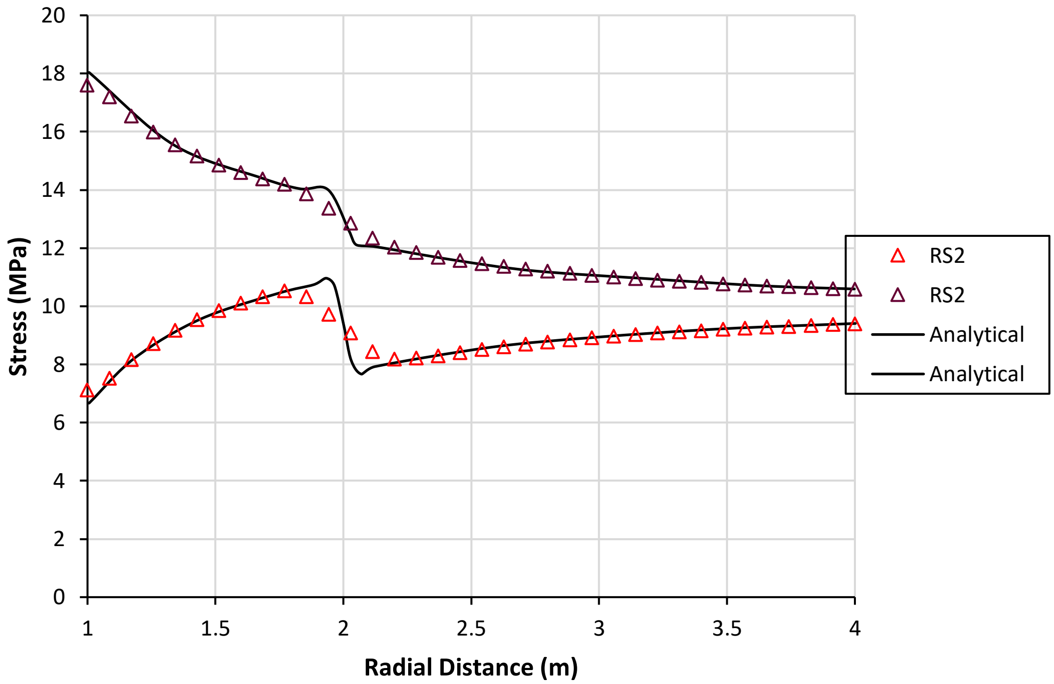

Figure 21.3: Radial and tangential stress distributions surrounding the tunnel reinforced with end-anchored bolts

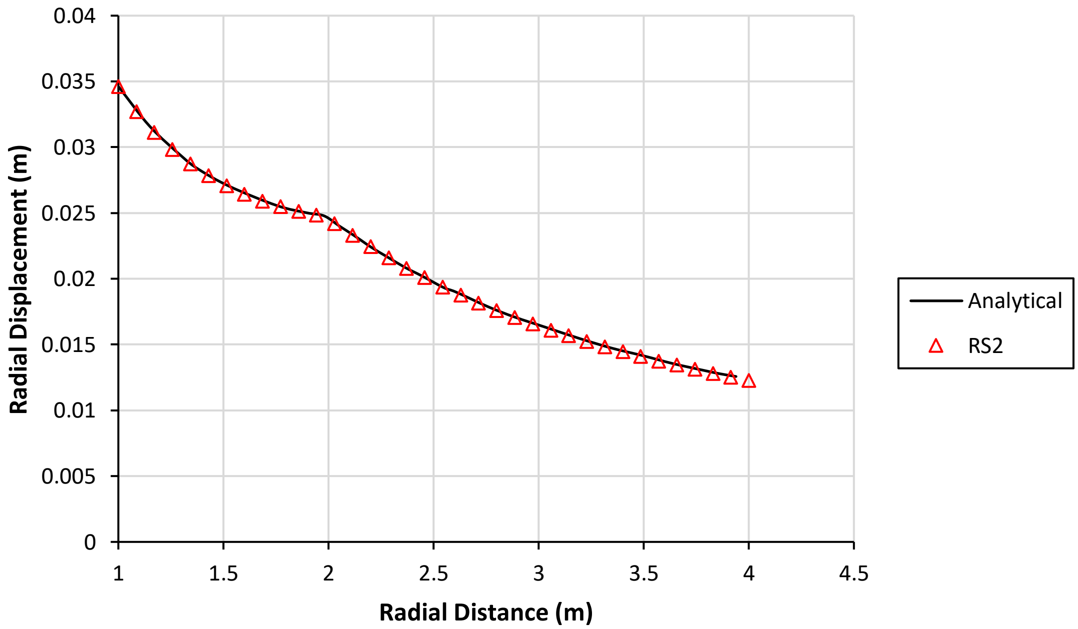

Figure 21.4: Radial displacement distributions surrounding the tunnel reinforced with end-anchored bolts

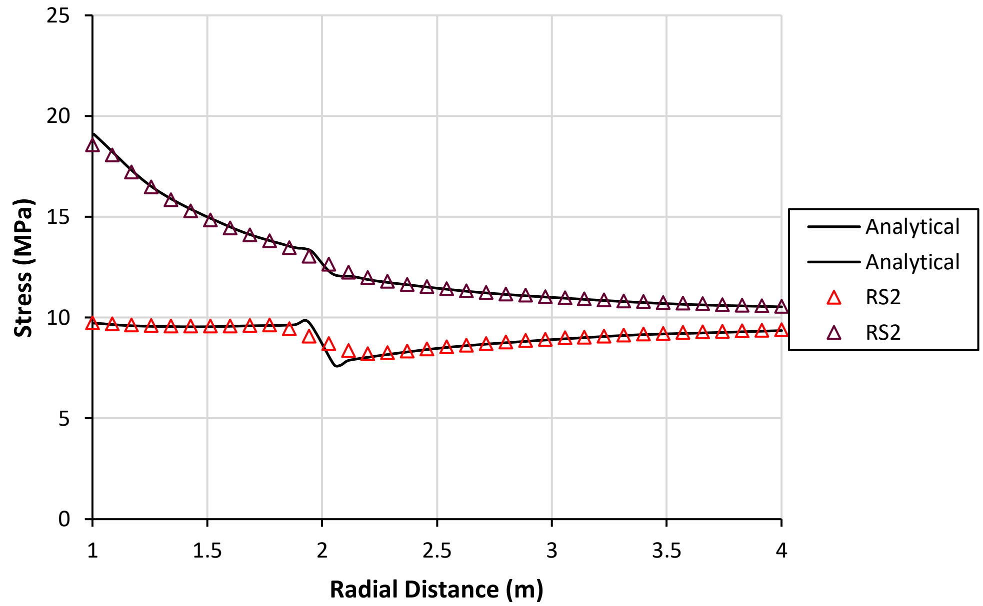

Figure 21.5: Radial and tangential stress distributions surrounding the tunnel reinforced with fully grouted bolts

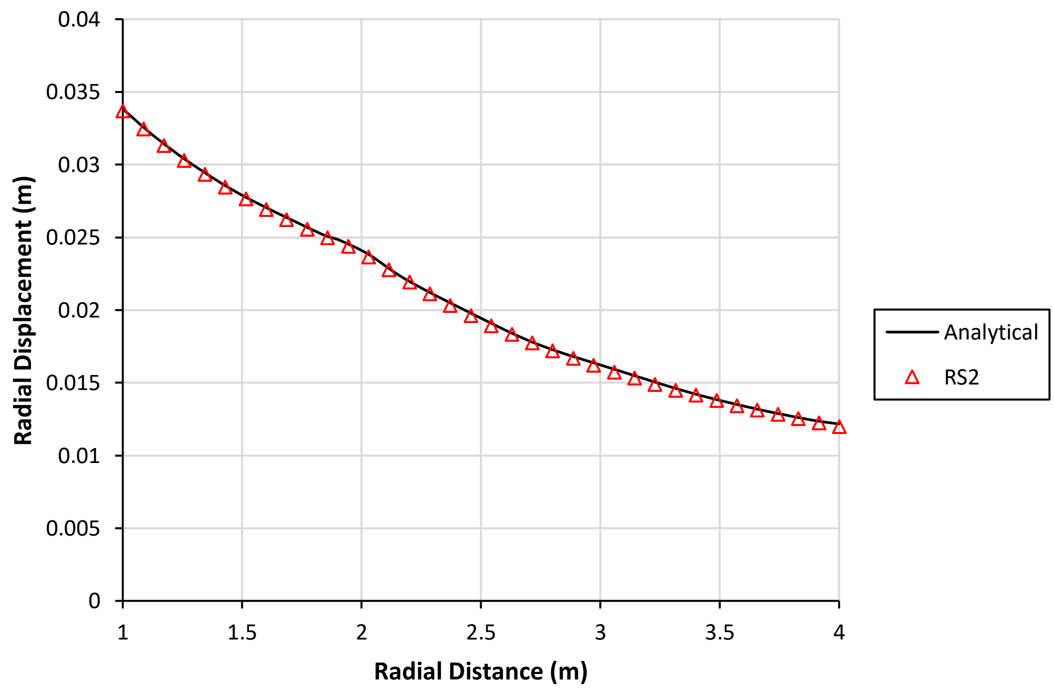

Figure 21.6: Radial displacement distributions surrounding the tunnel reinforced with end-anchored bolts

21.4 References

1. Carranza-Torres, C. (2002). "Elastic solution for the problem of excavating a circular tunnel reinforced by i) *anchored* or ii) *fully grouted* rockbolts in a medium subject to

uniform far-fields stresses" Note for the International Canada/US/Japan joint cooperation on rockbolt analysis.

21.5 Data Files

The input data files **stress#021_01.fez** (end-anchored) and **stress#022_02.fez** (fully grouted) can be downloaded from the RS2 Online Help page for Verification Manuals.

22 Bearing Capacity of Foundation on a Slope of Cohesive Soil Material

22.1 Problem Description

This problem considers a shallow footing supported by a slope composed of a purely cohesive soil and having angle of elevation β. The footing is assumed to be flexible and has width B = 1 m. The effect of the soil self-weight is neglected (i.e. no gravity loading). The collapse load q_u is determined for two cases in which the depth of the footing D_f is assumed to be zero and B respectively. In all cases the soil has cohesion c' = 50 kPa.

Figure 22.1 illustrates the problem schematically, while Figure 22.2 shows the footing as constructed in ***RS2***.

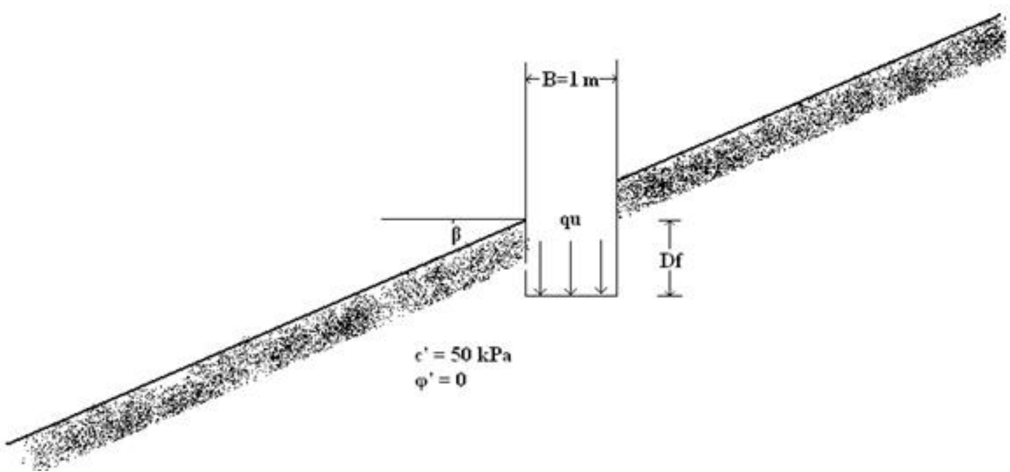

Figure 22.1: Shallow foundation on purely cohesive slope

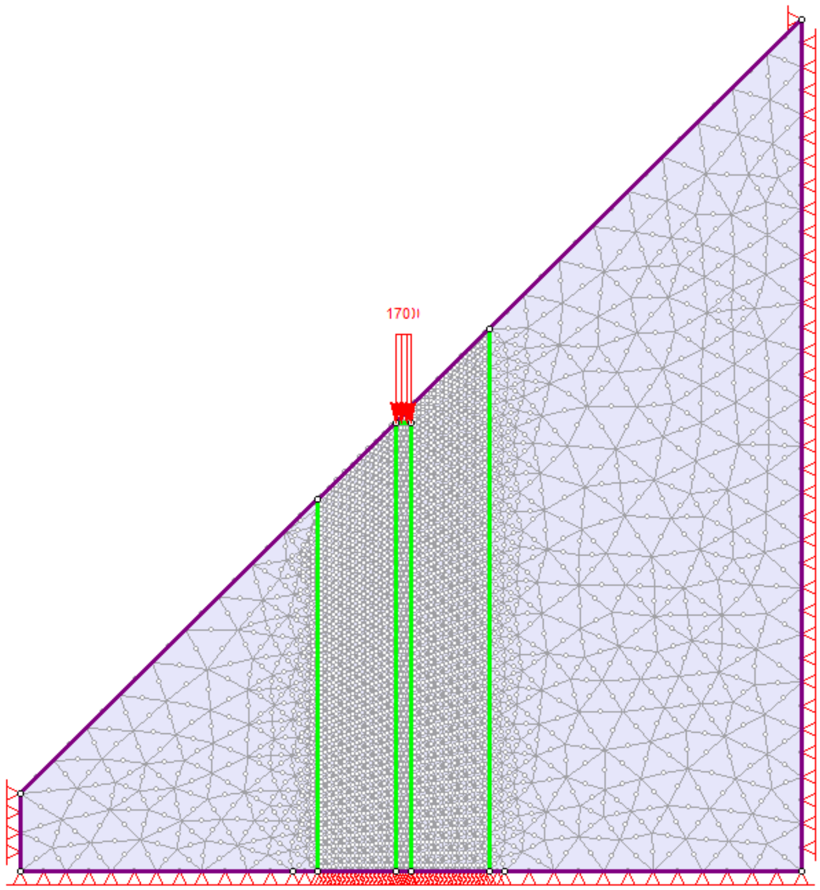

Figure 22.2: RS2 model of footing on slope

The model shown in Figure 22.2 uses a six-noded triangular mesh; the mesh is mapped in the region directly underlying the footing.

22.2 Analytical Solution

A theoretical solution for the ultimate bearing capacity of a shallow foundation located on the face of a slope was developed by Meyerhof (1957) [1]. Based on this solution, the ultimate bearing capacity can be expressed as:

$$q_u = cN_c \text{ (for purely cohesive soil, that is, } \varphi = 0\text{)} \tag{1}$$

and,

$$q_u = 0.5\gamma BN_c \text{ (for granular soil, that is c' = 0)} \tag{2}$$

where c is the undrained cohesion, and N_c , N_γ are the bearing capacity factors of the soil. Another term, called stability number (N_s) is a dimensionless number defined as:

$$N_s = \gamma \frac{H}{c} \tag{3}$$

In the present problem we have not considered the effect of unit weight of soil on the bearing capacity of soil, i.e. the effect of γ is neglected, and thus, the bearing capacity factors so obtained correspond to $N_s = 0$.

Figure 22.3 shows the distributions of N_c presented in [1]. The upper two lines on this graph correspond to the two cases studied in this problem.

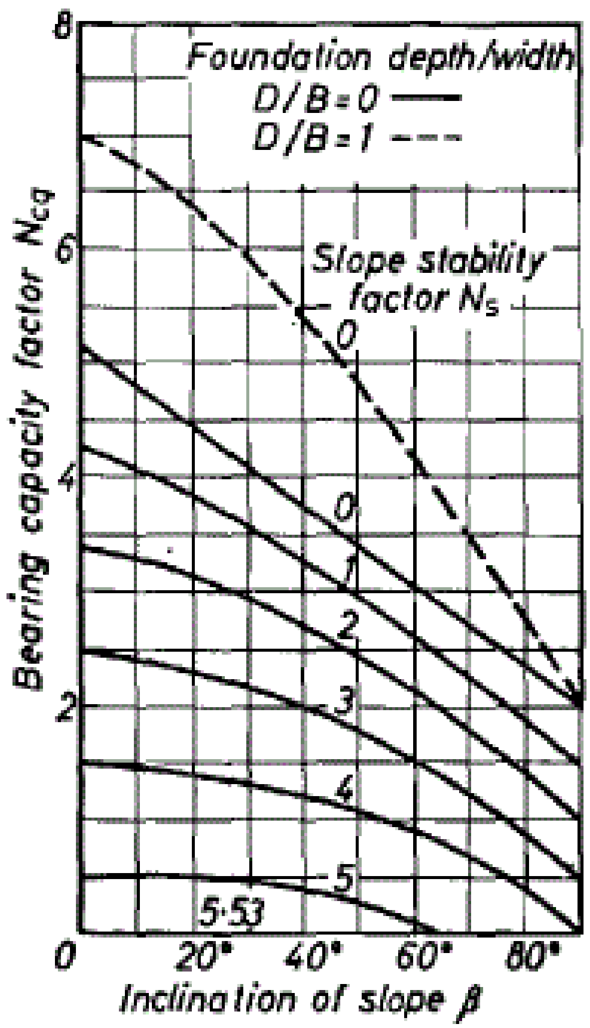

Figure 22.3: Variation of bearing capacity factor N_c with slope inclination [1].

22.3 Results

Figure 22.4 and Figure 22.5 compare the bearing capacity factors determined by ***RS2*** to the data extracted from Figure 22.3.

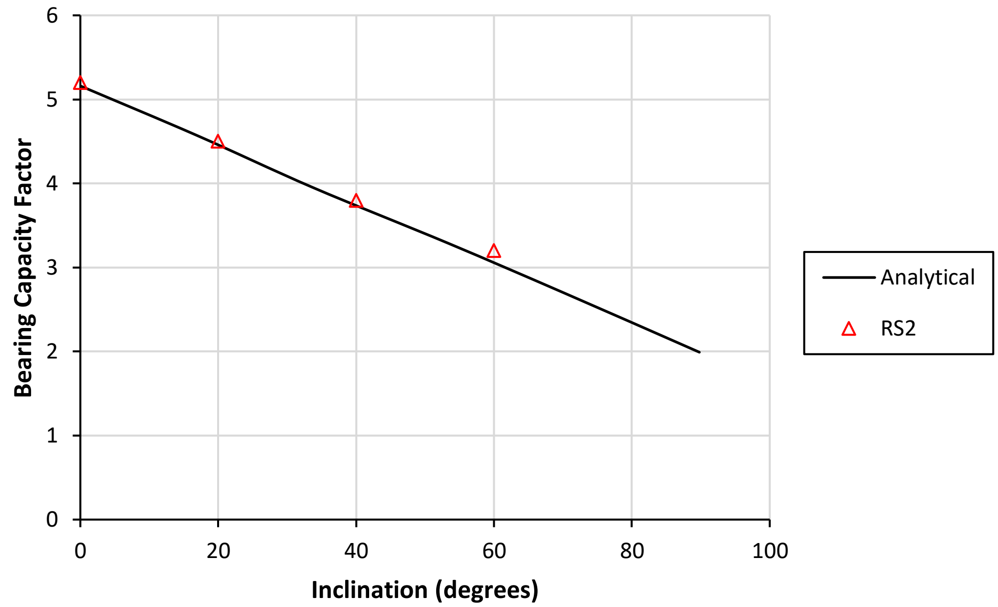

Figure 22.4: Bearing capacity factors for inclined foundations with zero depth (D_f = 0)

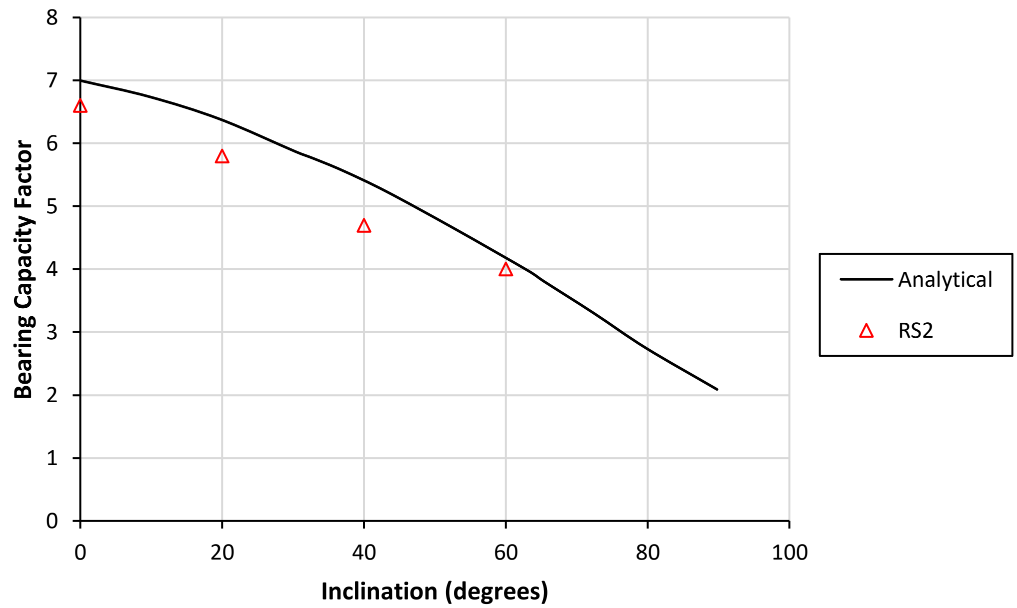

Figure 22.5: Bearing capacity factors for inclined foundations with $D_f = B$

22.4 References

1. Meyerhof, G. (1957), "The Ultimate Bearing Capacity of Foundations on Slopes". *Proceedings of the Fourth International Conference on Soil Mechanics and Foundation Engineering*, August 1957. pp. 384-86

22.5 Data Files

The input data files **stress#023_01.fez** to **stress#023_08.fez** can be downloaded from the RS2 Online Help page for Verification Manuals. Table 22.1 identifies the model parameters for each file.

Table 22.1: Input data files for shallow footing on incline

File	*Footing depth D_f*	*Slope inclination β*
stress#022_01.fez	0	0°
stress#022_02.fez	0	20°
stress#022_03.fez	0	40°
stress#022_04.fez	0	60°
stress#022_05.fez	*B*	0°
stress#022_06.fez	*B*	20°
stress#022_07.fez	*B*	40°
stress#022_08.fez	*B*	60°

23 Bearing Capacity of Undrained Footing on Clayey Soil

23.1 Problem Description

This problem considers the maximum bearing capacity of a shallow footing on a purely cohesive soil containing two discrete strata. Each stratum is assumed to be homogenous and isotropic, and to have Young's modulus E_i and cohesion c_i. (i= 1,2). A uniform strip load is applied at the material surface; the footing is assumed to be flexible. In the first case considered, $c_1 = c_2$ and the soil is effectively uniform. A surcharge is applied at the material surface to distinguish this case from the Prandtl's classic bearing capacity problem.

In the two subsequent cases, c_1 and c_2 are varied. In all cases, the width of the strip load B is 1 m and the depth of the upper stratum H is 0.5 m (i.e. H/B = 0.5). Figure 23.1 shows the model of the second case as constructed in ***RS2***. Note that half-symmetry is used.

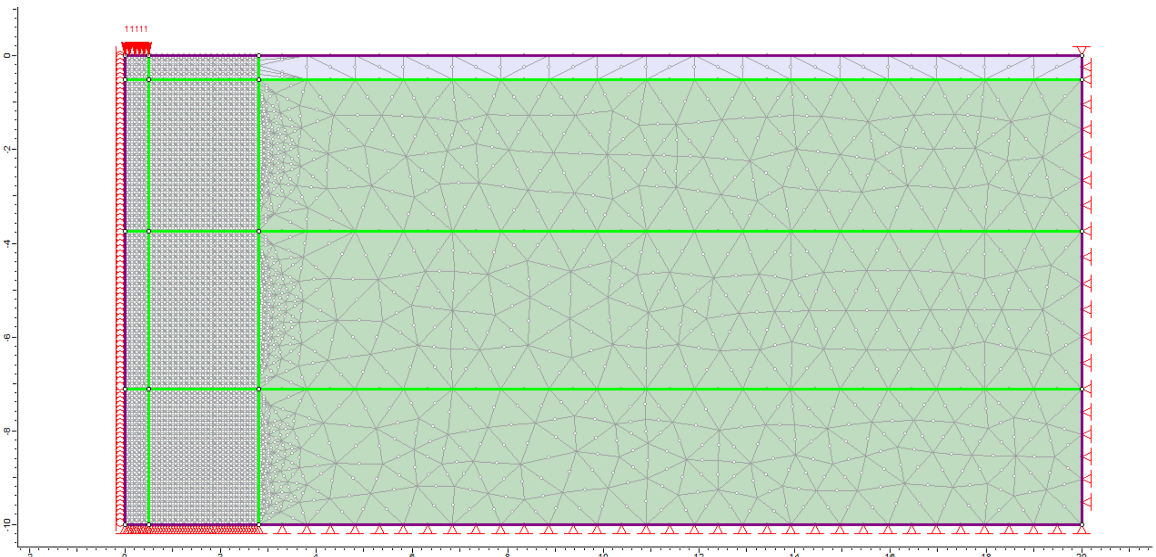

Figure 23.1: Strip loading on two-layered clay as modeled in *RS2*

The model in Figure 23.1 uses a six-noded triangular mesh; a mapped mesh is used in the vicinity of the load.

Table 23.1 summarizes model parameters for each case.

Table 23.1: Model parameters

Parameter	*Value*		
Young's modulus (E)	10000 kPa		
Poisson's ratio (v)	0.3		
Upper layer cohesion (c_1)	1 kPa	1 kPa	1 kPa
Lower layer cohesion (c_2)	1 kPa	0.667 kPa	0.4 kPa
Upper layer depth (H)	0.5 m		
Load width (B)	1 m		

23.2 Analytical Solution

The bearing capacity of a shallow strip footing on a clay layer can be written in the form

$$q_u = c_u N_c + q \qquad (1)$$

where N_c is a bearing capacity factor and q is a surcharge. For a surface strip footing without a surcharge, this equation reduces to

$$q_u = c_u N_c \qquad (2)$$

Note that the ultimate bearing capacity for undrained loading of a footing is independent of the soil unit weight. This follows from the fact that the undrained strength is assumed to be independent of the mean normal stress.

For the case of a layered soil profile, it is convenient to rewrite equation (2) in the form

$$N_c^* = \frac{q_u}{c_{u1}} \qquad (3)$$

Where c_{u1} is the undrained shear strength of the top layer, and N_c^* is the modified bearing capacity factor, which is a function of both H/B and c_{u1}/c_{u2}. The value of N_c^* is computed using the result from both upper and lower bound analyses for each ratio of H/B and c_{u1}/c_{u2}. For a homogeneous profile where $c_{u1}=c_{u2}$, N_c^* equals the well-known Prandtl's Wedge solution of $(2+\pi)$.

The lower bound solution is obtained by modeling a statically admissible stress field using finite elements with stress nodal variables, where stress discontinuities can occur at the interface between adjacent elements. Application of the stress boundary conditions, equilibrium equations and yield criterion leads to an expression of the collapse load which is maximized subjected to a set of linear constraint on the stresses.

An upper bound on the exact collapse load can be obtained by modeling a kinematically admissible velocity field. To be kinematically admissible, such a velocity field must satisfy the set of constraints imposed by compatibility, velocity boundary conditions and the flow rule. By prescribing a set of the velocities along a specified boundary segment, we can equate the power dissipated internally, due to plastic yielding within the soil mass and sliding of the velocity discontinuities, with the power dissipated by the external loads to yield a strict upper bound on the true limit load.

For this problem, upper and lower bounds can be found in [1] and are presented in Table 23.2 together with computational results from ***RS2*** .

23.3 Results

Figure 23.2, Figure 23.3 and Figure 23.4 show load-displacement data for the three cases studied. Results from ***RS2*** are in good agreement with the analytical bounds.

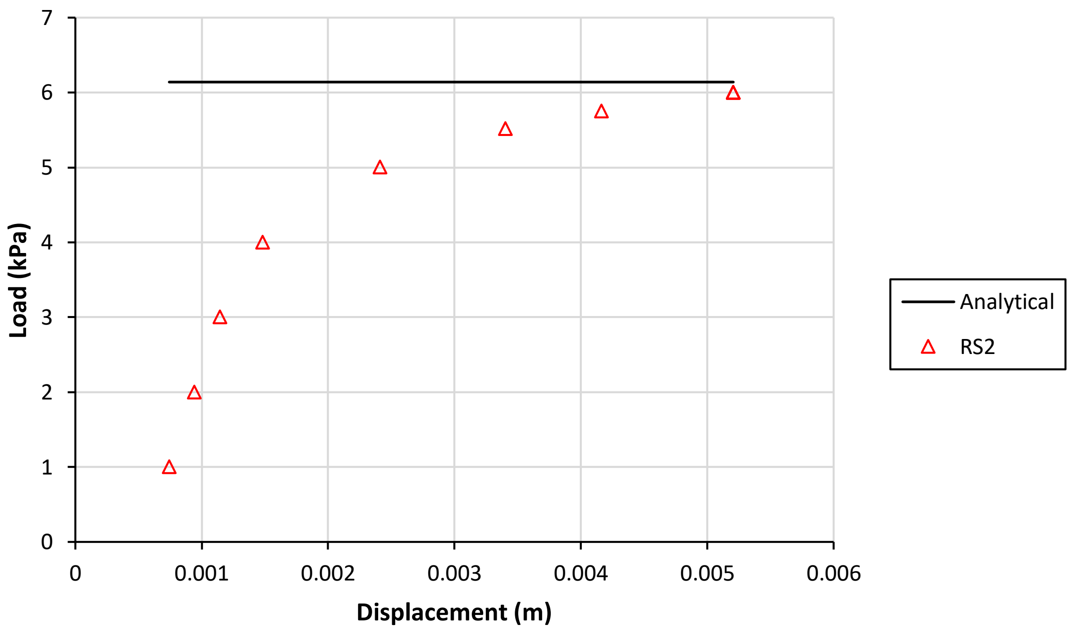

Figure 23.2: Load-displacement curve for $c_1 = c_2$

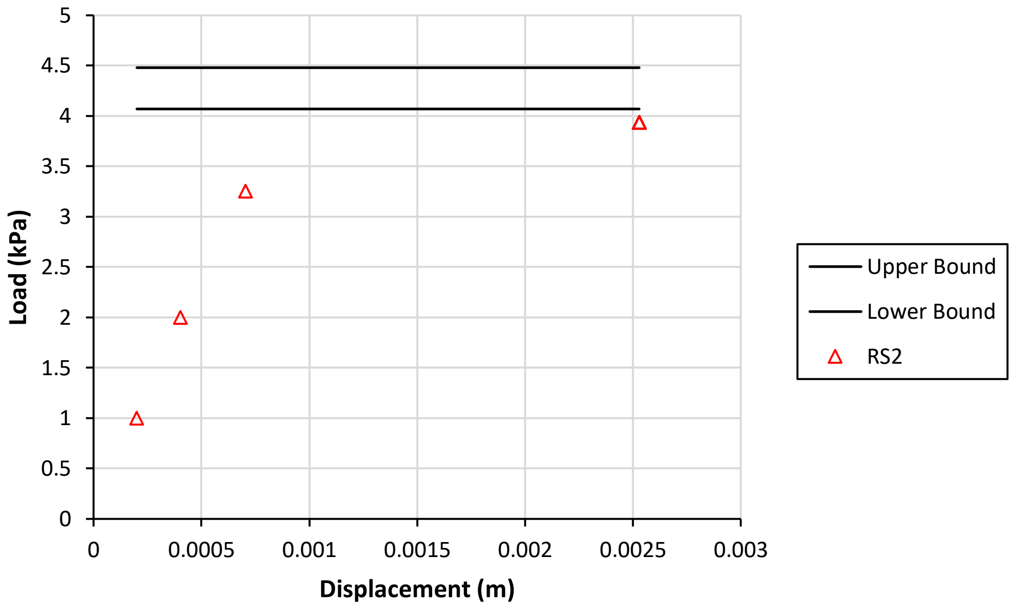

Figure 23.3: Load-displacement curve for $c_1/c_2 = 1.5$

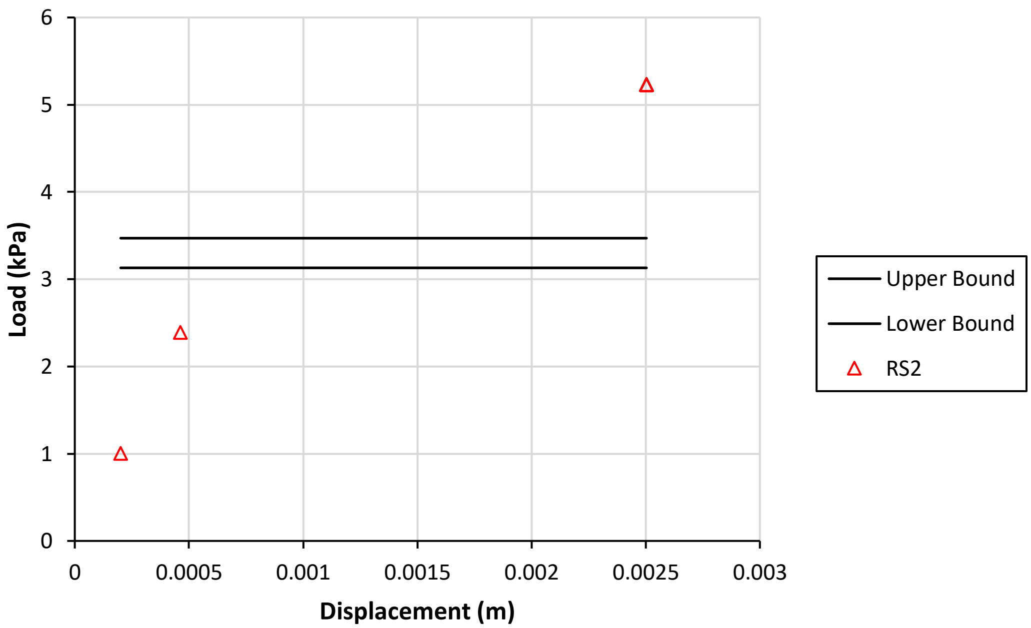

Figure 23.4: Load-displacement curve for $c_1/c_2 = 2.5$

Table 23.2: Theoretical and computational collapse loads for three cases

Collapse Loads			
c_1/c_2	Upper	Lower	*RS2*
1	6.14	6.14	6.15
1.5	4.48	4.07	4.4
2.5	3.47	3.13	3.2

23.4 References

1. Merifield, R.S., et al. (1999), “Rigorous plasticity solutions for the bearing capacity of two-layered clays”, *Geotechnique* 49, No. 4, pp. 471-490.

23.5 Data Files

The data files **stress#023_01** to **stress#024_03** can be downloaded from the RS2 Online Help page for Verification Manuals.

24 Passive Load Bearing Capacity of a Simple Retaining Wall

24.1 Problem Description

This problem considers the case of a simple retaining wall supporting a purely cohesive clay soil. An increasing passive horizontal load is applied to the wall until failure. The effect of the clay self-weight is neglected (i.e. no gravity loading). Three cases are considered; the adhesion at the soil surface is varied from zero (first case) to arbitrarily high (last case). To account for adhesion at the interface between the soil and wall, a stiff joint element is used in ***RS2***.

Figure 24.1 shows the problem as implemented in ***RS2***. Note the boundary conditions along the lower boundary – the bottom face of the clay is fixed while that of the wall is allowed to slip in the *x* direction.

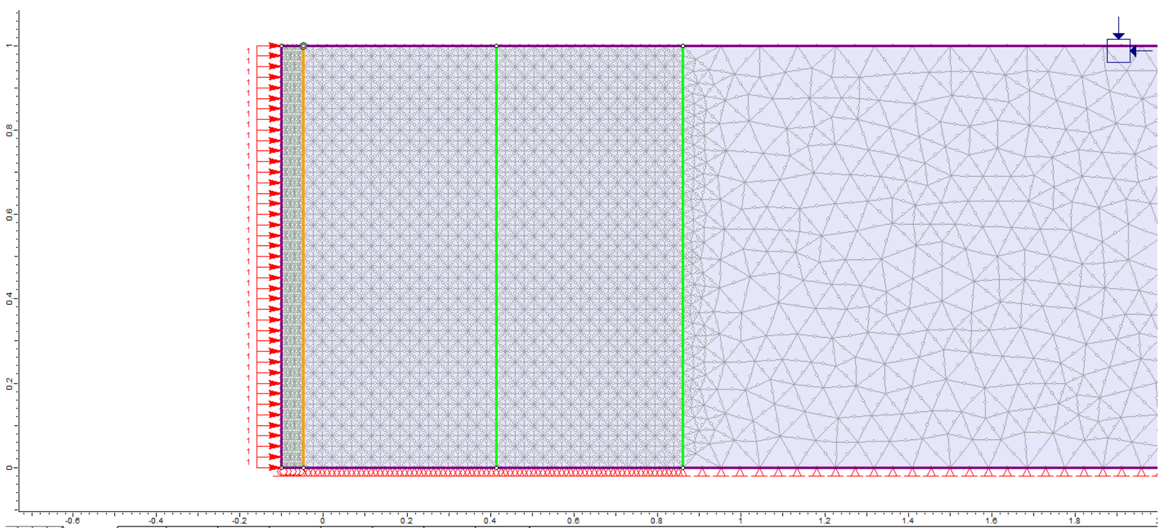

Figure 24.1: Model of retaining wall for second case in *RS2*

Table 24.1 summarizes the material and model parameters for each case.

Table 24.1: Model parameters

Parameter	*Value*		
Cohesion	1 kPa		
Young's modulus	10 000 kPa		
Wall height	1 m		
Poisson's ratio	0.3		
	Case 1	*Case 2*	*Case 3*
Joint cohesion (adhesion)	0	0.5 kPa	10 000 kPa

The ***RS2*** model shown in Figure 24.1 uses a six-noded triangular mapped mesh in the region close to the retaining wall, and an unmapped six-noded triangular mapped mesh elsewhere.

24.2 Analytical Solution

Published values for the critical passive loads in each case can be found in Chen (2007) [1]. These values are shown in Table 24.2 together with ***RS2*** results.

24.3 Results

Figure 24.2, Figure 24.3 and Figure 24.4 show load-displacement curves for each case. Results from ***RS2*** and ***RS3*** are compared to the analytical maxima in [1], being 2.00, 2.40 and 2.65 kPa respectively. Note that for the second (low-cohesion) case horizontal displacements in ***RS2*** are measured from the inner boundary of the joint separating the wall and soil (coordinates -0.048, 0.5).

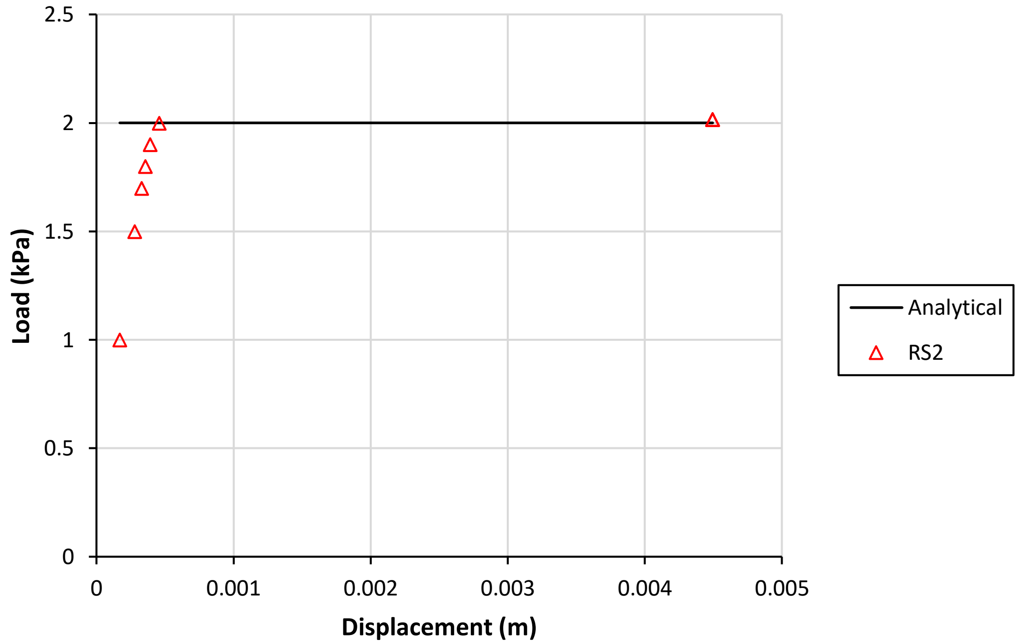

Figure 24.2: Load-displacement curve for first case (c = 0 kPa)

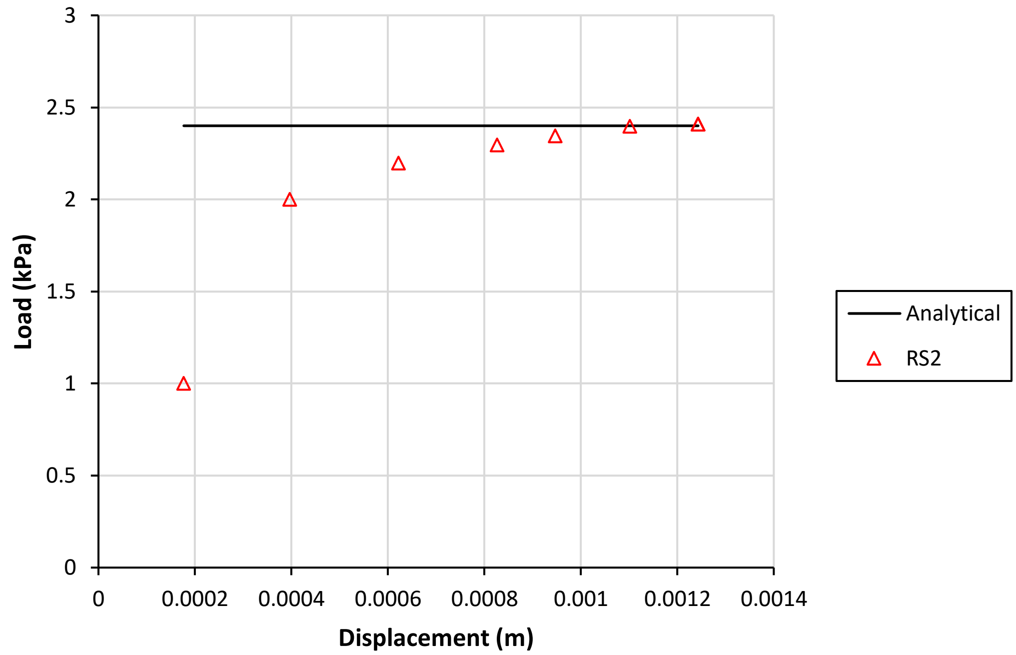

Figure 24.3: Load-displacement curve for second case (c = 0.5 kPa)

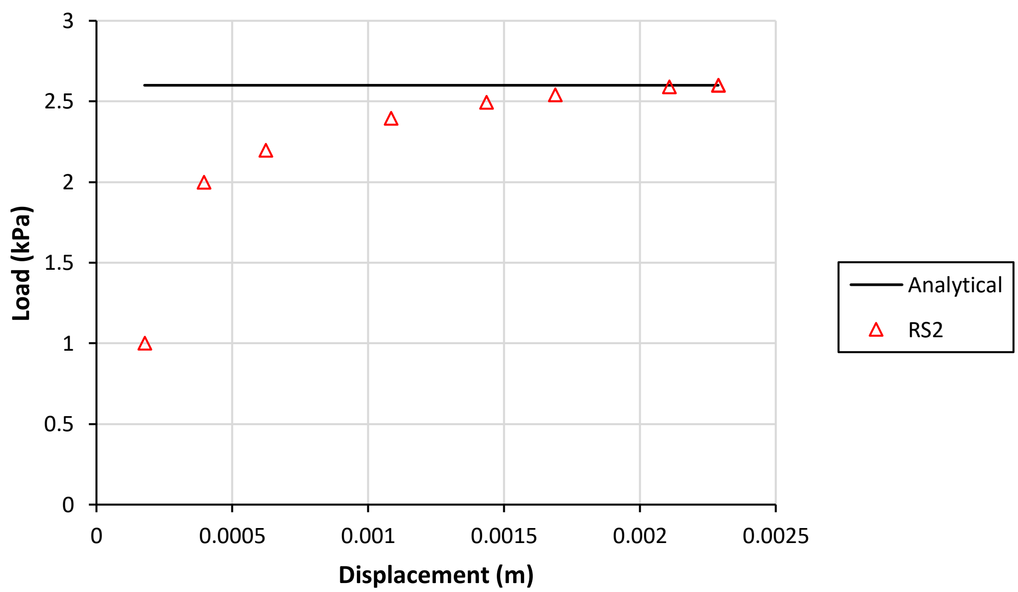

Figure 24.4: Load-displacement curve for third case (c = 10 000 kPa)

Table 24.2: Theoretical and computational collapse loads

Collapse Loads (kPa)		
Case	*RS2*	Analytical [1]
1	2.01	2
2	2.4	2.4
3	2.6	2.6

24.4 References

1. Chen, W. (2008). *Limit Analysis & Soil Plasticity*. J. Ross Publishing, Ft. Lauderdale, FL.

24.5 Data Files

The data files **stress#024_01.fez** to **stress#024_03** can be downloaded from the RS2 Online Help page for Verification Manuals.

25 Strip Loading on Elastic Gibson Soil

25.1 Problem Description

This problem considers the case of a linearly distributed load applied to an isotropic, elastic Gibson soil, in which Young's modulus increases linearly with depth. Table 25.1 summarizes pertinent model parameters. The model configuration and mesh for this problem are presented in Figure 25.1.

Table 25.1: Model parameters

Parameter	*Value*
Young's modulus at datum (E_0)	0.0001 kPa
Change in E per unit depth (α)	299 kPa/m
Poisson's ratio (v)	0.495
Applied load (P)	10 kPa

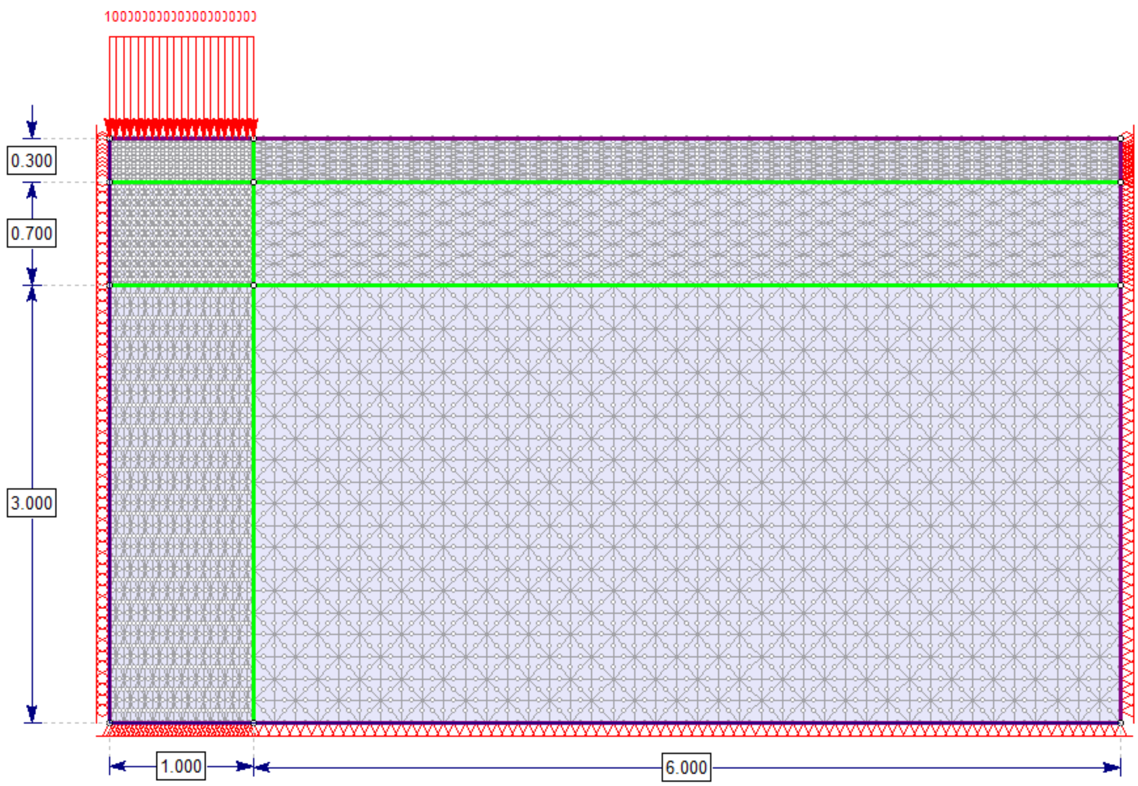

Figure 25.1: Model configuration

25.2 Analytical Solution

The analytical solution for settlement in this problem is described by Gibson (1967) [1]:

$$Settlement = \frac{P}{2\alpha}$$

where settlement is uniform beneath the load, P is the magnitude of the load, and α is the rate of increase of shear modulus with depth.

25.3 Results

Figure 25.2 shows the absolute vertical displacement contours for the model. Figure 25.3 magnifies the region directly underlying the load.

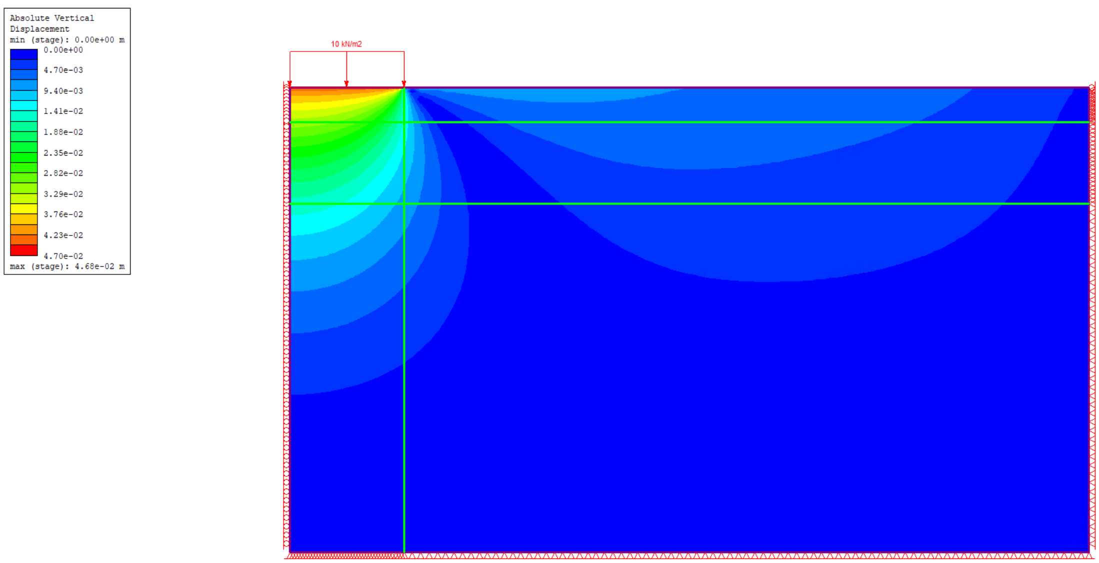

Figure 25.2: Absolute vertical displacement contour plot produced by *RS2*

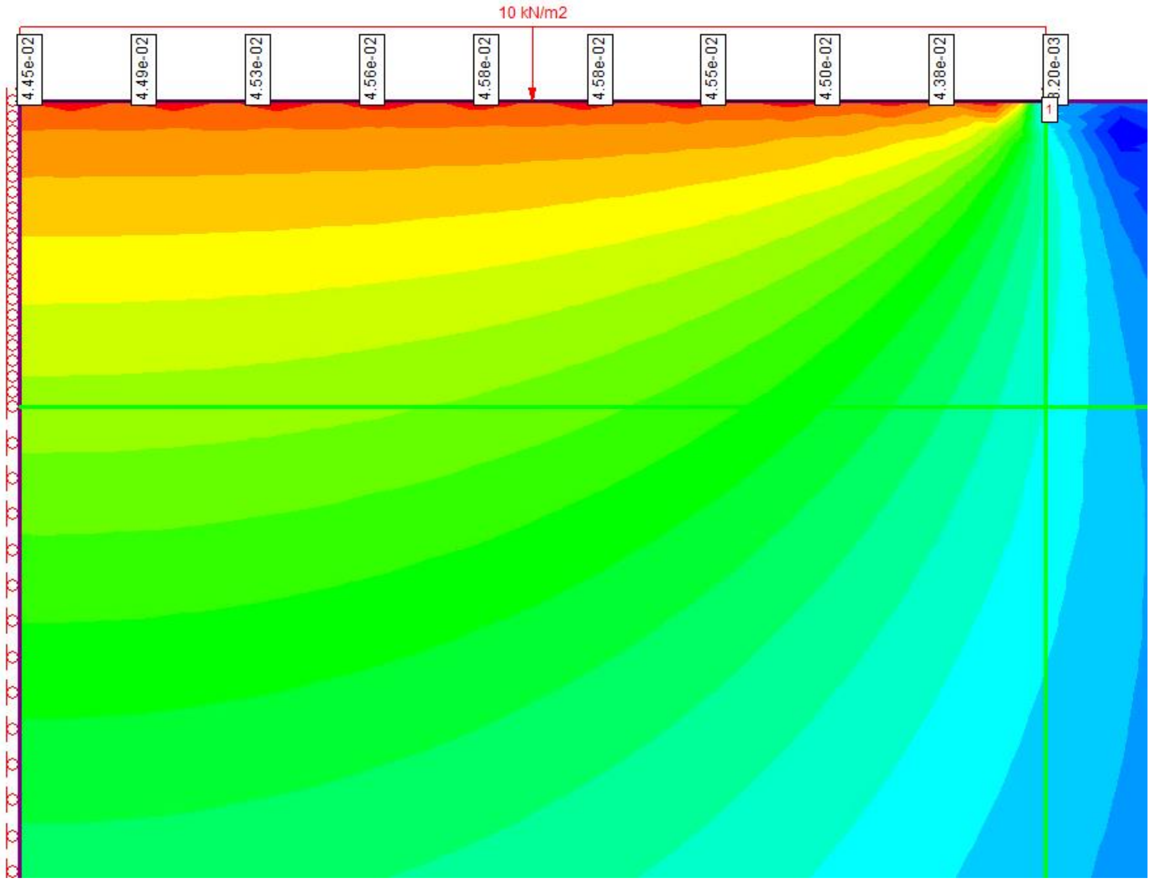

Figure 25.3: Vertical displacement contour plot immediately below strip load

RS2 predicts a maximum settlement of 46.8 mm. This is 6.4% lower than the analytical solution of 50 mm.

25.4 References

1. Gibson, R. E. (1967), "Some results concerning displacements and stresses in a non - homogeneous elastic half-space". *Geotechnique*, *17*(1), 58-67.

25.5 Data Files

The input data file **stress#025.fez** can be downloaded from the RS2 Online Help page for Verification Manuals.

26 Single- and Double-Jointed Rock Columns

26.1 Problem Description

This problem concerns a one-dimensional bar of elastic rock material subjected to a uniaxial load. The bar is loaded vertically with a uniform pressure P = 1 MPa and contains a joint at some distance y from the ground surface. In ***RS2***, this situation was modeled using a narrow two-dimensional column with the parameters shown in Table 26.1. The authors of [1] present an analytical solution to a very similar problem, as well as the results of their own analysis. Figure 26.1 shows the completed model in ***RS2***.

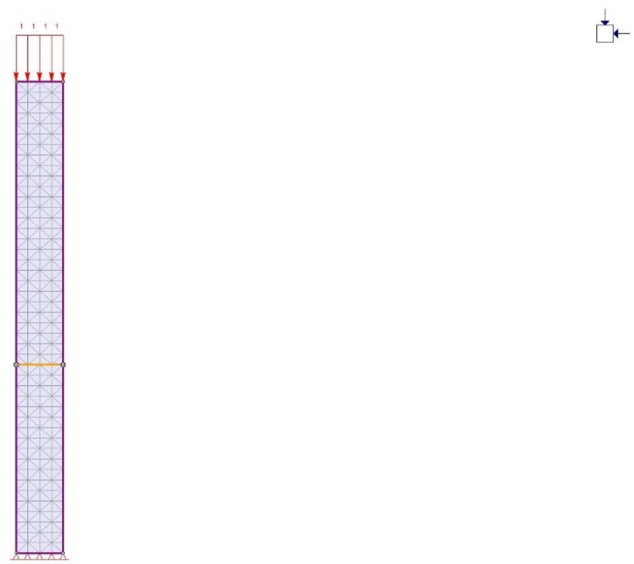

Figure 26.1: Jointed rock column as constructed in *RS2*

Table 26.1: Input parameters for one-dimensional rock column model

Parameter	***Value***
Young's modulus (E)	5000 MPa
Poisson's ratio (v)	0.01
Length (L)	1 m
Width (w)	0.1 m
Joint properties	
Height (h)	0.4 m
Normal stiffness (k_{nn})	100 GPa/m
End condition	Open

The case of a rock column containing two joints with differing properties was also considered. Figure 26.2 shows this situation as modeled in ***RS2*** and Table 26.2 summarizes the input parameters used. This second case was studied using extended finite element analysis (XFEM) in [2].

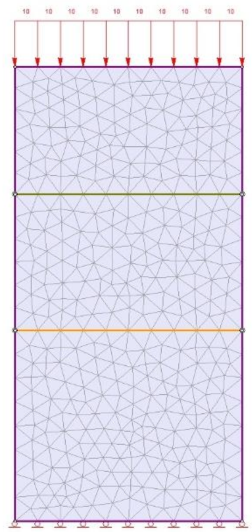

Figure 26.2: Two-jointed rock column as modeled in *RS2*

Table 26.2: Input parameters for two-jointed rock column model

Parameter	***Value***
Young's modulus (E)	5000 MPa
Poisson's ratio (v)	0.01
Length (L)	100 mm
Width (w)	50 mm
Applied pressure (P)	10 MPa
Joint 1 properties	
Height (h_1)	42 mm
Normal stiffness (k_{nn1})	30 GPa/m
Shear stiffness (k_{s1})	100 GPa/m
Cohesion (c_1)	2 MPa
Friction angle (ϕ_1)	30°
End condition	Open
Joint 2 properties	
Height (h_2)	72 mm
Normal stiffness (k_{nn2})	9 GPa/m
Shear stiffness (k_{s2})	30 GPa/m
Cohesion (c_2)	1 MPa
Friction angle (ϕ_2)	20°
End condition	Open

26.2 Analytical Solution

A modified version of the analytical solution presented in [1] was used to predict the behaviour of the ***RS2*** model. The displacement of the bar at some height y is given by:

$$\mu(y) = \frac{Py}{E} + \sum H\left(\frac{P}{k_m}\right)$$

where P is the applied pressure, E is the elastic modulus of the column, and k_{nn} is the normal stiffness of the joint. H is a form of the Heaviside function; it takes on the value of its argument when y exceeds the height of the joint and otherwise returns zero.

26.3 Results

Figure 26.3 shows the displacement field of the single-jointed bar along its vertical axis as produced by ***RS2***. The analytical solution is shown for reference.

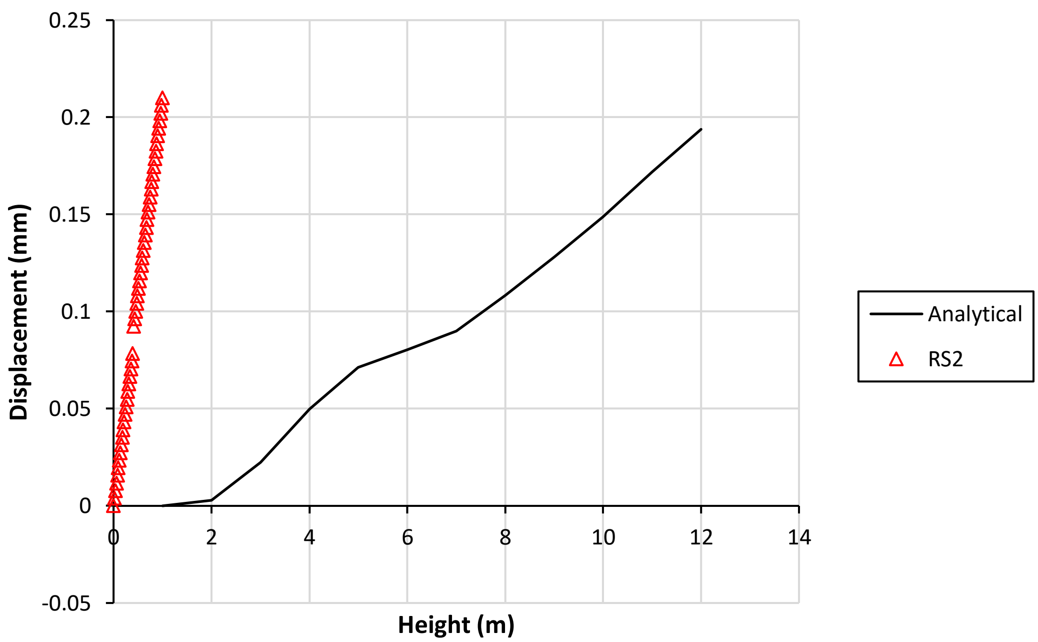

Figure 26.3: Analytical and numerical displacement fields along vertical axis

The discontinuity due to the joint at $y = 0.4$ has a magnitude of approximately 0.01 mm. Evidently, the results from ***RS2*** are in good agreement with the analytical approach.

Figure 26.4 shows the vertical displacement of the bar containing two joints, as well as the analytical solution.

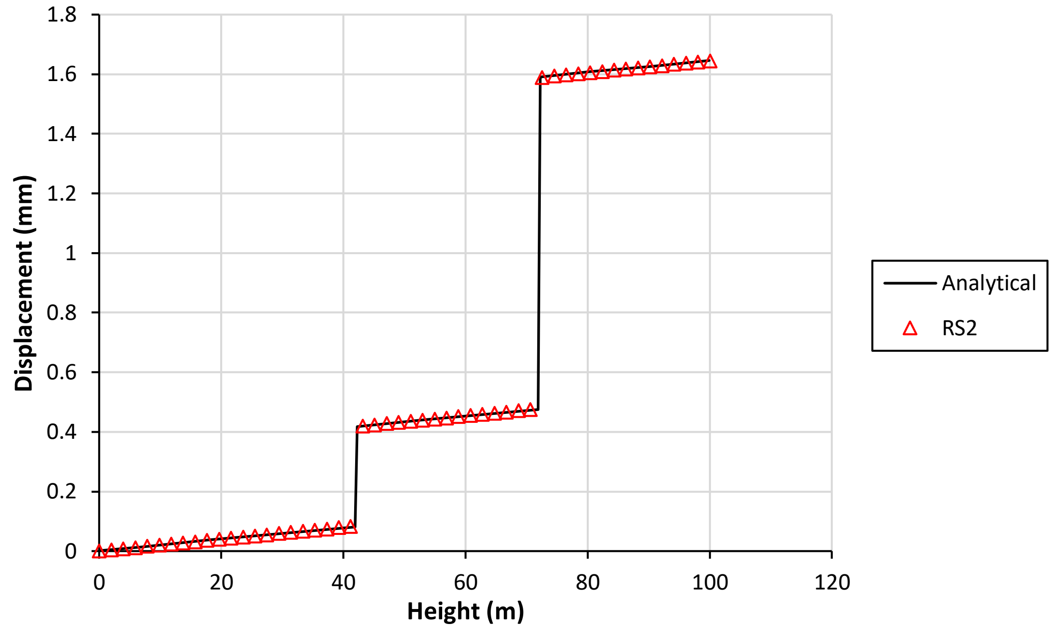

Figure 26.4: Analytical and numerical displacement fields along vertical axis of two-jointed rock column

Again, the ***RS2*** results are very similar to the analytical solution. Note the larger discontinuity at y = 72 mm due to the weaker Joint 2.

26.4 References

1. Deb, Debasis & Das. Kamal Ch (2009), "Extended finite element method for the analysis of cohesive rock joint". *Journal of Scientific and Industrial Research*, Vol. 68, pp. 575-583.

2. Deb, Debasis & Das. Kamal Ch (2010), "Extended finite element method for the analysis of discontinuities in rock masses". *Geotech. Geol. Eng.*, Vol. 28, pp. 643-659

26.5 Data Files

The input data files **stress#026_01.fez** and **stress#026_02.fez** can be downloaded from the RS2 Online Help page for Verification Manuals.

27 Triaxial Loading of a Jointed Rock Column

27.1 Problem Description

This problem concerns an elastic rock column containing a single planar joint and subjected to triaxial loading. In ***RS2***, this situation is modeled two-dimensionally as shown in Figure 27.1. The compressive strength of the column for various angles of the joint is of interest, assuming joint slip to be the mode of failure. Table 27.1 summarizes the material and joint properties used in the model. Two cases are considered; both the secondary principal (horizontal) field stress and joint cohesion are varied. The shear strength of the joint is defined using the Mohr-Coulomb criterion. This problem is solved using an alternate computational method in [1].

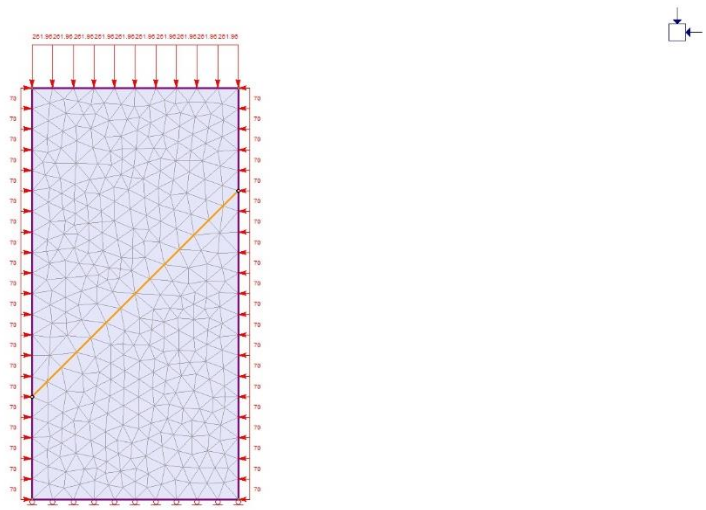

Figure 27.1: *RS2* model of a jointed rock column with σ_3 = 70 MPa and a joint angle of 45°

Table 27.1: Model parameters

Parameter	***Case 1***	***Case 2***
Young's modulus (rock)	100 GPa	
Aspect ratio of column	2:1	
Poisson's ratio (rock)	0.3	
Secondary stress (σ_3)	35 MPa	70 MPa
Joint properties		
Cohesion (c)	11.135 MPa	0.2749 MPa
Friction angle (ϕ)	30°	
Normal stiffness	100 GPa	
Shear stiffness	100 GPa	

27.2 Analytical Solution

According to [1], the primary (vertical) stress required for joint slip is given by the following equation. Failure stress is a function of the friction angle and cohesion of the joint, as well as the joint angle β. Note that [1] defines β with reference to the horizontal axis; this convention will be followed in this document.

$$\sigma_1 = \sigma_3 + \frac{2(\sigma_3 \tan\phi + c)}{(1 - \tan\phi \cot\beta)\sin 2\beta}$$

where c and ϕ are the cohesion and friction angle of the joint and σ_3 is the secondary principal stress.

27.3 Results

The results of ***RS2*** computations for both test cases are shown in Figure 27.2 and Figure 27.3. ***RS2*** is in close agreement with both the analytical solution and the results obtained from XFEM modeling in [1]. A maximum value of $\beta = 63^\circ$ was tested. At higher joint angle values, the shear plane intersected the top and bottom surfaces of the column; a higher column aspect ratio would allow larger joint angles to be tested. As the compressive strength of each column was determined by applying a progressively finer range of stresses, the ***RS2*** strength results are in the form of a small range of values. Both upper and lower limits of this range are plotted.

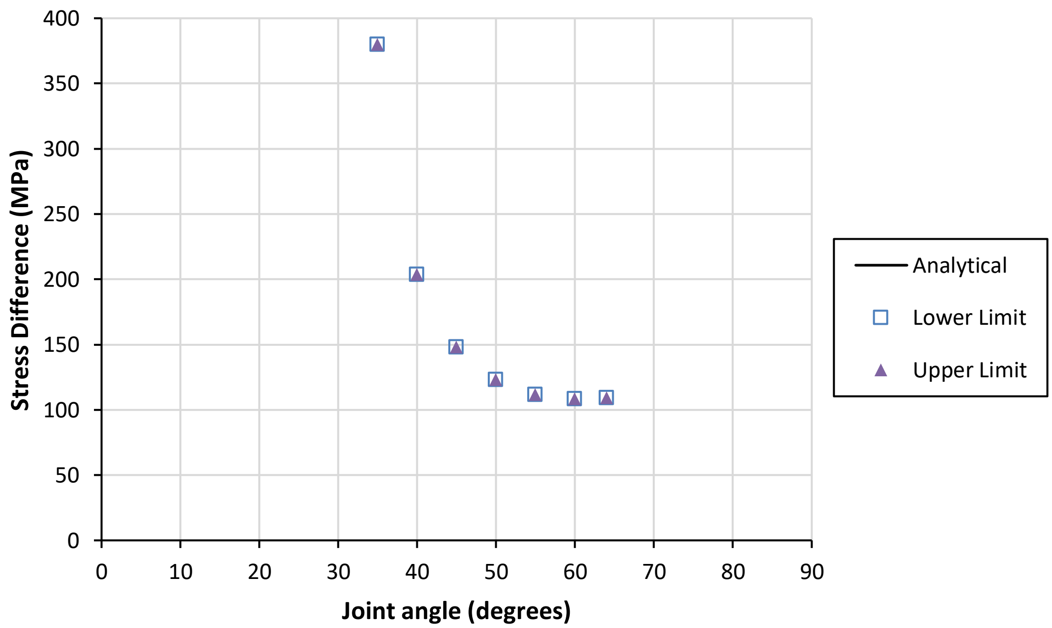

Figure 27.2: Case 1 - Difference between principal stresses (σ_1 - σ_3) as determined analytically and using *RS2*

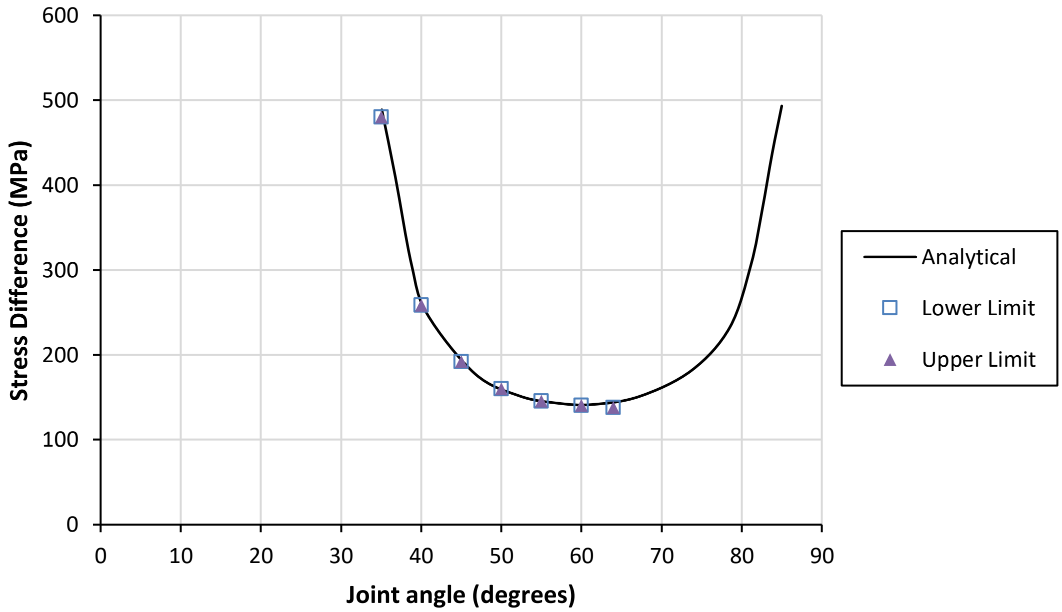

Figure 27.3: Case 2 - Difference between principal stresses (σ_1 - σ_3) as determined analytically and using *RS2*

27.4 References

1. Deb, Debasis & Das. Kamal Ch (2010), "Extended finite element method for the analysis of discontinuities in rock masses". *Geotech. Geol. Eng.*, Vol. 28, pp. 643-659

27.5 Data Files

The input data file **stress#027.fez** can be downloaded from the RS2 Online Help page for Verification Manuals.

28 Intersection of a Joint Plane and Tunnel

28.1 Problem Description

This problem concerns a circular excavation intersecting a single joint in an infinite elastic rock mass. The joint is assumed not to slip, and the minimum friction angle of the joint required for this condition to hold is calculated. Figure 28.1 shows the problem as implemented in ***RS2***. This situation has previously been analyzed using alternate computational methods in [1].

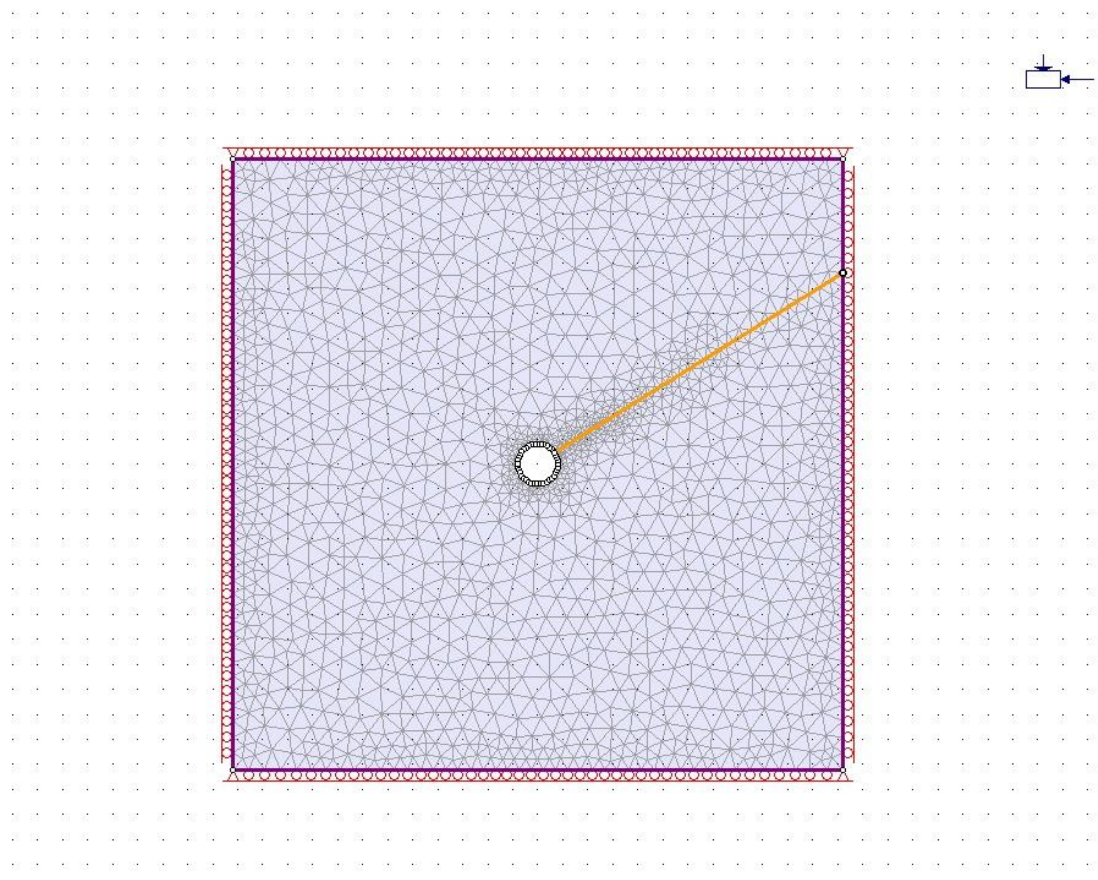

Figure 28.1: Tunnel with intersecting joint as modeled in *RS2*

Table 28.1 summarizes the material and joint properties supplied to ***RS2***. A six-noded triangular mesh was used; the discretization density was increased in the region surrounding the tunnel.

Table 28.1: Model parameters

Parameter	*Value*
Young's modulus (*E*)	5000 MPa
Poisson's ratio (*v*)	0.3
Length (*L*)	122 m
Width (*w*)	122 m
Tunnel radius (*a*)	4 m
Field stress (horizontal)	4 MPa
Field stress (vertical) (*p*)	8 MPa
Joint properties	
Normal stiffness/shear stiffness	100 GPa/m
End condition	Open
Angle of inclination (*β*)	32°

28.2 Analytical Solution

Assuming no slip occurs, the normal and shear stresses along the joint can be predicted using the Hirsch equations as follows:

$$\sigma_n = \frac{p}{2}\left((1+k)\left(1+\frac{a^2}{r^2}\right)+(1-k)\left(1+\frac{3a^4}{r^4}\right)\cos 2\beta\right)$$

$$\tau = \frac{p}{2}\left((1-k)\left(1+\frac{2a^2}{r^2}-\frac{3a^4}{r^4}\right)\sin 2\beta\right)$$

where *p* is the primary field stress (8 MPa), and *k* is the field stress ratio (in this case 0.5). Of primary interest is the stress ratio τ/σ_n, from which the minimum angle of friction without joint slip can be calculated.

Because these equations assume a homogenous material and do not account for the presence of a joint, when calculating normal and shear stresses along the joint in ***RS2*** it was necessary to use a material query as opposed to a joint query. The axial stresses obtained from the joint query were then converted to normal and shear stresses using the stress transformation equations:

$$\sigma_n = \frac{1}{2}(\sigma_{xx}+\sigma_{yy})+\frac{1}{2}(\sigma_{yy}-\sigma_{xx})\cos 2\alpha - \tau_{xy}\sin 2\alpha$$

$$\tau = \tau_{xy}\cos 2\alpha + \frac{1}{2}(\sigma_{yy}-\sigma_{xx})\sin 2\alpha$$

28.3 Results

Figure 28.2 shows the stress ratio τ/σ_n as computed by ***RS2***, which is in good agreement with the analytical solution.

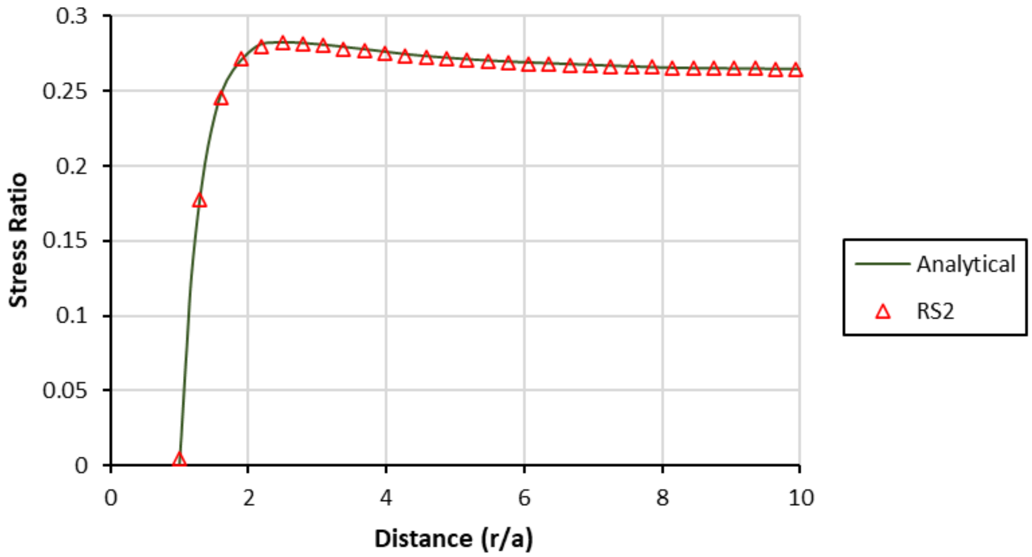

Figure 28.2: Variation of stress ratio with relative distance from hole centre

From Figure 28.2 it can be determined that the maximum stress ratio is approximately 0.283. Assuming negligible cohesion and according to the equation below, this corresponds to a critical friction angle of 15.8°.

$$\tan\phi = \frac{\tau}{\sigma_n}$$

28.4 References

[1] Deb, Debasis & Das. Kamal Ch (2010), "Extended finite element method for the analysis of discontinuities in rock masses". *Geotech. Geol. Eng.*, Vol. 28, pp. 643-659

28.5 Data Files

The input data file **stress#028.fez** can be downloaded from the RS2 Online Help page for Verification Manuals.

29 Non-Linear Behavior of Sand (Duncan-Chang Model)

29.1 Problem Description

This problem demonstrates the applicability of Duncan-Chang model in simulation of nonlinear behavior of soils. The nonlinear behavior of dense and loose Silica sand in triaxial tests is the focus of this example. The experimental results are taken from the article by Duncan and Chang (1970). The stress paths of the experiments include loading, unloading and reloading of the samples. The Duncan-Chang model parameters for the dense and loose Silica sands are presented in Table 29.1.

Table 29.1: Duncan-Chang model parameters

Parameter	*Dense Silica Sand*	*Loose Silica Sand*
Modulus number (K_E)	2000	295
Unloading Modulus(K_{ur})	2120	1090
Modulus exponent (n)	0.54	0.65
Failure ratio (R_f)	0.91	0.90
Cohesion (c)	0 kPa	0 kPa
Friction angle (ϕ)	36.5°	30.4°
Poisson's ratio (v)	0.32	0.32

29.2 *RS2* Model

The drained compressive triaxial tests of the sample were modeled in ***RS2*** using a single 8-noded quadrilateral element. The simulation is axisymmetric. The deviatoric stress is generated in the sample in a load-control process. The axial load is increased in a number of stages, and automatic load stepping is considered in each stage. The mesh, boundary conditions, and an example of the applied axial and radial loads used are shown on Figure 29.1.

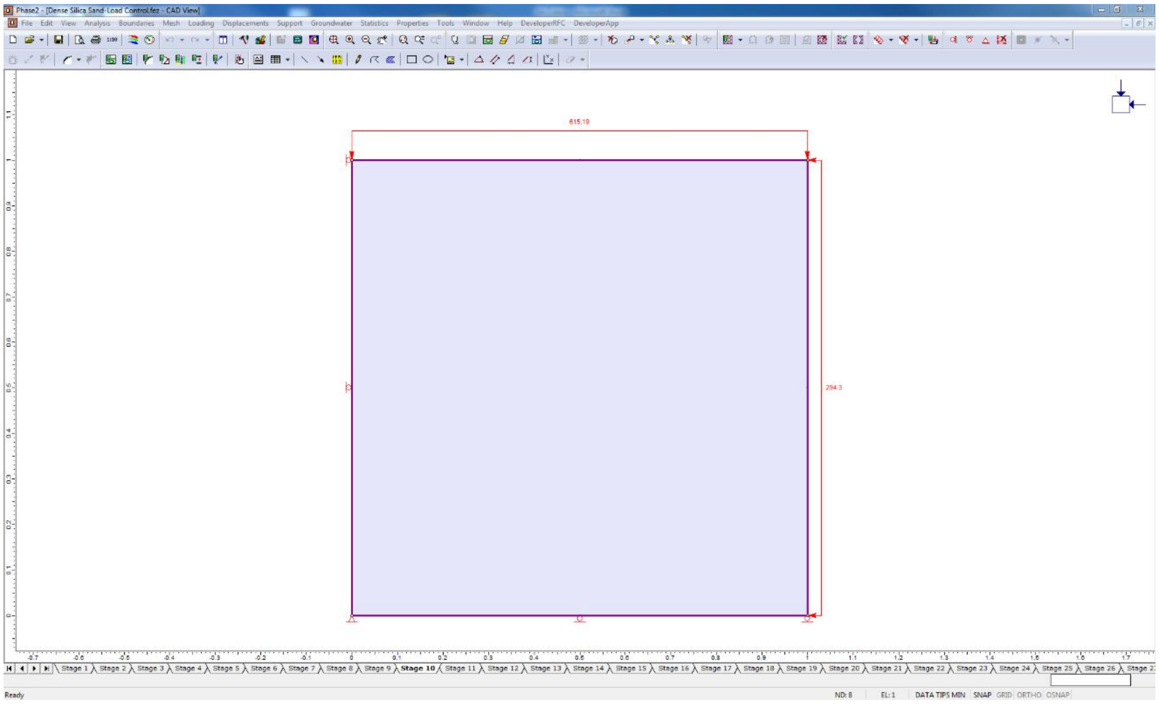

Figure 29.1: Mesh, boundary conditions and loads for axisymmetric *RS2* analysis

29.3 Results

Figure 29.2 and Figure 29.3 show the plots of $\varepsilon_a - q$ obtained in numerical simulations using ***RS2*** in comparison with the observed behavior and the numerical results obtained by Duncan and Chang (1970). There is a good agreement between the experimental data and the numerical results. The difference between the numerical results of ***RS2*** and the ones presented by Duncan and Chang is because in ***RS2*** the elastic parameters, from load step *n* to *n+1*, are calculated based on the state of material at step *n* while in the latter they are averaged over the increment.

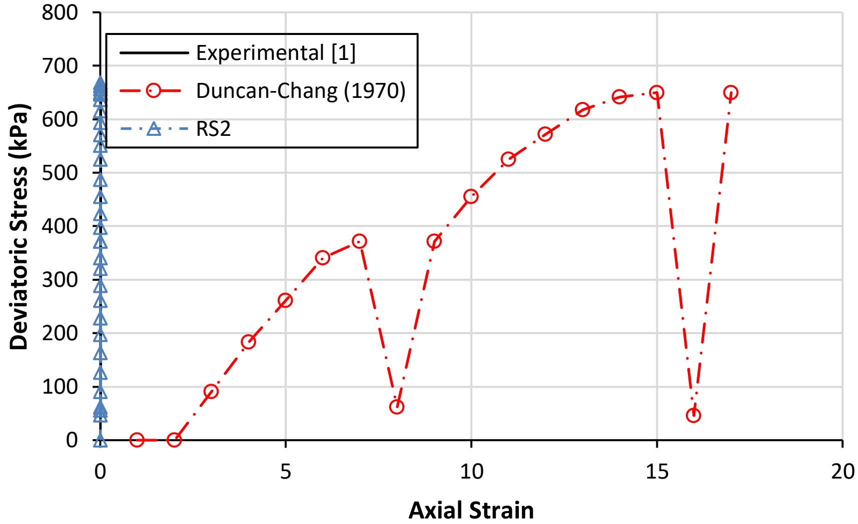

Figure 29.2: Triaxial test on dense Silica sand, variation of deviatoric stress with axial strain

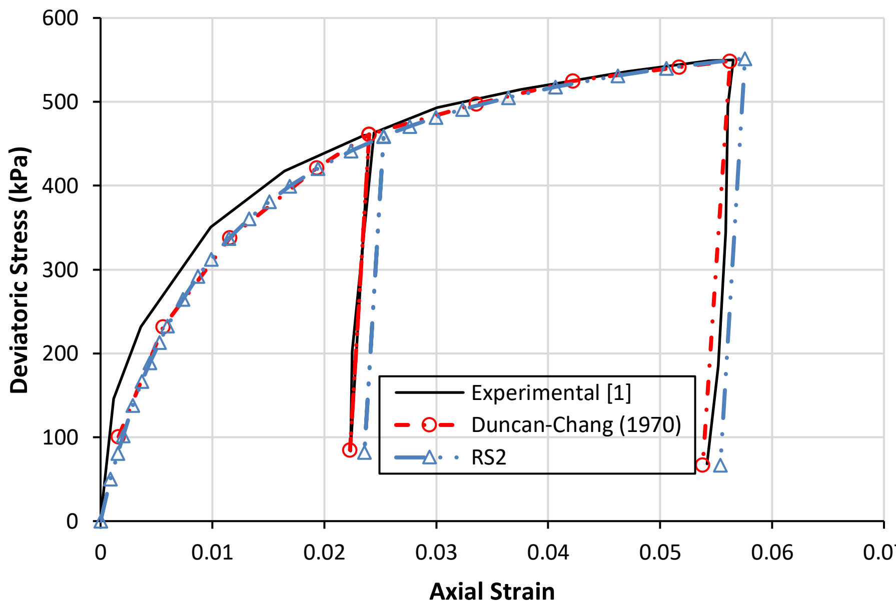

Figure 29.3: Triaxial test on loose Silica sand, variation of deviatoric stress with axial strain

29.4 References

1. J. M. Duncan and C. Y. Chang (1970), "Nonlinear analysis of stress and strain in soils", J. of Soil Mech. and Foundation Division, ASCE, 96 (SM5), pp. 1629-1653.

30 Cylindrical Hole in an Elastic Brittle-Plastic Infinite Mohr-Coulomb Medium

30.1 Problem Description

This problem addresses the case of a cylindrical tunnel in an infinite Mohr-Coulomb medium subjected to a uniform compressive in-situ stress field. Plane strain condition is assumed.

Figure 3.1Figure 30.1 shows the model configuration and Table 30.1 summarizes the model parameters.

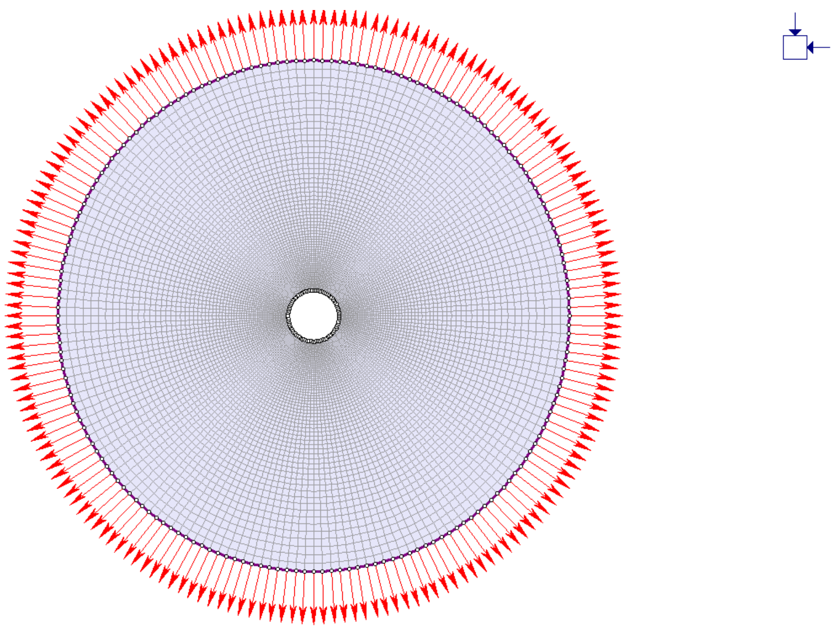

Figure 30.1: Circular tunnel in Mohr-Coulomb medium as constructed in *RS2*

Table 30.1: Model parameters

Model Specification and Material Properties	***Value***
Hole radius (r_o)	2 m
Young's modulus (E)	40000 MPa
In-situ stress field (q)	30 MPa
Poisson's ratio (v)	0.2
Tensile Strength (peak, residual)	10 MPa
Friction angle (ϕ) (peak, residual)	30°
Cohesion (c) (peak, residual)	30, 5 MPa
Dilation angle (ψ)	30°

The ***RS2*** model constructed uses a radial mesh with 12060 4-noded quadrilateral elements and an in-situ hydrostatic stress field of 30 MPa. The opening is discretized into

90 segments; infinite elements are used on the external boundary, which is located 40 m from the centre of the hole.

30.2 Analytical Solution

According to [1], the radial and tangential stresses in the elastic zone are given by:

$$\sigma_r = q - (\bar{r}/r)^2 \left[(k-1)q + \sigma_c\right] / (k+1)$$

$$\sigma_c = q + (\bar{r}/r)^2 \left[(k-1)q + \sigma_c\right] / (k+1)$$

where

$$k = \frac{1+\sin\phi}{1-\sin\phi}$$

$$\sigma_c = \frac{2c\cos\phi}{1-\sin\phi}$$

$\bar{r}$ = location of the elastic-plastic boundary

In the plastic (yielded) region, the radial and tangential stresses are given by:

$$\sigma_r = (p + p')(r/r_o)^{k-1} - p'$$

$$\sigma_\theta = k(p + p')(r/r_o)^{k-1} - p'$$

where

$$p' = \sigma'_c / (k-1)$$

$$k = \frac{1+\sin\phi}{1-\sin\phi}$$

p = stress at r = r_o

30.3 Results

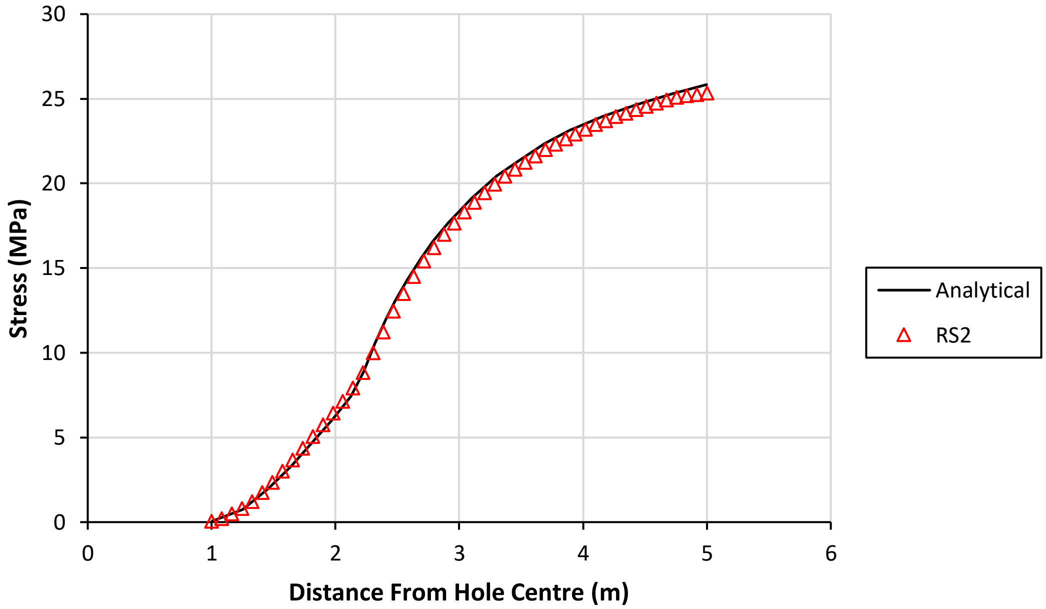

Figure 3.2

Figure 30.2 and Figure 30.3 compare the stress distributions calculated by ***RS2*** with the analytical solution. Figure 30.4 compares the radial displacements calculated by ***RS2*** with the analytical solution.

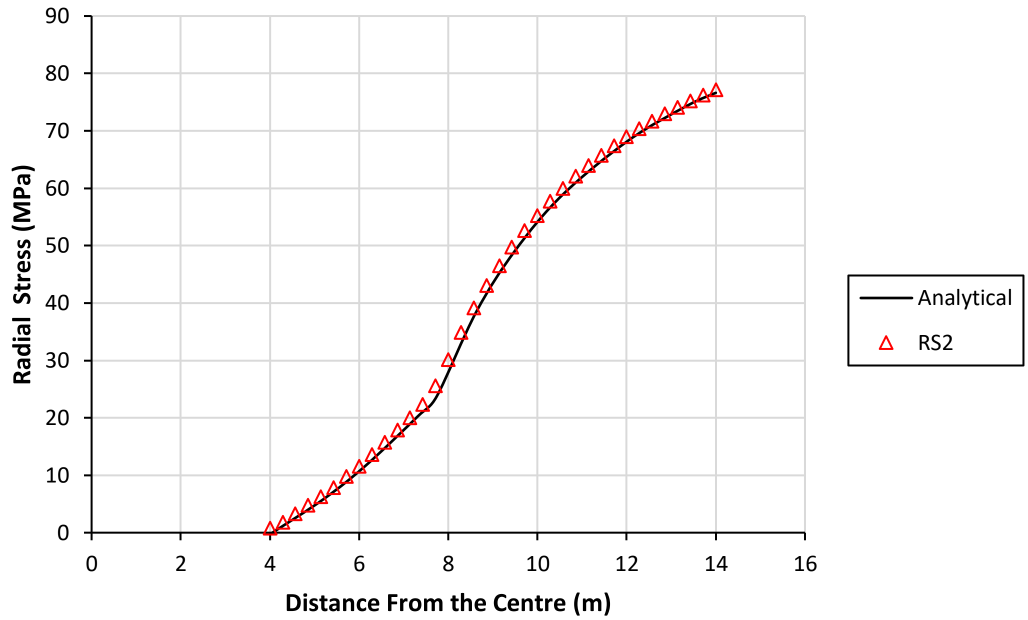

Figure 30.2: Comparison of radial stress distributions

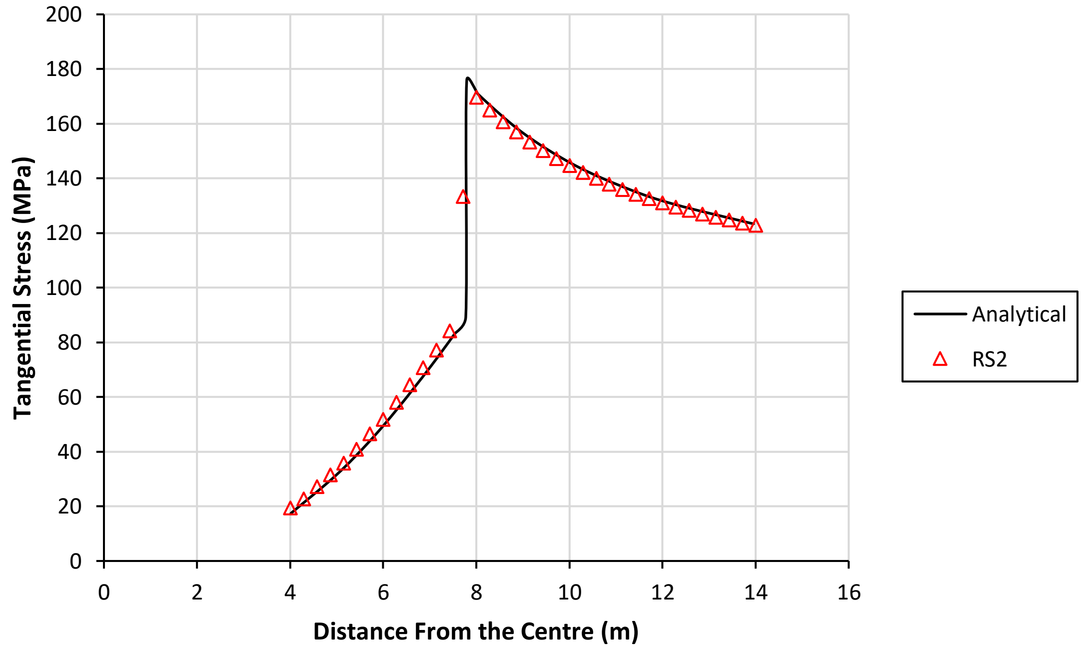

Figure 30.3: Comparison of tangential stress distributions

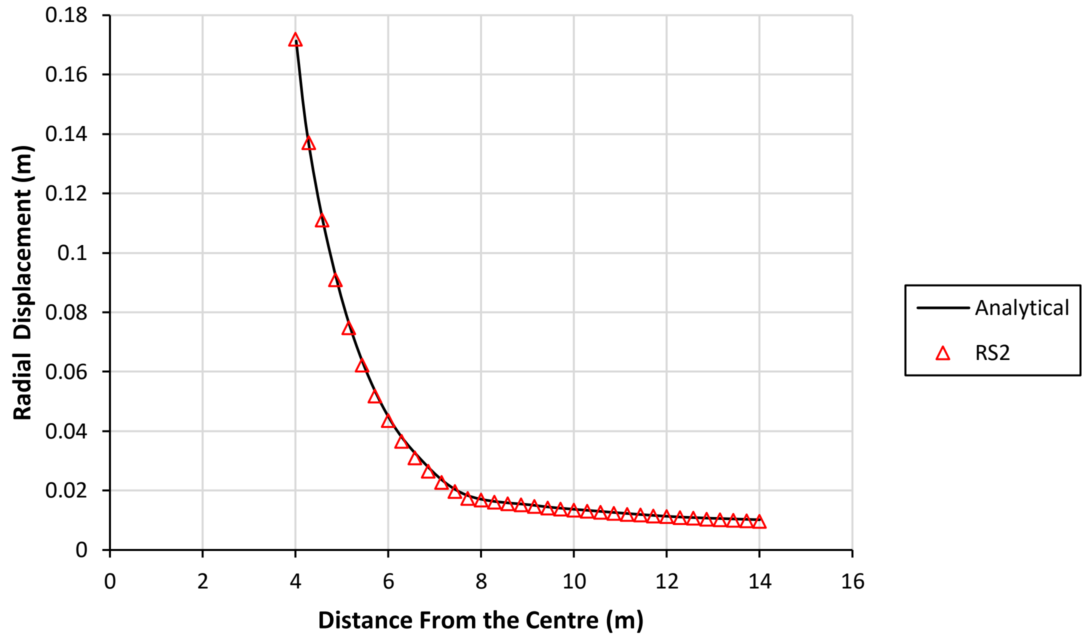

Figure 30.4: Comparison of radial displacements

Figure 30.5, Figure 30.6, and Figure 30.7 illustrate the radial stress, tangential stress, and displacement contour plots produced by ***RS2***.

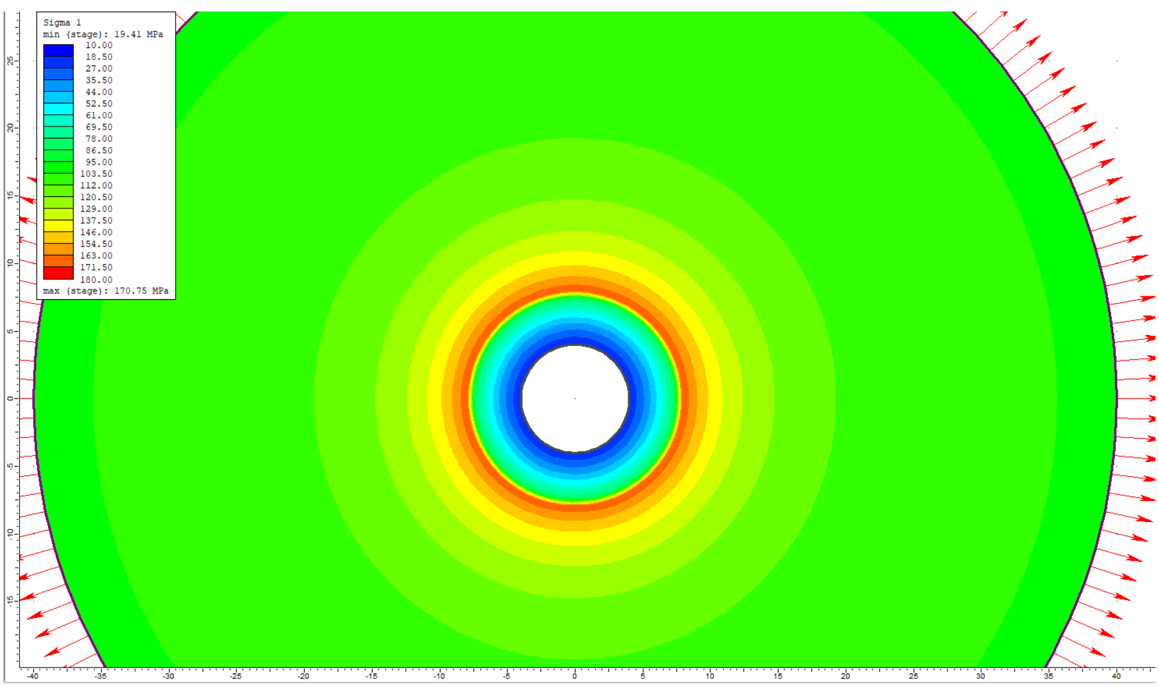

Figure 30.5: Tangential stress contour plot in *RS2*

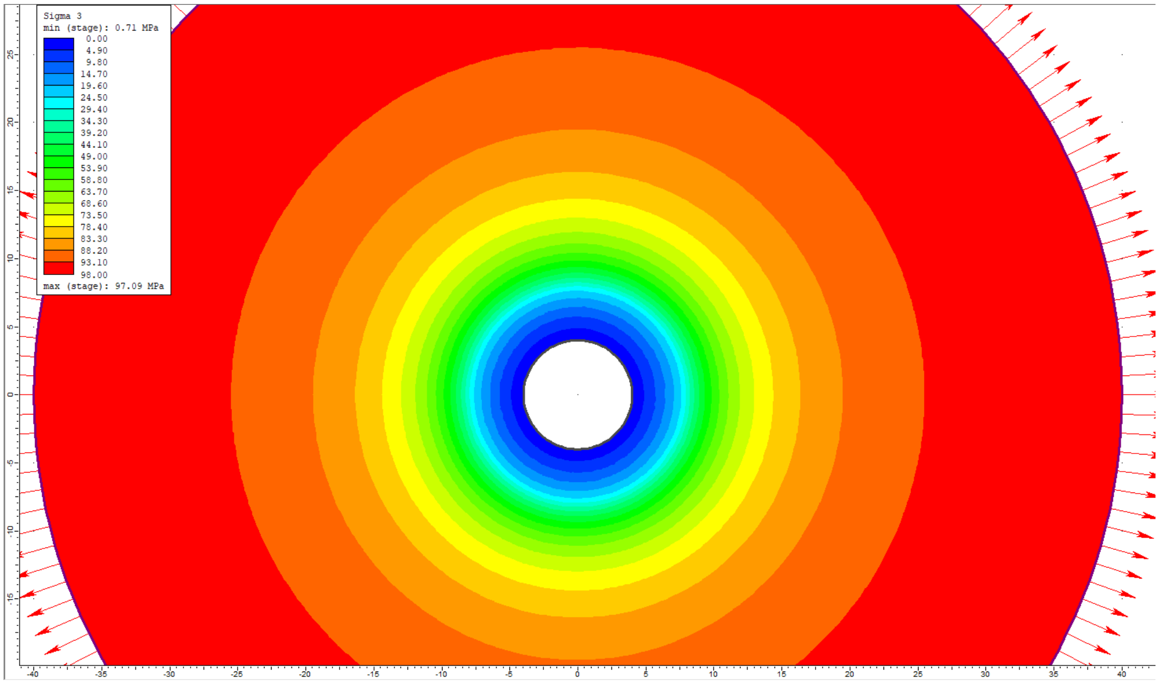

Figure 30.6: Radial stress contour plot in *RS2*

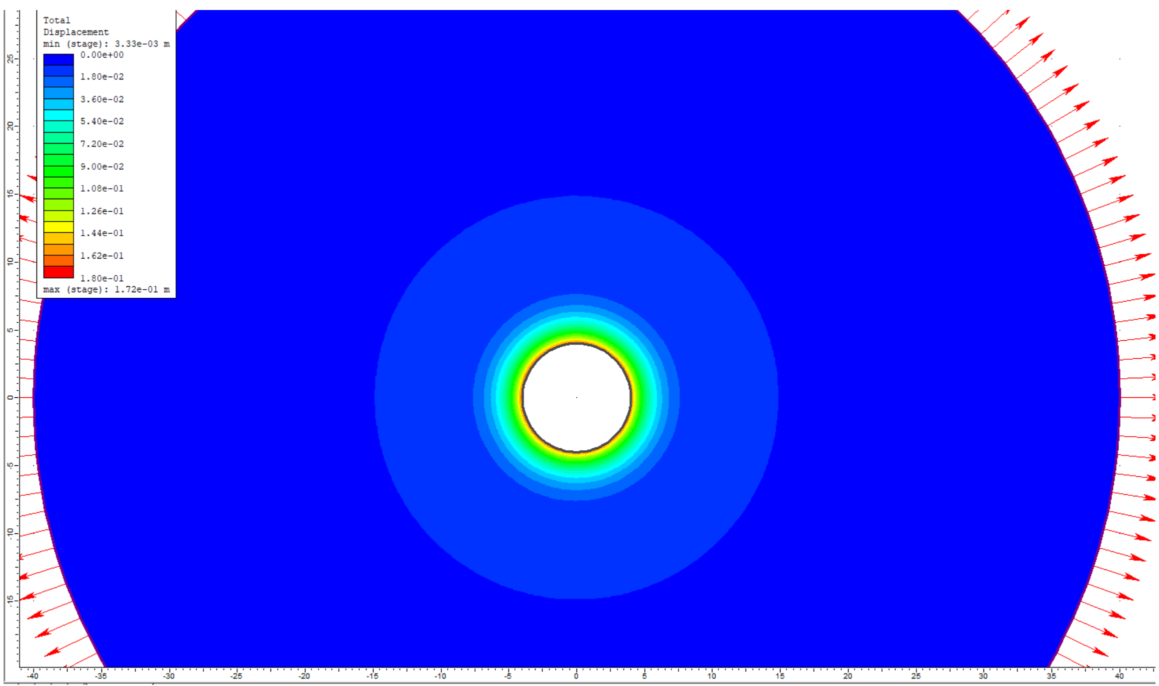

Figure 30.7: Radial displacement contour plot in *RS2*

30.4 References

1. Reed, M. B., (1986) "Stress and Displacements around a Cylindrical Cavity in Soft Rock", IMA Journal of Applied Mathematics, 36, pp. 223-245.

30.5 Data Files

The input file **stress#030.fez** can be downloaded from the RS2 Online Help page for Verification Manuals.

31 Axially Loaded Piles in Cohesionless Soil

31.1 Problem Description

This problem examines two load transfer mechanisms in axially loaded piles: skin friction along the shaft, and end-bearing. The pile is first subjected to axial loads until failure resisted only by skin friction along the shaft. End-bearing effects are then included and the simulation is repeated. The ultimate bearing capacity for both conditions are calculated and compared.

31.2 Analytical Solution

The following equations were taken from the FLAC3D - Structural Elements Manual (Itasca Consulting Group Inc., 2002). Cernica (1995) calculates the ultimate bearing capacity of a single pile in cohesionless soil from shaft resistance due to skin friction as:

$$Q_s = \sum_i L_i (a_s)_i (s_s)_i$$

where L_i = pile length at i increment
$(a_s)_i$ = area of pile surface per length in contact with soil at increment i
$(S_s)_i$ = unit shaft resistance at increment i

The equation can be simplified assuming uniform soil material and constant pile cross section, a_s and s_s become constant:

$$Q_s = L a_s s_s$$

In free draining cohensionless soil, unit shaft resistance, s_s, is given by:

$$s_s = K_s \sigma_{avg} \tan \phi_s$$

where K_s = average coefficient of earth pressure on the pile shaft
σ_{avg} = average effective overburden pressure along pile shaft
ϕ_s = angle of skin friction

The end-bearing capacity, Q_p, of a single pile in cohesionless soil is given by (Cernica, 1995):

$$Q_p = A_p \gamma L N_q$$

where A_p = cross sectional area of pile tip
γ = unit weight of soil
N_q = $\left(\frac{1+\sin\phi}{1-\sin\phi}\right)^2$, bearing capacity factor where ϕ is the soil friction angle

The total pile bearing capacity is simply the sum of skin resistance and end-bearing:

$$Q = Q_s + Q_p = La_s K_s \sigma_{avg} \tan\phi_s + A_p \gamma L \left(\frac{1+\sin\phi}{1-\sin\phi}\right)^2$$

31.3 Model Information

The model shown in Figure 31.1 is made up of a host material containing a 7m pile to which various axial forces (10kN to 500kN) were applied. The soil properties are shown below in Table 31.1 and the pile properties are shown in Table 31.2.

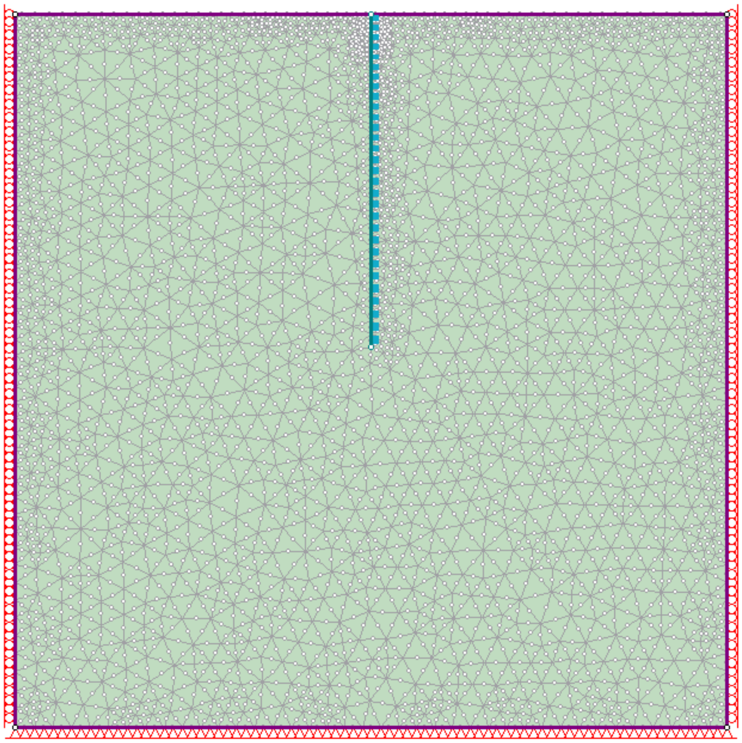

Figure 31.1: Axially loaded pile as modeled in *RS2*

Table 31.1 Soil Properties

Parameter	Value
Young's modulus (*E*)	2812.5 MPa
Unit weight	0.02 MN/m^3
Poisson's ratio	0.40625
Friction angle	10º
Cohesion strength	0 MPa
Average coefficient of earth pressure, (K_s)	1

Table 31.2 Pile Properties

Parameter	Value
Young's modulus (E)	80000 MPa
Poisson's ratio	0.3
Length	7 m
Diameter	1 m
Out-of-Plane Spacing	15 m
Shear stiffness	2812.5 MPa/m
Normal stiffness	28125 MPa/m
Base normal stiffness	28125 MPa
Base force resistance	0.222 MN
Skin friction angle	10º
Skin cohesion	0 MPa

31.4 Results

The graphs below show the load displacement response for axial load tests. Figure 31.2 shows the load-displacement response of piles considering only skin resistance. Figure 31.3 shows the load-displacement response after considering end-bearing effects. The graphs illustrate a clear plateau at the expected ultimate bearing capacity.

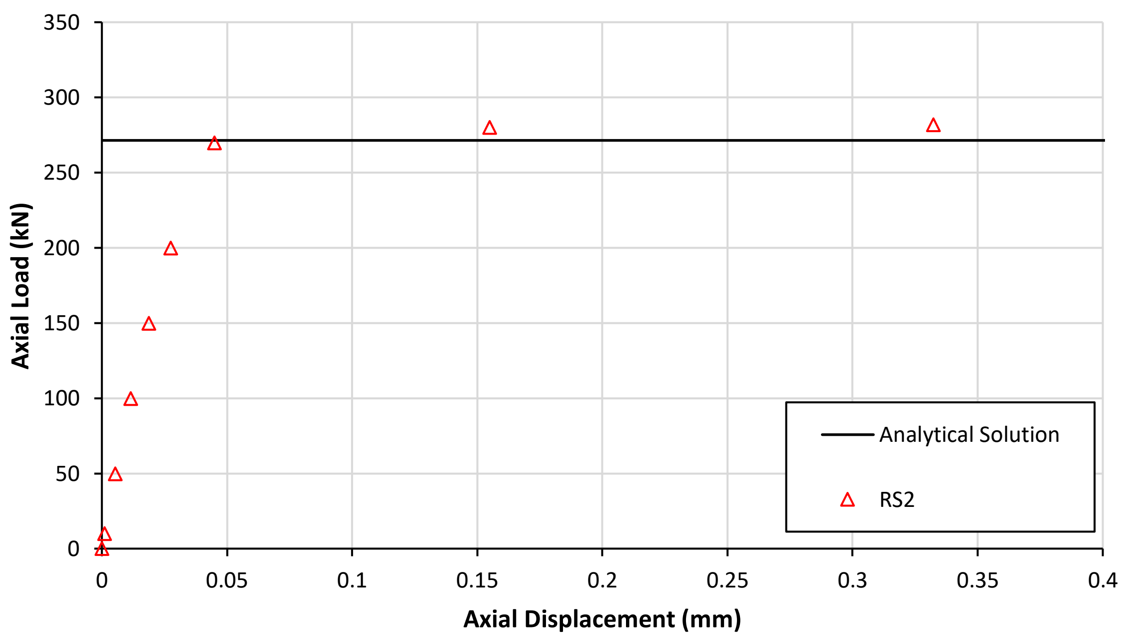

Figure 31.2: Load-displacement response of piles considering only skin resistance

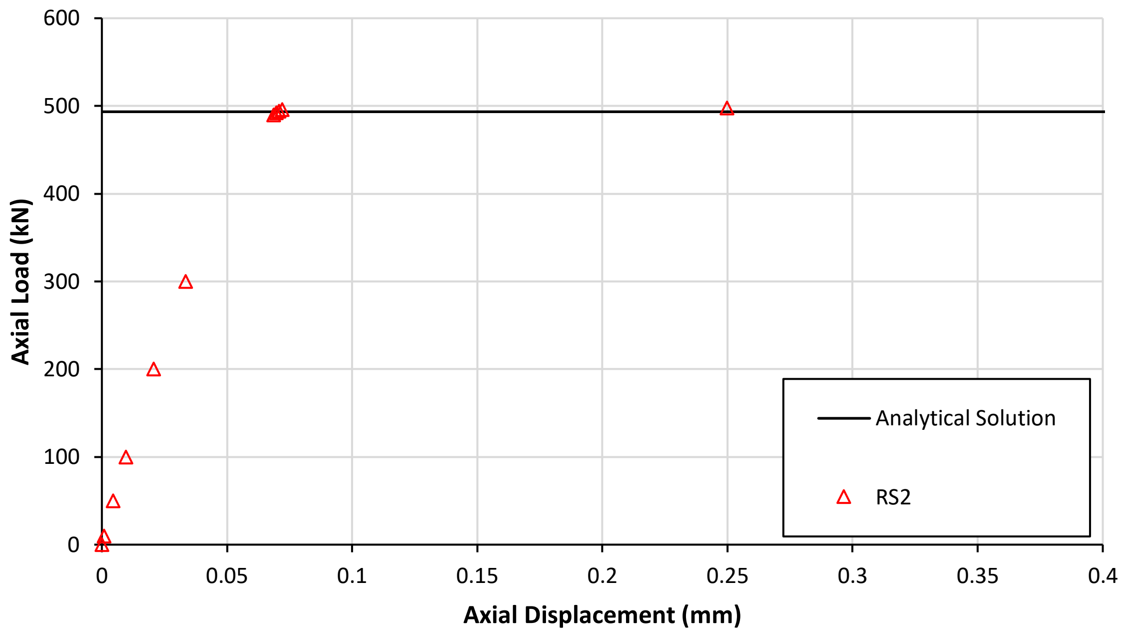

Figure 31.3: Load-displacement response of piles considering skin resistance and end-bearing effects

Table 31.3: Comparison of ultimate bearing capacity results

Effects considered	*RS2* Results	Analytical Solution
Skin resistance only	280 kN	271 kN
Skin resistance and end-bearing	498 kN	493 kN

The graphs and the table above show that ***RS2*** results are in close agreement with the analytical solution.

31.5 References

1. Cernica, J. N. (1995). *Geotechnical Engineering: Foundation Design*, New York: John Wiley & Sons,Inc.
2. Itasca Consulting Group Inc., 2004. *FLAC3D v 2.1 User's Guide - Structural Elements*, Minneapolis, Minnesota, USA.

31.6 Data Files

The input data file **stress #031 no end bearing.fez** and **stress #031 end bearing.fez** can be downloaded from the RS2 Online Help page for Verification Manuals.

32 Undrained behaviour modelling in consolidation analysis of strip footing

32.1 Problem Description

This problem analyzes the consolidation of a smooth flexible strip footing to which a constant pressure is applied. It is similar to RS2 Consolidation Verification Example #5. However, this example focuses on undrained modelling in consolidation analysis with different approaches.

32.2 Background Information

In geotechnical engineering, the behaviour of soil can be either drained or undrained. It refers to the soil's ability to dissipate excess pore pressure induced due to loading. Two factors determine whether the soil is under drained or undrained condition: 1) soil permeability and 2) rate of loading. The soil permeability differs depending on soil types. For instance, sand has high permeability and clay has low permeability.

For drained conditions, when the soil is subjected to loading, excess pore pressure can dissipate out freely. The rate of dissipation is governed by the soil permeability. More permeable soil allows faster dissipation. For drained conditions, loads should be applied slowly, allowing soils to respond and dissipate water out, and eventually achieve equilibrium with respect to pore pressure. In addition, some time might be required after the loading process for fully dissipation. The slow loading is essentially crucial to low permeable soils, as soils can experience undrained condition under quick loads.

For undrained conditions, excess pore pressure is not able to dissipate out from the pores of soil mass. For cases where the rate of dissipation is very low, they will as well be considered as undrained conditions. Undrained condition can be due to zero or low permeable soils, or (and) quick loads. The undrained strengths are obtained when the soils are loaded to failure.

It is up to the practicing engineer to assess the soil properties and loading conditions of a project to determine whether they should use drained or undrained strength parameters. For more information, see the RS2 Undrained Behaviour of Soil topic.

32.3 RS2 Model

32.3.1 Analysis Overview

Three different approaches are presented to modelling undrained behaviours. Strength parameters, stiffness parameters, as well as material/stage behaviours are taken into consideration.

All three approaches can be used to model short term behaviors in clays. However, for consolidation analysis, approach 1 cannot be used since no pore pressure is generated and approach 2 is not recommended since the pore pressure generation is not accurate. Therefore, to consider effects of consolidation and changes in pore pressure, approach 3 would be the most appropriate method.

1. Using undrained strength parameters and undrained stiffness parameters. Material behaviour set to drained.
2. Using undrained strength parameters and effective stiffness parameters.
    a. Consolidation Option = Uncoupled
    b. Consolidation Option = Coupled (Biot)
    c. Consolidation Option = None
3. Using effective strength parameters and effective stiffness parameters.
    a. Consolidation Option = Uncoupled
    b. Consolidation Option = Coupled (Biot)
    c. Consolidation Option = None

The undrained analysis can be performed by defining the material behaviour to "undrained", or by defining the stage behaviour to "undrained" for consolidation analysis. The undrained behaviour setting for each approach is listed in Table 32.1 below.

Table 32.1: Drainage behaviour setting for each approach

Approach	Stage behaviour	Material behaviour
1	-	Drained
2a	Undrained	Drained
2b	Undrained	Drained
2c	-	Undrained
3a	Undrained	Drained
3b	Undrained	Drained
3c	-	Undrained

32.3.2 Geometry

The strip footing is 16m by 8m in dimension. A graded 6-noded triangle mesh was used. The load incremented from 0 to 4.98 kPa/m^2 are applied through 14 stages until collapse load, as shown in Table 32.2 below. Figure 32.1 below shows the model geometry.

Table 32.2: Load increments

Stage	Load (kPa/m^2)
1	0
2	2
3	2.5
4	3
5	3.5
6	4

7	4.5
8	4.6
9	4.7
10	4.8
11	4.9
12	4.91
13	4.95
14	4.98

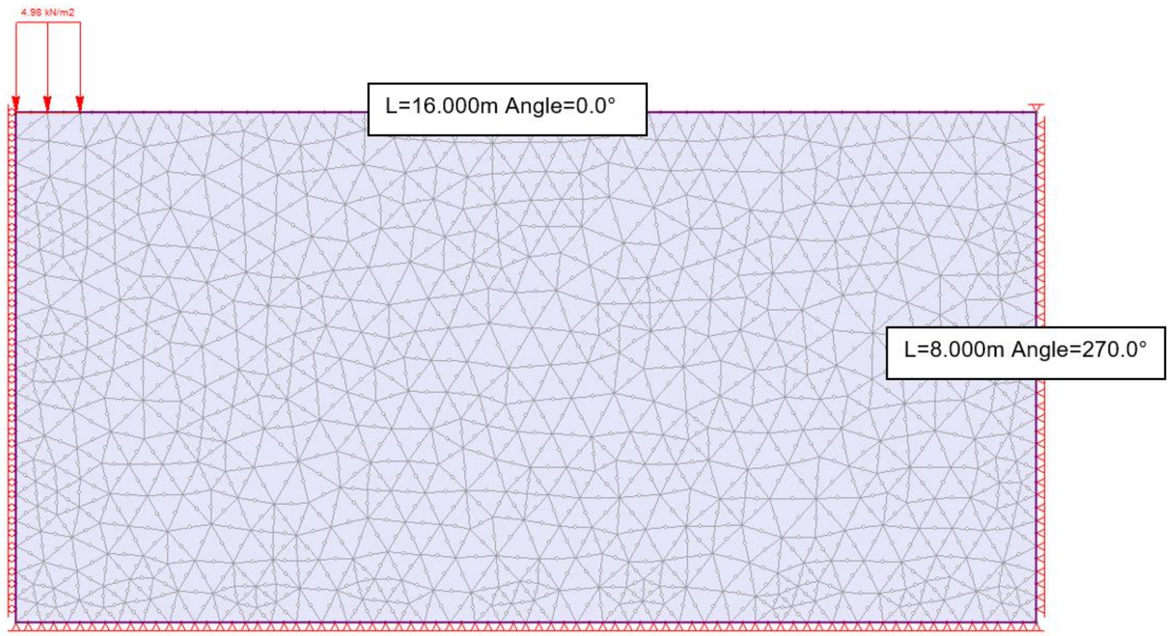

Figure 32.1: Flexible strip footing on elastoplastic layer

32.3.3 Material Properties

Table 32.3 below showcases the material parameters for each of the analyses (seven in total).

Table 32.3: Material Properties for seven models

Approach Followed	1	2a	2b	2c	3a	3b	3c
Young's modulus (E') (kPa)	230	200	200	200	200	200	200
Poisson's ratio (v') (-)	0.499	0.3	0.3	0.3	0.3	0.3	0.3
Friction angle (ϕ') (º)	0	0	0	0	20	20	20
Cohesion (c) (kPa)	0.941	0.941	0.941	0.941	1	1	1
Dilitancy angle (ψ') (º)	0	0	0	0	0	0	0
Unit Weight (kN/m3)	27	27	27	27	27	27	27
Porosity (-)	0.5	0.5	0.5	0.5	0.5	0.5	0.5
Initial Water Condition	-	Dry	Dry	-	Dry	Dry	-
Failure Criterion	Mohr-	Mohr-	Mohr-	Mohr-	Mohr-	Mohr-	Mohr-

		Coulomb	Coulomb	Coulomb	Coulomb	Coulomb	Coulomb	Coulomb
Material Type		Plastic	Plastic	Plastic	Plastic	Plastic	Plastic	Plastic
Peak Tensile Strength (kPa)		100	100	100	100	100	100	100
Residual		Peak	Peak	Peak	Peak	Peak	Peak	Peak
Material Behaviour		Drained	Drained	Drained	Undrained	Drained	Drained	Undrained
Static Water Mode		Dry	-	-	Dry	-	-	Dry
Fluid Bulk Modulus (kPa)		-	2.20E+06	2.20E+06	2.20E+06	2.20E+06	2.20E+06	2.20E+06
Hydraulic Parameters	**Ks (m/s)**	-	1.00E-07	1.00E-07	-	1.00E-07	1.00E-07	-
	K2 / K1	-	1	1	-	1	1	-
	K1 Definition	-	Angle	Angle	-	Angle	Angle	-
	K1 Angle (º)	-	0	0	-	0	0	-
	WC sat (m3/m3)	-	0.4	-	-	0.4	-	-
	WC res (m3/m3)	-	0	-	-	0	-	-
	mv (m3/m3/kPa)	-	0.0002	-	-	0.0002	-	-
Simple Parameters	**Soil Type**	-	General	General	-	General	General	-

32.4 Results

To account for different consolidation options in all three approaches, seven analyses were conducted using different approaches in modelling undrained behaviour with RS2. All analyses failed at the last two stages. Approach 1, 2b, and 3b failed at load of 4.95kPa. Approach 2a, 2c, 3a, and 3c failed at load of 4.98kPa. The total displacement and pore pressure results were compared and discussed.

Figure 32.2 below shows the total displacement contour of approach 3b at stage 6. The total displacement results of a defined point (0.5, -0.5) over the loading increments for all analyses were plotted in Figure 32.3 below.

As seen from Figure 32.3, results for total displacement vs. load are basically identical for all approaches. For converged stages, the minimum displacement happened at stage 2 of around 0.0147m while the maximum displacement is about 0.168m in stage 13. Among seven analyses, the minimum differential displacement is around 0.76% with the max being around 4.30% when the load approaching the collapse threshold, entailing that RS2’s results are very consistent for all approaches when using equivalent input parameters.

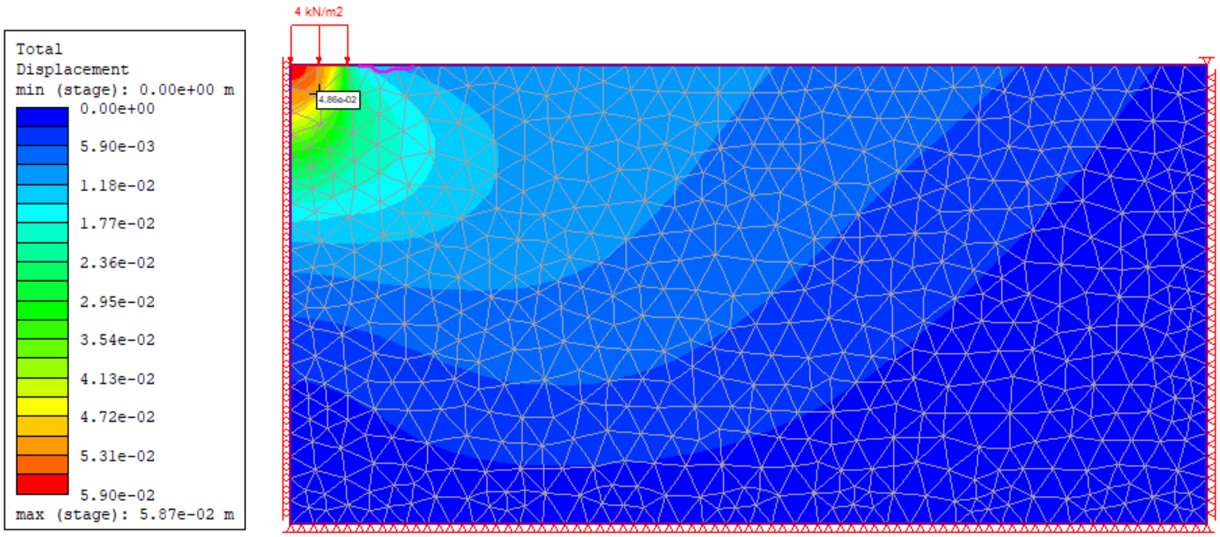

Figure 32.2: Total displacement contour (approach 3b)

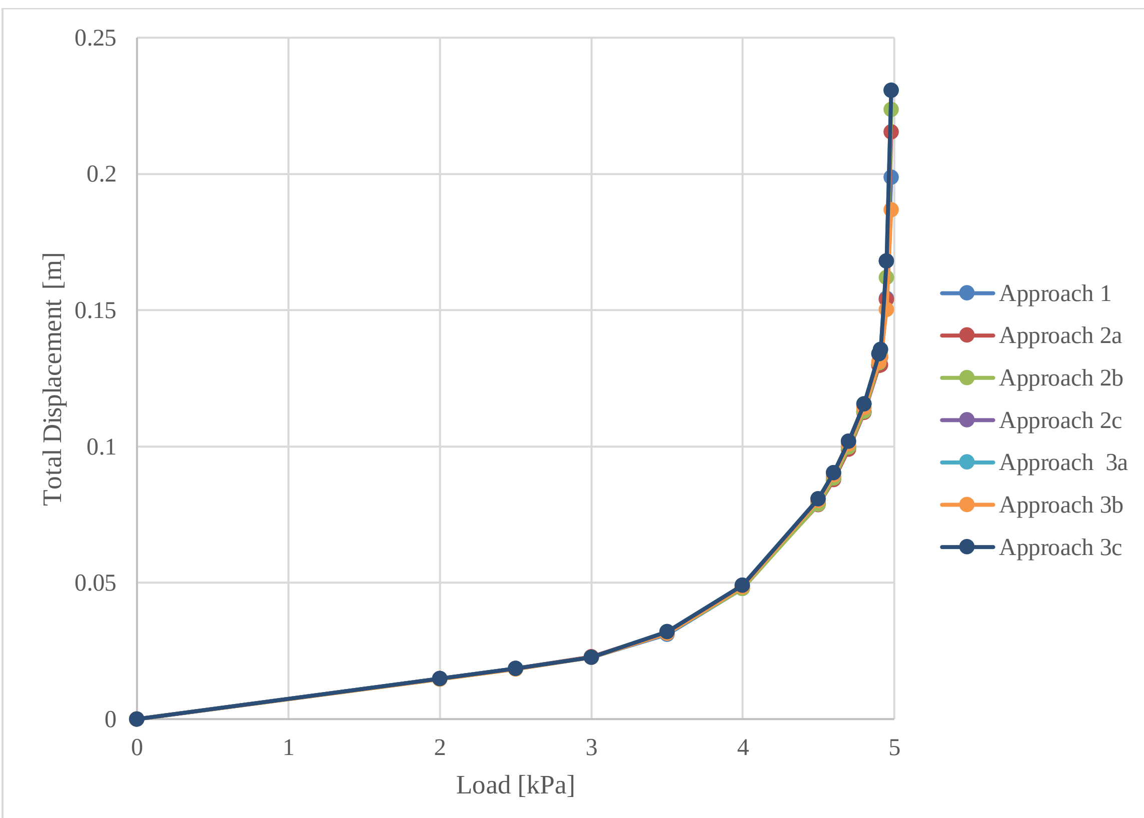

Figure 32.3: Total displacement as a function of load of all approaches

Figure 32.4 below shows the pore pressure contour of approach 3b at stage 6. The pore pressure results of a defined point (0.5, -0.5) over the loading increments for all analyses were plotted in Figure 32.5 below.

As seen from Figure 32.5, no pore pressure is accounted for with approach 1. Approach 2a, 2c, 3a and 3c have almost identical results. Approach 2b and 3b have mostly identical results as well. The pattern for approach 2a, 2c, 3a and 3c are similar to that of approach 2b and 3b, while the former ones have slightly lower results after the load of 3kPa.

It means that the results of Pore Pressure vs. Load are matching well between approach 2 and 3, while their consolidation options do have a slight effect. The coupled (Biot) consolidation analysis results in a bit lower pore pressure after load of 3kPa, compared to uncoupled and none consolidation analysis.

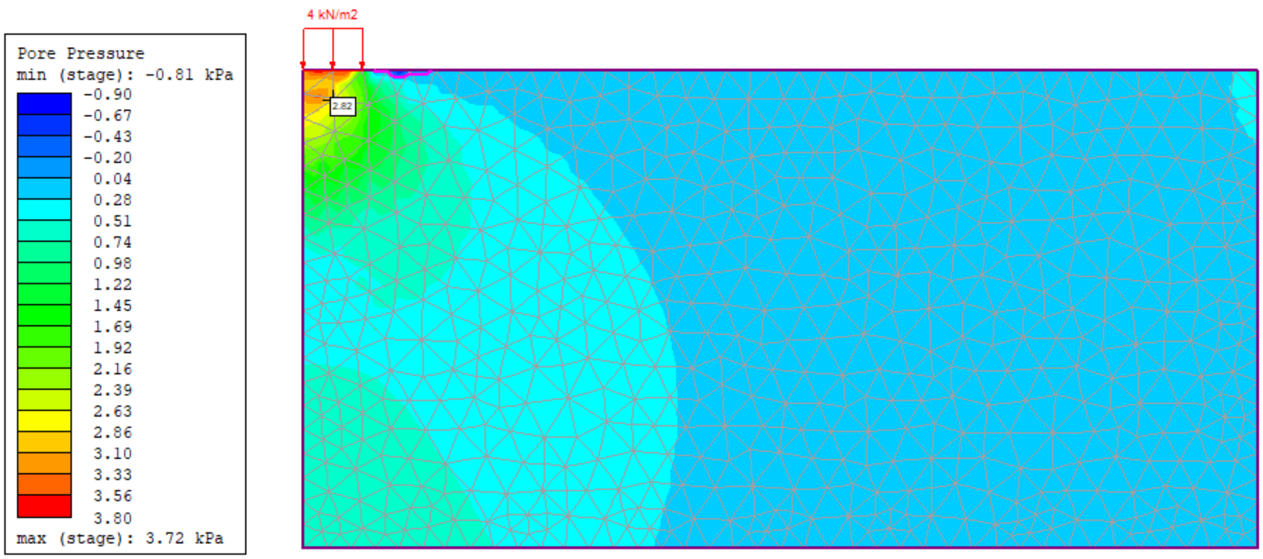

Figure 32.4: Pore pressure contour (approach 3b)

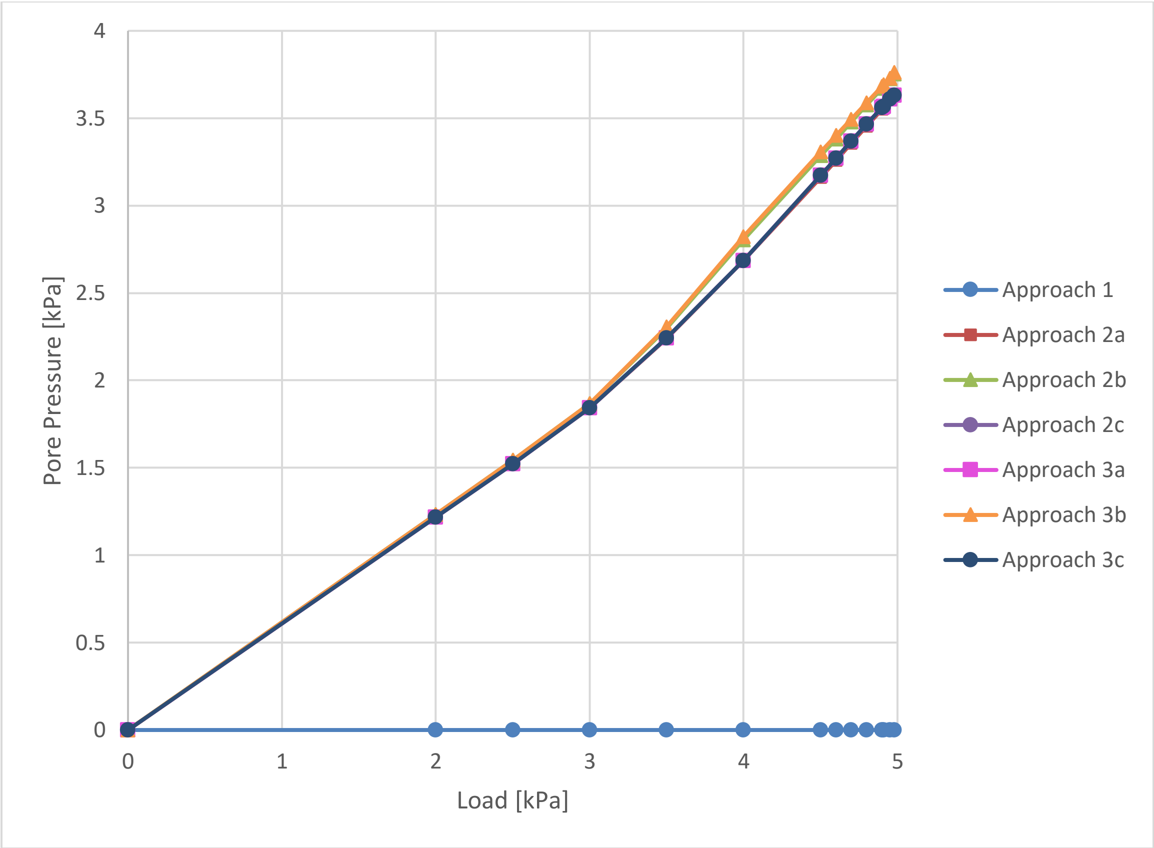

Figure 32.5: Pore pressure as a function of load for all approaches

In conclusion, generally, approach 2 and 3 give very similar results in undrained behaviour modelling in consolidation analysis. In terms of consolidation options, the coupled (Biot) consolidation analysis will lead to slightly lower pore pressure when loading increases. Approach 1 has the same total displacement results as other two approaches, but it does not account for any pore pressure.

Note that for the sake of simplicity, no body weight was included in this verification since the undrained shear strength should be varied by depth when accounting for the body force. The excess pore pressure generation between approach 2 and 3 in more complicated cases should also be varied depending on the material types, loading sequences (excavation, embankment, etc).

32.5 References

1. Small, J.C., Elasto-plastic consolidation of Soils, PhD thesis, University of Sydney, 1977.

2. Prandtl, L., ‘Spannungsverteilung in plastischen Koerpern’, in Proceedings of the 1st International Congress on Applied Mechanics, Delft, 43-54, 1924.

32.6 Data Files

The input files:

stress#032_1.fez
stress#032_2a.fez
stress#032_2b.fez
stress#032_2c.fez
stress#032_3a.fez
stress#032_3b.fez
stress#032_3c.fez

can be downloaded from the RS2 Online Help page for Verification Manuals.